University of Bath

PHD

Computation of Rim-sealed Ingestion for Gas Turbines

Teuber, Roy

Award date:
2014

Awarding institution:
University of Bath

Link to publication

General rights
Copyright and moral rights for the publications made accessible in the public portal are retained by the authors and/or other copyright owners and it is a condition of accessing publications that users recognise and abide by the legal requirements associated with these rights.

- Users may download and print one copy of any publication from the public portal for the purpose of private study or research.
- You may not further distribute the material or use it for any profit-making activity or commercial gain
- You may freely distribute the URL identifying the publication in the public portal ?

Take down policy
If you believe that this document breaches copyright please contact us providing details, and we will remove access to the work immediately and investigate your claim.

Download date: 22. May. 2019

Computation of Rim-Sealed Ingestion for Gas Turbines

submitted by

Roy Teuber

for the degree of Doctor of Philosophy

of the

University of Bath

Department of Mechanical Engineering

August 2014

COPYRIGHT

Attention is drawn to the fact that copyright of this thesis rests with the author. A copy of this thesis has been supplied on condition that anyone who consults it is understood to recognise that its copyright rest with the author and that they must not copy it or use material from it except as permitted by law or with the consent of the author.

This thesis may be made available for consultation within the University Library and may be photocopied or lent to other libraries for the purposes of consultation with effect from 16.02.2017

Signed on behalf of the Faculty/School of .....

Abstract

This thesis focuses on the ingress problem in rotor-stator system in turbines with the primary emphasis on numerical methods.

The first part of this dissertation implemented a newly-developed orifice model for externally-induced (EI) ingress into a non-commercial one-dimensional (1D) flow network solver. The massflow functions of the EI ingress model are solved with an iterative procedure with inner and outer loop iterations. The comparison of this model against a standard procedure where the fluid exchange is modelled with multiple branches was in good agreement despite a diverging behaviour at high sealing effectiveness.

An extrapolation method was developed to extrapolate the sealing parameter Φ_{min} from one Mach number regime to another. This procedure, which uses the linear saw-tooth model for EI ingress, showed good agreement with the computed values of Φ_{min} over the investigated subsonic range. It was proposed to use this method to scale the experimentally determined Φ_{min} value obtained at incompressible test rig conditions to a geometric similar engine at compressible conditions.

The effect of aerodynamic off-design conditions (varying flow coefficient, C_F) and their impact on ingress in rotor-stator systems was investigated with transient CFD computations. Pressure measurements behind the trailing edge of the vane showed a linear variation of the non-dimensional pressure coefficient in the form of $\Delta C_p^{1/2}$ with flow coefficient. This behaviour was confirmed numerically with the exception of a diverging behaviour with an increase of ΔC_p at low values of C_F. This effect could be isolated and associated with the rotor blade at large deviation angles.

Various rim-seal concepts were numerically investigated with the intent to minimise the ingress levels in the wheel-space of a high pressure turbine. These concepts were experimentally tested at the ingress facility of the University of Bath and confirmed predicting the ranking order of these seals by the numerical investigation. An optimised rim-seal design was developed from this study which addresses the root cause of the EI ingress by attenuating the tangential pressure variation; the new rim-seal reduced the sealing parameter Φ_{min} by about 40% compared a the baseline case.

A numerical study investigated several rotor endwall concepts with the objective to minimise the mixing loss associated with the interaction of the egress with the mainstream flow. A 3D concept with leading edge feature along with an incorporated egress channel within the endwall reduces not only the interaction loss but also losses associated to secondary flows, (i.e. horse show vortex and cross passage flow), without negatively impacting the ingress levels of the upstream located wheel-space.

This thesis is dedicated to Mika and my family for the support and patience.

Acknowledgements

First and foremost I would like to thank my academic supervisors Prof. G.D. Lock and Dr Mike Wilson for providing the opportunity to undertake my Ph.D research as KTP Associate in an industrial environment with the partner Siemens Industrial Turbomachinery Ltd. They provided invaluable advice and support throughout this programme which significantly helped me to develop as a researcher. Furthermore, I am deeply grateful of the support of Prof. Mike Owen and the passion for his research will always be remember with appreciation.

Special thanks goes to Dr Yan Sheng Li for the support as industrial supervisor over the course of the three-year programme. Yan Sheng provided me with his invaluable advice that contributed to the outcome of this research.

Technical acknowledgement is given to the Aero-thermal group in Lincoln and Finpång (S) at Siemens, special thanks to Dr John Maltson, Dr Daniel Eriksson, Dr Peter Jaksch and Pete Smith of the SAS Group and to Dr Li Shing Wong, Dr Senthil Krishnababu, Dawid Frach and Dr Semiu Ghadebo for their technical support, advice given and the fruitful discussions we have had over the last three years.

Furthermore, I'd like to thank the Gas Turbine Research Team and in particular James Scobie for the support and guidance during the ingress experiments at the University of Bath.

Contents

List of Figures

List of Tables

Nomenclature

List of Symbols

Symbol	Description	Equation
$a_o - a_4$	constants for polynomials	
A	constant for variable C_d	$A'/C_{d,e'}C_{\beta 1}^{1/2}$
A'	constant for variable C_d	
A_c	seal-clearance	$2\pi bs_c$ $= A_e + A_i$
b	radius of seal	
$b_o - b_5$	constants for polynomials	
c	CO_2 concentration	
C	empirical constant	
C	Ethylene concentration	
c_{ax}, c_x	axial chord of aerofoil	
C_d	discharge coefficient in theoretical model	
$C_{d,e'}$	value of $C_{d,e}$ for RI ingress	
C_F	flow coefficient	Re_W/Re_ϕ
C_p	external pressure coefficient	$(p_2 - \overline{p_2})$ $/(1/2\varrho\Omega^2 b^2)$
C_P	specific heat capacity at constant pressure	
$C_{p,max}$		$\Delta p_{max}/$ $(1/2\varrho\overline{W}^2)$
C_V	specific heat capacity at constant volume	
C_w	non-dimensional flow rate	$\dot{m}/(\mu b)$
$C_{w,e}, C_{w,i}$	value of c_w for egress, ingress	
$C_{w,min}$	minimum value of $C_{w,o}$ to prevent ingress	
$C_{w,o}$	non-dimensional flow rate	
C_1	absolute nozzle guide vane exit velocity	
$C_{\beta 1}$	modified internal swirl ratio	$\beta/(1 - r_1^2/r_2^2)$
f	factor shape for gas path pressure	$(p_2 - p_{2,min})$ / $(p_{2,max} - p_{2,min})$

Symbol	Description	Equation
g	normalised wheel-space pressure	$(p_1 - p_{2,min})$ $(p_{2,max} - p_{2,min})$
G	axial gap ratio	S/b
G_c	seal-clearance ratio	s_c/b
$g^\star$	value of g when when $C_w = C_{w,o}$	
h	enthalpy	$C_P T$
h	distance between hub and casing	
I	integral for EI model	
k	thermal conductivity	
k_a	empirical constant	
k_c	empirical constant	
k_{eff}	effective thermal conductivity	
K	empirical constant	$\sqrt{(2/\Delta C_p)}\Phi_{min,EI}$
$\dot{m}_1$	freestream mass flow rate	
$\dot{m}_L$	leakage mass flow rate	
$\dot{m}$	mass flow rate	
M	isentropic external Mach number	
p	static pressure	
P_{max}	external pressure coefficient	$1/2 C_{P,max} Re_W^2$
Pr_t	Prandtl number	
$\overline{p_2}$	mean absolute static pressure across 1 vane pitch	
$p^\star$	value of p when $C_w = C_{w,o}$	
$P_{0,CAV,REL}$	average total pressure in the cavity	
$P_{01,EFF}$	ave freestream total pressure upstream of the aerofoil	
q_{in}	heat transfer per unit area into control volume	
r	radius	
R	hub radius of stator and rotor	
R	gas constant	
Re_{C1}	external flow Reynolds number	$C_1 \varrho R/\mu$
Re_u	rotational Reynolds number	$\varrho \Omega R^2/\mu$
Re_W	axial Reynolds number	$\varrho \Omega b^2/\mu$
Re_ϕ	rotational Reynolds number	$\varrho \Omega b^2/\mu$
s	axial spacing between rotor and stator	
s	specific entropy	
s_c	seal clearance	
$\dot{S}'''_{gen}$	Entropy generation rate per unit volume	
T	static temperature	
T_o, T_t	total or stagnation temperature	

Symbol	Description	Equation
T_c, T_h	cold and hot reference temperature	
u	rotational velocity	
u_t	friction velocity	$(\tau_w/\varrho)^{(1/2)}$
$\vec{V}$	velocity vector	
V_z, V_r, V_ϕ	axial, radial and tangential comp. of velocity	
w	specific work	
W	axial velocity in gas path	
W_o	axial velocity in gas path at design	
$\overline{W}$	uniform value of W in inner part of annulus	
x	axial coordinate starting at TE vane	
y	distance of near-wall node from wall surface	
Y	loss coefficient	
y^+	non-dimensional wall distance	$yu_t\varrho/\mu$
z	axial distance between TE vane and LE blade	
z	axial direction	
α	vane angle	
β	swirl ratio	$V_\phi/(\Omega b)$
β	blade relative angle	
β_o	blade relative angle at design	
$\beta - \beta_o$	deviation angle	
δ	boundary layer thickness	
δ	error threshold	
δA	area of streamtube	
ΔC_p	external pressure coefficient	$\Delta p_2/(1/2\varrho\Omega^2 b^2)$
Δp_2	peak-to-trough pressure difference	$p_{2,max} - p_{2,min}$
ε	sealing effectiveness	Φ_o/Φ_e
ε_c	concentration sealing effectiveness	$(c_s - c_a)/(c_o - c_a)$
ε_p	pressure sealing effectiveness	
ε_{cc}	computed concentration sealing effectiveness	c_s/c_o
ϕ	angular coordinate	
Φ	non-dimensional sealing parameter	$C_w/(2\pi G_c Re_\phi)$
Φ_e	value of Φ when $C_w = C_{w,e}$	$C_{w,o}/(2\pi G_c Re_\phi)$
Φ_i	value of Φ when $C_w = C_{w,i}$	$C_{w,i}/(2\pi G_c Re_\phi)$
Φ_o	value of Φ when $C_w = C_{w,o}$	$C_{w,e}/(2\pi G_c Re_\phi)$
Φ_{min}	value of Φ_o when $\varepsilon_c = 1$	
Φ'_{min}	value of Φ_o when $\varepsilon_c = 0.95$	
γ	ratio of specific heats	C_P/C_V
Γ_c	ratio of discharge coefficients	$C_{d,i}/C_{d,e}$
Γ_p	pressure parameter	$C_p/C_{\beta 1}$

Symbol	Description	Equation
$\Gamma_{\Delta p}$	external pressure coefficient	$\Delta C_p / C_{\beta 1}$
Γ_T	summation of Γ parameters	
η	cooling effectiveness	$\Psi / \Psi_{coolant}$
η_S	sealing effectiveness (Ethylene)	C_{Seal} / C_L
λ_T	turbulent flow parameter	$C_{w,o} / Re_{\phi}^{0.8}$
μ	dynamic viscosity	
μ_{eff}	effective viscosity	
θ	angular coordinate between vanes	
θ	cooling effectiveness	$(T - T_c)(T_h - T_c)$
θ'	value of θ when $V_r = 0$	$1/2(1 - g)$
ϱ	density	
τ_w	wall shear stress	
τ_{ij}	shear stress tensor	
Ψ	CO_2 concentration	
Ω	angular speed of rotating disc	
ϕ	angular coordinate	

List of Acroyms

Symbol	Description
B	baseline case
BPP	blade passing period
$BSL\ \ RSM$	baseline Reynolds Stress model
CFD	computational fluid dynamics
CFX	commercial CFD code
CI	combined ingress
$C\#$	C Sharp
$C.1$	rim-seal concept 1
$C.2$	rim-seal concept 2
$C.3$	rim-seal concept 3
$C.4$	rim-seal concept 4
EI	externally-induced ingress
$EPSRC$	Engineering and Physical Sciences Research Council
FR	Frozen Rotor
GGI	General Grid Interface
GUI	Graphical User Interface

Symbol	Description
HP	high pressure
$ICEM$	commercial mesher
KTP	Knowledge Transfer Partnership
$k-\varepsilon$	2-equation turbulence model
LE	leading edge
LP	low pressure
$MAGPI$	Main Annulus Gas Path Interactions
NGV	nozzle guide vane
NLH	Non-linear Harmonic
O	optimised rim-seal
OM	orifice model
$PLIF$	Planar Laser-Induced Fluorescence
RB	rotor blade
RI	rotationally-induced ingress
SAS	secondary air system
S	stator
$SSG \quad RSM$	Reynolds Stress Model by Speziale-Sarkar-Gatski
$SST \quad k-\omega$	2-equation turbulence model by Menter
$S1$	blade-to-blade surface streamline
$S2$	hub-to-tip surface streamlime
TE	trailing edge
TET	turbine entry temperature
WS	wheel-space
$1D$	one-dimensional
$3D$	three-dimensional

Subscripts

Symbol	Description
a	ambient
ave	average
ax	axial
CI	combined ingress
com	compressible regime
$coolant$	sealant flow
D	design condition
e	egress
EI	externally-induced ingress
eng	compressible regime

Symbol	Description
ext	extrapolated
gp	gas path
i	ingress
in	at inlet
inc	incompressible regime
L	cavity
max	maximum
min	minimum
mix	mixed out
o	superimposed flow
rad	radial
rig	incompressible condition
RI	rotationally-induced ingress
$rotor$	rotor
$s,\ SP$	sampling point
$Seal$	at the control plane underneath the rim seal
$stator$	stator
$therm$	due to thermal effects
tot	total or stagnation properties
$t1$,$t2$	stagnation quantity at inflow and outflow
$t2s$	stagnation quantity after ideal expansion
$visc$	due to viscous effects
WS	wheel-space
1,2	location in wheel-space and gas path

Chapter 1

Introduction

1.1 Secondary/Internal Air System

The drive for higher engine efficiencies in industrial gas turbines and aero engines has resulted to the continuous increase in the compressor pressure ratio and turbine entry temperature (TET) in the last century. Fig. 1.1-1 shows this development of the TET from 1950 to 2000 for both aero engines and industrial gas turbines. Historically, aero engines have had higher turbine entry temperatures than gas turbines with an increase of $\approx 100°C$ per decade but the recent increase of the turbine temperature in gas turbines approaches the trend set by aero engines.

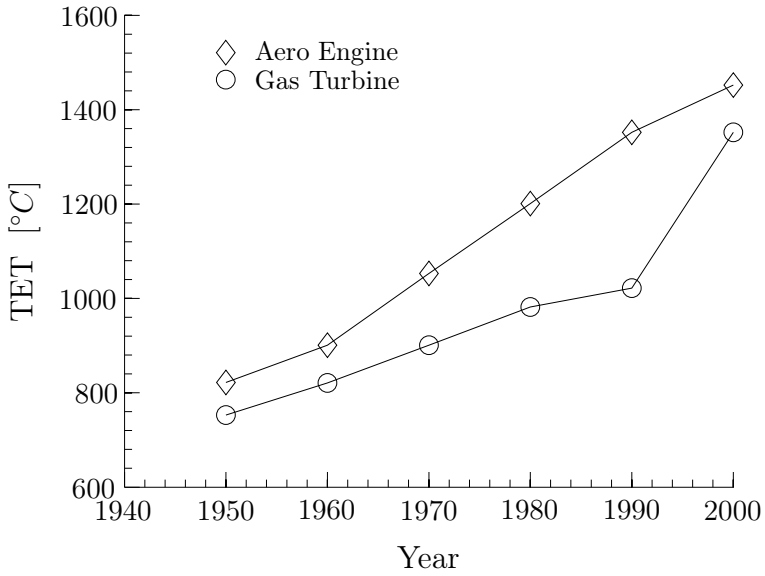

Fig. 1.1-1: Historical development of the turbine entry temperature between aero engines and gas turbines (data extracted from Boyce (1996))

To deal with these constantly increasing temperatures, the capability of the heat resistant materials in turbines has been increased significantly as illustrated

by Fig. 1.1-2. This has resulted in an increase of the capability of the material by roughly $350°C$ between 1940 and 2000, achieved principally by improvements in the heat resistant material and the manufacturing techniques. The latter category includes the shift from traditional casting procedures to directionally solidified turbine components and to the single crystal technology (Rolls-Royce, 1996).

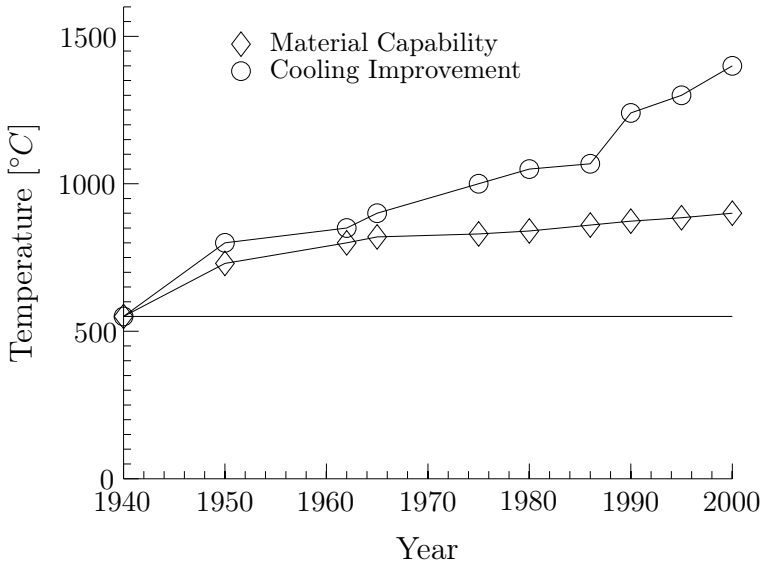

FIG. 1.1-2: Historically development of the material temperature limits (data extracted from Hunt (2011))

Despite these improvements, higher turbine entry temperatures can only be achieved by the introduction of cooling techniques applied to the hot side of the engine. This cooling air is extracted at various stages in the low pressure (LP)/high pressure (HP) compressor and channelled through the engine to the turbine side. To improve efficiency, the air from the last stages of the compressor is supplied to the high pressure turbine, while the low pressure compressed air is supplied to the turbine components further downstream. Fig. 1.1-3 (here shown for an aero engine) shows such a system for controlling the temperatures, referred to as an internal or secondary air system.

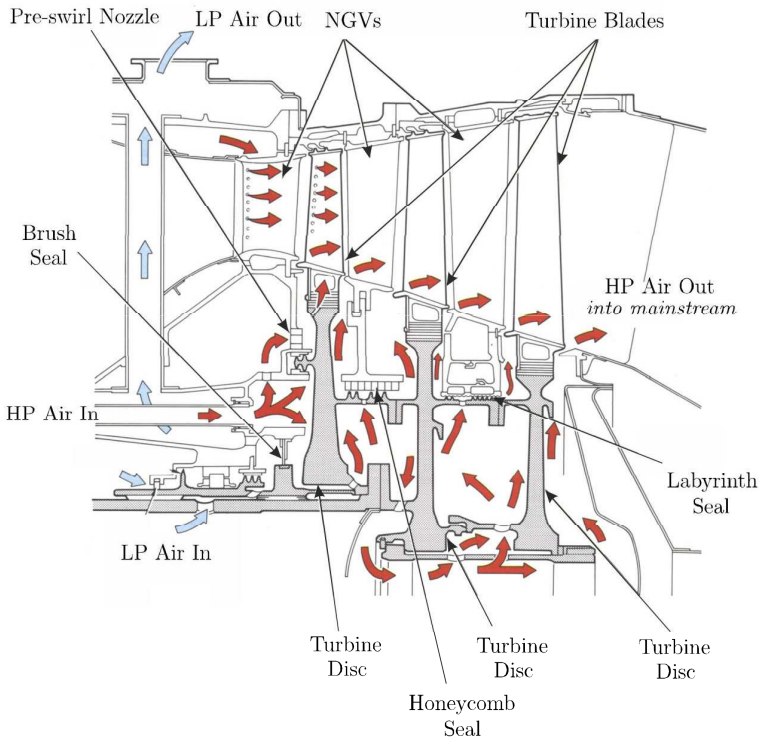

FIG. 1.1-3: Internal air system of an aero engine (Rolls-Royce, 1996)

This air is used along with advanced cooling techniques to control the metal temperature of critical components in the high pressure turbine, such as the nozzle guide vane, rotor blade and the rotor disc as shown in Fig. 1.1-4(a). State-of-the-art cooling concepts include the film cooling of blades and vanes, and the application of ceramic thermal barriers.

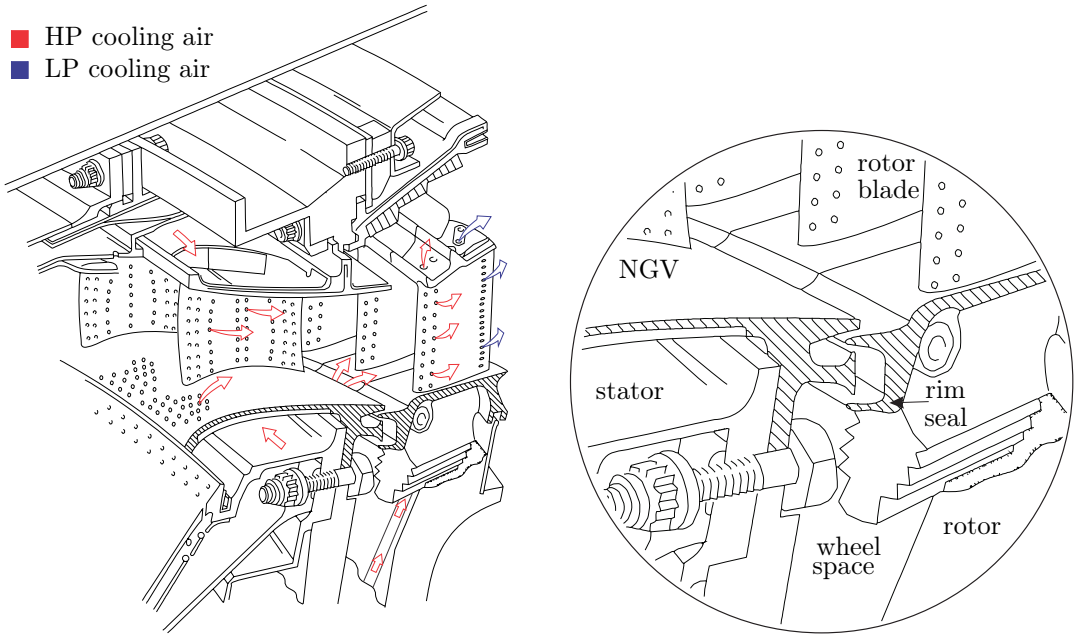

FIG. 1.1-4: High pressure turbine stage (adapted from Rolls-Royce (1996); Owen et al. (2010b); (a) internal air system; (b) rim-seal configuration

The objective is to balance the heat flux into the metal components from the primary gas path fluid by increasing the heat transfer coefficient of the internal cooling channels in vanes, blades and platforms. Designers use pedestals, ribs and impingement techniques to remove this heat flux. These cooling technologies ensure that the constantly increasing turbine entry temperature can be tolerated by the metal components without compromising their mechanical integrity by oxidation, exceeding the allowable creep levels or exceeding the low and high cycle fatigue limits.

Fig. 1.1-4(b) shows a typical rim-seal configuration separating the primary gas path from the wheel-space. Ingress from the primary gas path into the wheel-space can threaten the mechanical integrity of the rotor disc; overheating can occur if a sealing flow is not supplied in sufficient quantity to the wheel-space to suppress the gas path flow entering the system.

Rising energy costs and stringent environmental restrictions force the manufacturers of industrial gas turbines and aero engines to increase the overall performance of their engines. Continuous improvements to the internal or secondary air system are important to this performance. Even in highly efficient gas turbines, such as the Siemens *SGT5-8000H* with a combined efficiency in excess of 60%, the secondary air massflow is $\approx$ 10% of the engine mainstream, where $\approx$ 1% is used to seal a single rotor-stator cavity in the high pressure turbine. The focus of the current research is to develop theoretical models to accurately predict this required sealing flow rate and to design new rim-seal with the ability to minimise ingress levels with a simultaneously reduced sealing flow. As a rule of thumb, a 1% reduction in the sealing air increases the thermal turbine efficiency of approximately by 0.4% (Mirzamoghadam et al., 2008). Furthermore, recent activities have investigated the aerodynamic interaction between the discharged egress from rotor-stator systems with the primary gas path flow with the objective to minimise the losses associated with the mixing.

1.2 Thesis Aims and Objectives

The research presented in this dissertation was conducted as part of a Knowledge Transfer Partnership (KTP) between the University of Bath and Siemens Industrial Turbomachinery Ltd., with the objective to transfer academic knowledge and research into an industrial environment. This programme draws on the expertise of the research undertaken at University of Bath on rotating flows in rotor-stator

systems in gas turbines and it enabled its research output to be tailor-made to the needs of the industrial partner to enhance their competitiveness. Additional research beyond the KTP project was undertaken to fulfil the requirements of this Ph.D programme.

This thesis consists of three major objectives: The implementation of a theoretical model into the design practice of Siemens, the development of a numerical fluid-dynamic model to address the ingress problem with subsequent exploitation to derive a novel rim-seal concept and the numerical investigation of the egress-mainstream interaction.

A newly-developed orifice model for predicting the amount of ingested hot gas from the primary gas path into rotor-stator cavities only existed as a research tool. This work translated the academic aspects of this orifice model to an engine-design methodology and transferred it into a usable operational tool suited to design and development at the company. By integrating this model into the design practice at Siemens, uncertainties in predicting the accurate sealing flow rate to prevent ingress has been minimised. The input parameters for this model are obtained from the ingress test facility at the University of Bath. Extensive experimental work has been conducted with this facility for a series of rim-seal geometries to investigate the fluid-mechanics at quasi-incompressible conditions ($0.22 \preceq M \preceq 0.45$). This data needs to be extrapolated to enable its usage within the orifice model at engine operating conditions in a compressible regime ($0.7 \preceq M \preceq 0.85$). This requires an extrapolation method for the sealing flow parameter Φ_{min}. The outcome of this research is to establish a new procedure to address the ingress problem with reasonable accuracy and reduced uncertainties.

The second objective of this dissertation is mainly CFD based with the intent to capture the governing fluid-dynamics of the ingress problem using numerical models. In an industrial environment, the engine designer relies largely on numerical models to investigate and optimise the fluid mechanics in gas turbines. In the first stage of this computational work, the ingress CFD model was validated against the experimental data obtained at the ingress test rig at the University of Bath. This knowledge and the CFD modelling technique was employed to create a model representing the high pressure turbine stage of an industrial gas turbine. This model was used to investigate the fluid-mechanics associated with various rim-seal concepts with the intent to find a novel rim-seal concept to minimise the ingress levels. These computations were complemented by ingress experiments as part of the validation process.

An additional investigation focused on the aerodynamic interaction between the egress and the mainstream flow. This study provides a better understanding of the coolant leakage flow interaction with the primary gas path flow, with the aim to reduce the losses associated with the mixing. Furthermore, various endwall concepts were investigated with the objective to minimise the secondary flows in the rotor passage, induced by the horseshoe vortex and the cross passage flow without negatively impacting the ingress levels of the upstream located wheel-space.

Further research focused on aerodynamic off-design conditions of an ingress rig and its effect on hot gas ingestion.

1.3 Thesis overview

Chapter 1 introduces the topic of this dissertation to the reader with a detailed discussion of the objectives and its scope and the motivation.

Chapter 2 reviews the literature on the ingress problem from a theoretical, experimental and numerical-modelling point of view. Externally-induced (EI)ingress is highlighted as the engine relevant case without neglecting the rotationally-induced and combined ingress case.

Chapter 3 discusses the translation of the orifice model for EI ingress into a practical tool for industrial purposes with subsequent implementation of the mass-flow equations into the Siemens SAS solver. This model is implemented into the solver structure as a subroutine written in C# and the solution is obtained by an iterative inner and outer loop procedure.

Chapter 4 validates the CFD model to address the ingress problem from a numerical point of view, with a comparison of the results with experimental data obtained at the ingestion facility at the University of Bath. Sensitivity studies with numerous model settings are investigated to find the best compromise between accuracy, numerical robustness and computational efficiency.

Chapter 5 describes an extrapolation method to scale the sealing parameter Φ_{min} obtained at incompressible test rig condition to the compressible regime that prevails in a gas turbine. This method uses the pressure coefficient ΔC_p at engine and test rig conditions to extrapolate Φ_{min} to the required compressible conditions.

Chapter 6 investigates aerodynamic off-design conditions with its impact on the potential flow field and its implication on ingress. It discusses the regime change from *EI* to *RI* ingress with decreasing flow coefficient, and it investigates an anomaly referred to as the "Blade Effect".

Chapter 7 discusses the computational investigation of novel rim-seal concepts to minimise hot gas ingestion into a rotor-stator cavity from the primary gas path in a high pressure turbine stage. These rim-seals were translated into generic seals and tested in an ingress test facility.

Chapter 8 numerically investigates endwall concepts in the rotor blade passage in a high pressure turbine with the intention to minimise the loss associated with the mixing of the discharged egress flow from the upstream wheel-space with the primary gas path flow. An endwall concept with 3D design features, i.e. an elongated leading edge feature and a channel incorporated into the endwall, allows the egress flow to join the gas path in a controlled fashion with less viscous mixing. Furthermore, the leading edge feature along with the contoured rotor passage reduces the secondary flow losses.

1.4 Project funding

The research presented in this dissertation was part of a Knowledge Transfer Partnership and has been jointly funded by the UK Technology Strategy Board and Siemens Industrial Turbomachinery Ltd.

1.5 Publication

The following papers were and will be published in conjunction with this dissertation.

Teuber, R., Li, Y.S., Maltson, J., Wilson, M., Lock, G.D. and Owen, J.M. (2012). Computational Extrapolation of Turbine Sealing Effectiveness from Test Rig to Engine Conditions. Proceedings of the Institution of Mechanical Engineers, Part A: Journal of Power and Energy, 227 (2), pp. 167-178

Scobie, J.A., Sangan, C.M., **Teuber, R.**, Pountney, O.J., Owen, J.M., Wilson, M. and G.D (2013). Experimental Measurements of Ingestion through Turbine Rim Seals. Part 4: Off-Design Conditions. ASME Paper GT2013-94147.

Siemens has submitted three patent applications as outcome of the research undertaken in the KTP project.

1. **Teuber, R.**, Li, Y.S., (2013). Siemens Patent Application 1.
2. **Teuber, R.**, Li, Y.S., (2013). Siemens Patent Application 2.
3. Li, Y.S., **Teuber, R.**, (2013). Siemens Patent Application 3.

Due to patents restrictions the following papers have been delayed but are expected to appear at the ASME 2015 conference.

Teuber, R., Scobie, J.A., Li, Y.S., Wilson, M., Lock, G.D., Sangan, C.M. and Owen, J.M. (2015). Investigation of Rim-Seal Concepts in High Pressure Turbine Stage.

Teuber, R., Li, Y.S., Wilson, M., and Lock, G.D. (2015). Endwall contouring.

Chapter 2

Literature Review - Hot Gas Ingestion

This chapter reviews the literature on the ingress problem from the theoretical, experimental and numerical modelling points of view. This has been supplemented with more specific information at the introductory section of each chapter.

2.1 Ingress Problem - Fundamentals

2.1.1 Governing Non-dimensional Variables

This section introduces the characteristic numbers used in the context of rotating flows in rotor-stator systems. The first number non-dimensional is the rotational Reynolds number, which is defined as:

$$Re_\phi = \frac{\varrho \Omega b^2}{\mu} \tag{2.1-1}$$

where Ω and b refer to the rotational speed of the rotor disc and to the radius of the rim-seal respectively. Rig tests are typically conducted in the range of $Re_\phi \approx 10^6$ whereas engines operate one order of magnitude higher in the region $\approx 10^7$.

The swirl ratio β is used to describe either the axial or radial variation of the tangential velocity, V_ϕ, in a rotor-stator system

$$\beta = \frac{V_\phi}{\Omega b} \tag{2.1-2}$$

The sealing flow rate supplied to a rotor-stator system is expressed in non-

dimensional form as

$$C_{w,o} = \frac{\dot{m}_o}{\mu b} \tag{2.1-3}$$

The turbulent flow parameter λ_T is given by

$$\lambda_T = \frac{C_{w,o}}{Re_\phi^{0.8}} \tag{2.1-4}$$

2.1.2 Driving Mechanisms

This section describes the two fundamental mechanisms that drive hot fluid from the primary gas path into the wheel-space of a rotor-stator system.

Fig. 2.1-1(a) depicts a schematic turbine stage with simplified geometry, i.e. nozzle guide vane, rotor blade and the wheel-space. The presence of the stationary vanes and rotating blades induce a circumferential pressure asymmetry as shown in Fig. 2.1-1(b) with regions of high and low pressure caused by the NGV and the rotor blade potential effect. Ingress and egress through the rim-seal clearance occur when the local pressure gradient between gas path and wheel-space is positive or negative respectively. This kind of ingestion is defined as externally-induced ingress or *EI* ingress by Owen (2009b).

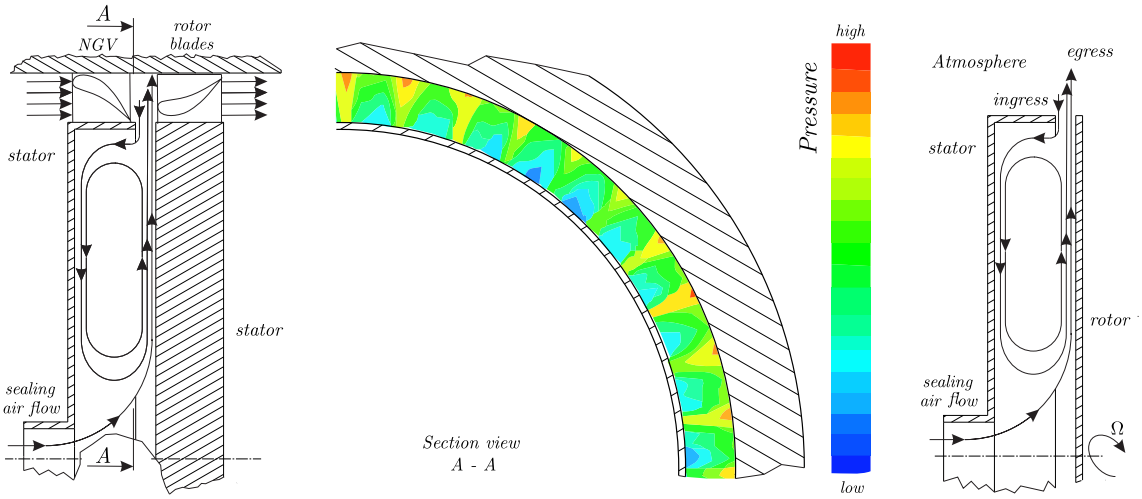

Fig. 2.1-1: The fundamental ingestion mechanisms (a) Externally-induced ingress (*EI* ingress), (b) Static pressure distribution in the gas path owing to the presence of NGVs and RBs (adapted from Elliott et al. (2005)), (c) Rotationally-induced ingress (*RI* ingress) (adapted from (Phadke and Owen, 1988a))

Even though there is no variation in circumferential pressure in the gas path in

the absence of any vanes and blades, ingress can still occur. This kind of ingress is defined as rotationally-induced ingress or *RI* ingress by Owen (2009a) where the wheel-space fluid is entrained into the rotor boundary layer and pumped radially outwards by the centrifugal forces. The static pressure of this highly swirled fluid drops below the pressure outside the wheel-space, drawing fluid into the rotor-stator system as shown in Fig. 2.1-1(c).

Johnson et al. (1994) summarised additional factors that can enhance the *RI* and *EI* ingress case as follows:

- ❒ 3D geometry in the rim-seal region
- ❒ Asymmetries in the rim-seal geometry
- ❒ Turbulent transport in the platform/outer cavity region
- ❒ Flow entrainment
- ❒ 3D, time-dependent flow structure within the rotor-stator system

The dominant mechanism for practical applications is *EI* ingress. Nonetheless, there persist flow conditions and geometric configurations where rotational effects contribute at the same order of magnitude to the ingress caused by the external pressure asymmetry. These situations are at off-design conditions and with special rim-seal configurations where the pressure variation is attenuated. Owen (2009b) refers to this as combined ingress or *CI* ingress.

2.1.3 Flow Structure Rotor-Stator System

To explain the complex flow structures in rotor-stator systems, it is beneficial to first look at a rotating disc in acquiescent fluid. Fig. 2.1-2 shows a turning disc with rotational speed Ω and radius b. The rotating motion of the disc entrains fluid with an axial velocity component V_z into the rotor boundary layer near the rotational axis. The centrifugal force transferred into the boundary layer causes a radial outflow; this effect is known as the disc pumping effect. The tangential velocity on the disc increases linearly with radius and reaches it peak velocity at the outer rim of the disc with Ωb. The rotor boundary layer is continuously fed by the axial inflow of the free-stream leading to an increase of the boundary layer thickness δ with radius. The tangential velocity component decreases with increasing distance from the disc and reaches the value of the free-stream outside the boundary layer,

while the radial component shows a skewed profile with an initial increase owing to the rotating forces with subsequent drop to the freestream value.

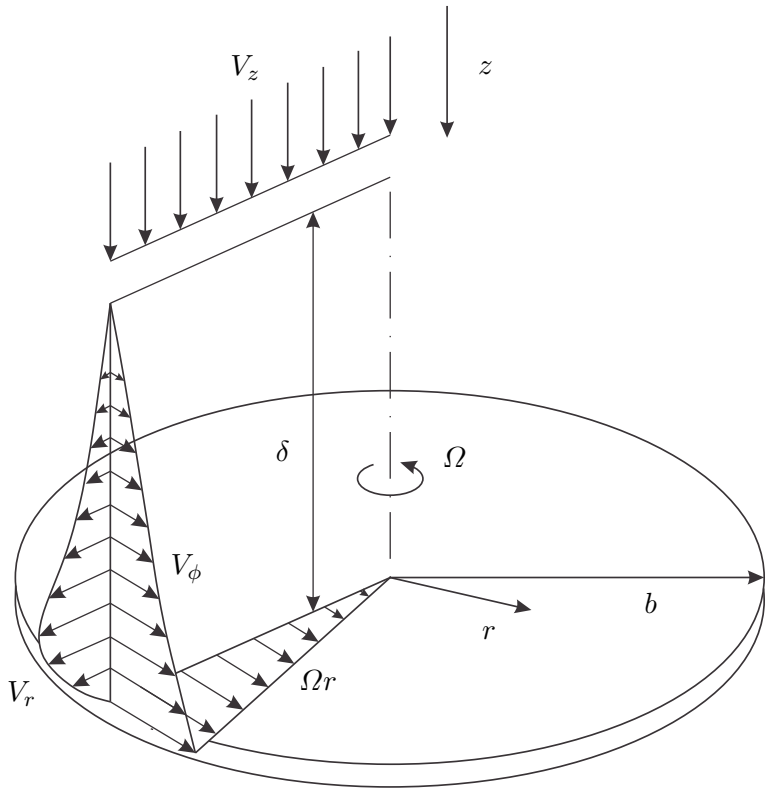

FIG. 2.1-2: Rotating disc in the free-stream (adapted from Childs (2011))

The same mechanism is also observed in a rotor-stator system with the exception that the rotor boundary layer is fed by the stator boundary layer which continuously losses mass radially inward. The sealing flow, $C_{w,o}$, is typically supplied to the cavity at low radius. Fig. 2.1-3 shows the flow structure with a rotating core in between the stator and the rotor boundary layers.

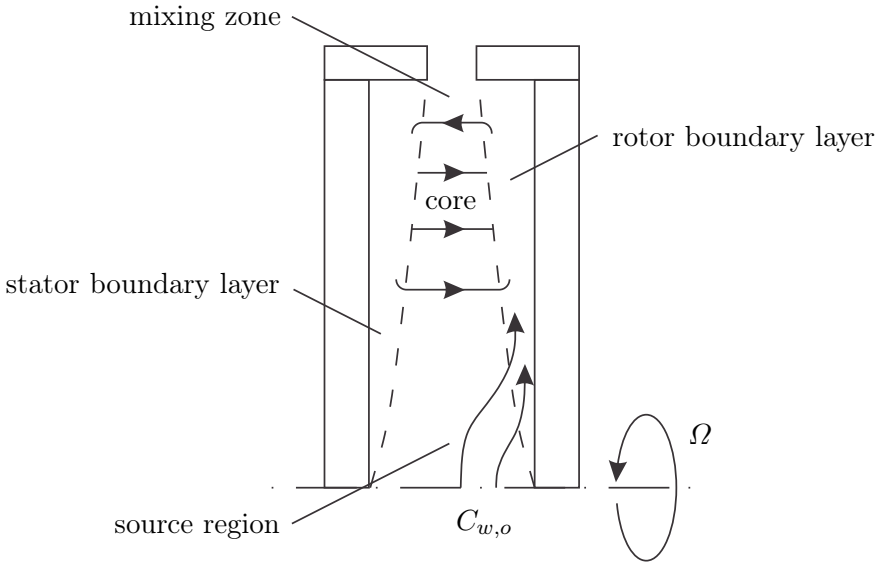

Fig. 2.1-3: Flow structures in a rotor-stator system (adapted from Pountney (2012))

The ingress mixes with the rotating core at high radius in the so-called mixing zone; the mixed-out ingress is entrained into the stator boundary layer with some of it leaving the system. This is defined as egress.

Batchelor (1951) predicted the existence of a rotating core between the stator and rotor boundary layer and proposed the velocity profiles for this type of flow, now known as the Batchelor type flow. The velocity profiles were confirmed by Chen et al. (1996) who investigated the variation of the radial and tangential velocity components with a laser-doppler anemometry. They showed that the inviscid core rotates with a uniform speed of $V_\phi = 0.4\Omega r$ and with a radial component of $V_r = 0$. It should be mentioned that this experiment was done at the absence of any sealing flow.

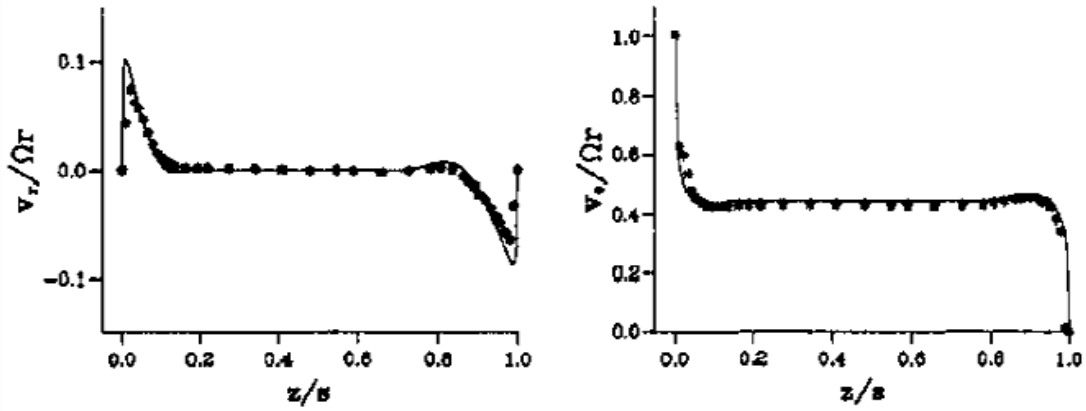

Fig. 2.1-4: Velocity components across a rotor-stator system measured with laser-doppler anemometry (adapted from Chen et al. (1996))

Phadke and Owen (1988a) deduced simplified streamlines from a flow visualisation study for a shrouded rotor-stator system with seven rim-seal configurations at

$C_{w,o} \preceq 500$ and $Re_\phi \preceq 15 \times 10^5$. Fig. 2.1-5 summarises the results in the order-of-merit. All rim-seals show the entrained sealing flow being pumped radially upwards (shown by the black line) and the secondary flows with the entrainment into the stator boundary layer (with the dashed line). The radial configurations shown in Fig. 2.1-5(a) and Fig. 2.1-5(b) an impinging jet phenomenon is observed, causing an inversion pressure effect in the shrouded rotor-stator system. Over a certain sealing flow rate both configurations exhibit an increase in pressure with increasing rotational speed in the outer wheel-space. This build-up in static pressure reduces ingress and makes the radial configurations more effective than the other rim-seals by requiring less sealing air to seal the wheel-space.

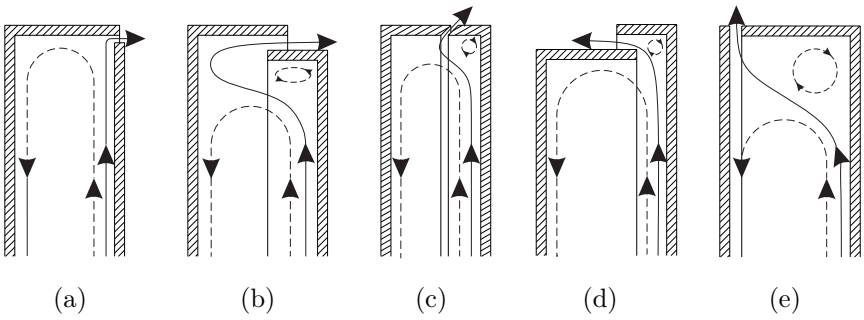

FIG. 2.1-5: Flow pattern derived from the flow visualisation experiments for a rotor-stator system (adapted from Phadke and Owen (1988a))

2.2 Latest Ingress Research and Development

This section describes the latest development and the state-of-the-art of the ingress research.

The orifice model (OM) developed by Owen (2009a,b) was derived for inviscid flow by placing an imaginary ring or an orifice in the seal region with two streamtubes to account for the fluid exchange in and out the wheel-space (Fig. 2.2-6).

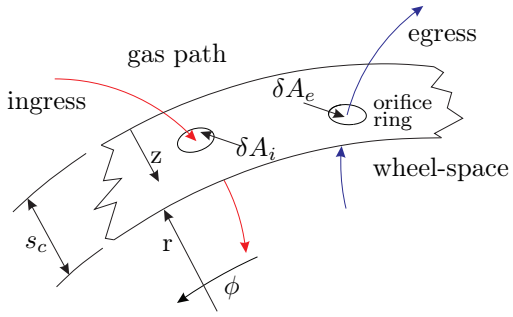

FIG. 2.2-6: Imaginary orifice ring (adapted from Owen (2009a))

The sum of the elementary areas for the egress and ingress streamtubes, δA_e and δA_i, corresponds to the clearance area A_c. Angular momentum is conserved

across the seal clearance, i.e. $V_\phi r = \text{const}$. Ingress occurs when the external static pressure p_2 is greater than the static pressure p_1 (and vice versa for egress) with $V_{r,1}^2 \ll V_{r,2}^2$. Within these streamtubes mass and energy are conserved but there is a discontinuity of the static pressure across the imaginary ring. By introducing two discharge coefficients, $C_{d,e}$ for egress and $C_{d,i}$ for ingress, losses are associated with the viscous mixing process and turbulent shear stresses within the seal region are accounted for.

The steady-state incompressible OM equations were derived from the frictionless radial momentum equation by assuming that the radial velocity gradient are higher than the tangential and axial ones. With this assumption the radial momentum equation can be re-written as follows:

$$V_r \frac{\partial V_r}{\partial r} - \frac{V_{\phi^2}}{r} = -\frac{1}{\varrho}\frac{\partial p}{\partial r} \tag{2.2-5}$$

By integrating eq. 2.2-5 between the wheel-space (1) and gas path location (2), the equation can be re-written

$$\int_{r_1}^{r_2} (V_r \frac{dV_r}{dr} - \frac{V_\phi^2}{r}) dr = -\frac{1}{\varrho}\int_{r_1}^{r_2} \frac{\partial p}{\partial r} dr \tag{2.2-6}$$

With the conservation of the angular momentum, it follows

$$\left(V_{r_2}^2 - V_{r_1}^2\right) + \left(V_{\phi,2}^2 - V_{\phi,1}^2\right) = 2\left(\frac{p_1 - p_2}{\varrho}\right) \tag{2.2-7}$$

For the radially outward flow, $V_{r,2} = V_{r,e}$, through the streamtube A_e, it is assumed that $V_{r,e} \gg V_{r,i}$ where $V_{r,1} = V_{r,i}$ and for the radially inward flow $V_{r,i}$ through A_i, it is assumed that $V_{r,i} \gg V_{r,e}$. With these assumptions, Eq. 2.2-7 can be expressed as follows

$$\frac{V_{r,e}}{\Omega b} = \sqrt{\frac{p_1 - p_2}{1/2\varrho\Omega^2 b^2} + \beta_1^2\left(\frac{r_2^2}{r_1^2} - 1\right)} \tag{2.2-8}$$

$$\frac{V_{r,i}}{\Omega b} = \sqrt{\frac{p_2 - p_1}{1/2\varrho\Omega^2 b^2} - \beta_2^2\left(\frac{r_2^2}{r_1^2} - 1\right)} \tag{2.2-9}$$

where the swirl ratio β is defined as $\beta = V_\phi/(\Omega b)$.

Viscous effects are incorporated in the inviscid equations by introducing $C_{d,e}$ and $C_{d,i}$.

$$\frac{V_{r,e}}{\Omega b} = C_{d,e}\sqrt{C_{\beta,1} - C_p} \tag{2.2-10}$$

when $C_{\beta,1} \succeq C_p$

$$\frac{V_{r,i}}{\Omega b} = C_{d,i}\sqrt{C_p - C_{\beta,2}} \tag{2.2-11}$$

when $C_p \succeq C_{\beta,2}$, where

$$C_p = \frac{p_2 - p_1}{1/2\varrho\Omega^2 b^2}, C_{\beta,1} = \beta_1^2\left(1 - \frac{r_1^2}{r_2^2}\right), C_{\beta,2} = \beta_2^2\left(\frac{r_2^2}{r_1^2} - 1\right) \tag{2.2-12}$$

The mass flow rates can be obtained by integrating the radial velocity components across the seal-clearance.

$$\dot{m}_e = \varrho \int_{A_e} V_{r,e} dA_e \tag{2.2-13}$$

$$\dot{m}_i = \varrho \int_{A_i} V_{r,i} dA_i \tag{2.2-14}$$

where

$$A_e + A_i = A_c = 2\pi b s_c \tag{2.2-15}$$

The superimposed sealing flow rate, $\dot{m}_o$, is obtained by the mass continuity as follows

$$\dot{m}_o = \dot{m}_e - \dot{m}_i \tag{2.2-16}$$

2.2.1 Solution of Orifice Equations

The flow parameter, Φ_o, is defined as

$$\Phi_o = \frac{C_{W,o}}{2\pi G_c Re_\phi} = \frac{U}{\Omega b} \tag{2.2-17}$$

where U is the radial velocity component in the streamtube.

$$\Phi_{min} = \frac{C_{W,min}}{2\pi G_c Re_\phi} = \frac{U_{min}}{\Omega b} \tag{2.2-18}$$

From the mass continuity in the mixing zone, Φ_o is defined as follows

$$\Phi_o = \Phi_e - \Phi_i \tag{2.2-19}$$

and for $\Phi_o \preceq \Phi_{min}$, the sealing effectiveness ε can be defined as

$$\varepsilon = 1 - \frac{\Phi_i}{\Phi_e} = \frac{\Phi_o}{\Phi_e} = \frac{\Phi_o}{\Phi_o + \Phi_i} \tag{2.2-20}$$

$$\Gamma_c = \frac{C_{d,i}}{C_{d,e}} \tag{2.2-21}$$

$$\Delta C_p = \frac{\Delta p}{1/2 \varrho \Omega^2 b^2} \tag{2.2-22}$$

2.2.2 Rotationally-Induced Ingress

This section describes the derivation of the explicit solution for rotationally-induced ingress with the effectiveness equation derived by Sangan et al. (2011b). This form is based upon the analytical solution presented by Owen (2009a) and the interested reader is referred to his paper for more details.

Owen (2009a) showed that in the absence of external swirl, Φ_{min} can be expressed as follows:

$$\Phi_{min,RI} = C_{d,e} C_{\beta 1}^{1/2} \tag{2.2-23}$$

This equation forms a vital theoretical solution of the orifice model for rotationally-induced ingress. The validation of the equation shows good agreement with the experimental data presented also by Sangan et al. (2011b) which is discussed briefly in section 2.2.5.

The egress, ingress and sealing flow were defined as follows:

$$\frac{\Phi_e}{\Phi_{min,RI}} = \frac{1 - \Gamma_p}{\Gamma_T} \tag{2.2-24}$$

$$\frac{\Phi_i}{\Phi_{min,RI}} = \frac{\Gamma_c^2 \Gamma_p}{\Gamma_T} \tag{2.2-25}$$

$$\frac{\Phi_o}{\Phi_{min,RI}} = \frac{\Phi_e - \Phi_i}{\Phi_{min,RI}} = \frac{1 - \Gamma_p\left(1 + \Gamma_c^2\right)}{\Gamma_T} \tag{2.2-26}$$

where

$$\Gamma_c = \frac{C_{d,i}}{C_{d,e}} \quad \Gamma_p = \frac{C_p}{C_{\beta 1}} \quad \Gamma_T = \left[(1 - \Gamma_p)^{1/2} + \Gamma_c \Gamma_p^{1/2}\right] \tag{2.2-27}$$

The sealing effectiveness can be expressed as

$$\varepsilon = 1 - \frac{\Phi_i}{\Gamma_e} = \frac{1 - \Gamma_p\left(1 + \Gamma_c^2\right)}{1 - \Gamma_p} \tag{2.2-28}$$

Re-arranging Eq. 2.2-28 gives

$$\Gamma_p = \frac{1 - \varepsilon}{(1 - \varepsilon) + \Gamma_c^2} \tag{2.2-29}$$

Eq. 2.2-26 was re-arranged by eliminating Γ_p with Eq. 2.2-29

$$\frac{\Phi_o}{\Phi_{min,RI}} = \frac{\varepsilon}{\left[1 + (1 - \varepsilon)^{1/2}\right]\left[1 + \Gamma_c^{-2}(1 - \varepsilon)\right]^{1/2}} \tag{2.2-30}$$

Eq. 2.2-30 is referred to as the *RI* effectiveness equation which describes the variation of Φ_o with the sealing effectiveness.

Furthermore, Sangan et al. (2011b) derived for Φ_i an expression to determine the ingress level as follows:

$$\varepsilon = \frac{\Phi_o}{\Phi_{e,RI}} = \frac{\Phi_o}{\Phi_o + \Phi_{i,RI}} \tag{2.2-31}$$

and so

$$\frac{\Phi_{i,RI}}{\Phi_o} = \varepsilon^{-1} - 1 \tag{2.2-32}$$

As

$$\frac{\Phi_{i,RI}}{\Phi_{min,RI}} = \frac{\Phi_{i,RI}}{\Phi_o}\frac{\Phi_o}{\Phi_{min,RI}} \tag{2.2-33}$$

Eq. 2.2-33 can be re-written with Eq. 2.2-30 and 2.2-32 to give the following useful expression

$$\frac{\Phi_{i,RI}}{\Phi_{min,RI}} = \frac{1-\varepsilon}{\left[1+(1-\varepsilon)^{1/2}\right]\left[1+\Gamma_c^{-2}(1-\varepsilon)\right]^{1/2}} \tag{2.2-34}$$

$$\Phi_e = \Phi_i + \Phi_o \tag{2.2-35}$$

Fig. 2.2-7 summarises the theoretical solutions for RI ingress with the variation of ε, Φ_e and Φ_i with Φ_o. When $\Phi_o \to 0$, i.e. $\Phi_i = \Phi_e$, $\Phi_i \to \Phi_{i,max}$ while $\Phi_e \to \Phi_{e,min}$. With increasing Φ_o, $\Phi_i \to 0$ and $\Phi_e \to \Phi_{min}$ for $\Phi_o \preceq \Phi_{min}$.

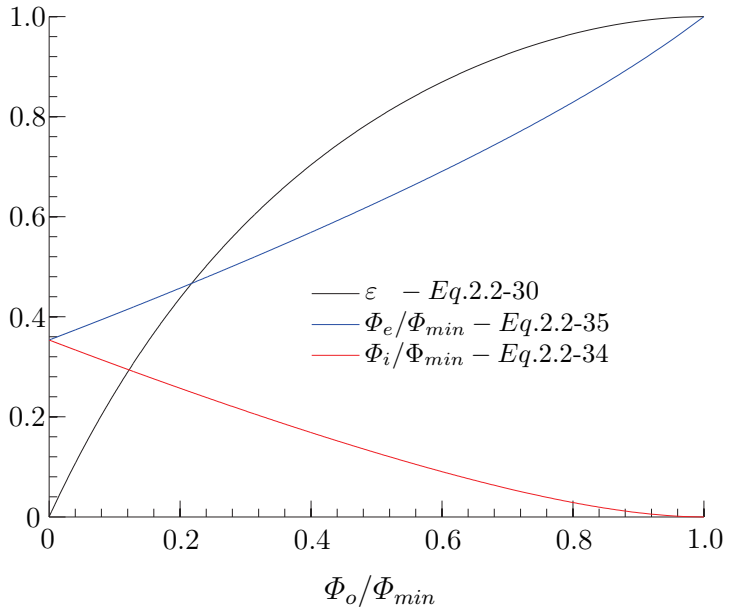

FIG. 2.2-7: Variation of ε, Φ_i and Φ_e with Φ_o for RI ingress ($\Gamma_c = 1$)

2.2.3 Externally-Induced Ingress

Owen (2009b) used a linear saw-tooth model to approximate the circumferential pressure variation across one vane pitch as shown in Fig. 2.2-8. Owen et al. (2010b) have proven that the model is a good approximation and that the shape of the profile itself is of secondary importance. One advantage of this model is that it can be solved analytically and hence does not need numerical integration of the pressure distribution.

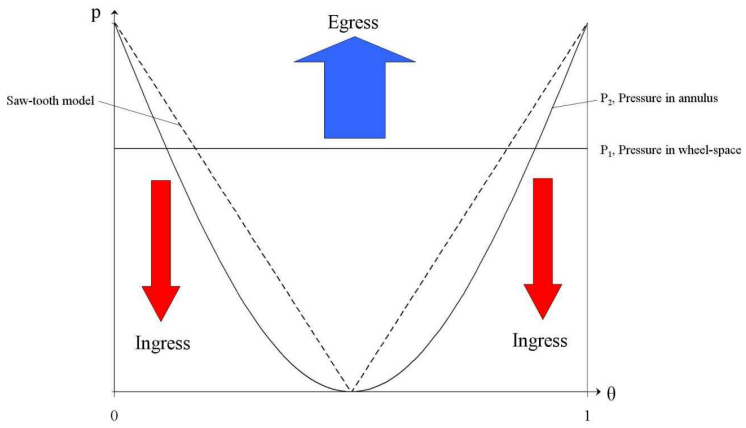

FIG. 2.2-8: Circumferential pressure variation across a vane pitch approximated by a linear saw-tooth model (OWEN, 2010)

The saw-tooth model describes the relationship between Φ_{min} and $\Delta C_p^{1/2}$ as follows

$$\Phi_{min,EI} = \frac{2}{3} C_{d,e} \Delta C_p^{1/2} \tag{2.2-36}$$

The normalised wheel-space pressure g is defined as

$$g = \frac{p_1 - p_{2,min}}{p_{2,max} - p_{2,min}} \tag{2.2-37}$$

where $p_{2,max}$ and $p_{2,min}$ are the static peak and trough of the circumferential distribution pressure of Fig. 2.2-8. p_1 refers to the uniform wheel-space pressure underneath the rim-seal.

Owen (2009b) expressed the non-dimensionalised sealing flow rate and the sealing effectiveness variation with g as follows

$$\frac{\Phi_o}{\Phi_{min,EI}} = g^{3/2} - \Gamma_c \left(1 - g\right)^{3/2} \tag{2.2-38}$$

$$\varepsilon = 1 - \Gamma_c \left[\frac{1-g}{g}\right]^{3/2} \tag{2.2-39}$$

Eq. 2.2-39 can be re-arranged and substituted into Eq. 2.2-38 to eliminate g

$$g = \frac{1}{\left[\frac{1-\varepsilon}{\Gamma_c}\right]^{2/3} + 1} \tag{2.2-40}$$

$$\frac{\Phi_o}{\Phi_{min,EI}} = \frac{\varepsilon}{\left[1 + \Gamma_c^{-2/3} \left(1 - \varepsilon\right)^{2/3}\right]^{3/2}} \tag{2.2-41}$$

Eq. 2.2-41 was derived by Sangan et al. (2011b) and is referred to it as sealing effectiveness equation for EI ingress. For the engine designer it is equally important to be able to predict the amount of ingress into the rotor-stator systems.

The sealing effectiveness (see Sangan et al. (2011b)) was defined as

$$\varepsilon = \frac{\Phi_o}{\Phi_{e,EI}} = \frac{\Phi_o}{\Phi_o + \Phi_{i,EI}} \tag{2.2-42}$$

Re-arranging Eq. 2.2-42 gives

$$\frac{\Phi_{i,EI}}{\Phi_o} = \varepsilon^{-1} - 1 \tag{2.2-43}$$

As

$$\frac{\Phi_{i,EI}}{\Phi_{min,EI}} = \frac{\Phi_{i,EI}}{\Phi_o}\frac{\Phi_o}{\Phi_{min,EI}} \tag{2.2-44}$$

and it follows with Eq. 2.2-43 and Eq. 2.2-41 that the effectiveness equation for ingress can be expressed as

$$\frac{\Phi_{i,EI}}{\Phi_{min,EI}} = \frac{1-\varepsilon}{\left[1 + \Gamma_c^{-2/3}\left(1-\varepsilon\right)^{2/3}\right]^{3/2}} \tag{2.2-45}$$

The egress parameter Φ_e is obtained by mass continuity

$$\Phi_e = \Phi_i + \Phi_o \tag{2.2-46}$$

Fig. 2.2-9 shows the effectiveness equations for EI ingress, which are similar to the effectiveness equations for RI ingress but quantitatively different. The effectiveness equations have uncoupled the ingress for its root cause, i.e. ΔC_p for EI ingress and $C_{\beta 1}$ for RI ingress.

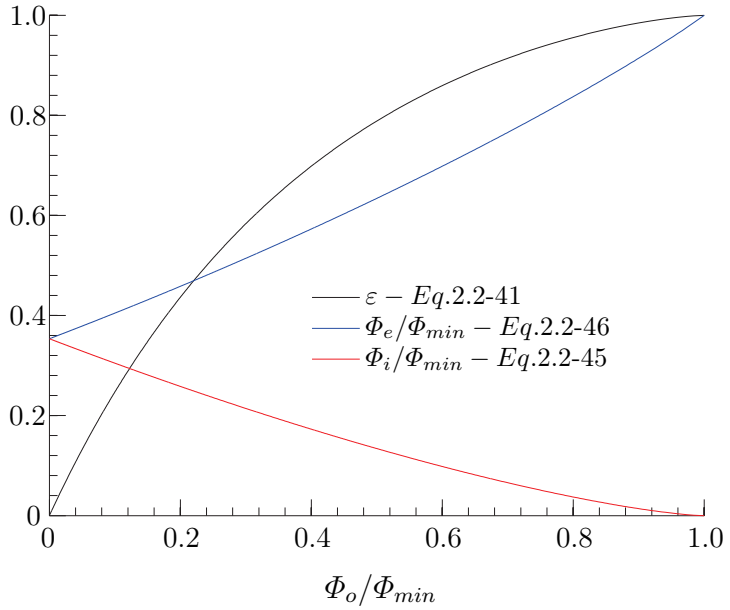

FIG. 2.2-9: Variation of ε, Φ_i and Φ_e with Φ_o for EI ingress ($\Gamma_c = 1$)

Φ_{min} and Γ_c will be experimentally determined as described in the subsequent section; Φ_{min} marks the sealing flow rate where ingress is eliminated and Γ_c describes the shape of the effectiveness curve as shown in Fig. 2.2-10. A $\Gamma_c \succ 1$ signifies $C_{d,i} \succ C_{d,e}$ and vice versa for $\Gamma_c \prec 1$. Both parameters must be determined from experimental concentration measurements with the effectiveness equations fitted to the data by a statistical fitting method as discussed below.

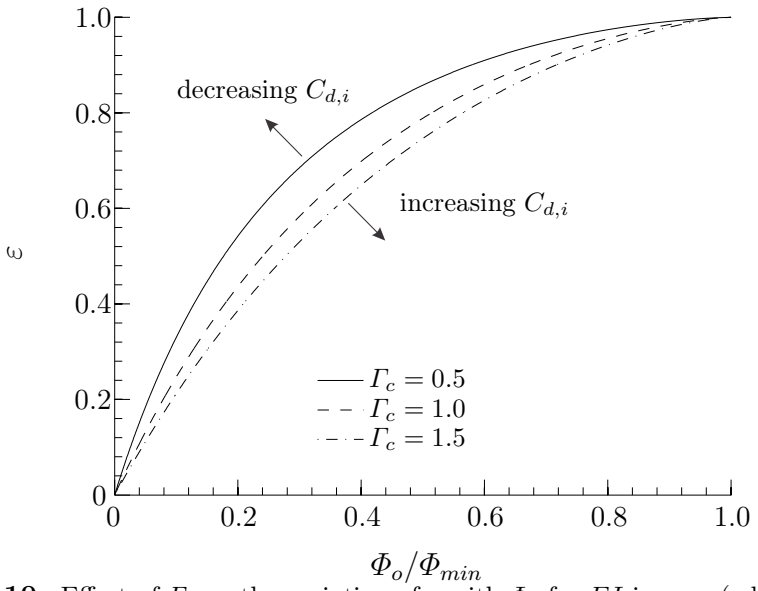

FIG. 2.2-10: Effect of Γ_c on the variation of ε with Φ_o for EI ingress (adapted from Owen (2009b))

2.2.4 Combined Ingress

This section introduces the fundamental concept of the ingress regime where both rotational effects and the external flow have a significant influence on ingestion,

Owen (2009b) refers to this as combined or CI ingress. This section reviews only the theoretical solution by Owen (2009b) and a broader overview on combined ingress with experimental validation is discussed at the introductory section of chapter 6: "Off-Design Conditions".

Owen (2009b) solved the orifice equations for CI ingress and the solution described by Eq. 2.2-47 shows a transition from RI to the EI regime with increasing external pressure asymmetry as shown in Fig. 2.2-11.

$$\frac{\Phi_{min,CI}}{\Phi_{min,RI}} = \frac{2}{3}\frac{C_{d,e}}{C_{d,e'}}\frac{[1+\Gamma_{\Delta p}]^{3/2}-1}{\Gamma_{\Delta p}} \tag{2.2-47}$$

$$\text{where} \quad \Gamma_{\Delta p} = \frac{\Delta C_p}{C_{\beta 1}} = \frac{C_{p,max}}{C_{\beta 1}}\left(\frac{Re_W}{Re_\phi}\right)^2 \tag{2.2-48}$$

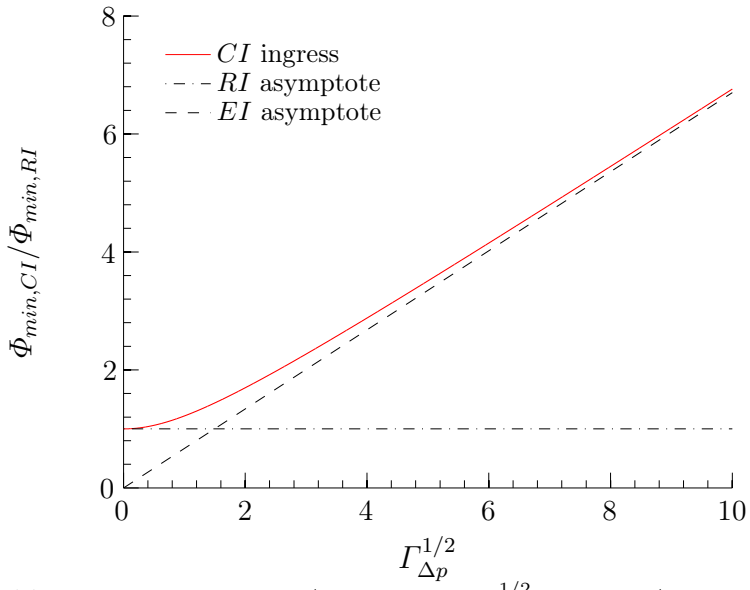

FIG. 2.2-11: Variation of $\Phi_{min,CI}/\Phi_{min,RI}$ with $\Gamma_{\Delta p}^{1/2}$ with $C_{d,e}/C_{d,e'} = 1$ (adapted from Owen (2009b))

In the absence of the external flow, i.e. $\Gamma_{\Delta p} = 0$, Eq. 2.2-47 can be simplified when $C_{d,e} = C_{d,e'}$ to give

$$\Phi_{min,CI} = C_{d,e'}C_{\beta 1}^{1/2} \tag{2.2-49}$$

Eq. 2.2-49 is identical to the $\Phi_{min,RI}$ expression in Eq. 2.2-23 which forms the RI asymptote at $\Phi_{min,CI}/\Phi_{min,RI} = 1$.

With increasing pressure asymmetry, i.e. $\Gamma_{\Delta p} \to \infty$, Eq. 2.2-47 can be rearranged to give the EI asymptote

$$\Phi_{min,CI} = \frac{2}{3} C_{d,e} \Delta C_p{}^{1/2} \tag{2.2-50}$$

Eq. 2.2-50 is identical to the linear saw-tooth model for EI ingess as shown in Eq. 2.2-36.

This section introduced the fundamental concept and equations of the CI regime and the interested reader is referred to Owen et al. (2010a) and to chapter 6 for more information.

2.2.5 Experimental Work on Ingress

Sangan et al. (2011a) built and commissioned an ingestion test rig at the University of Bath consisting of 32 NGVs and 41 symmetric NACA0018 RBs as shown in Fig. 2.2-12. The rig was designed to be operating at a flow coefficient of $C_F = Re_W/Re_\phi = 0.538$; at this point the flow field is aligned relative to the rotor blade in a way that the blade loading is symmetric and no work is generated by the blades. An electric motor driven facility operates in the incompressible regime with an axial and rotational Reynolds number of up to $Re_W = 5.21 \times 10^5$ and $Re_\phi = 9.68 \times 10^5$ respectively.

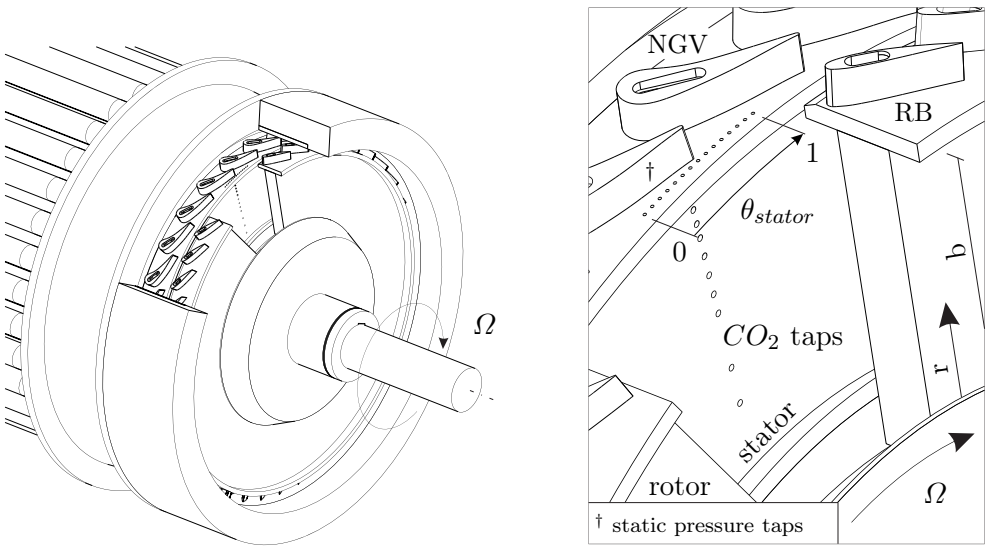

(a) (b)

Fig. 2.2-12: Ingestion test facility at the University of Bath; (a) Turbine stage; (b) Close-up view of rotor-stator wheel-space

The rig was equipped with a Scanivalve measurement system to measure the static pressure downstream of the trailing edge of the vane on the hub platform and

on the outer casing. Fig. 2.2-12(b) shows this set-up with 15 pressure taps across the vane pitch for the hub location, referred to it as location A, and an additional location at the outer casing as location B (not shown here). Fig. 2.2-13 shows the variation of the static pressure expressed, as pressure coefficient C_p, with θ_{stator}, the pitch ratio across one vane pitch. The measurement was done for three rotational Reynolds numbers with a constant flow coefficient, i.e. $C_F = 0.538$. The results show almost identical profiles with ΔC_p invariant with Re_ϕ, where ΔC_p refers to the peak-to-trough pressure.

$$\Delta C_p = \frac{p_{2,max} - p_{2,min}}{\frac{1}{2}\varrho\Omega^2 b^2} \tag{2.2-51}$$

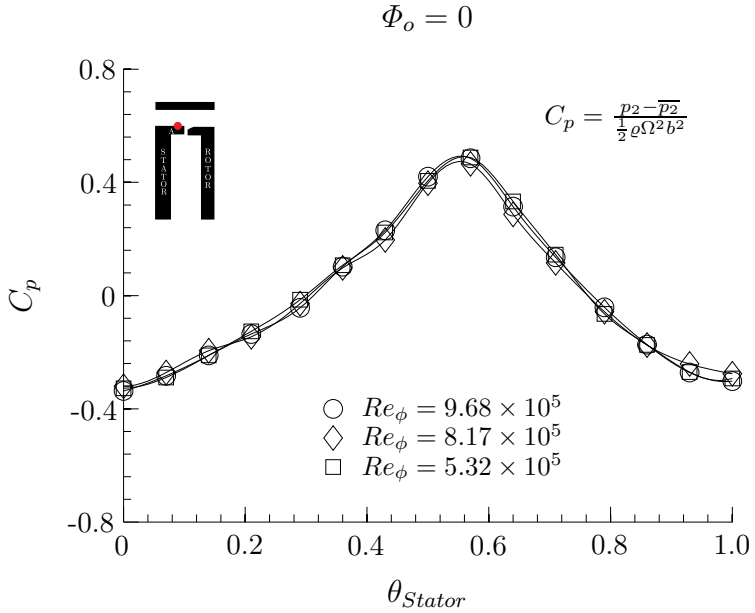

FIG. 2.2-13: Effect of Re_ϕ on the variation C_p with non-dimensionalised vane pitch (adapted from Sangan et al. (2011a))

The rig incorporates a wheel-space formed between the stationary wall of the stator and the rotating wall of the rotor disc. Sealing flow is introduced at low radius into the cavity. This sealing flow is seeded with a tracer gas with a typical concentration of 1% carbon dioxide to track ingested fluid from the gas path into the wheel-space. The CO_2 concentration was measured with 15 tubes distributed radially on the stator wall in the following range: $0.55 \prec r/b \prec 0.993$. The tubes were connected to a gas analyser and the concentration of the unseeded mainstream flow and the concentration at wheel-space inlet were also monitored. The concentration sealing effectiveness ε_c and the ingress parameter Φ_i were determined as follows:

$$\varepsilon_c = \frac{c_s - c_a}{c_o - c_a} \tag{2.2-52}$$

$$\Phi_i = \Phi_o \left(\frac{c_o - c_s}{c_s - c_a} \right) \tag{2.2-53}$$

where c_s refers to the concentration at a defined sampling point at the stator wall, c_a to the CO_2 concentration of the unseeded gas path flow and c_o to the concentration at the wheel-space inlet. The sealing flow rate $\dot{m}_o$ was expressed by the sealing parameter Φ_o:

$$\Phi_o = \frac{C_{w,o}}{2\pi G_c Re_\phi} \tag{2.2-54}$$

$$\text{where } C_{w,o} = \dot{m}_o/\mu b \text{ and } G_c = s_c/b$$

Fig. 2.2-14(a) shows data for an axial-clearance seal experimentally determined by Sangan et al. (2011a) for a constant flow coefficient, i.e. $C_F = 0.538$. This data is for concentration collected at $r/b = 0.958$. They plotted the variation of the sealing effectiveness with the sealing parameter Φ_o (instead of $\dot{m}_o$ or $C_{w,o}$) and their data collapsed onto a single curve. This enabled them to derive a single parameter Φ_{min} which is invariant with Re_ϕ. The red curve describes the ingress behaviour of the seal, with the highest level at $\Phi_o = 0$, that is $\Phi_i \approx 0.24\ \Phi_{min}$. With increasing Φ_o, $\Phi_i \to 0$.

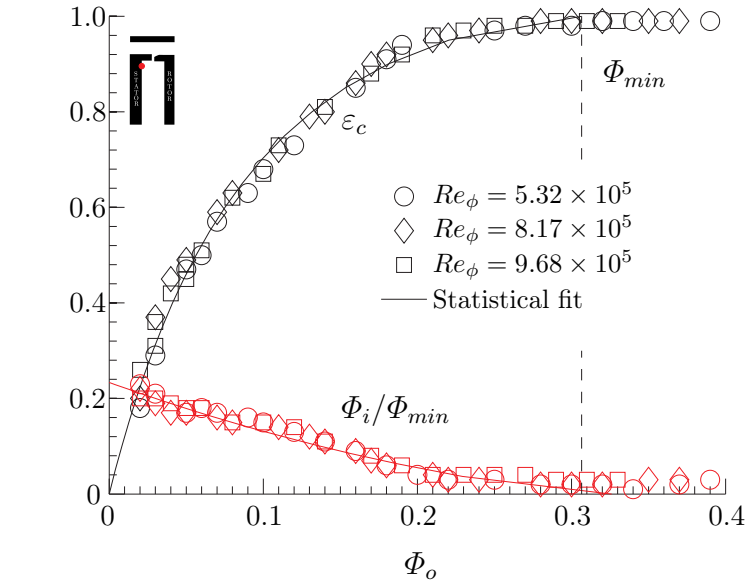

(a)

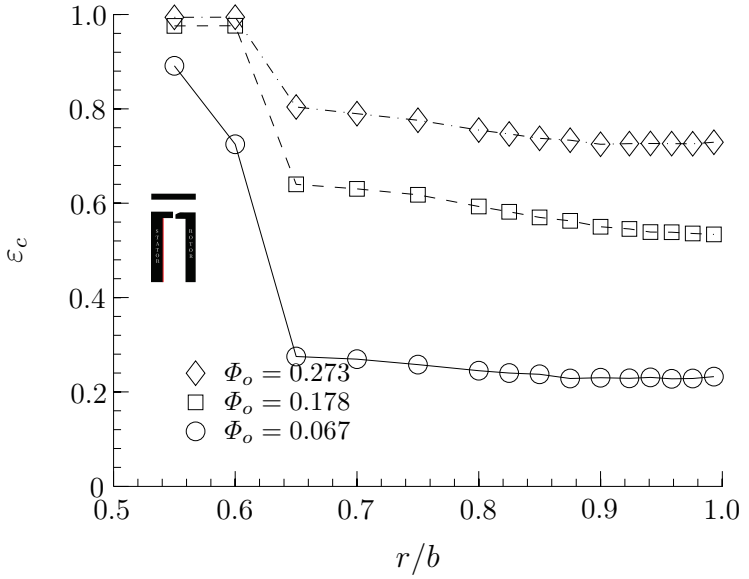

(b)

FIG. 2.2-14: Experimental data for an axial-clearance seal for EI ingress at $C_F = 0.538$ (adapted from Sangan (2011)); (a) Effect of Re_ϕ on the variation of ε_c and Φ_i with Φ_o with sampling point at $r/b = 0.958$; (b) Variation of ε_c with the non-dimensional radius r/b

Fig. 2.2-14(b) depicts the effect of Φ_o on the variation of ε_c with the non-dimensional radius r/b on the stator wall. The increase of Φ_o suppresses ingress whereby ε_c increases. At higher radius, i.e. $r/b \succ 0.90$, the sealing effectiveness is virtually invariant with radius owing to a fully mixed-out fluid, but there is a slight increase of ε_c radially inward. The rapid increase in ε_c at low radii was caused by an inner seal from which the sealing flow is supplied.

In section 2.2.2 and 2.2.3 the effectiveness equations were introduced with the two parameters: Φ_{min} and Γ_c. For convenience, the effectiveness equations for EI

ingress are re-written here:

$$\frac{\Phi_o}{\Phi_{min,EI}} = \frac{\varepsilon}{\left[1+\Gamma_c^{-2/3}\left(1-\varepsilon\right)^{2/3}\right]^{3/2}} \tag{2.2-55}$$

$$\frac{\Phi_{i,EI}}{\Phi_{min,EI}} = \frac{1-\varepsilon}{\left[1+\Gamma_c^{-2/3}\left(1-\varepsilon\right)^{2/3}\right]^{3/2}} \tag{2.2-56}$$

Zhou et al. (2011) used a statistical method with a maximum likelihood estimation to determine these parameters (Φ_{min}, Γ_c) by fitting the aforementioned equations to the experimental data shown in Fig. 2.2-14(a). This method shows good agreement with the experimental data, both for EI and RI ingress (only the EI ingress data are shown here). For more information the reader is referred to Zhou et al. (2011), but the method requires a number of experimental data points in excess of $n \succeq 16$ to provide the most accurate values of Φ_{min} and Γ_c, a criterion which was satisfied for all the experimental data presented in this dissertation.

Sangan (2011) conducted for a series of rim-seals concentration experiments in the RI and EI regime, Fig. 2.2-15 summarises the results for an axial- and a radial-clearance seal, both for EI and RI regimes. EI ingress is the dominant case with a Φ_{min} value significant larger for both seals than for the RI case. The radial seal was superior to the axial seal with a $\Phi_{min,radial} \approx 1/3\ \ \Phi_{min,axial}$.

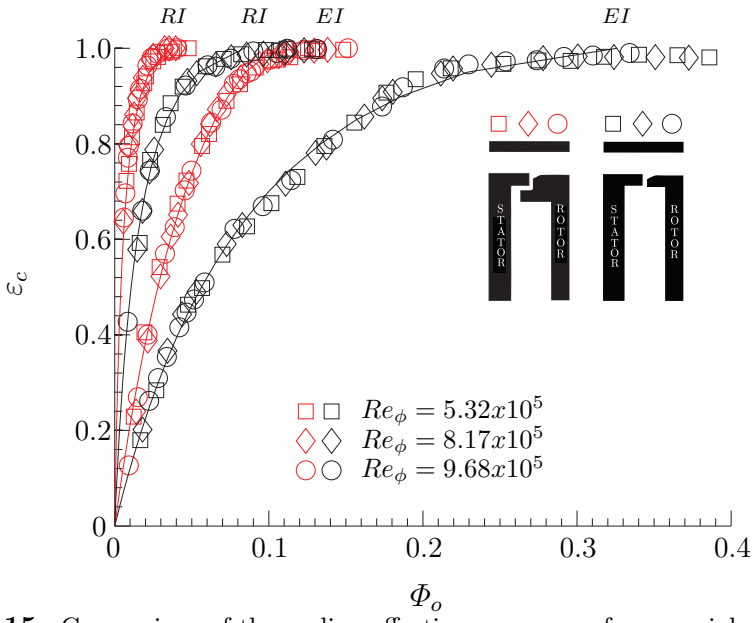

FIG. 2.2-15: Comparison of the sealing effectiveness curves for an axial- and radial clearance seal for EI and RI ingress with sampling point at $r/b = 0.958$ at $C_F = 0.538$ (adapted from Sangan (2011))

2.3 Computational Fluid Dynamics

2.3.1 Hot Gas Ingestion

The increased capability of CFD codes to handle complex flows along with continuing improvements in processing power, have allowed to gain insight into the fluid mechanics of ingress in high pressure (HP) turbines. The significant number of defined input parameters, assumptions and simplifications, such as mesh type and mesh size, turbulence model, level of geometry details are just a few parameters which not only influence the complexity, computing time and convergence behaviour of these models but also the accuracy of the results. It is therefore paramount to conduct validation tests with experimental data.

Fig. 2.3-16(a) shows a typically vane-blade arrangement of a high pressure turbine with rim-seal arrangement and rotor-stator cavity. To address the ingress problem numerically, the complex engine geometry is translated into a CFD domain by simplifying the wheel-space geometry, the main gas path and the vane and blade count. The stator and rotor sector are connected by an interface, i.e. frozen rotor or mixing plane for a steady-state computation, or a sliding plane for a transient run. Ideally, the pitch ratio between the stationary and rotating domain is 1 or nearly to 1 to avoid scaling errors.

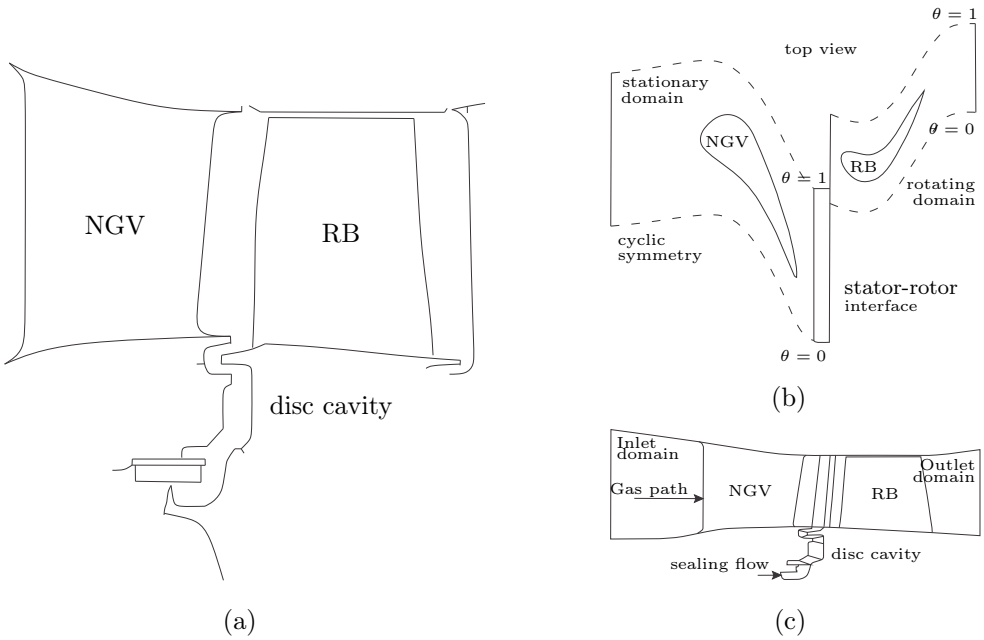

Fig. 2.3-16: CFD modelling technique to capture the ingress problem (adapted from (Mirzamoghadam et al., 2008)), (a) Engine geometry; (b) vane-blade arrangement; (c) simplified CFD domain

The European Union funded project *MAGPI* (Main Annulus Gas Path Inter-

actions) with a two-stage turbine test rig with rotor-stator cavity at the University of Sussex, here referred to as stator well, provided a range of experimental data for validation purposes. The interested reader is referred to Coren et al. (2010) for a detailed description of this facility.

Smith et al. (2012) used these measurements to validate their CFD model sensitivity studies to find the parameter that best matched the experimental data. They used a conjugate CFD analysis by coupling the fluid domain of the first stage of rotor blade row and the second stage of guide vanes with the solid domains in a 1/39th sector model. Fig. 2.3-17 shows the effect of the well mesh size on the computed streamlines, where a coarse mesh captures the overall flow structures but misses important re-circulating flow details. They investigated the mesh sensitivity study with the *SST* $k-\omega$ turbulence model solved as a steady-state case with a mixing plane computation where the coarse mesh relied on the wall function with a y^+ of 115. The fine mesh with a $y^+ \approx 2$ used the low Reynolds number formation of the $SSTk-\omega$ turbulence model, while the intermediate mesh was based on the blending function.

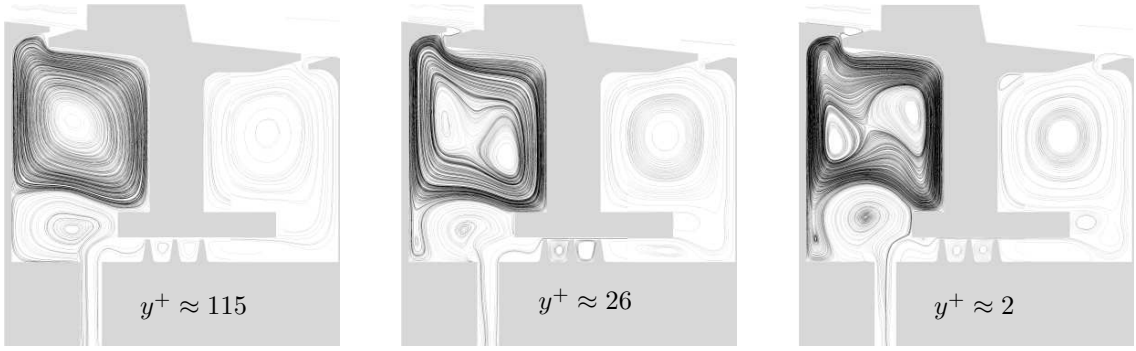

Fig. 2.3-17: Effect of the mesh size on the computed streamlines in a stator well (adapted from Smith et al. (2012)) ; (a) coarse mesh; (b) intermediate mesh; (c) fine mesh

They extended this study by investigating the influence of the turbulence model on the computed metal temperature across the stator. They used for this study the *SST* $k-\omega$ turbulence model by Menter (1994), the $k-\varepsilon$ model, and the Reynolds Stress models, the *BSL* by Wilcox (1986) and the *SSG* by Speziale et al. (1991). These simulations were computed with the fine mesh with the mixing plane interface and additionally investigated a transient case with the *SST* $k-\omega$. The computed temperatures were compared with the rig temperatures obtained by thermocouples. Fig. 2.3-18 shows the surface temperature in the form of the cooling effectiveness θ as follows:

$$\theta = \frac{T - T_c}{T_h - T_c} \tag{2.3-57}$$

where T_c and T_h are the reference temperature of the sealant at the inlet of the stator well and the temperature in the gas path at the leading edge of the vane respectively.

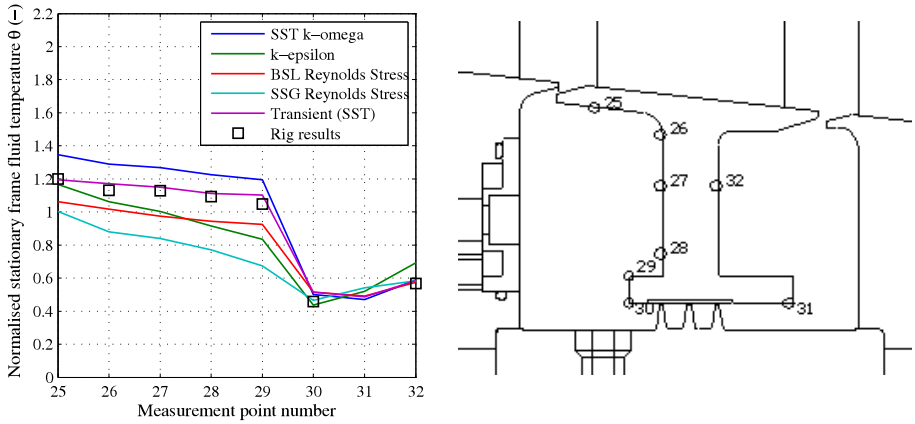

FIG. 2.3-18: Effect of the turbulence model on metal surface temperature (Smith et al., 2012)

The time-averaged temperatures of the transient computation with the *SST* $k-\omega$ turbulence model showed the best agreement by matching the rig temperatures reasonably well across all measurement locations. The steady-state approach with mixing plane could not match the rig data, even though the *SST* $k-\omega$ agrees well of all the turbulence models. There was no additional benefit to solving the complex Reynolds Stress models, even though they are theoretically more suitable for rotating flows as the 2-equation models.

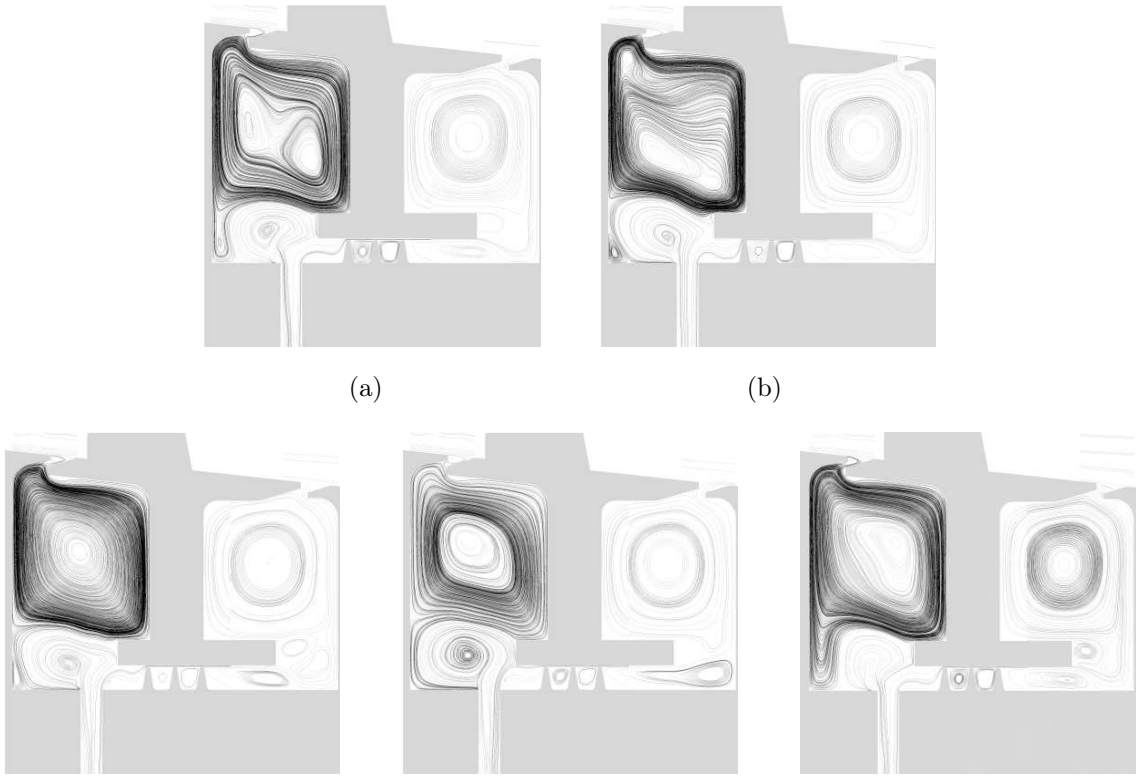

Fig. 2.3-19: Effect of the turbulence model on the computed streamlines in the stator wall (Smith et al., 2012); (a) *SST* $k-\omega$; (b) $k-\varepsilon$; (c) *BSL RSM*; (d) *SSG RSM*; (e) *SST* $k-\Omega$ transient

Smith et al. (2012) compared the streamlines in the stator well for all turbulence models, where the most complex flow structure was computed by the *SST* $k-\omega$ model with two re-circulating structures in the core region as shown in Fig. 2.3-19. The Reynolds Stress models have shown simplified flow patterns with the core being located in the well centre while the $k-\varepsilon$ shows a distorted flow pattern with a minor re-circulating area underneath the rotor platform and the core moved downwards towards the bottom of the well. The transient calculation showed, with the time-averaged streamlines, a more simplified pattern but with a strong unsteadiness of the interaction of sealing jet with the cavity flow and a time-dependent core structure.

Jakoby et al. (2004) captured, with their 360° CFD model, the transient phenomenon of a rotating pressure structure in the wheel-space of a 1.5 stage turbine test facility. Fig. 2.3-20 shows the structure which is similar to a "Mercedes star" where regions of low pressure and provide an additional driving mechanism for ingress.

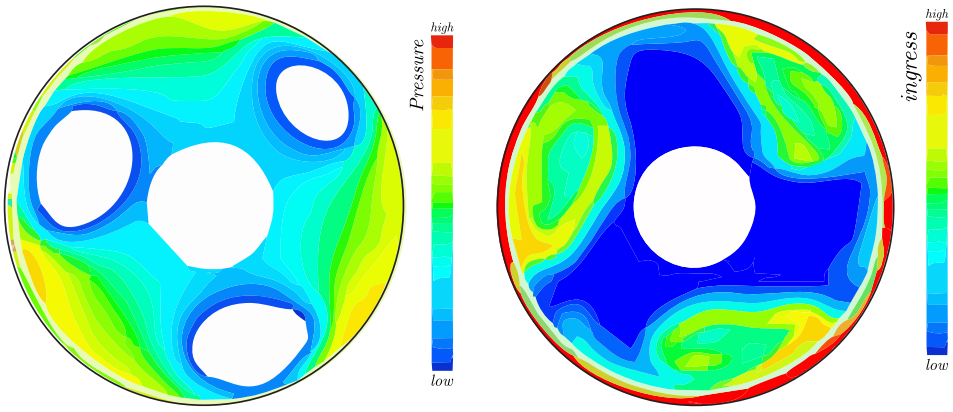

(a) (b)

FIG. 2.3-20: Rotating structure in wheel space cavity at the midplane at a random timestep (Jakoby et al., 2004); (a) Static pressure distribution in the wheel space cavity; (b) Level of ingress into the wheel space cavity

Wang et al. (2013) carried out 360°, time-dependent numerical simulations of a complete turbine stage with rim-seal and cavity. The results showed complex pressure fields which resulted from interactions between the blade and vane, and provided insight into the irregular circumferential pressure distribution to be the driving force for ingress. They also showed that the circumferential distribution of velocity of the ingress through the seal did not have a periodicity associated with either the blade or vane exit pressure variations.

2.3.2 Egress-Mainstream Interaction

This section reviews the history of turbine aerodynamics with steady and unsteady computational fluid dynamics, its milestones and the state-of-the-art technology. This literature survey is supplemented by reviewing various approaches to minimise secondary flow losses in the blade passage by introducing blade endwall profiling. This forms the basis for Chapter 8 of this dissertation: „Egress-Mainstream Interaction“.

2.3.2.1 Gas Path Steady and Unsteady Flow

The design of modern compressors and turbines have become unthinkable without the computational fluid dynamics models and this reliance has increased even further with the improved capability of numerical models to predict complex flows (Denton and Dawes, 1999).

Wu (1951) formulated numerical methods for turbomachinery applications even before the arrival of computers by describing the flow field with two surface streamlines, i.e. one describes the blade-to-blade flow field referred to it as S1 while the

other one describes the hub-to-tip flow field which is known as S2 or throughflow calculation. Both approaches are still valid today and Denton and Dawes (1999) refer to them as the backbone of turbomachinery design where the S1 method is used as standard approach to derive the aerofoil shape and S2 to compute the spanwise variation of the inlet and outlet flow angles through the turbine or compressor blade rows. Gallimore (1997) improved the throughflow method by incorporating losses due to endwall and tip leakage effects, however this approach is based upon empiricism and is only accurate for turbines or compressors for which it was derived. The inherent weakness of most surface streamline curvature methods is that enthalpy and entropy convect along the streamlines between the domain inlet and outlet, and hence it cannot predict re-circulating zones in the meridional direction (Denton and Dawes, 1999). The interested reader is referred to Hirsch and Denton (1981) for a summary on various throughflow methods with their theoretical and practical background.

In the 1980's three-dimensional single blade row flow solvers emerged with the advantage over the surface curvature methods that 3D effects due to blade lean, sweep or twist as well as secondary flow losses can be predicted. Compared to the surface curvature methods, this approach has much of the empiricism removed and it avoids the iterative procedure between S1 and S2 to obtain the solution, but this comes at the expense of higher resource requirement. Initially, the Euler or Navier-Stokes equations were solved with time marching algorithms such as the methods by Denton (1985); Dawes (1986) but the Runge-Kutta scheme was preferred due to the improved convergence which was obtained with variable time steps across the mulitgrid. Despite the improvements of the single blade row simulations, this method still relied upon the streamline methods for extracting the boundary conditions, i.e. inlet stagnation properties as well as the velocity vectors and the static pressure at outlet (Denton and Dawes, 1999).

Further improvement could be obtained by extending the single blade row to multistage domains. The transient effects of the rotor blade on the upstream and downstream located aerofoils was averaged out by introducing a mixing plane. The simplest method such as the one provided by Denton (1979) assumes an instantaneous mixing, i.e. a circumferential averaging of the upstream located flow field and feeding it into the downstream located rotating domain, at the location of the mixing plane. This concept assumes that losses associated with viscous mixing occur at this location instead of the downstream located passage (Denton and Dawes, 1999). Denton (1982) developed an improved mixing plane method where due to its non-uniform treatment the plane can be located adjacent the trailing or leading edge

of the aerofoil without impacting the flow field. This mixing plane treatment along with the incorporated losses due to leakages and tip flows allowed the prediction of the overall engine performance.

However, despite of all of these modelling improvements, the flow field in turbomachinery application is highly unsteady, and the key to performance improvements can only be made if the transient nature of the flow field can be accurately predicted. Various transient methods have been established which can be grouped into three categories: time-marching methods (time domain), time-linearised harmonic methods (frequency domain) and the non-linear harmonic methods (Vasanthakumar, 2003).

Time marching methods in steady-state problems were already successfully established by Denton (1982); Dawes (1992) among others with the pseudo time step along with the mixing plane treatment. In an unsteady problem, however, the time marching has a physical meaning where the transient nature of the flow progresses in time and reaches a periodic state, which depends on the time and length scale of the unsteady flow feature.

Time-linearised harmonic techniques are an efficient method to compute transient flow behaviour in turbomachinery. This approach linearises the transient perturbations over time and forms with the steady flow the transient flow field. It is assumed that any unsteady perturbations arising from flow separations, shock oscillations, etc. do not exceed 10% of the mean steady flow field and that their behaviour is periodic and harmonic over time. This assumption removes the time-dependency from the method and the equations are solved with a pseudo-time marching technique. Phase-shifted boundary conditions reduce the model to a single blade domain model owing to the harmonic time-independent flow assumptions (Vasanthakumar, 2003).

He (1996) formulated the non-linear harmonic method which superimposes unsteady harmonic perturbations onto the time-averaged flow field. Unsteady non-linear effects due to flow separations and shock oscillations are accounted for but by keeping the efficiency of time-linearised methods. Vasanthakumar (2003) implemented this method into a 3D Navier-Stokes solver and the predicted non-linearities are in good agreement with the results of a linear compressor cascade with oscillating aerofoils.

The most recent development includes the usage of an accelerated 3D Navier-Stokes solver for gas path aerodynamics running on a set of Graphics Processing

Units (GPUs) developed by Brandvik and Pullan (2009). This method uses the dual time stepping approach as proposed by Jameson (1991) to accelerate the convergence behaviour in transient simulations. This leads to an acceleration of the computational times by an order of magnitude compared to traditional methods with CPU based solvers as it was demonstrated with a 360° three stage compressor simulations as shown in Fig. 2.3-21. This method is described in more detail in Chapter 6 „Off-Design Conditions“ where it has been used for transient turbine off-design computations.

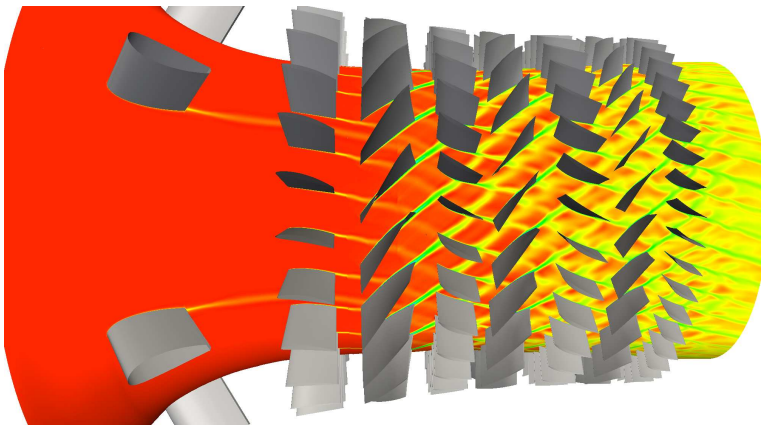

Fig. 2.3-21: Computation of a three-stage compressor test rig with entropy function contours at midspan (Brandvik and Pullan, 2010)

2.3.2.2 Leading Edge Fillet/Endwall Blade Profiling

This section reviews the literature on the leading edge fillet and the endwall-blade profiling of blade passages and their implications on the secondary flow losses.

Praisner et al. (2007) show with Fig. 2.3-22(a) the schematic endwall flow of an aerofoil row where the incoming low-momentum boundary layer, here coloured in yellow, re-organises itself into two 3D vortex structures due to the adverse pressure gradient imparted by each aerofoil. The separated structures bypass the leading edge of the aerofoil with one vortex adjacent to the pressure side, also referred to as pressure side leg, and the other one next to the suction side, known as suction side leg. Both vortices convect downstream and form the passage vortex with one or several loss cores. Praisner et al. (2007) state that as much as 30% of the turbine losses are induced by the secondary flow losses. For completeness, it must be noted that the flow structures shown in Fig. 2.3-22(a) are in the absence of any upstream ejected coolant due to rotor-stator cavities.

The secondary flow vortices as shown in Fig. 2.3-22(b) by Schlienger et al. (2004) dissipate their kinetic energy by shear gradients while the rotor blade wake convects

to the downstream located vane row and is chopped to form a wake avenue as Hodson (1985) describes this which can be identified in Fig. 2.3-21.

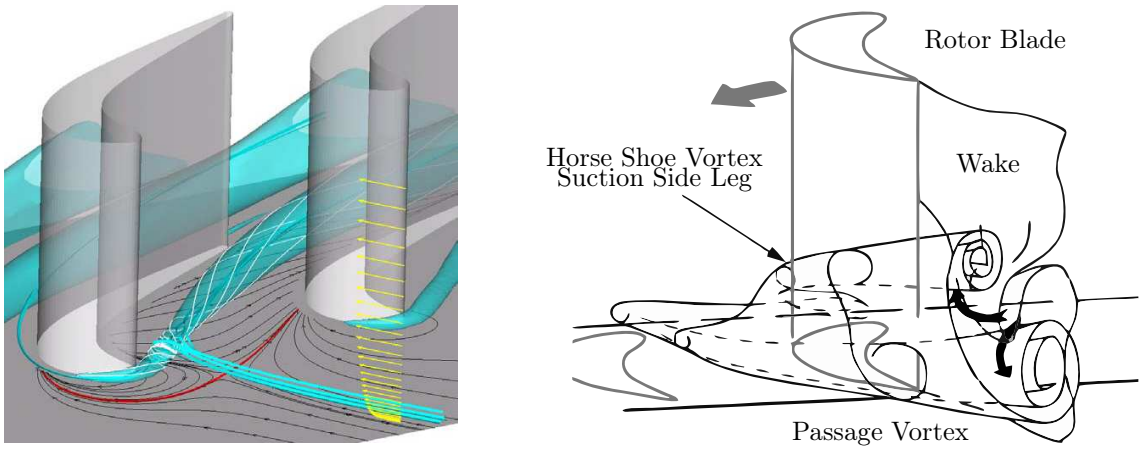

FIG. 2.3-22: Secondary flow losses in turbine passages; (a) (Praisner et al., 2007); (b) Formation of secondary flow vortices Schlienger et al. (2004)

The concept of introducing design features in front of aerofoil and within the blade passage to minimise secondary flow losses goes back to the 1960's where Dejc and Zarjankin (1960) attempted to increase the turbine efficiency by contracting strongly the axisymmetric endwall near the leading edge of the blade, resulting in a thinner boundary layer. Morris and Hoare (1975) found in an experimental investigation of non-axisymmetric endwall contours that the losses reduce but this was off-set by adverse effects in the vicinity of the 3D endwall and a strong deviation of the flow exit angle. These observations were confirmed by Aktins (1987) with their investigation of secondary flow losses in a linear cascade that the pressure field in the blade passage can be influenced, both favourable and unfavourable to the secondary flow losses, but adverse effects, i.e. flow separations in the profiled endwall and a strong twisting of the aerofoil wake, cause an increase of the overall losses. Rose (1994) applies the non-axisymmetric endwall profiling to the exit plane of the NGV and by influencing the circumferential pressure variation the egress flow can be reduced.

Ingram et al. (2002) extended the work of Hartland et al. (1999) with the investigation of non-axisymmetric endwall profiles in the Durham cascade. This study included the „first generation" of profiling as used by Hartland et al. (1999), a new design as proposed by Gregory-Smith et al. (2001) and a reference case. This study shows that the contoured endwall impacts the flow structure in the early part of the blade passage, which translates further downstream into reduced secondary flow losses of 24% compared to their reference case. Even tough these findings could con-

firm the results of Hartland et al. (1999) in terms exit deviation angle, there is an inconsistency between both results in secondary flow losses as Ingram et al. (2002) reverse the ranking order of Hartland et al. (1999).

Brennan et al. (2001); Rose et al. (2001) investigated newly designed profiled endwalls in a rotating engine representative test rig and they observed an improvement of the stage efficiency of 0.59 compared to their reference case.

Schuepbach et al. (2008a,b) investigate in a 1.5 stage highly loaded axial turbine non-axisymmetric endwall profiles which were designed and optimised with a numerical optimiser based upon a sequential quadratic programming algorithm with the objective to reduce the secondary kinetic energy and the secondary flow losses. The numerical results were validated with experimental measurements obtained with a torquemeter and pressure measurements with 5-hole probes with 41 circumferential and 40 radial positions for several axial planes. The measurements confirms the predicted results with an improvement of the stage efficiency by $1.0\% \pm 0.4\%$, even though the CFD method underestimated this improvement. They conclude that the observed improvement was due to the reduced losses in the first blade row, and hence the more homogeneous flow field downstream of the stator vanes.

Popovic and Hodson (2012a,b) investigated the effect of various rim-seals/outer axisymmetric platforms and their implications on the sealing effectiveness as well as the stage efficiency in a large-scale linear cascade. They found that the requirement for efficient sealing of the upstream located rotor-stator cavity and reduced spoiling effects due to the interaction of the egress with the mainstream flow leads to contradictory design philosophies. Rim-seal designs with recirculation zones improve the sealing characteristic by attenuating the circumferential pressure variation, but cause additional losses due to increase aerodynamic interaction. Their derived rim-seal design, a reasonable compromise between good rim-seal performance and reduced aerodynamic losses, minimises the aerodynamic losses by 33% compared to the baseline case while the unsteady computation predicts an efficiency improvement of 0.2%.

Chapter 3

Secondary Air Systems

This chapter discusses the translation of the academic aspects of the orifice model introduced by Owen for EI ingress into a practical tool for industrial purposes, with subsequent implementation into the Siemens SAS solver.

3.1 Introduction

The term "Secondary Air Systems (SAS)" refers to the compressed air that is extracted at various compressor stages to bypass the combustion process in order to be used on the hot side of a gas turbine for sealing and cooling purposes. This internal air system is modelled in 1D flow networks to determine the required massflow rates to fulfil their function. The engine designer still relies on these massflow models which to a large extent is beyond the capability of CFD codes.

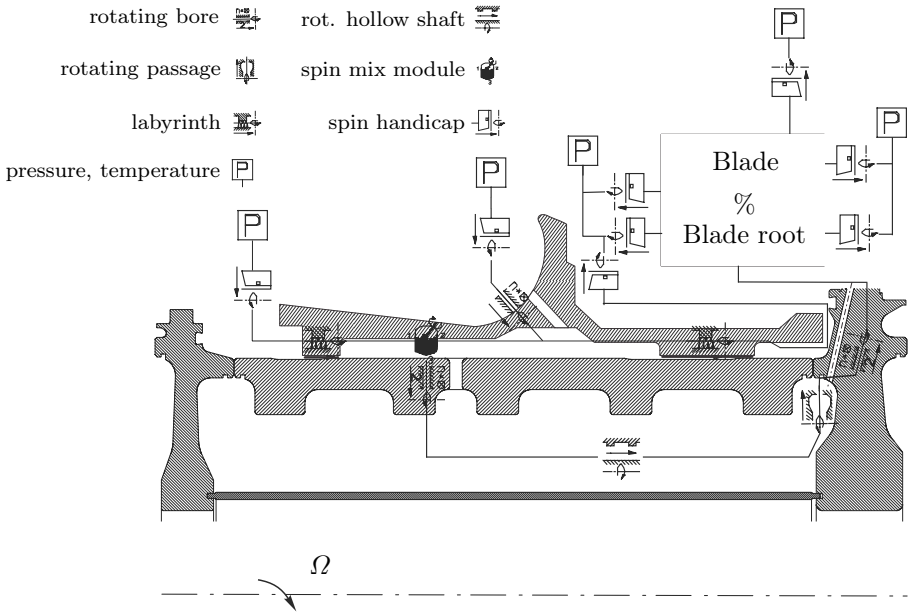

FIG. 3.1-1: Massflow model for an internal air system (adapted from Brillert (2001))

Fig. 3.1-1 shows such a massflow model where relevant engine features are represented by theoretical 1D models and correlations. These networks solve of the conversation laws for mass, energy, linear and angular momentum.

Paramount for the engine designer is the ability to accurately predict massflow rates throughout the engine. An underprediction comes at the expense of a failure of the engine integrity or a reduced engine life span, while an overprediction has a negative impact on the overall efficiency.

A newly-developed orifice model was successfully validated at the University of Bath which will improve the predictions of the fluid exchange between the gas path and rotor-stator cavities through rim-seals. The reader is referred to the following papers for more detailed information on this orifice model: Owen (2009a,b); Owen et al. (2010a,b).

3.2 Theoretical Orifice Model

Owen (2009b) provides, with a linear saw-tooth model, an analytical solution to the orifice equations for EI ingress. He used the approach by Hamabe and Ishida (1992) to approximate the external circumferential peak-to-trough variation with a triangular shape to obtain the following relationship:

$$\Phi_{min,EI} = \frac{C_{w,min,EI}}{2\pi G_c Re_\phi} = I_{min} C_{d,e,EI} \Delta C_p^{1/2} \tag{3.2-1}$$

where the integral I_{min} is defined as

$$I_{min} = \int_0^1 (1-f)^{1/2}\, d\theta \tag{3.2-2}$$

where the pressure shape factor f is expressed as

$$f(\theta) = \frac{p_2 - p_{2,min}}{p_{2,max} - p_{2,min}} \tag{3.2-3}$$

The shape factor f is in the range $0 \preceq f(\theta) \preceq 1$ where $0 \preceq \theta \preceq 1$. I_{min} was obtained by integrating the pressure shape factor (see Eq. 3.2-2) across one non-dimensional vane passage which gives an integral value of $I_{min} = 2/3$. With this constant, Eq. 3.2-1 can be re-written to the important analytical solution as follows:

$$\Phi_{min,EI} = \frac{2}{3} C_{d,e} \Delta C_p^{1/2} \tag{3.2-4}$$

Fig. 3.2-2 shows the pressure distribution approximation across θ for the saw-tooth model for three sealing flow rates with their corresponding radial velocity profiles. When the wheel-space pressure p_1 approaches $p_{2,max}$, then $\Phi_o \to \Phi_{min}$ and there exists no radial velocity component that drives ingress into the rotor-stator cavity. For $p_1 \prec p_{2,max}$, the symmetric velocity profiles shows an increasing radial component with decreasing Φ_o, with its peak at $\Phi_o = 0$.

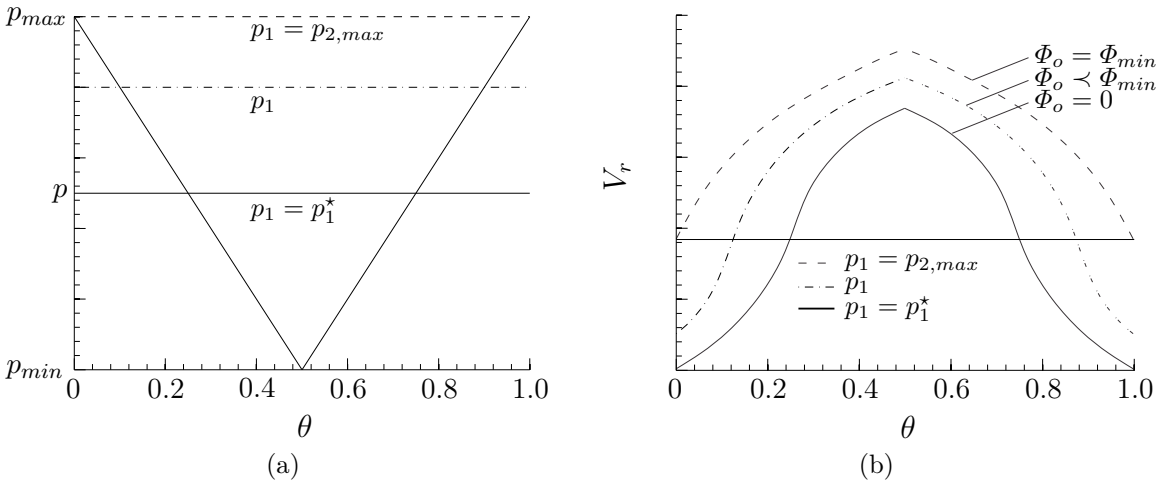

FIG. 3.2-2: Saw-tooth model approximation one non-dimensionalised vane pitch θ (adapted from (Owen, 2009b)); (a) Circumferential variation of static pressure; (b) radial velocity profiles for three wheel-space pressures

Owen et al. (2010b) validated the saw-tooth model with the data by Johnson et al. (2008) as shown in Fig. 3.2-3. The computed pressure variation of Johnson et al. (2008) was fitted and re-plotted as a shape factor and compared to the saw-tooth

model and to a cosine approximation. The cosine approximation requires a numerical integration of the profile as there is no simple analytical solution.

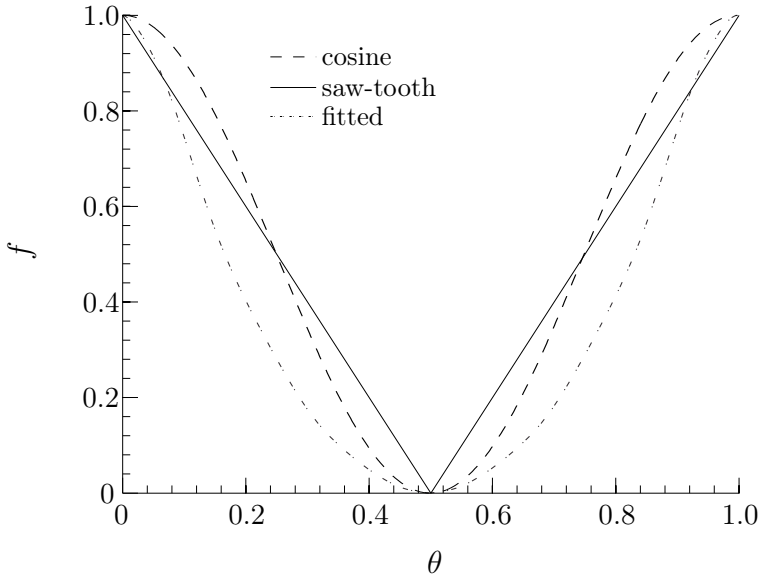

FIG. 3.2-3: Variation of f with θ for two models to approximate the peak-to-trough pressure (adapted from Owen et al. (2010b))

The integral I_{min}, I_i and I_e were solved numerically for all three profiles, where

$$I_e = \int_{\theta'}^{1} (g - f)^{1/2} \, d\theta \tag{3.2-5}$$

$$I_i = \int_{0}^{\theta'} (f - g)^{1/2} \, d\theta \tag{3.2-6}$$

I_e and I_i are the integrals for egress and ingress respectively. The sealing effectiveness was computed with Eq. 3.2-7 with a $\Gamma_c = 1$

$$\varepsilon_{EI} = 1 - \frac{\Gamma_c I_i}{I_e} \tag{3.2-7}$$

The $\varepsilon_{EI} - \Phi_o$ data points (Johnson et al., 2008) were then used to estimate Φ_{min}. Johnson et al. (2008) investigated two configurations, i.e. configuration 1a and 1c with a peak-to-trough pressure of $\Delta C_p = 0.55$ and $\Delta C_p = 0.085$ respectively. Owen et al. (2010b) calculated with this data the discharge coefficient for egress, $C_{d,e}$. The results for the three pressure profiles are tabulated in Tab. 3-1 for configuration 1a and in Tab. 3-2 for configuration 1c along with the parameters of the orifice model. K represents a constant used by Phadke and Owen (1988b) and Bohn and Wolff (2003), which is discussed in detail in Chapter 7.

Tab. 3-1: Computed parameters for the orifice model with the data of Johnson et al. (2008) for configuration 1a with $\Delta C_p = 0.55$ (Owen et al., 2010b)

f - distribution	$\Phi_{min,EI}$	I_{min}	$C_{d,e}$	K
Fitted	0.215	0.756	0.377	0.403
Cosine	0.173	0.637	0.360	0.324
Saw-tooth	0.205	0.667	0.408	0.384

Tab. 3-2: Computed parameters for the orifice model with the data of Johnson et al. (2008) for configuration 1c with $\Delta C_p = 0.085$ (Owen et al., 2010b)

f - distribution	$\Phi_{min,EI}$	I_{min}	$C_{d,e}$	K
Fitted	0.083	0.674	0.422	0.403
Cosine	0.079	0.637	0.425	0.383
Saw-tooth	0.093	0.667	0.479	0.451

Owen et al. (2010b) assume that the fitted pressure profile provides the most accurate prediction of the orifice model parameter for all three profiles, and that the saw-tooth model estimation is more accurate than the cosine prediction of Φ_{min} for configuration 1a but there is less agreement for configuration 1c. They concluded that Φ_{min} is governed by the magnitude of the peak-to-trough pressure and that the shape of the pressure profile is of secondary importance.

Further validation of the saw-tooth model provided Sangan et al. (2011a) with their comparison of the experimental data for various rim-seals with the effectiveness equations. These equations were derived by Owen et al. (2010b) for the saw-tooth model, and are given by Sangan et al. (2011b) in an explicit form. The reader is referred to Section 2.2.3 "Externally-Induced Ingress" for more information on the derivation of these equations. Fig. 3.2-4 compares the concentration experiments for a double radial overlapping rim-seal at the sampling points at $r/b = 0.958$ and $r/b = 0.85$ with the sealing effectiveness curves. The comparison between the experimental data and the EI theory shows good agreement, not only for the double rim-seal shown in Fig. 3.2-4 but also for a variety of seal configurations as demonstrated by Sangan et al. (2012, 2013).

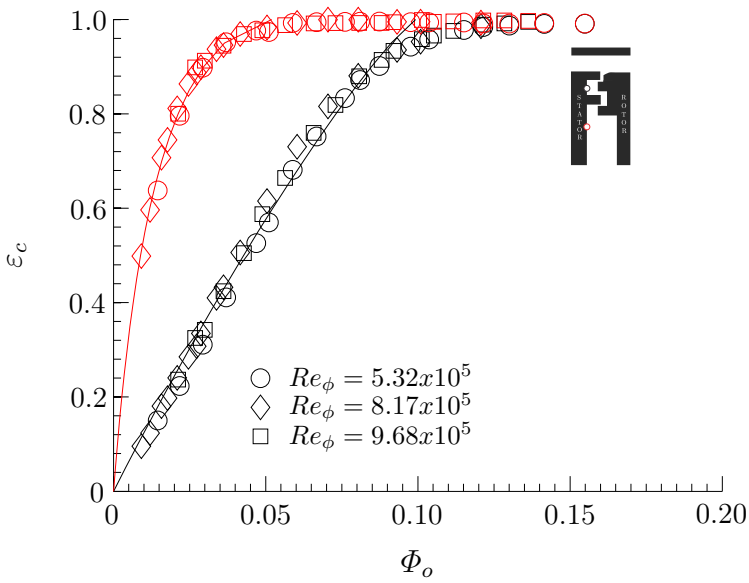

FIG. 3.2-4: Comparison of the EI theory with the experimental concentration measurements for a double radial overlapping seal with sampling point at $r/b = 0.958$ and 0.85 (source: University of Bath)

The saw-tooth model forms the base for the implementation of the orifice model into the flow network solver 2ndFlow. The derivation of the mass flow functions, i.e. the sealing parameter Φ_i, Φ_e and Φ_o as variation of the wheel-space and peak-to-trough pressure, is described below.

3.3 Massflow Equations - EI Ingress

This section derives the orifice model massflow equations as function of the wheel-space pressure p_1 and driving force Δp_2. In order to implemented these equations as a subroutine into the solver, the model must be arranged in a way that it complies with the solver structure.

The starting point of the derivation is the relationship between the linear saw-tooth model for EI ingress

$$\Phi_{min} = \frac{2}{3} C_{d,e,EI} \Delta C_p^{1/2} \tag{3.3-8}$$

This equation was re-arranged to give, for a known ΔC_p and Φ_{min}, the discharge coefficient for egress as follows:

$$C_{d,e,EI} = \frac{\Phi_{min}}{\frac{2}{3}\Delta C_p^{1/2}} \tag{3.3-9}$$

The ratio of discharge coefficients, Γ_c, is used to determine $C_{d,i}$, the discharge coefficient for ingress,

$$C_{d,i,EI} = \Gamma_c C_{d,e,EI} \tag{3.3-10}$$

The normalised wheel-space pressure, g, is defined as function of the external peak-to-trough pressure variation, Δp_2, and the wheel-space pressure p_1

$$g = \frac{p_1 - p_{2,min}}{p_{2,max} - p_{2,min}} \tag{3.3-11}$$

The highest ingress occurs in the absence of the sealing flow, i.e. $\Phi_o = 0$, where $g = g^\star$ and $\Phi_i = \Phi_e$. This point is given by:

$$g^\star = \frac{1}{1 + \Gamma_c^{-2/3}} \tag{3.3-12}$$

When g approaches 1, $\Phi_i \to 0$ and $\Phi_e \to \Phi_{min}$. A value of $g \succ 1$ corresponds to a state where there is no ingress, i.e. $\Phi_o \succ \Phi_{min}$.

The egress and ingress integral for EI ingress is expressed as

$$I_e = \int_{\theta'}^{1} (g - f)^{1/2}\, d\theta = \frac{2}{3} g^{3/2} \tag{3.3-13}$$

$$I_i = \int_{0}^{\theta'} (f - g)^{1/2}\, d\theta = \frac{2}{3}(1 - g)^{3/2} \tag{3.3-14}$$

These equations can be expressed in their non-dimensional form

$$\Phi_e = C_{d,e,EI} \Delta C_p^{1/2} I_e \tag{3.3-15}$$

$$\Phi_i = C_{d,i,EI} \Delta C_p^{1/2} I_i \tag{3.3-16}$$

Equations 3.3-15 and 3.3-16 can be re-written as

$$\Phi_e = \frac{2}{3} C_{d,e,EI} \Delta C_p^{1/2} \left(\underbrace{\frac{p_1 - p_{2,min}}{p_{2,max} - p_{2,min}}}_{g} \right)^{3/2} \tag{3.3-17}$$

$$\Phi_i = \frac{2}{3} C_{d,i,EI} \Delta C_p^{1/2} \left(1 - \underbrace{\frac{p_1 - p_{2,min}}{p_{2,max} - p_{2,min}}}_{g} \right)^{3/2} \tag{3.3-18}$$

Eqs. 3.3-17 and 3.3-18 are converted to massflow rates with Eq. 3.3-19

$$\dot{m} = 2\pi b \mu Re_\phi \Phi G_c \tag{3.3-19}$$

The mass continuity gives the sealing flow rate $\dot{m}_o$

$$\dot{m}_o = \dot{m}_e - \dot{m}_i \tag{3.3-20}$$

The pressure sealing effectiveness, ε_p, can be computed by

$$\varepsilon_p = 1 - \Gamma_c \left(\frac{1-g}{g} \right)^{3/2} \tag{3.3-21}$$

3.4 Implementation of Orifice Model

This section describes the translation of the academic aspects of the orifice model into a practical tool with subsequent implementation of the massflow functions into the Siemens SAS solver. The orifice model was modelled as a separate flow network branch, implemented into the solver structure as a subroutine written in C#. Fig. 3.4-5 shows the practical usage of this branch. An external node, i.e. the gas path node with fixed properties with defined static and stagnation pressures and temperatures along with the swirl is connected to an inner node which connects the orifice branch to the flow network.

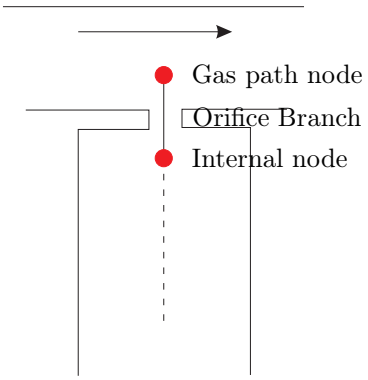

FIG. 3.4-5: Orifice model branch

The orifice branch requires as input the geometric information of the seal in form of Γ_c and G_c and the parameters that describe the simulation condition, i.e.

Φ_{min}, the peak-to-trough pressure variation and the rotational speed Ω. The orifice model provides with this data the mass flow rates for ingress, egress and the sealing flow. This information is summarised in the orifice branch GUI as shown in Fig. 3.4-6.

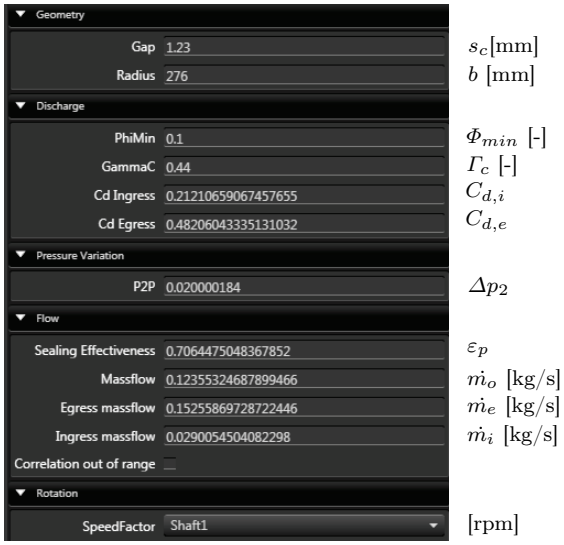

FIG. 3.4-6: 2ndFlow GUI for orifice branch

Fig. 3.4-7 shows the characteristic of the massflow functions for ingress, egress and the sealing flow rate as variation of g. In a steady-state simulation with a fixed external peak-to-trough pressure, g varies only with the wheel-space pressure p_1.

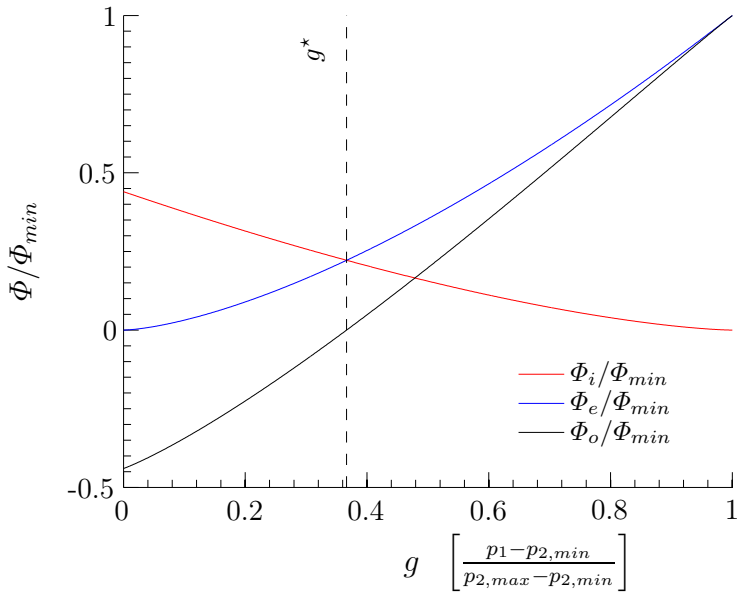

FIG. 3.4-7: Massflow functions for Φ_i, Φ_e and Φ_o as variation of the normalised wheel-space pressure g

In the absence of the sealing flow, i.e. $g = g^\star$, $\Phi_i = \Phi_e$ and with increasing Φ_o, g approaches 1, hence $\Phi_i \to 0$ and $\Phi_e \to \Phi_{min}$. The solver determines the parameter

g and uses the massflow functions to compute the flow rates through the rim-seal in an iterative procedure using the conservation laws for mass, energy and angular momentum, as summarised in the flow charts in Fig 3.4-8 and 3.4-9.

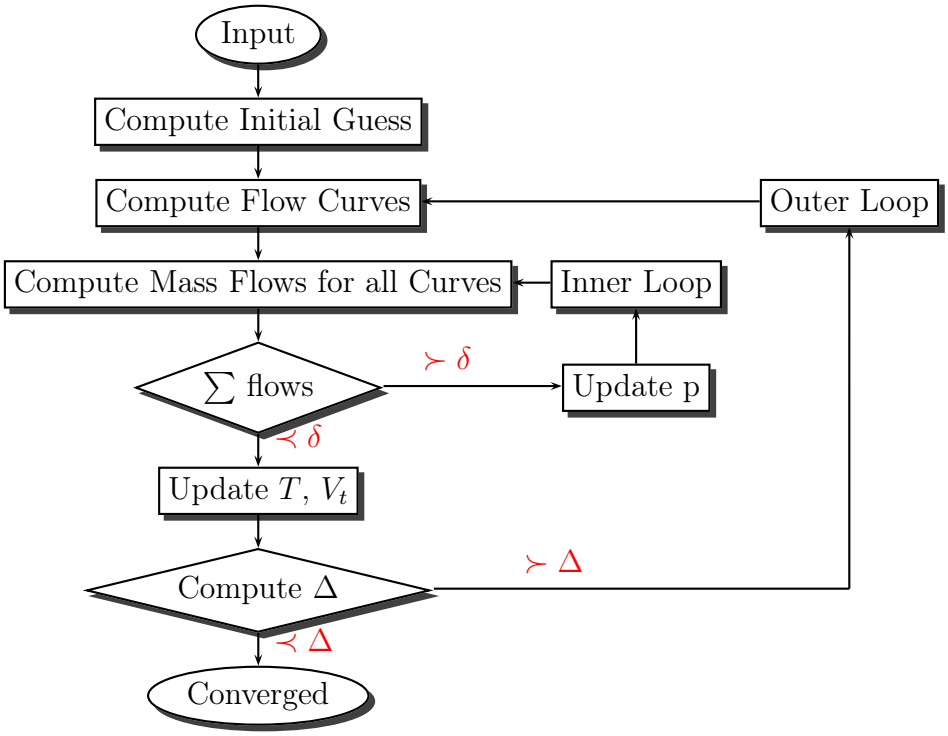

FIG. 3.4-8: Solver procedure

The solver consists of a two loop iterative procedure: in the inner loop iteration, the internal nodal pressures are adjusted while the temperatures and the tangential momentum is kept constant. This process continues until the mass balance across the entire flow network reaches a defined threshold:

$$\sqrt{\frac{1}{N}\sum_{i=1}^{N}\left(\Delta\dot{m}_i\right)^2} \prec \delta \tag{3.4-22}$$

The outer loop iteration fixes the internal nodal static and stagnation pressures, and adjusts the mixed static and total temperatures and the swirl. The solver performs after every outer loop iteration and inner one to update the nodal pressures and hence the mass flows. The convergence of the outer loop iteration is obtained when the change of the temperatures and the swirl from the previous iteration reached a threshold.

The massflow equations require the density at the internal and external node which is computed by the state equation, here shown for the egress case as follows:

$$\varrho_{mix} = \frac{p_1}{RT_{mix}} \tag{3.4-23}$$

where T_{mix} is the mixed out temperature at the internal node computed in the outer loop with the updated swirl with the following procedure:

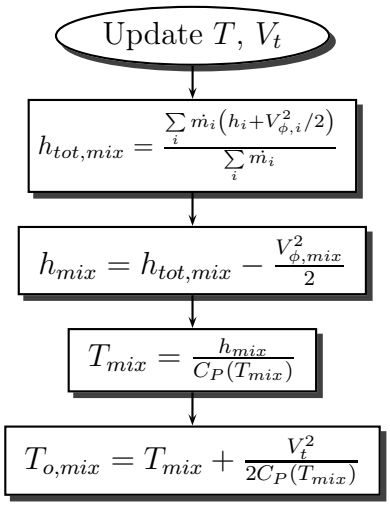

Fig. 3.4-9: Procedure to compute the mixed-out temperature at the internal node in the outer loop iteration

3.5 Validation

This section describes the validation of the implemented orifice model against a standard method to calculate the massflow rates. This benchmark method treats the rim-seal as an orifice or constrictor and uses the standard orifice equation to relate the pressure drop across the constriction to the massflow.

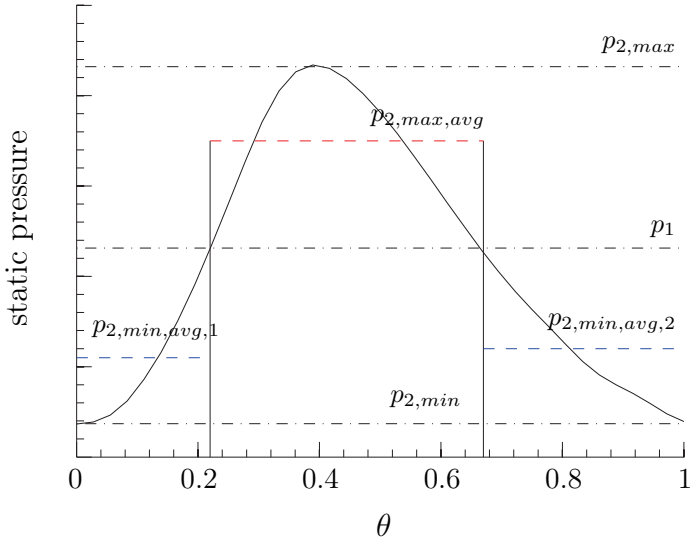

FIG. 3.5-10: Tangential pressure variation across one vane pitch downstream of the trailing edge of the nozzle guide vane of a high pressure turbine of an industrial gas turbine

Fig. 3.5-10 shows the pressure profile which was used to derive the pressure input for both methods. This computed profile was obtained from a CFD model of the first stage of an industrial high pressure turbine downstream of the trailing edge of the nozzle guide vane. The reader is referred to Chapter 7 for more information on the CFD model.

The orifice model uses as input the peak-to-trough pressure, i.e. $\Delta p_2 = p_{2,max} - p_{2,min}$. The reference model uses multiple orifice links to compute the fluid exchange between the gas path and the wheel-space. The wheel-space pressure p_1 separates the profile into three regions at which $p_1 \succ p_2$ and $p_1 \prec p_2$ as illustrated in Fig. 3.5-10. Each section has been modelled as separate orifice branch with the corresponding rim-seal area fraction. The mean pressure was taken as representative pressure.

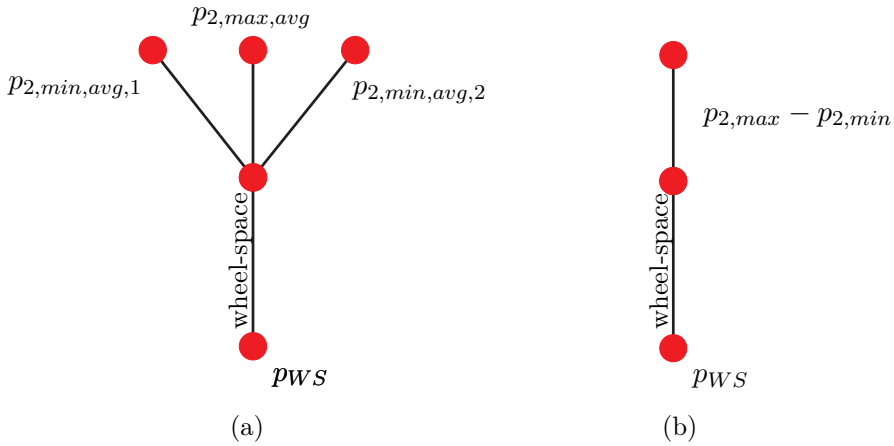

FIG. 3.5-11: Pressure boundary conditions for both rim-seal models; (a) 3-link approach; (b) Rim-seal model

Fig. 3.5-11 shows the flow network of the multi-link approach and the model of the implemented orifice model with the pressure boundary conditions. The discharge coefficients for ingress and egress were calculated by the orifice model for a double-rim seal with $\Phi_{min} = 0.1$ and $\Gamma_c = 0.44$. This resulted in a $C_{d,e} = 0.357$ and $C_{d,i} = 0.163$. Both values were assigned to the appropriate branch of the 3-link method.

Fig. 3.5-12 compares the 3-link method with the OM solution across the sealing flow range: $0 \preceq \Phi_o/\Phi_{min} \preceq \Phi_{min}$, by adjusting the wheel-space delivery pressure p_{WS}. It should be noted that for the 3-link method the area fraction was adjusted in each branch accordingly. Furthermore, the effectiveness equations were incorporated in Fig. 3.5-12.

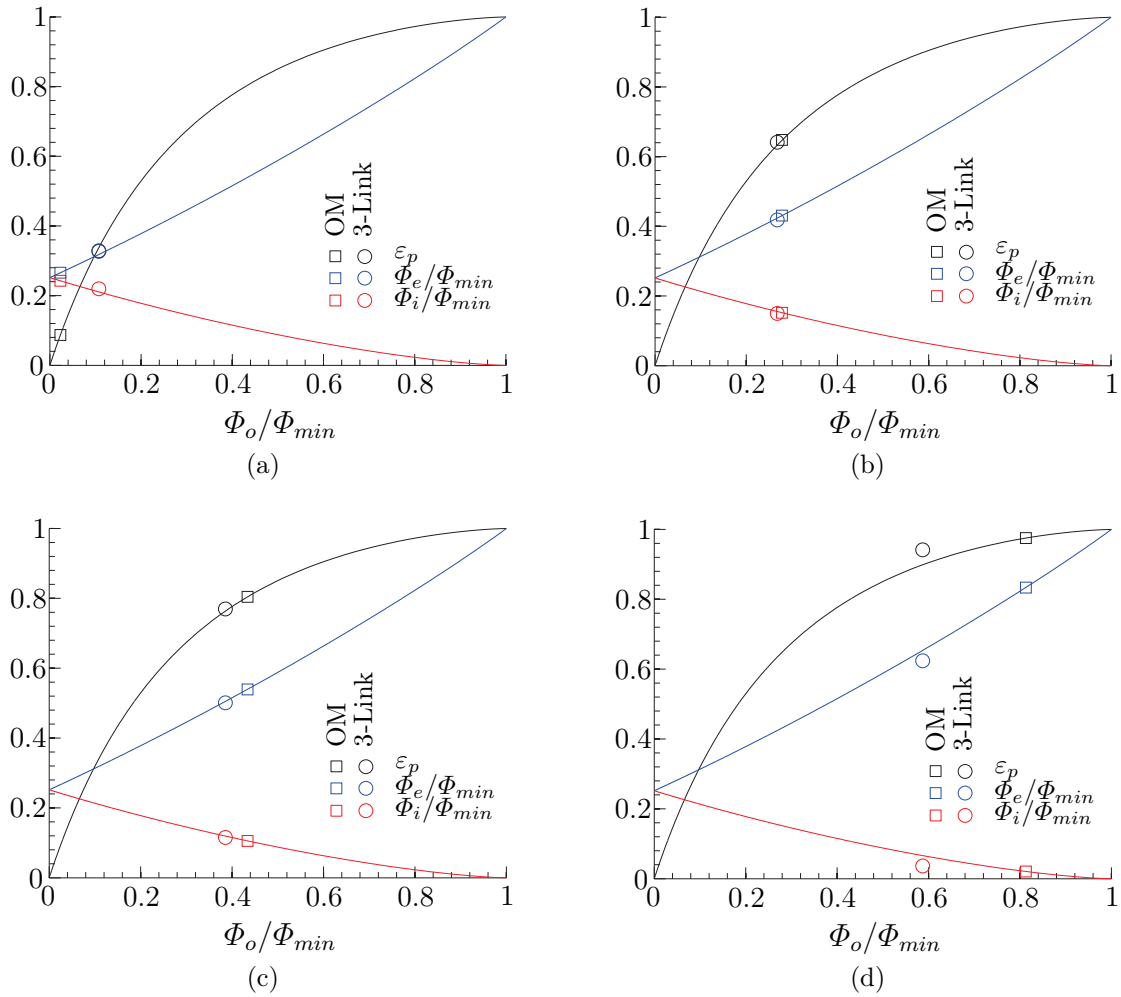

FIG. 3.5-12: Comparison of the 3-link method with the implemented OM

There is in general good agreement of the ingress levels between both methods across the entire range of Φ_o/Φ_{min}. The same behaviour applies to the sealing and

egress flow for $\varepsilon \prec 0.8$. With increasing ε there is some discrepancy in the egress levels predicted by the 3-link method and the orifice model.

The data points for the sealing effectiveness for the 3-link method were fitted and re-plotted with the analytical solution of the orifice model in Fig. 3.5-13 to emphasise this discrepancy. The 3-link method diverges from the analytical solution of the orifice model at the point where there is a disproportional increase in Φ_o at high ε.

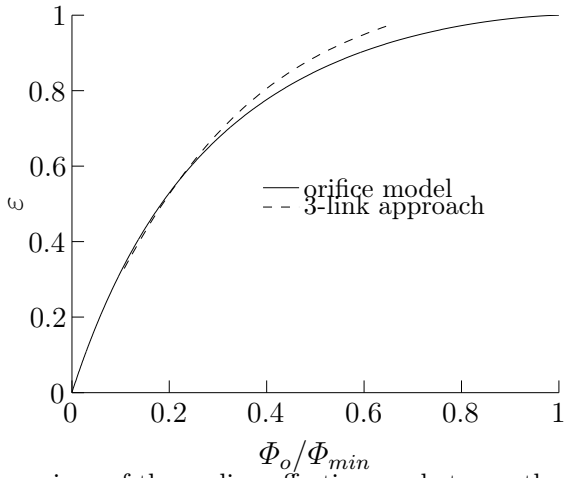

Fig. 3.5-13: Comparison of the sealing effectiveness between the multi-link approach and the orifice model

3.6 Practical Implications

This chapter discussed the implementation of a newly-developed orifice model for EI ingress into a non-commercial flow network solver. The orifice model massflow functions are solved with an iterative procedure until a defined threshold has been reached to satisfy the conservation laws. The comparison of the orifice model against a standard procedure where the fluid exchange is modelled with multiple links was in general good agreement despite a discrepancy a high ε.

To support the engine designer with a selection of the appropriate orifice model parameters, a database with a variety of experimental tested generic rim-seal geometries was created. The tests were conducted with the 1-stage ingress test facility at the University of Bath with a symmetric rotor blade. To further improve the quality of the input parameter, further tests will focus on ingress tests with a 1.5-stage test facility with a turned rotor blade with engine representative aerofoils to allow a more accurate prediction of the ingress, egress and sealing flow rates.

Chapter 4

CFD Model Validation

This chapter describes the CFD model used to address the ingress problem in rotor-stator systems, its settings and the validation against experimental data obtained in the 1-stage ingress test facility at the University of Bath. The commercial computational fluid dynamics code CFX 12.1 has been employed to conduct URANS computations for an axial- and radial clearance seal. This work focuses on the *EI* regime and it provides the basis for the numerical investigation of the rim-seal concepts and the egress-mainstream interaction study discussed in chapter 7 and Chapter 8. This validation work was part of the extrapolation method published by Teuber et al. (2013).

4.1 Computational Model

Fig. 4.1-1 depicts the 1-stage ingress test facility used by Sangan et al. (2011a) for their investigation of the fluid mechanics associated with hot gas ingestion. This rig has been described in detail in Chapter 2 "Literature Review - Hot Gas Ingestion" and the reader is referred to this part of the thesis for more information on the design, the experimental set-up and the results.

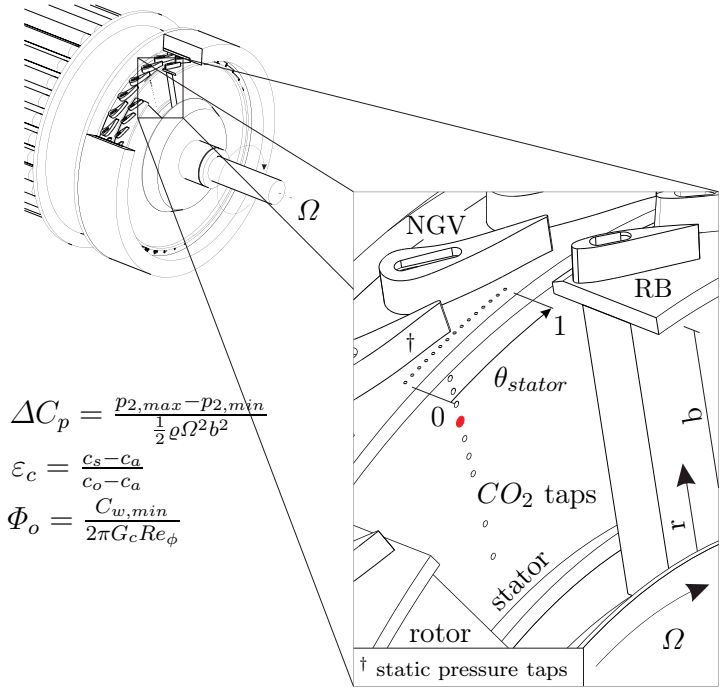

Fig. 4.1-1: Ingestion test facility at the University of Bath with tracer gas instrumentation on the stator wall and static pressure taps in the primary gas path

The CFD domain was derived from this rig, identical in the geometric dimensions but with a simplification of the rotor blade (RB) count. The number of RBs were decreased from 41 to 32 to satisfy a pitch ratio of 1, i.e. 32NGVs/32RBs, to minimise the scaling error across the sliding plane for transient computations. With this simplification, the CFD domain could be reduced to one guide vane and one rotor blade in a 11.25° sector. Fig. 4.1-2(a) shows the domain, where the nozzle guide vane and the wheel-space sector were modelled in a stationary frame of reference connected by a general grid interface (GGI) and the rotor blade domain modelled in the rotating frame. The boundary conditions and boundary type settings are summarised in Fig. 4.1-2(c) where the domain inlets were set-up as massflow boundaries and the outlet was defined as pressure boundary condition. Adiabatic conditions were used for all solid walls. The tracer gas was simulated with a passive scalar which was solved by an additional mass transport equation. The computed sealing effectiveness which is used throughout this dissertation is defined as

$$\varepsilon_{cc} = \frac{c_s}{c_o} \tag{4.1-1}$$

where s refers to the CO_2 concentration at the sampling point on the stator wall and o to the concentration in the sealing flow.

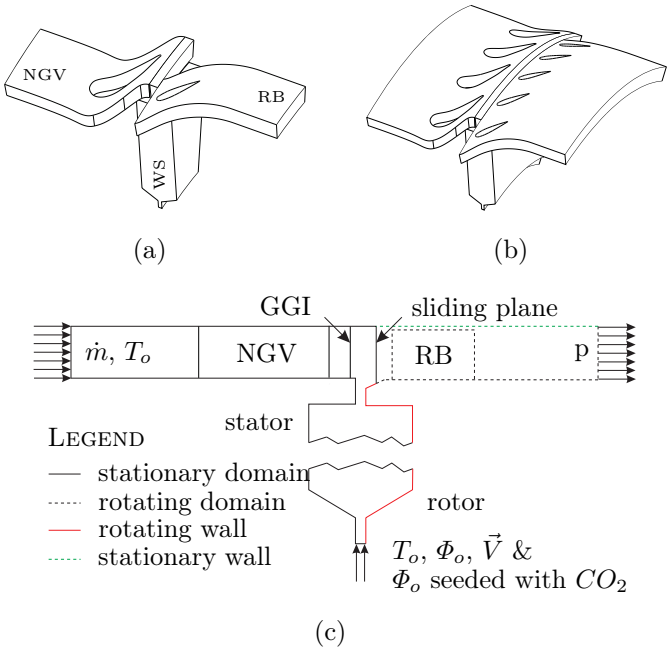

FIG. 4.1-2: Computational model; (a) Single sector model with 11.25° domain (referred to as the 1:1 model), (b) Multi sector with 45° domain (referred to as the 4:5 model), (c) Boundary conditions and boundary type settings

Fig. 4.1-2(b) shows a CFD domain with a 45° sector with 4 NGVs and 5RBs which corresponds to 32 NGVs and 40 RBs. This approach allows a better representation of the test rig at the expense of increased computing times.

Throughout this thesis, the 2-equation SST $k-\omega$ turbulence model was employed with a "High Resolution" advection scheme. A blending function in the near wall region was used to allow for a smooth transition from the near wall low Reynolds number formulation to the wall function. The total energy heat transfer model was chosen where the fluid density is a function of the pressure to account for compressibility effects. The viscous work term was included to incorporate the temperature increase due to frictional heating.

C_P and k were expressed as polynomials as shown by Eq. 4.1-2 and Eq. 4.1-3 and their functions were sourced with the data by Irvine (1998)*† to model temperature dependence as follows:

$$C_P = (a_o + a_1 T + a_2 T^2 + a_3 T^3 + a_4 T^4) \times 1000 \tag{4.1-2}$$

*$a_o = 0.103409 \times 10^1 J/(kgK)$; $a_1 = 0.2848870 \times 10^{-3} J/(kgK)$; $a_2 = 0.7816818 \times 10^{-6} J/(kgK)$; $a_3 = 0.4970786 \times 10^{-9} J/(kgK)$; $a_4 = 0.1077024 \times 10^{-12} J/(kgK)$

†$b_o = 2.276501 \times 10^{-3} W/(mK)$; $b_1 = 1.2598485 \times 10^{-4} W/(mK)$; $b_2 = 1.4815235 \times 10^{-7} W/(mK)$; $b_3 = 1.73550646 \times 10^{-10} W/(mK)$; $b_4 = 1.066657 \times 10^{-17} W/(mK)$

$$k = b_o + b_1 T + b_2 T^2 + b_3 T^3 + b_4 T^4 + b_5 T^5 \tag{4.1-3}$$

The temperature dependent dynamic viscosity, μ, is computed by the Sutherland's law as follows:

$$\mu = \frac{1.46 \times 10^{-6} T^{3/2}}{T + 110.33} \tag{4.1-4}$$

Fig. 4.1-3 shows the structured grid generated with ICEM v12.1 using hexahedral mesh cells, with a J-Grid topology for the stator domain and H-Grid topology for the rotor domain. The domains were discretised with 70 elements in the circumferential direction and 51 mesh cells radially. The y^+ value for near-wall cells in the wheel-space was set $\preceq$ 1 to satisfy the requirements of the low Reynolds number formulation. In the gas path this was around 10 with a volumetric change between adjacent cells of less than 2.5. The single sector model, referred to as the 1:1 model, contains 2.2 million mesh cells and the 4:5 multi sector model (with the same mesh density) about 7.6 million grid points.

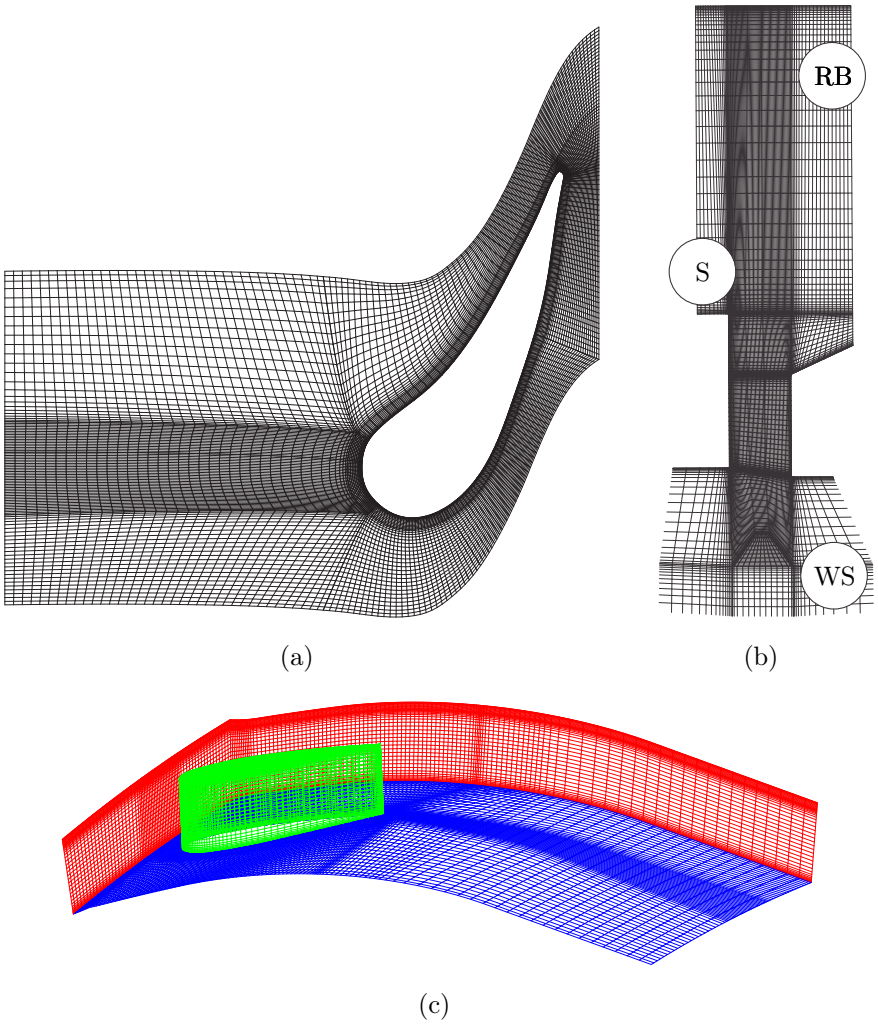

Fig. 4.1-3: Single sector 1:1 CFD model; (a) Stationary domain with stator vane, (b) Seal gap region (stator side left, rotor side right), (c) Rotating domain with rotor blade

Sangan (2011) investigated the fluid mechanics in the wheel-space and the primary gas path with their ingress rig. This information has been used to validate this computational model for an axial- and radial clearance rim-seal. The geometric dimensions of these seals are summarised in Fig. 4.1-4.

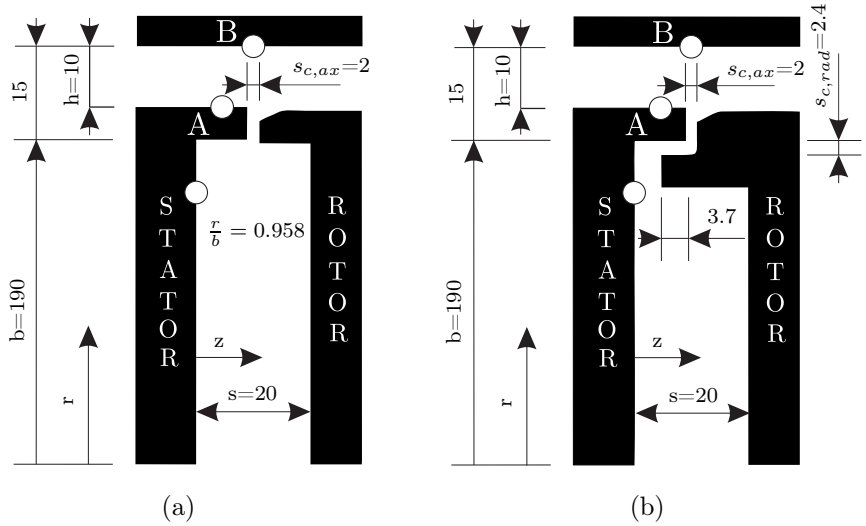

Fig. 4.1-4: Generic dimensions (mm) and measurement locations for; (a) axial-clearance seal; (b) radial-clearance seal

The URANS computations were started from a frozen-rotor solution and the inner loop iteration was set to a convergence target of 5×10^{-3} for maximum residual level for the mass, momentum and energy equations and the additional mass transport equation. Owing to the different length and time scale in the gas path and wheel-space, the flow reached periodic behaviour within 1/2 revolution of the rotor disc in the annulus but required around 8 revolutions before the computed tracer concentration was fully convected and statistical convergence was obtained.

A time-step sensitivity study determined a time-step of 1.78×10^{-5} was required, with a second order backward Euler transient scheme. This time-step corresponding to 30 time intervals per blade passing period was used for the validation work.

4.2 Validation

Sangan et al. (2011a) measured the circumferential variation of the static pressure with a Scanivalve system across one vane at two locations (Fig. 4.1-4), location A 2.5mm behind the TE of the vane on the hub platform and location B which is located mid-way of the rim-seal on the outer casing. They distributed 15 pressure taps evenly across one vane pitch (Fig. 4.2-5) at four circumferential positions shifted by 90° and used an average as the representative distribution, for both location A and B.

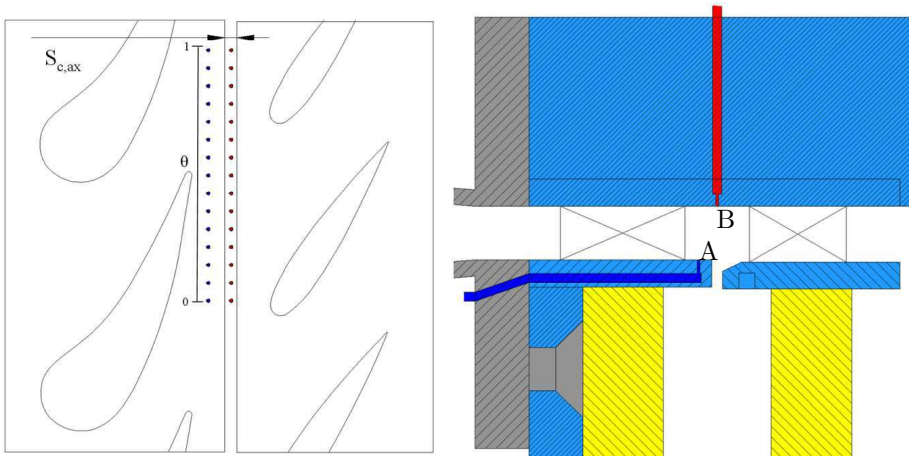

FIG. 4.2-5: Instrumentation pressure taps in the gas path (source from Sangan (2011))

The computed static pressure at three monitoring points shows repeatedly cyclic behaviour, i.e. 5 blade passing periods (bpp) for the gas path, within 1/2 a revolution, see Fig. 4.2-6.

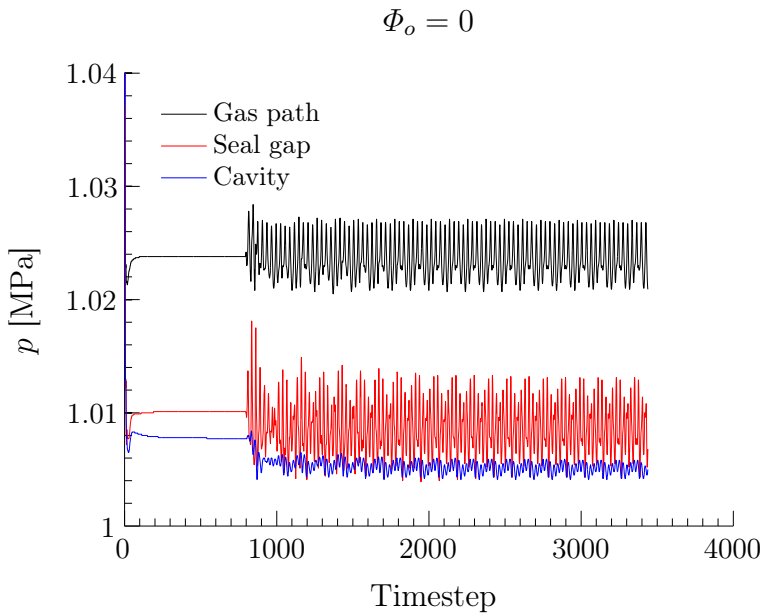

FIG. 4.2-6: Convergence behaviour of static pressure at three monitoring points

This pressure was time-averaged across 4 cycles or 20 bpp and compared to the experimental data for the variation of the pressure coefficient C_p with non-dimensional vane pitch θ_{stator} as shown in Fig. 4.2-7. The pressure coefficient was defined as follows:

$$C_p = \frac{p_2 - \bar{p_2}}{\frac{1}{2}\varrho\Omega^2 b^2} \tag{4.2-5}$$

where p_2 is the variation of the static pressure with θ and $\bar{p_2}$ the average value of p_2 across one vane pitch.

There is reasonable agreement between the measured and computed pressure distribution at location A for the single sector model within an over- and underprediction of the measured peak and trough pressure respectively. A better match was obtained at location B with the exception of an under-estimated peak value for C_p. The pressure profiles produced by the 1:1 and 4:5 sector models at location A are almost identical, suggesting that the EI driving force is dominated by the potential flow field of the vane for the unloaded symmetric rotor blade case investigated.

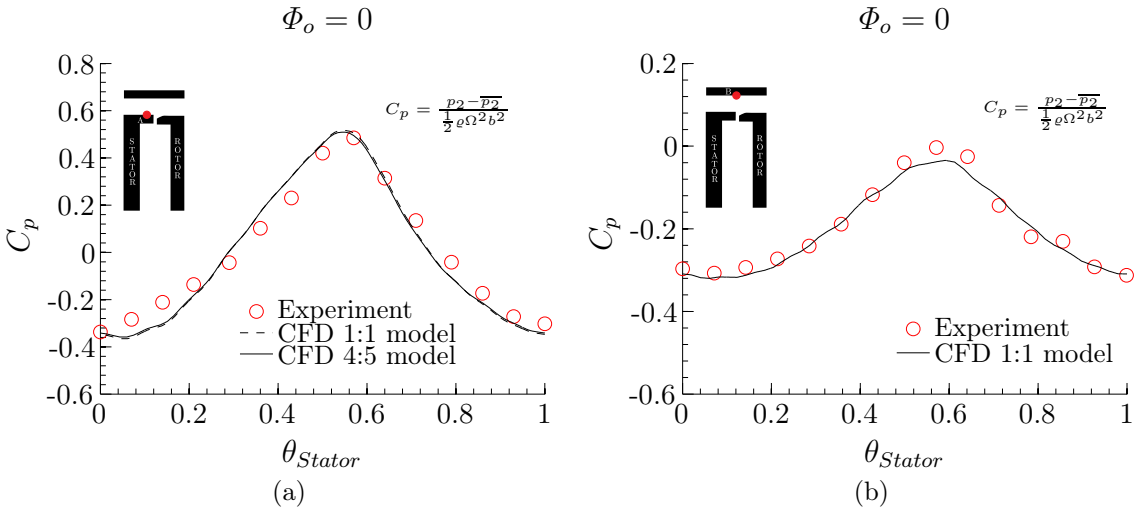

FIG. 4.2-7: Comparison between measured and computed circumferential distribution of static pressure in the gas path at $C_F = 0.538$ (experimental data from Sangan et al. (2011a)); (a) location A, $Re_\phi = 9.68x10^5$; (b) location B, $Re_\phi = 8.17x10^5$

Sangan (2011) equipped the ingress rig with 7 pitot tubes in the wheel-space to measure the variation of the core swirl (tangential velocity) with r/b at $z/s = 0.25$. Fig. 4.2-8 compares the measured swirl ratio with the computed time-averaged results of the unsteady simulations for the axial-clearance seal at two sealing flow rates, $\Phi_o = 0$ and $\Phi_o = 0.113$. The unsteady CFD captures reasonably well the high angular momentum that the ingress carries into the wheel-space. The good agreement between the measured and computed values of β within the wheel-space suggests that the ingress levels and the mixing process can be predicted by the transient computations.

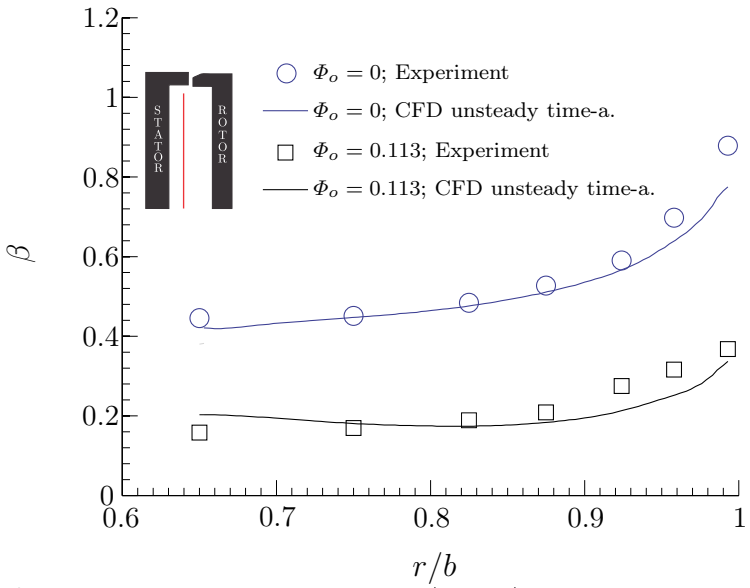

FIG. 4.2-8: Variation of swirl ratio β with r/b at $z/s = 0.25$ for the axial-clearance seal at $Re_\phi = 8.17 \times 10^5$ (experimental data from Sangan (2011))

Fig. 4.2-9 shows the variation of the measured sealing effectiveness with r/b for $\Phi_o = 0.1$ at $Re_\phi = 9.68 \times 10^5$. This is compared to the sealing effectiveness computed with the SST $k-\omega$ turbulence model and the 1:1 model. At higher radii, i.e. $r/b \succeq 0.9$, there is a good match with the experimental data, however in the inner part of the wheel-space, the CFD over-predicts the sealing effectiveness. This situation could neither be improved by the larger sector model nor by the use of a Reynolds Stress (BSL) turbulence model. The Reynolds Stress turbulence model is theoretically more appropriate for this type of rotating flow but returned similar results to the SST $k-\omega$ model, while increasing the computational time by the factor of 2.5. A similar overprediction of the sealing effectiveness at lower radii was found by Jakoby et al. (2004) and Rabs et al. (2012).

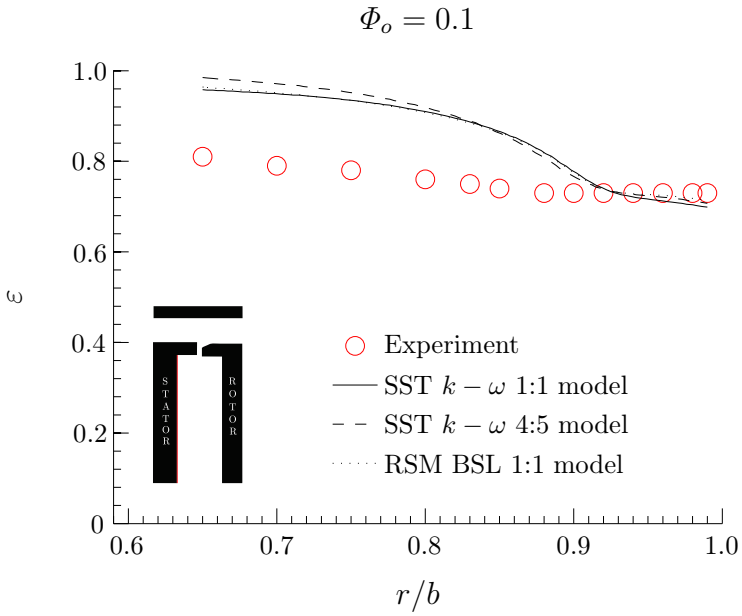

FIG. 4.2-9: Variation of ε with r/b for the axial-clearance seal for $\Phi_o = 0.10$; Comparison between the experimental data and the 1:1 model with the SST $k-\omega$ and *BSL RSM* model and the 4:5 sector model (experimental data from Sangan (2011))

Fig. 4.2-10 summarises the variation of sealing effectiveness measurements for the axial- and radial clearance seals with the variatio of Φ_o for the sampling point at $r/b = 0.958$ (see inset figure). The comparison with computations shows good agreement over the sealing flow range for the axial seal. For this seal, the computations were limited to the sealing flow range $0.1 \preceq \Phi_o \preceq 0.2$ for which $0.70 \preceq \varepsilon_{cc} \preceq 0.92$. This restriction is discussed below. For the radial-clearance seal, the CFD model underestimates the sealing effectiveness, however the range of sealing effectiveness is extended up to the fully-sealed condition. The computed and measured results were both fitted to the effectiveness equation for *EI* ingress (see Eq. 2.2-41) using the statistical method described by Zhou et al. (2011). The reader is referred to Chapter 2 „Literature Review - Hot Gas Ingestion“ for a detailed description on the fitting procedure.

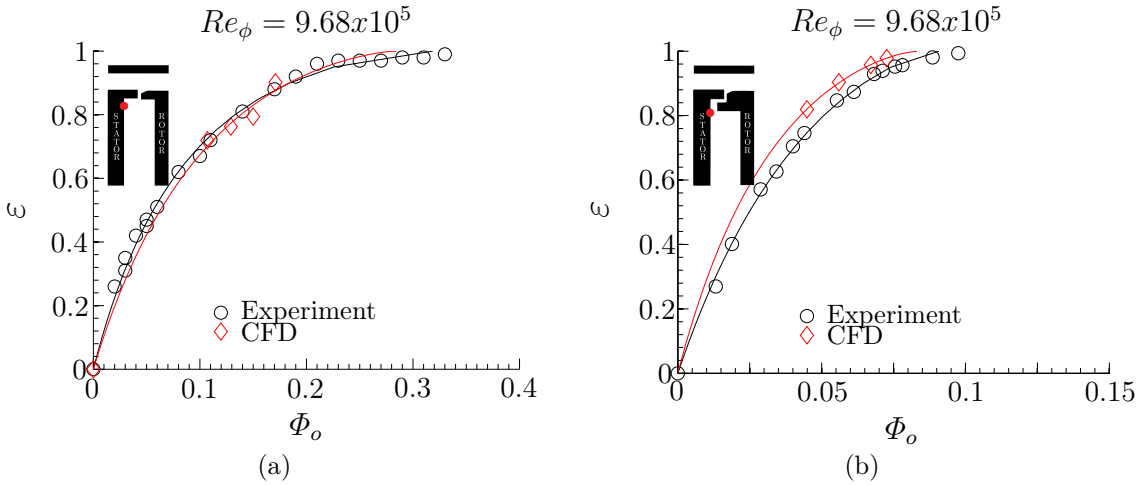

FIG. 4.2-10: Comparison between the measured and computed variation of ε with Φ_o with sampling at $r/b = 0.958$ (experimemental data from Sangan et al. (2011a)); (a) axial-clearance seal; (b) radial-clearance seal

Limitation of CFD model

The computations for the axial-clearance seal were restricted to the sealing flow range: $0.10 \preceq \Phi_o \preceq 0.20$. Below $\Phi_o \prec 0.1$, the CFD model experienced convergence difficulties which believed to be induced by the occurrence of large-scale rotating structures in the wheel-space that could not be captured correctly because of the cyclic symmetry restriction for the 1:1 single sector approximation. The 4:5 sector model or an even larger model might be able to extend the sealing flow range to lower limits but this becomes computationally too expensive and is beyond the scope of the thesis. With increasing Φ_o, the large-scale structures reduce in magnitude and are suppressed at sufficiently high sealing flow rates; similar observations were made by Julien et al. (2010) and Dunn et al. (2010). Computations conducted above $\Phi_o = 0.2$, were affected by significant variation of ingress levels over a succession of blade passing periods, for which no converged solution could be obtained. This behaviour was eliminated for $\Phi_o = 0.4$, for the fully-sealed case where the solution converged fully.

Remarks on the Steady-State Frozen Rotor Approach

Even though the focus of this thesis is the URANS computation of ingestion, a steady-state solution is still required as an initial condition to start the transient computation. Contrary to the transient computation, the frozen rotor steady-state approach was unable to predict any ingress, independently of the seal configurations and the flow conditions. To shed more light on this discrepancy, the frozen rotor approach is investigated in more detail below.

Fig. 4.2-11 shows two modelling approaches to the ingress problem with the difference being the definition of the frame of reference of the wheel-space. In set-up 1, the wheel-space domain is solved in a stationary frame of reference where the angular momentum is transferred into the domain by the rotating wall by means of viscous forces. To enable this mechanism correctly, the boundary layer should be refined according to the turbulence model requirements, i.e. in this case $y^+ \approx 1$. In set-up 2, the angular momentum is applied explicitly to the domain where the driving force has an immediate influence on the domain which results in a faster development of the pressure and velocity profiles within the domain.

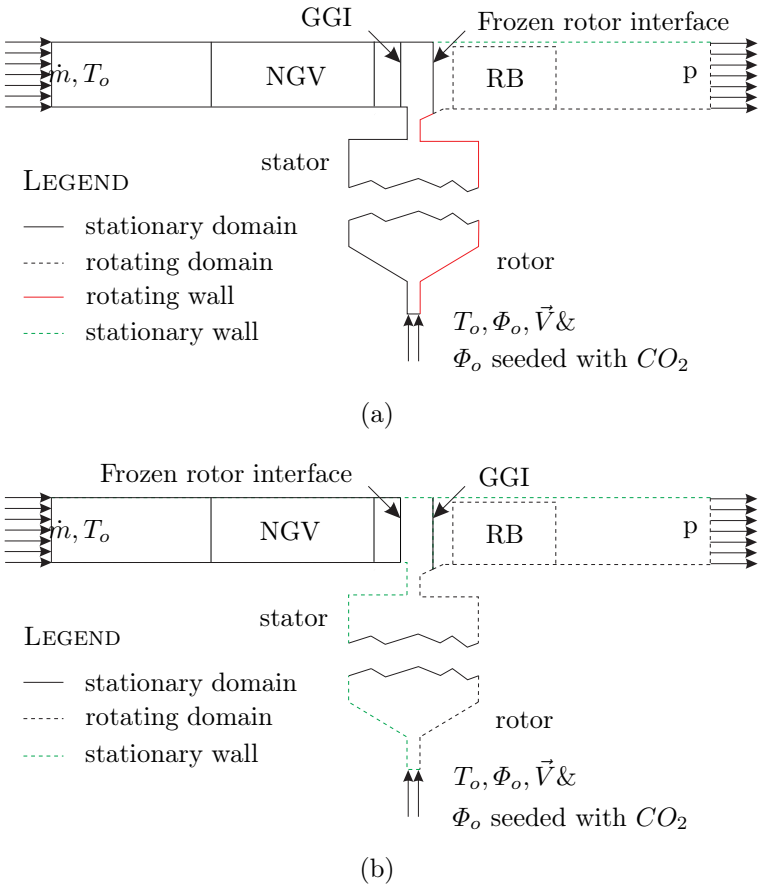

FIG. 4.2-11: Frozen rotor approach with boundary conditions for; (a) set-up 1, (b) set-up 2

Both models were solved with a physical time scale of $0.1/\Omega$, with the exception of the transport equation of the tracer gas which was set to $1/\Omega$. This procedure balances out the difference in time scale between the gas path and the wheel-space and helps to accelerate the convection of the tracer gas within wheel-space domain which reduces the computational times.

In contrast to the steady-state approach with a mixing plane, at which properties are circumferentially averaged across the interface, the rotor blade position relative

to the NGV influences the potential flow field and hence the ingress. To obtain representative results with the frozen rotor approach, four blade clocking positions across θ_{stator} were investigated and the results were averaged.

Discussion on the Sealing Effectiveness

Fig. 4.2-12 shows the measured sealing effectiveness curve for the axial-clearance seal compared to computations for two sealing flow rates. Model 1 shows no ingress, and the results were independent of the relative position of the rotor blade to the vane. Model 2, however, agrees well with the rig data and the ingress levels were sensitive to the relative location of the rotor blade to the vane.

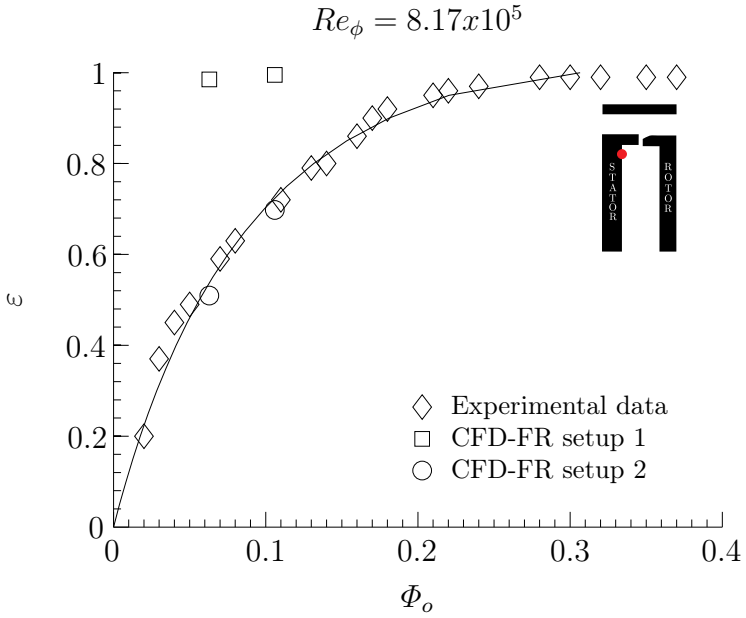

FIG. 4.2-12: Variation of ε with Φ_o for the axial-clearance seal; Comparison between the measurements and computations for two frozen rotor approaches

Discussion on Swirl Ratio

Fig. 4.2-13 shows the variation of the swirl ratio β with r/b. The computed swirl ratio for CFD model set-up 2 shows reasonable agreement with the experimental data at higher radii, but with underprediction of the swirl in the inner part of the wheel-space. Model set-up 1 under-predicts the tangential velocity over the entire range, and in particular at high radii. This can be explained by the absence of high angular momentum ingress flow entering the wheel-space. The underestimation of the swirl ratio in the inner part of the wheel-space for both models is attributed to the swirl applied as a boundary condition to the sealing flow was not fully representative.

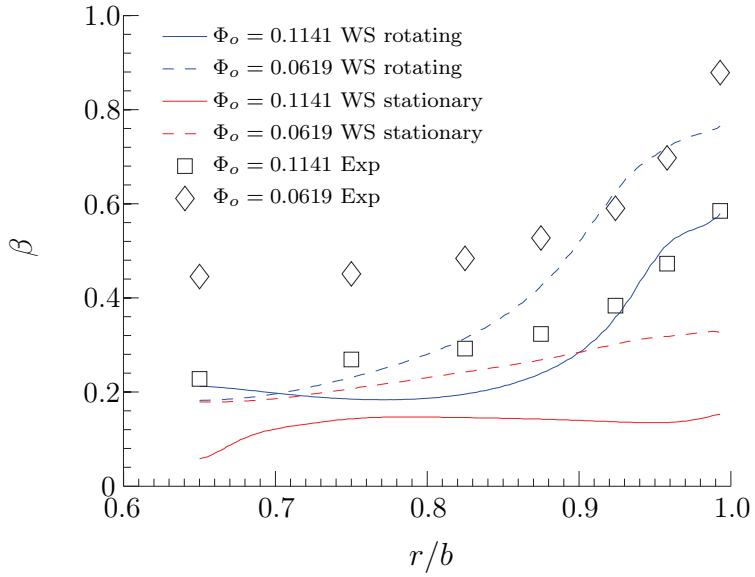

FIG. 4.2-13: Influence of the frame of reference of the wheel-space on ingestion

This study illustrates a fundamental discrepancy between the two theoretically equivalent steady-state modelling approaches. The difference was traced to the frame of reference used for the wheel-space domain and not to the re-located frozen rotor interface in the gas path. It is speculated that one of the rotating forces, i.e. the Coriolis force, is not completely accounted for in the stationary frame of the wheel-space in steady-state computations. Over the course of the 3-year programme the author worked with the support team of CFX to find a satisfactory explanation as yet without conclusion.

Lalwani (2014) expanded on this work with the model-setup 2 approach and found reasonable agreement for simple and complex rim-seal configurations. The interested reader is referred to Lalwani's thesis for more information on this steady-state approach.

4.3 Practical Implications

The transient computations with the 1:1 model have shown reasonable agreement with experimental data even though over a restricted range for Φ_o that could not be extended to low values. This restricted range lies in the region of interest of this thesis and this avoids the need for use of the larger sector model, which would be too expensive computationally and beyond the resources available.

The frozen rotor approach showed good agreement with the experimental data, but it has not been considered for the work in the following chapters and in particular for Chapter 8 „Egress-Mainstream Interaction". However, this might be a

useful CFD approach for the engine designer, who normally cannot afford the time-consuming transient calculations.

Chapter 5

Extrapolation Method

This chapter describes an extrapolation method to translate the sealing parameter Φ_{min} obtained in a 1-stage test facility at the University of Bath to engine relevant conditions. Sangan et al. (2011a) conducted their ingestion concentration measurements at low speed, i.e. quasi-incompressible gas path condition, with a low speed blading geometry and they could prove that the sealing effectiveness is invariant with Mach number or Re_ϕ when the sealing flow is expressed in form of Φ_o instead of $C_{w,o}$ while maintaining the velocity triangle. This work establishes an extrapolation method to scale Φ_{min} from low to high speed conditions by incorporating compressibility effects before it can be used in an industrial context as described in Chapter 3 "Secondary Air Systems". However, this method is a preliminary approach to exploit the already existing ingestion test data for engine relevant conditions. Future experimental work accounts for compressibility effects by translating the high speed blading to a low speed counterpart before being tested in a low speed rig by maintaining the blade loading, hence Φ_{min} becomes invariant with Mach number. This approach will later supersede the extrapolation method introduced in this Chapter. This chapter is an account of this method as published by Teuber et al. (2013).

5.1 Incompressible Condition

Sangan et al. (2011a) investigated the fluid mechanics for various rim-seals in an experimental rig with an isentropic vane exit Mach number $M \prec 0.44$. The test facility is described in detail in chapter 2 "Literature Review - Hot Gas Ingestion". They used 15 static pressure taps with a Scanivalve system to measure the peak-to-trough tangential pressure variation, across one vane pitch, at four circumferential different locations 2.5mm downstream of the trailing edge of the vane. The measurements were made in the absence of any sealing flow, i.e. for $\Phi_o = 0$, and the averaged pres-

sure coefficient C_p is depicted in Fig. 5.1-1 for an axial rim-seal. C_p is plotted across one non-dimensionalised vane pitch for three Mach number conditions. This main driving force for EI ingress is invariant with M when the flow coefficient is kept constant. This result was confirmed by the computation of time-averaged pressure distributions with the CFD model described in chapter 4 "CFD Model Validation".

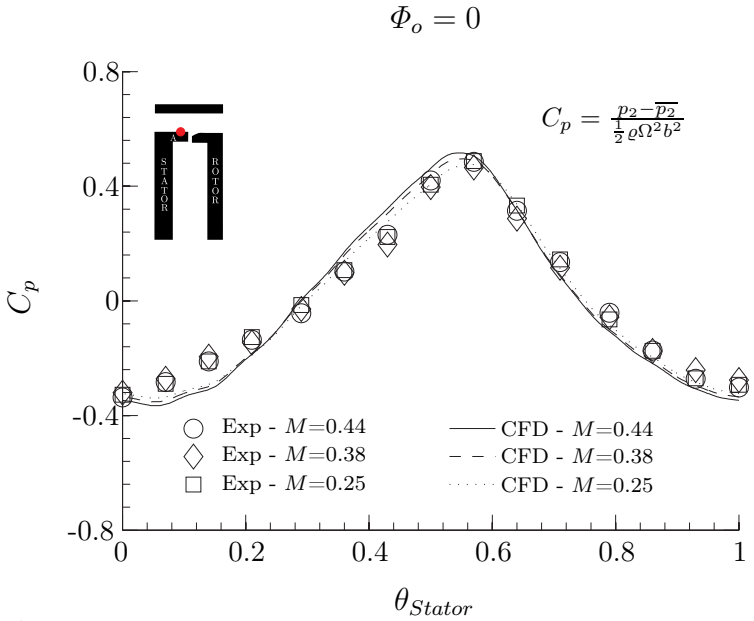

FIG. 5.1-1: Effect of isentropic Mach number M on the variation of C_p across the nozzle pitch ratio θ_{stator} at incompressible conditions (experimental data re-produced from Sangan et al. (2011a))

It should be mentioned that Sangan et al. (2011a) maintained the rig design condition flow coefficient for their investigation, i.e.

$$C_F = \frac{Re_W}{Re_\phi} = \frac{W}{\Omega b} = 0.538 \tag{5.1-1}$$

Fig. 5.1-2(a) shows their results for tracer gas measurements of sealing effectiveness in the wheel-space of the test rig at the sampling point on the stator wall, i.e. $r/b = 0.958$, for an axial-clearance seal for the same Mach number conditions as in Fig. 5.1-1. With increasing M, a higher value of $C_{w,o}$ is required in order to achieve the same ε_c. When re-plotted against the non-dimensional sealing flow parameter Φ_o, Sangan et al. (2011a) found out that the experimental data collapsed onto a single curve, as shown in Fig. 5.1-2(b). A single value of Φ_{min}, invariant with M at incompressible conditions, was obtained with the statistical fitting method of Zhou et al. (2011).

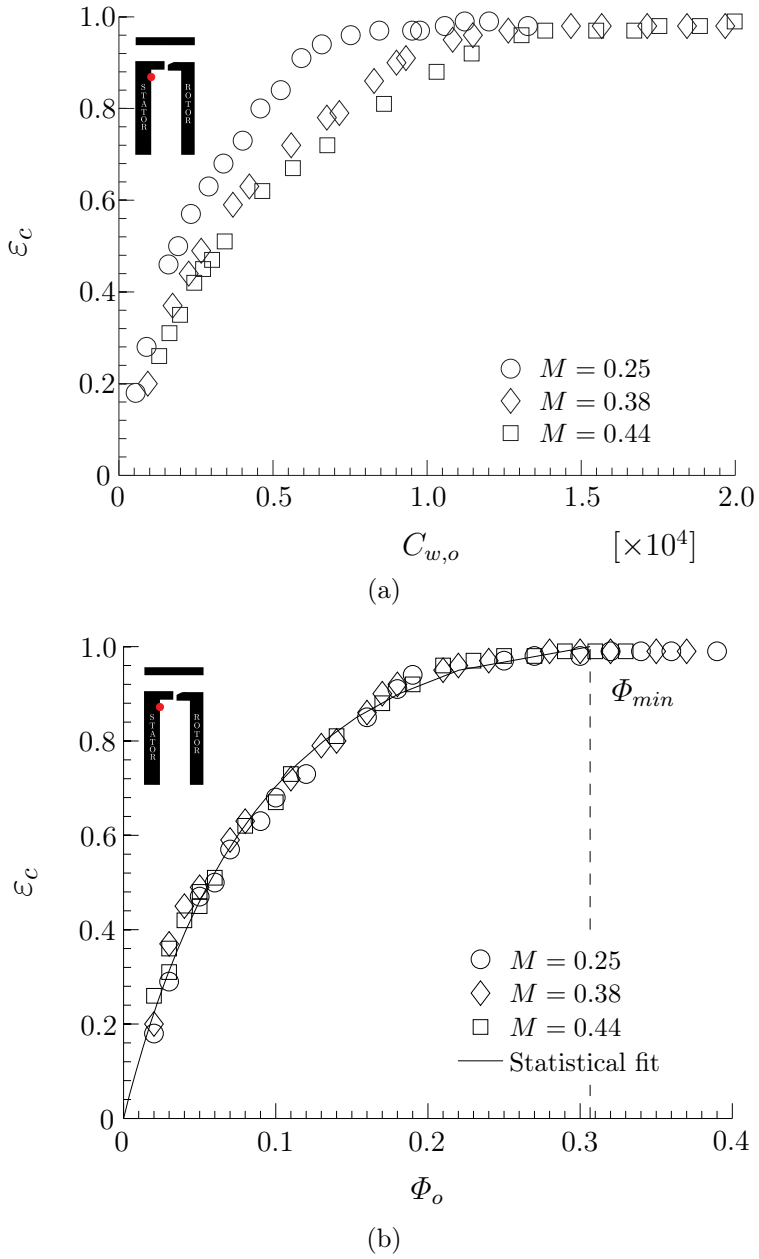

FIG. 5.1-2: Effect of isentropic Mach number M on the measured variation of ε_c with the sealing parameter (re-produced from Sangan et al. (2011a)); (a) $C_{w,o}$; (a) Φ_o

5.2 Compressible Condition

This section discusses the effect of the Mach number on the circumferential pressure distribution in the gas path and its implication on Φ_{min} in the compressible regime. Compressible flow conditions exceeded the capability of the ingestion test facility, hence the work was based upon the validated CFD approach described in chapter 4. The Mach number range $0.44 \prec M \prec 0.86$ was investigated with a rig design condition flow coefficient $C_F = 0.538$.

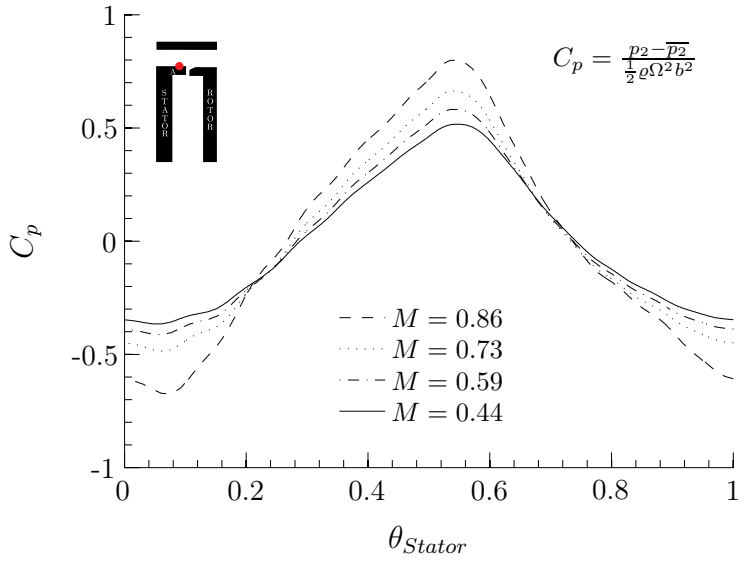

(a)

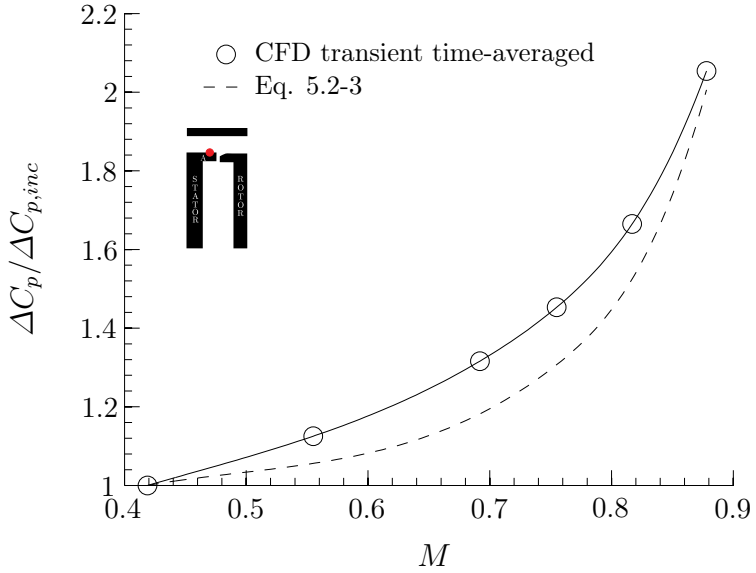

(b)

FIG. 5.2-3: Effect of the isentropic Mach number M on the tangential pressure variation for $C_F = 0.538$; (a) C_p distribution; (b) Variation of ΔC_p with M

The computed C_p distribution in Fig. 5.2-3(a) shows an increase of the peak-to-trough variation with increasing M. This data has been re-plotted in terms of ΔC_p to illustrate the progressive increase of the tangential pressure asymmetry with M owing to compressibility effects, as shown in Fig. 5.2-3(b). The pressure coefficient ΔC_p is defined as follows:

$$\Delta C_p = \frac{p_{2,max} - p_{2,min}}{\frac{1}{2}\varrho\Omega^2 b^2} \tag{5.2-2}$$

This coefficient was normalised by the value of $\Delta C_{p,inc}$ at $M = 0.44$, a case which is quasi-incompressible.

The compressibility correction of Laitone (1951) is plotted in Fig. 5.2-3(b). This correction was introduced to extrapolate the pressure distribution C_p for an aerofoil from incompressible to compressible conditions. This correction has been adapted here (see Eq. 5.2-3) to express the correction in terms of ΔC_p rather than C_p. There is good agreement between the computed ΔC_p distribution and the correction method and both show the progressive increase in peak-to-trough pressure variation with increasing M.

$$\frac{\Delta C_p}{\Delta C_{p,inc}} = \frac{1}{\sqrt{1-M^2} + \frac{\Delta C_{p,inc}}{2}\left(M^2\left[1+\frac{\gamma-1}{2}M^2\right]\right)\sqrt{1-M^2}} \tag{5.2-3}$$

To investigate the impact of the increase of ΔC_p with increasing M on the wheel-space, two sealing effectiveness curves at high subsonic conditions were obtained computationally for the axial-clearance seal, for $M = 0.73$ and $M = 0.86$. Fig. 5.2-4 shows the computed sealing effectiveness curves at these conditions for $r/b = 0.958$. In order to maintain the same ε_{cc}, Φ_o needs to be increased with increasing M, hence $\Phi_{min} \propto M$.

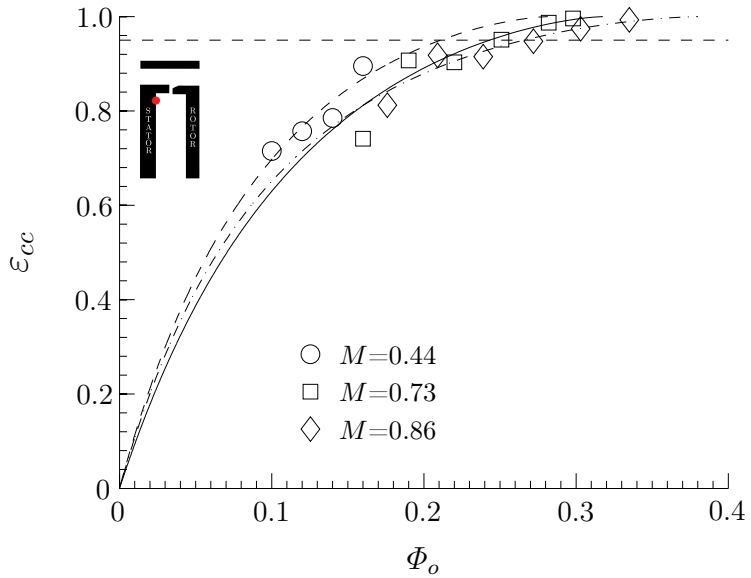

FIG. 5.2-4: Effect of the isentropic Mach number M on the computed variation of ε_{cc} with Φ_o ($C_F = 0.538$ and $r/b = 0.958$)

5.3 Extrapolation Procedure

Owen et al. (2010b) obtained an analytical solution for the EI ingress model using a linear saw-tooth approximation for the circumferential pressure profile. They also

established the proportional relationship between the EI ingress driving force, ΔC_p, and the sealing parameter Φ_{min}, as follows:

$$\Phi_{min} = \frac{2}{3} C_{d,e} \Delta C_p^{1/2} \tag{5.3-4}$$

This relationship can be used to derive an extrapolation method to scale Φ_{min} obtained at incompressible conditions to the compressible regime. This method is based upon the following explicit assumptions:

- Geometries between both conditions is unchanged or similar
- $C_{d,e}$ is constant
- Γ_c is constant
- The "shape factor" (or relationship between the saw-tooth model and the actual pressure distribution in the annulus) is constant

The last assumption must be treated with caution in the case of extreme Off-design conditions where the shape factor is not invariant with flow coefficient. This issue is discussed in detail in chapter 6: “Off-Design Conditions“.

With the aforementioned assumptions, Eq. 5.3-4 can be used to write

$$\frac{\Phi_{min,com}}{\Phi_{min,inc}} = \left(\frac{\Delta C_{p,com}}{\Delta C_{p,inc}} \right)^{1/2} \tag{5.3-5}$$

where $_{inc}$ refers to the incompressible conditions usually found in test facilities and $_{com}$ to compressible conditions. Eq. 5.3-5 enables $\Phi_{min,inc}$ to be extrapolated to compressible conditions through the $\Delta C_p^{1/2}$ ratio.

Tab. 5-1 summarises the values of Φ'_{min}, the value of Φ_o at $\varepsilon_{cc} = 0.95$, for the three Mach number conditions computed in Fig. 5.2-4. Φ'_{min} was preferred to Φ_{min} in order to increase the confidence interval with the fitting procedure of Zhou et al. (2011) owing to the limited number of data points available. $\Phi'_{min,ext}$ is the extrapolated value of $\Phi'_{min,inc}$ obtained by Eq. 5.3-5 using the computed values of ΔC_p tabulated in Tab. 5-1.

Tab. 5-1: Computed and extrapolated values of Φ'_{min} with Eq. 5.3-5

	M	ΔC_p	Φ'_{min}	$\Phi'_{min,ext}$
CFD	0.44	0.88	0.211	0.211
CFD	0.73	1.14	0.245	0.240
CFD	0.86	1.44	0.265	0.270

Fig. 5.3-5 shows the extrapolation curve obtained using Eq. 5.3-5 for the increase of Φ'_{min} due to increasing $\Delta C_p^{1/2}$ as the M increases. The comparison of the computed values with the extrapolation method shows good agreement, which indicates that $C_{d,e}$ is essentially invariant over the Mach number range investigated here. It should be noted, however, that $C_{d,e}$ depends on where it is measured in the gas path and that the range of appropriate locations to use to derive ΔC_p is restricted. The reader is referred to Owen et al. (2010b) who describe locations that give mathematical consistency with the orifice model. For the extrapolation of Φ_{min}, it is important that the location used to determine ΔC_p is the same at both Mach number conditions.

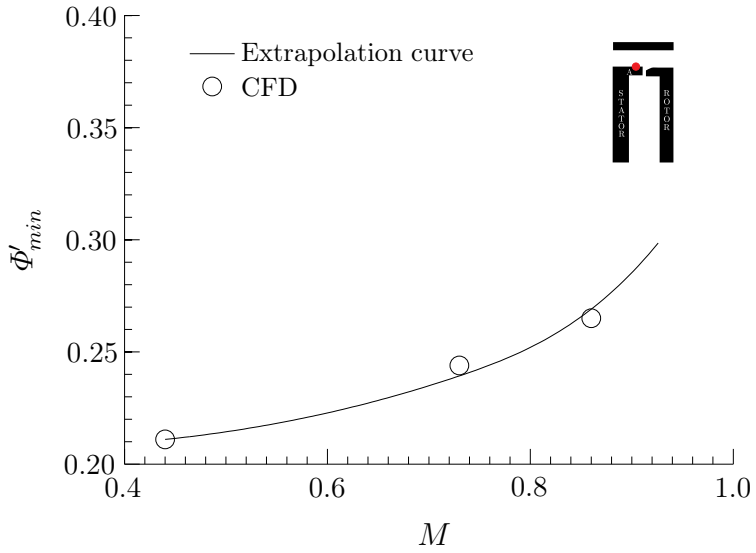

Fig. 5.3-5: Comparison between computed and extrapolated variation of Φ'_{min} with M for the axial-clearance seal

5.4 Practical Implications

This chapter has shown a simple technique to extrapolate Φ_{min} from one Mach number to another. This procedure uses the relationship from a theoretical orifice model derived by Owen et al. (2010b), where Φ_{min}, the non-dimensional sealing flow rate to prevent ingress, is governed by ΔC_p, the non-dimensional peak-to-trough pressure difference in the gas path. This extrapolation method has shown

good agreement with the computed values of Φ_{min} over the range of Mach number investigated.

It is proposed that this method can be used to extrapolate the measured sealing effectiveness obtained from a test facility to a geometrically-similar engine. $\Phi_{min,rig}$ would be provided by a test facility at incompressible conditions with quantitatively relevant engine geometry. Computations in the gas path determine ΔC_p at the rig and the engine relevant conditions and $\Phi_{min,eng}$ can be calculated as follows:

$$\frac{\Phi_{min,eng}}{\Phi_{min,rig}} = \left(\frac{\Delta C_{p,eng}}{\Delta C_{p,rig}} \right)^{1/2} \tag{5.4-6}$$

The advantage of this method is that good estimates of ΔC_p can be obtained by transient or even steady-state computations and that the time-consuming ingress simulations at the compressible flow condition are not required. This gives the engine designer a useful tool to adjust Φ_{min} to the relevant conditions.

It should be mentioned that this method was only tested for subsonic gas path conditions and that the onset of shockwaves in the transonic regime might have significant influence.

A caveat is that this extrapolation method was developed on the basis to scale the seal parameter Φ_{min} from incompressible to compressible conditions, i.e. from low to high speed, with an already existing low speed blading geometry of the test rig. However, if the compressibility effect is properly accounted for by aerodynamic scaling of the high speed blading to a low speed counterpart before being tested in a low speed rig, the blade loading and hence the C_p distribution across the vane and blade pitch would thus be matched. In this case Φ_{min} is invariant with Mach number whereby the experimental determined Φ_{min} parameter at low speed can be used directly at high speed condition, hence the procedure discussed above should not be used.

Chapter 6

Off-Design Conditions

This chapter investigates the aerodynamics off-design conditions in an experimental ingestion facility at the University of Bath and its influence on the ingress in rotor-stator systems. Sangan et al. (2011a) restricted their experimental ingress work to the design condition of their test facility with a flow coefficient of $C_F = 0.538$. Scobie et al. (2013) expanded this work by investigating the flow coefficient in the range: $0 \prec C_F \prec 0.8$. This work was supplemented by CFD computations to gain insight into the fluid mechanics of the potential field.

6.1 Introduction

This section reviews aerodynamic off-design conditions which are typical in the CI ingress regime. The first reported experiments were conducted by Phadke and Owen (1988b) who investigated the effect of Re_ϕ on the variation of the measured $C_{w,min}$, the minimum non-dimensional sealing flow to prevent ingress. Their tests were conducted in the absence of vanes and blades but they created an external pressure asymmetry by blocking sections of the gas path with honeycomb and wire mesh.

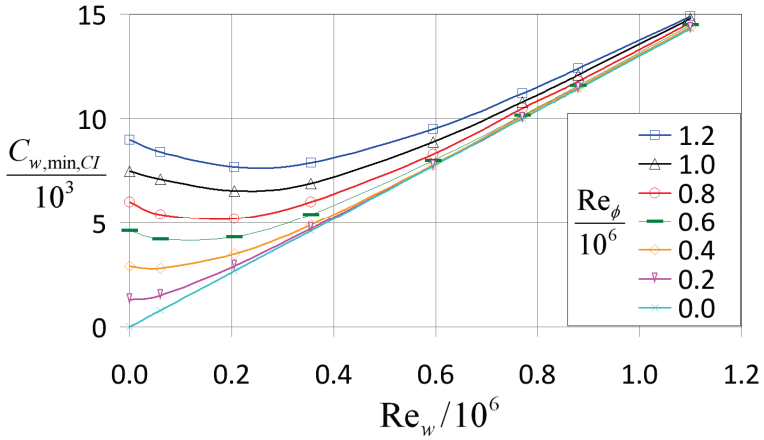

FIG. 6.1-1: Effect of Re_ϕ on the variation of $C_{w,min}$ with Re_W (re-produced from: Phadke and Owen (1988b))

They distinguished between two regions: the EI and the RI regime. At $Re_\phi = 0$, EI ingress occurs and $C_{w,min} \propto Re_W$; RI ingress occurs at $Re_W = 0$ where $C_{w,min} \propto Re_\phi$. With increasing Re_W, $C_{w,min}$ undergoes transition from the RI to the EI regime and approaches the EI asymptote at large values of Re_W. Owen (2009b) refers to this transition zone as combined ingress, CI ingress, where the rotational effects and the external pressure variation cause ingestion at the same order of magnitude.

Owen (2009b) obtained for this ingress regime an analytical solution by solving his orifice equations with the solution discussed in Chapter 2. For convenience Eq. 2.2-47 is re-produced below. This solution features a transition between the RI asymptote at $Re_W = 0$ and the EI asymptote at $Re_\phi = 0$ as shown by the red line in Fig. 6.1-2. The parameter $\Gamma_{\Delta p}$ can be understood as the ratio of driving forces for EI and RI ingress.

$$\frac{\Phi_{min,CI}}{\Phi_{min,RI}} = \frac{C_{w,min,CI}}{C_{w,min,RI}} = \frac{2}{3}\frac{C_{d,e}}{C_{d,e'}}\frac{[1+\Gamma_{\Delta p}]^{3/2}-1}{\Gamma_{\Delta p}} \tag{6.1-1}$$

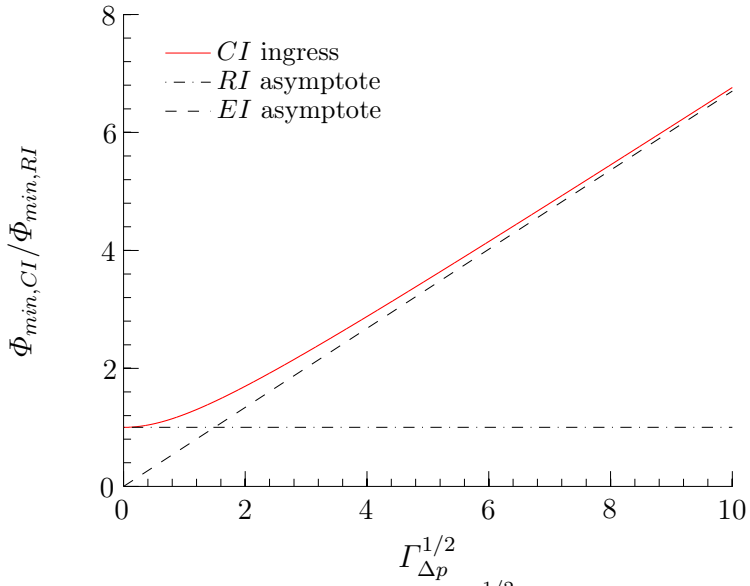

FIG. 6.1-2: Variation of $\Phi_{min,CI}/\Phi_{min,RI}$ with $\Gamma_{\Delta p}^{1/2}$ (re-produced from Owen (2009b))

Eq. 6.1-1 was re-arranged by Scobie et al. (2013) to express the CI model not is form of $\Gamma_{\Delta p}$ but as flow coefficient Re_W/Re_ϕ. The reader is referred to the paper of Scobie et al. (2013) for the derivation of this equation.

$$\frac{\Phi_{min,CI}}{\Phi_{min,RI}} = \frac{C_{w,min,CI}}{C_{w,min,RI}} = \frac{2}{3}\frac{\left[1 + k_c(Re_W/Re_\phi)^2\right]^{3/2} - 1}{k_c(Re_W/Re_\phi)^2} \tag{6.1-2}$$

$$\text{where } Re_W/Re_\phi = W/\Omega b = C_F$$

The CI solution can be re-written when $Re_W/Re_\phi \to \infty$ to obtain the EI asymptote as follows:

$$\frac{\Phi_{min,EI}}{\Phi_{min,RI}} = \frac{2}{3}k_c^{1/2}\frac{Re_W}{Re_\phi} \tag{6.1-3}$$

Owen et al. (2010a) validated the CI model by re-plotting the experimental data of Phadke and Owen (1988b) (see in Fig. 6.1-1) as the variation of $\Phi_{CI,min}/\Phi_{RI,min}$ with Re_W/Re_ϕ. Fig. 6.1-3 shows a close-up view of the transition region with the data of Phadke and Owen (1988b) collapsing onto a single line, which confirms Eq. 2.2-48 and shows that $\Gamma_{\Delta p}$ and hence $\Phi_{CI,min}/\Phi_{RI,min}$ is a unique function of the flow coefficient, as $C_{\beta 1}$ and $C_{p,max}$ are constants. There is reasonable agreement between the CI model and the experimental data, but the model fails to capture the undershoot at low values of Re_W/Re_ϕ.

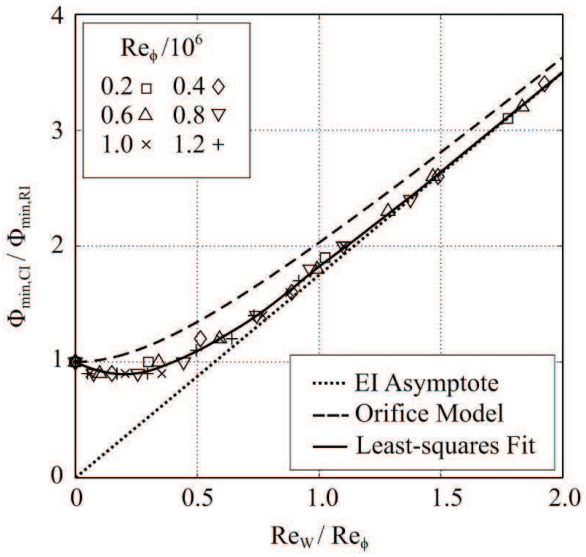

FIG. 6.1-3: Comparison between re-plotted data of Phadke and Owen (1988b) with the CI model as variation of $\Phi_{CI,min}/\Phi_{RI,min}$ with Re_W/Re_ϕ (initial source by Owen et al. (2010a) and re-produced by (Pountney, 2012))

Owen et al. (2010a) concluded that in order to re-produce the undershoot, the model needed to incorporate a variable discharge coefficient in the form of

$$\frac{C_{d,e}}{C_{d,e'}} = exp\left(-A\frac{Re_W}{Re_\phi}\frac{C_{w,min,RI}}{C_{w,min,CI}}\right) \tag{6.1-4}$$

$$\text{where} \quad A = A'/C_{d,e'}C_{\beta 1}^{1/2} \tag{6.1-5}$$

$$\frac{\Phi_{min,CI}}{\Phi_{min,RI}} = \frac{2}{3}\left(-A\frac{Re_W}{Re_\phi}\frac{C_{w,min,RI}}{C_{w,min,CI}}\right)\frac{[1+\Gamma_{\Delta p}]^{3/2}-1}{\Gamma_{\Delta p}} \tag{6.1-6}$$

Fig. 6.1-4 shows the CI model with variable discharge coefficients with the Phadke and Owen (1988b) data as presented in Fig. 6.1-3. The fitted curve with the empirical constant $A = 0$ is identical to the solution given by the CI model with constant discharge coefficient. A better fit to the experimental data could be obtained with $A = 0.89$, but there is still an overprediction of the data in the transition region.

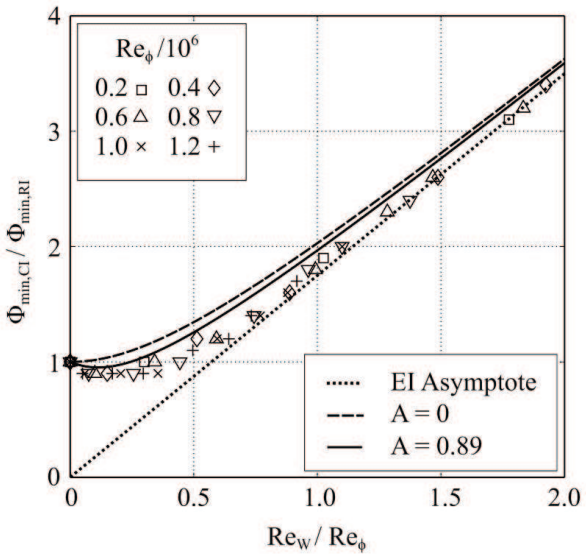

FIG. 6.1-4: Comparison between re-plotted data of Phadke and Owen (1988b) with the CI model with variable discharge coefficients as variation of $\Phi_{CI,min}/\Phi_{RI,min}$ with Re_W/Re_ϕ (Pountney et al., 2012)

Scobie et al. (2013) extended the validation of the CI model to the experimental data of Khilnani and Bhavnani (2001) by re-plotting it to show the variation of $C_{w,min,CI}/C_{w,min,RI}$ with Re_W/Re_ϕ, as shown in Fig. 6.1-5. There is good agreement between the CI model and the experimental data and the comparison shows that the CI model captures the transition zone reasonably well. The difference between this data set and the data of Phadke and Owen (1988b) is the higher slope of the EI asymptote which was contributed by the greater pressure asymmetry of the test facility of Khilnani and Bhavnani (2001).

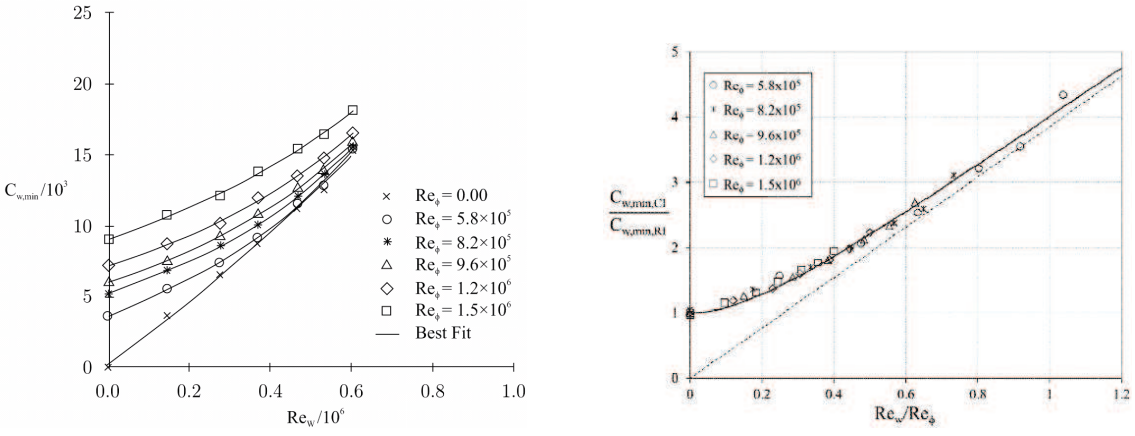

(a) (b)

FIG. 6.1-5: Comparison between re-plotted data of Khilnani and Bhavnani (2001) with the CI model as variation of $\Phi_{CI,min}/\Phi_{RI,min}$ with Re_W/Re_ϕ (source from Scobie et al. (2013))

Scobie et al. (2013) conducted more experimental work with the University of Bath 1-stage ingress rig for various rim-seals. This work has been complemented by

CFD computations across a wide range of flow coefficient. The investigated range is far in excess of the interval experienced in aero engines and gas turbines, where the typical variation is $C_{F,D} \pm 0.25$ around the design point. The objective of the study is to increase the understanding of the off-design conditions on the potential flow field across the entire CI ingress regime and its impact on ingress. Furthermore, the CFD provides insight in an anomaly (discussed below) experienced in the experimental data of Scobie et al. (2013).

6.2 Computational Model

The transient computations for the off-design study were conducted with the CFD code Turbostream v.2.2.4. The program is developed by Turbostream Ltd., a spin-off company from the Whittle Lab at the University of Cambridge. It is based on a series of CFD methods and solvers developed for turbomachinery applications by Denton (1975, 1982, 1990) which have been continuously developed since the 1970's. Brandvik and Pullan (2009) used the same algorithms of Denton's latest structured multi-block CFD code Tblock, however with its source code re-written in Cuda-C language to suit the multi-code architecture structure of GPU cards.

The computations conducted for this section were performed with 2 GPU Tesla 2075 cards ported to a cluster with 896 cores and 12 GB working memory. Speed-up factors of up to 45 were observed to a comparable CFX model solved with 20 parallel solvers.

Fig. 6.2-6 shows the computing environment of Turbostream and the procedure used to obtain the off-design solutions.

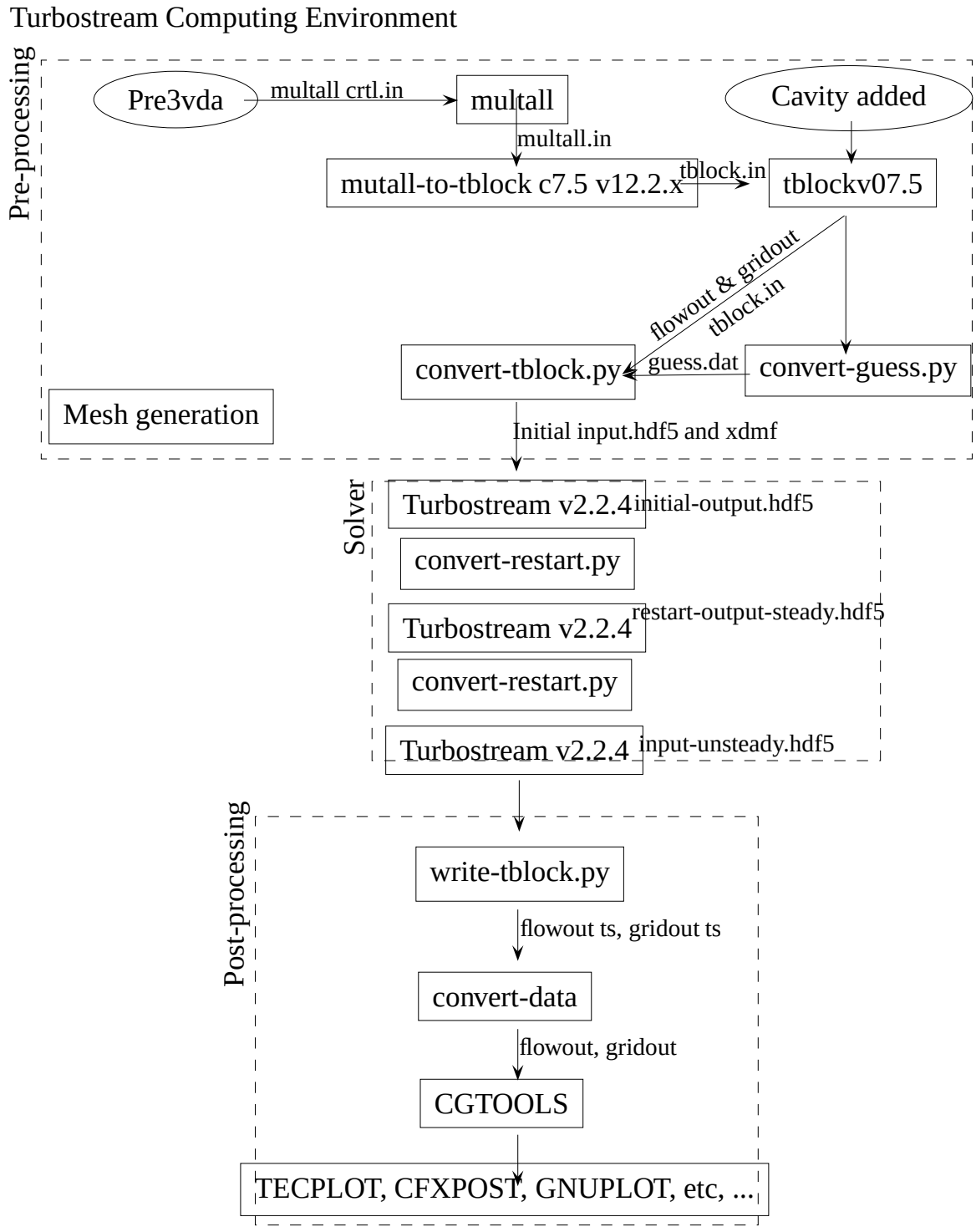

FIG. 6.2-6: Computing environment of Turbostream

In contrast to the CFD model discussed in Chapter 4 "CFD Model Validation", this model was set-up as a 45° sector domain with a pitch ratio of 1, with 4 NGVs and 5 RBs connected by a sliding interface upstream of the seal-clearance. The mesh consisted of 6.75 million hexahedral elements with a H-Grid topology for the vanes and blades. The Spalard-Allmaras turbulence model was used with a mixing plane computation with a CFL number of 0.4. The transient run was started from this steady-state solution with the time step size of 1.071×10^{-5}. With decreasing flow coefficient the time step was decreased to 2.678×10^{-6} to obtain a reasonable convergence behaviour. The flow solution was considered converged when periodic behaviour of the static pressure and the temperature at selected monitor points throughout the domain could be obtained along with a mass flux change of less than 1%.

6.3 Pressure Measurements in the Annulus

This section investigates the influence of the flow coefficient on the potential flow field of the rotor blade. The investigation was done numerically by the aforementioned CFD code and the results were compared to the experimental data collected by Scobie et al. (2013).

Fig. 6.3-7 shows the turbine velocity triangle for the Bath ingestion test facility with its symmetrical NACA0018 rotor blade profile.

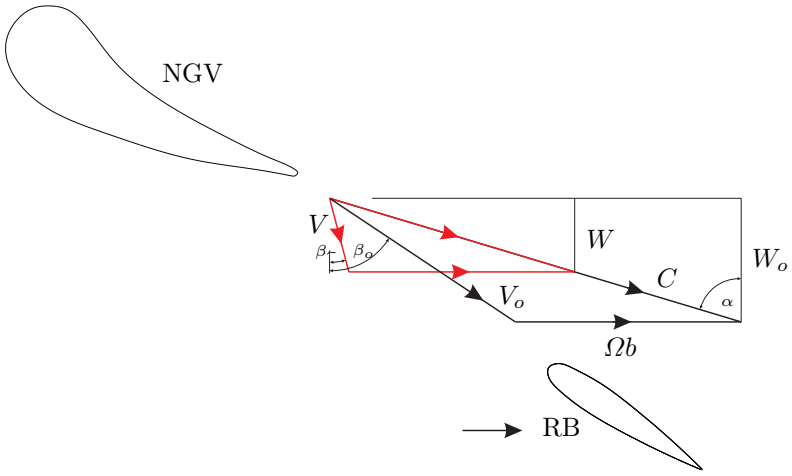

FIG. 6.3-7: Nomenclature for on- and off-design velocity triangle for the test facility with the symmetric NACA0018 rotor blade profile

The angle β_o between the relative velocity vector V_o and the axial velocity component W_o is determined by Eq. 6.3-8 where α is the angle between the absolute velocity and the axial velocity component and the flow coefficient C_F.

$$\tan\beta = \tan\alpha - \left(\frac{W}{\Omega b}\right)^{-1} = \tan\alpha - C_F^{-1} \tag{6.3-7}$$

$$\tan\beta_o = \tan\alpha - \left(\frac{W}{\Omega b}\right)_o^{-1} = \tan\alpha - C_{F,o}^{-1} \tag{6.3-8}$$

The rig "on-design" condition is indicated by the subscript $_o$ and it describes the condition at which the rotor blade loading is symmetric and the power output is zero. This state is given by the following parameter: $\alpha = 73°$, $C_F = 0.538$ and hence $\beta_o = 54.7°$.

The deviation angle, $(\beta - \beta_o)$, describes the theoretical off-design range as variation of the flow coefficient and it varies in the range: $-144.7° \prec (\beta - \beta_o) \prec 18.3°$ as shown in Fig. 6.3-8. At the design point, i.e. $C_F = 0.538$, the deviation angle is 0. At $C_F \succ 0.538$ and $\beta \succ \beta_o$, the sensitivity of the deviation angle decreases with increasing flow coefficient and it converges towards the highest theoretical value of 18.3°. At $C_F \prec 0.538$ and $\beta \prec \beta_o$, the deviation angle decreases significantly with decreasing flow coefficient and it reaches its smallest value at $(\beta - \beta_o)$ of −144.7°.

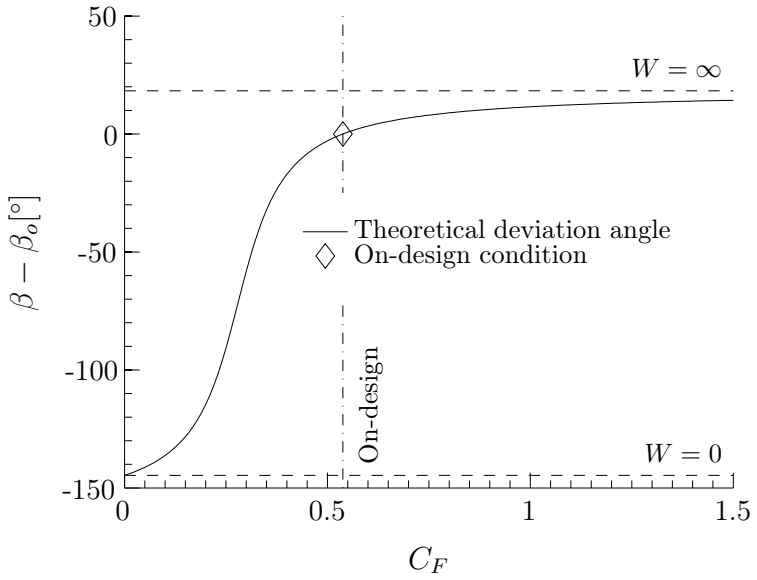

FIG. 6.3-8: Theoretical variation of the deviation angle $(\beta - \beta_o)$ with flow coefficient C_F (adapted from Scobie et al. (2013))

Experimentally, the flow coefficient has been investigated in the following off-design range: $0 \prec C_F \prec 0.8$, for an axial and radial-clearance seal. The dimensions of these rim-seals can be found in Fig. 4.1-4. Computationally, the flow coefficient range was restricted to a higher value of flow coefficient, i.e. $C_F \succ 0.1$, owing to a strong flow separation on the rotor blade whereby no converged solution could be obtained.

Fig. 6.3-9 shows the variation of the external pressure coefficient in the form of $\Delta C_p^{1/2}$ with C_F at location A (which is downstream of the trailing edge of the vane on the hub platform) and at location B (which is midway the seal-clearance on the outer casing). For convenience, the expression ΔC_p has been re-produced here:

$$\Delta C_p = \frac{P_{2,max} - P_{2,min}}{\frac{1}{2}\varrho\Omega^2 b^2} \tag{6.3-9}$$

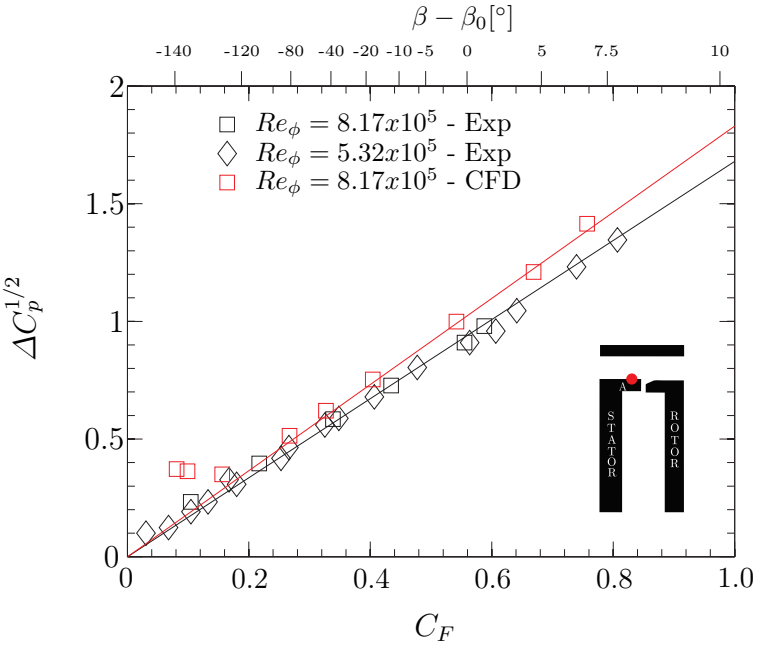

(a)

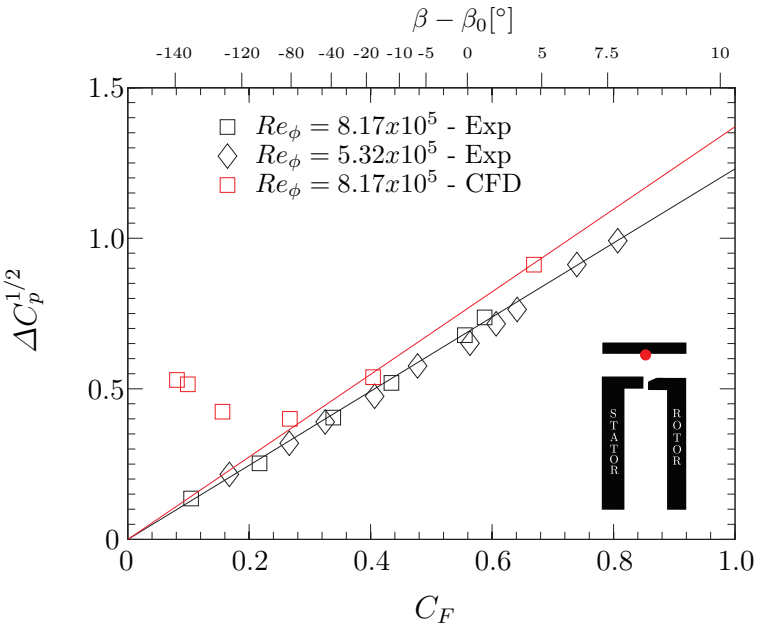

(b)

FIG. 6.3-9: Variation of $\Delta C_p^{1/2}$ with C_F at two locations in the gas path (experimental data from Scobie et al. (2013)); (a) location A; (b) location B

The experimental data shows across the entire range of C_F a linear behaviour. Scobie et al. (2013) correlated their data by

$$\Delta C_p^{1/2} = k_a C_F \tag{6.3-10}$$

where $k_a = 1.66$ for location A

The same linear behaviour with a slightly higher slope ($k_a = 1.94$) was observed for the time-averaged CFD results with a $C_F \succ 0.2$. At $C_F \prec 0.2$, the CFD data shows a departure from the linear trend with an increase in $\Delta C_p^{1/2}$ with decreasing C_F. Both position A and B show this divergence from the linear trend for the computed value of $\Delta C_p^{1/2}$ at low flow coefficients, but with an earlier departure for location B.

To investigate if this increase in $\Delta C_p^{1/2}$ was induced by the rotor blade, the aerofoil was removed from the CFD domain and computations were repeated. The comparison in Fig. 6.3-10 shows that the CFD data without blade collapses onto the data set with rotor blade at both locations without diverging from the linear behaviour at low C_F.

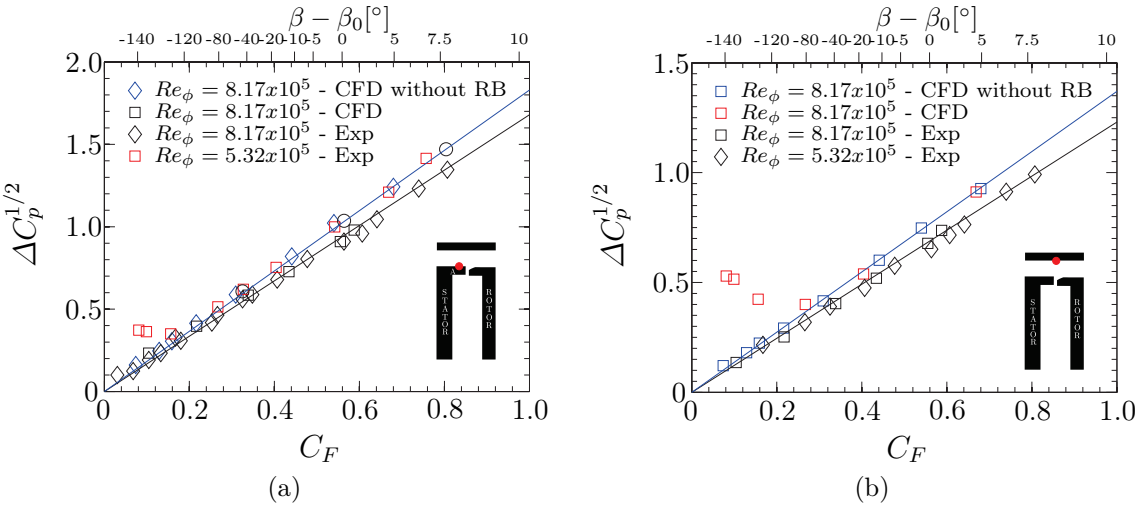

FIG. 6.3-10: Variation of $\Delta C_p^{1/2}$ with C_F with and without rotor blade at two locations in the gas path (experimental data from Scobie et al. (2013)); (a) location A; (b) location B

6.4 Gas Concentration Measurements

Scobie et al. (2013) further investigated the effect of the off-design behaviour on ingress by gas concentration measurements. The rim-seal characteristic was determined for the axial- and radial clearance seal for four flow coefficients. Fig. 6.4-11

shows their data as variation of ε_c with the sealing parameter Φ_o with the sampling point at $r/b = 0.958$. The experimental data were fitted to the sealing effectiveness equation with the fitting procedure described by (Zhou et al., 2011) to extract the parameter Γ_c and Φ_{min}. It proved to be challenging to determine the exact value of Φ_o when $\varepsilon_c = 1.0$ for the axial-clearance seal. Instead of Φ_{min}, Φ'_{min} the value of Φ_o at $\varepsilon = 0.95$ has been used for further consideration to increase the confidence intervals in the statistical fitting method.

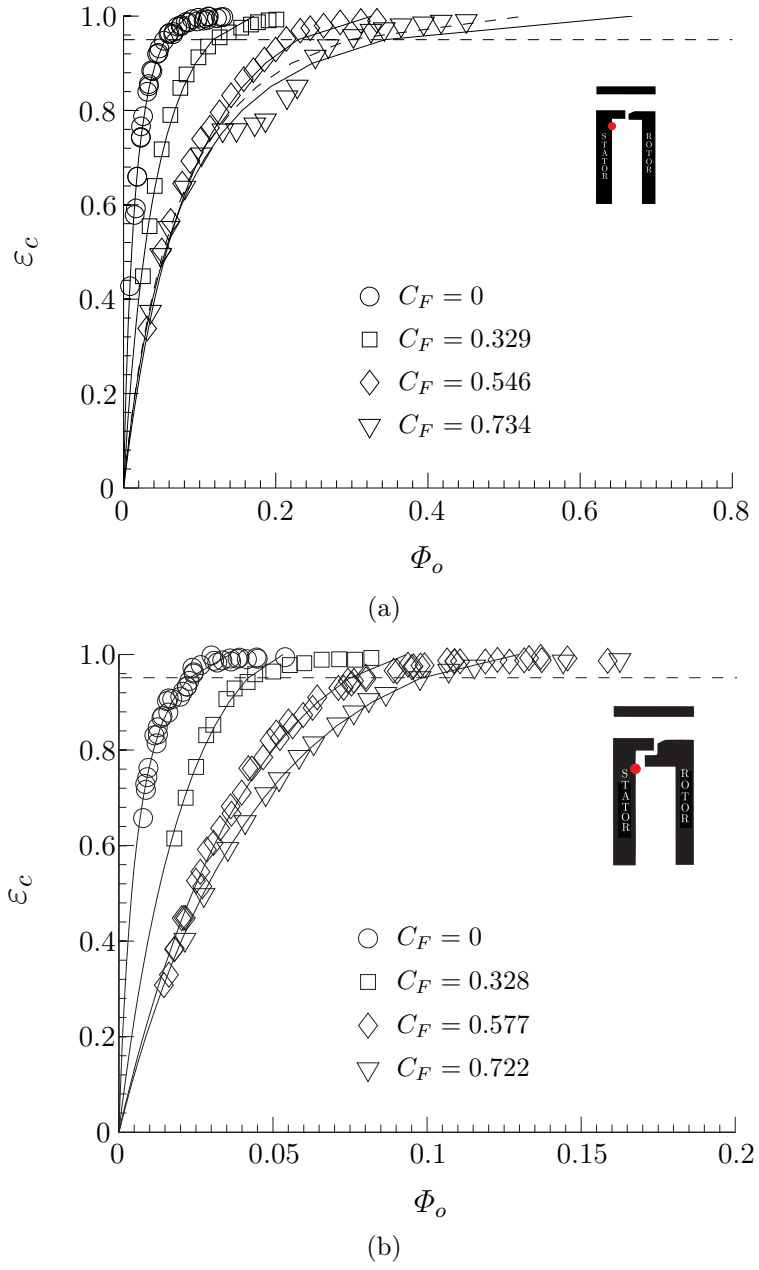

FIG. 6.4-11: Effect of flow coefficient on the variation of the sealing effectiveness with the sealing parameter Φ_o (Scobie et al., 2013); (a); axial-clearance seal; (b) radial-clearance seal

Scobie et al. (2013) collected numerous sealing effectiveness curves across the

entire flow coefficient range for the axial and radial-clearance seal. Fig. 6.4-12 shows the summary of this experiment with the variation of the derived parameter Φ'_{min} with flow coefficient.

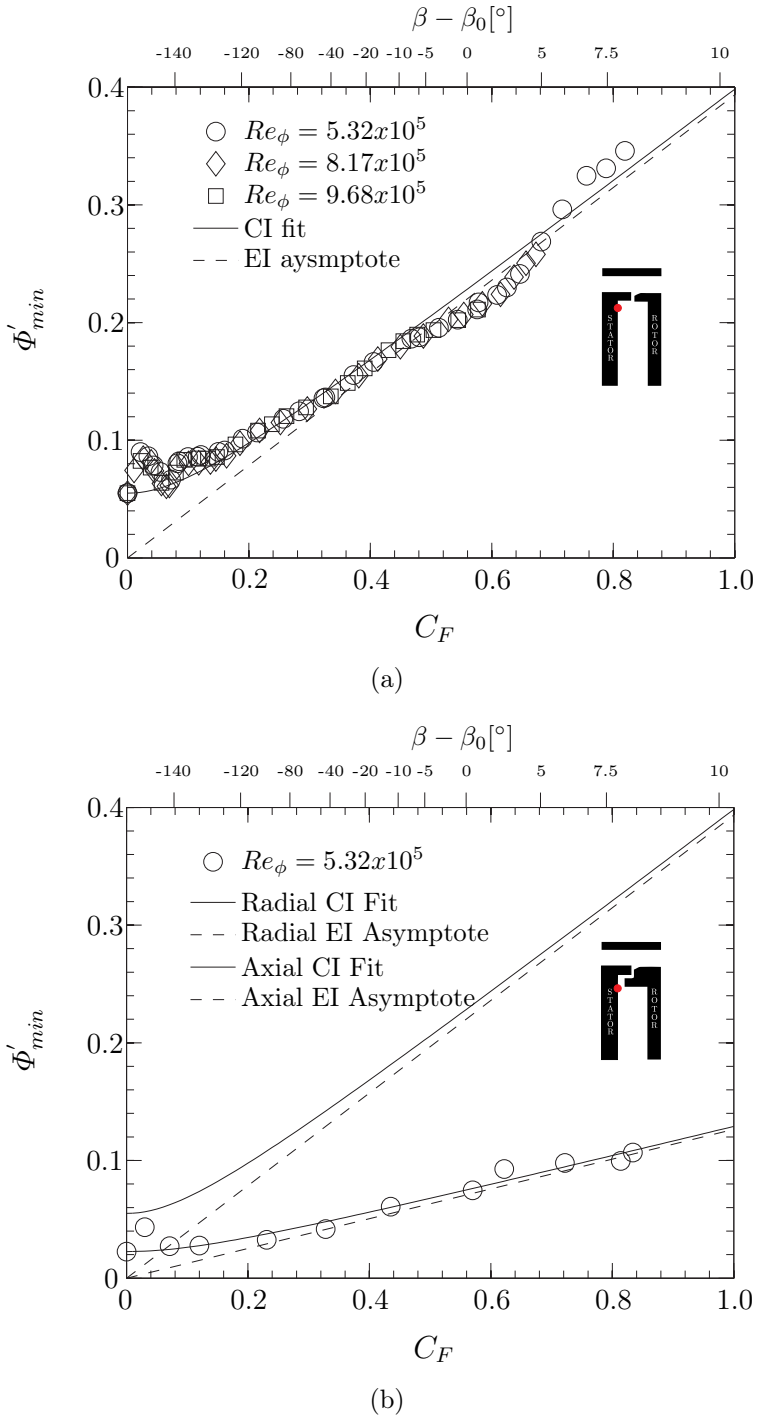

FIG. 6.4-12: Variation of Φ'_{min} with C_F (Scobie et al., 2013); (a) axial-clearance seal; (b) radial-clearance seal

Both data sets were fitted with the CI theory with Eq. 6.4-11 for combined ingress and Eq. 6.4-12 for EI ingress. For convenience, the equations used for fitting is re-produced here (Scobie et al., 2013):

$$\frac{\Phi'_{min,CI}}{\Phi'_{min,RI}} = \frac{2}{3}\frac{[1+k_c C_F^2]^{3/2}-1}{k_c C_F^2} \tag{6.4-11}$$

With increasing flow coefficient the influence of the rotational effects on ingestion reduces and the EI ingress becomes the dominant ingestion mechanism. Eq. 6.4-11 can be simplified as $C_F \longrightarrow \infty$ and $\Phi'_{min,CI} \longrightarrow \Phi'_{min,EI}$.

$$\frac{\Phi'_{min,EI}}{\Phi'_{min,RI}} = \frac{2}{3}k_c^{1/2} C_F \tag{6.4-12}$$

6.5 Discussion

This section discusses the increase of the experimentally determined Φ'_{min} value at large deviation angles and the corresponding increase of the computed ΔC_p.

Scobie et al. (2013) investigated four seals with the gas concentration measurements (only axial and radial-clearance seals are discussed here) and all seals experienced an increase in Φ'_{min} at $C_F \prec 0.1$. It was found that the increase in Φ'_{min} occurred at the same deviation angle and it was independent of the rim-seal geometry. They suggested that this phenomenon has been induced by the rotor blade and they referred to this as "blade effect".

Owen (2009b) correlated Φ_{min} to the ingress driving force ΔC_p by the linear saw-tooth model for EI ingress, which was later experimentally proven by Sangan et al. (2011a). For convenience, the saw-tooth model is re-produced here:

$$\Phi_{min} = \frac{2}{3} C_{d,e} \Delta C_p^{1/2} \tag{6.5-13}$$

The computations in Fig. 6.3-10 depict an increase in ΔC_p at large deviation angles and it could be shown that this increase was induced by the rotor blade. This "blade effect" is investigated in more detail below.

Fig. 6.5-13 depicts the decay of ΔC_p between the trailing edge of the vane (at $x/z = 0$) and the leading edge of the rotor blade (at $x/z = 1$) at midspan, with and without the rotor blade. The location of the seal gap has been visualised by the two vertical lines at $x/z \approx 0.415$ and ≈ 0.595. Without the rotor blade, ΔC_p decreases with decreasing C_F and decays towards the former position of the leading edge of the blade. In the presence of the rotor blade, ΔC_p increases towards the leading edge of the blade after having reached a minimum at $x/z \approx 0.61$. The increase

in ΔC_p near the rotor blade is induced by the stagnated flow field at the leading edge, and referred to as the rotor blade potential effect. Around the on-design condition, the small LE diameter of the rotor aerofoil, along with the symmetrical NACA0018 profile, induces a weak bow effect that propagates upstream with a rapid decay. With decreasing flow coefficient, and in particular at large deviation angle, the blade effect gets stronger and becomes the dominant driving force for ingress.

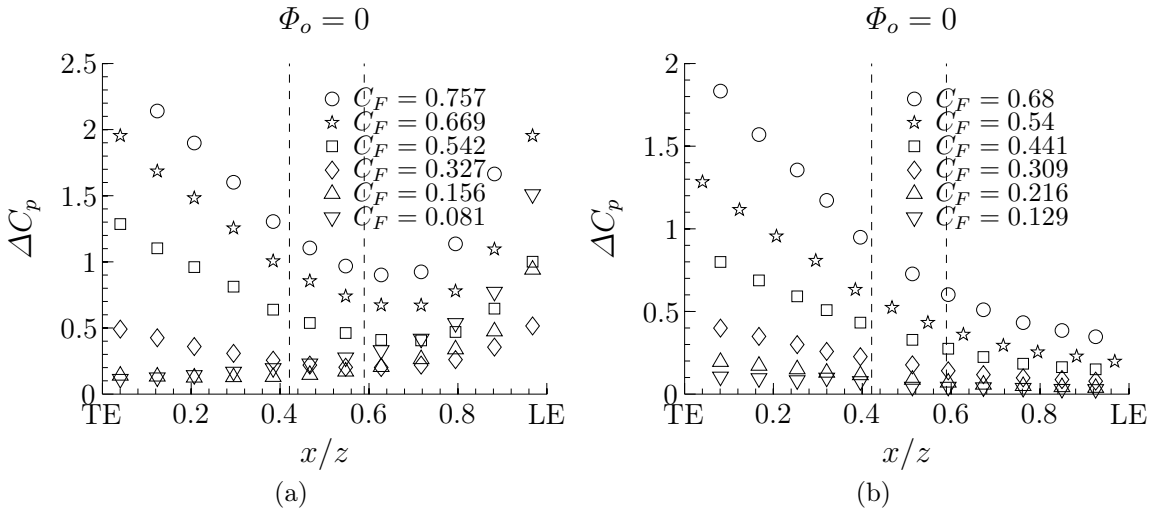

FIG. 6.5-13: ΔC_p decay at midspan for with axial-clearance seal (time-averaged); (a) with rotor blades; (b) without rotor blade

Fig. 6.5-14 shows the direct comparison of the ΔC_p decay between the trailing edge of the vane and the leading edge of the rotor blade with and without rotor blade for three flow coefficients. The influence of the rotor blade for the "on-design" condition is limited across the seal gap and only influences the flow field downstream of $x/z = 0.7$. According to the Φ_{min} relationship (Eq. 6.5-13), it is concluded that the NACA0018 rotor blade has only a negligible effect on ingestion for this condition. At $C_F \approx 0.68$, the same restricted influence on the static pressure field across the seal gap has been observed as for the on-design condition. The increase of the flow coefficient from 0.54 to 0.68 changes only the deviation angle by $\approx 6°$ with no major impact on the leading edge loading of the rotor blade. At large deviation angles, however, the presence of the blade provides the dominant pressure variation with a strong influence even upstream of the seal gap. This influence leads to the non-linear behaviour and to the departure of the linear trend of the $\Delta C_p^{1/2}$-C_F plot in Fig. 6.3-10.

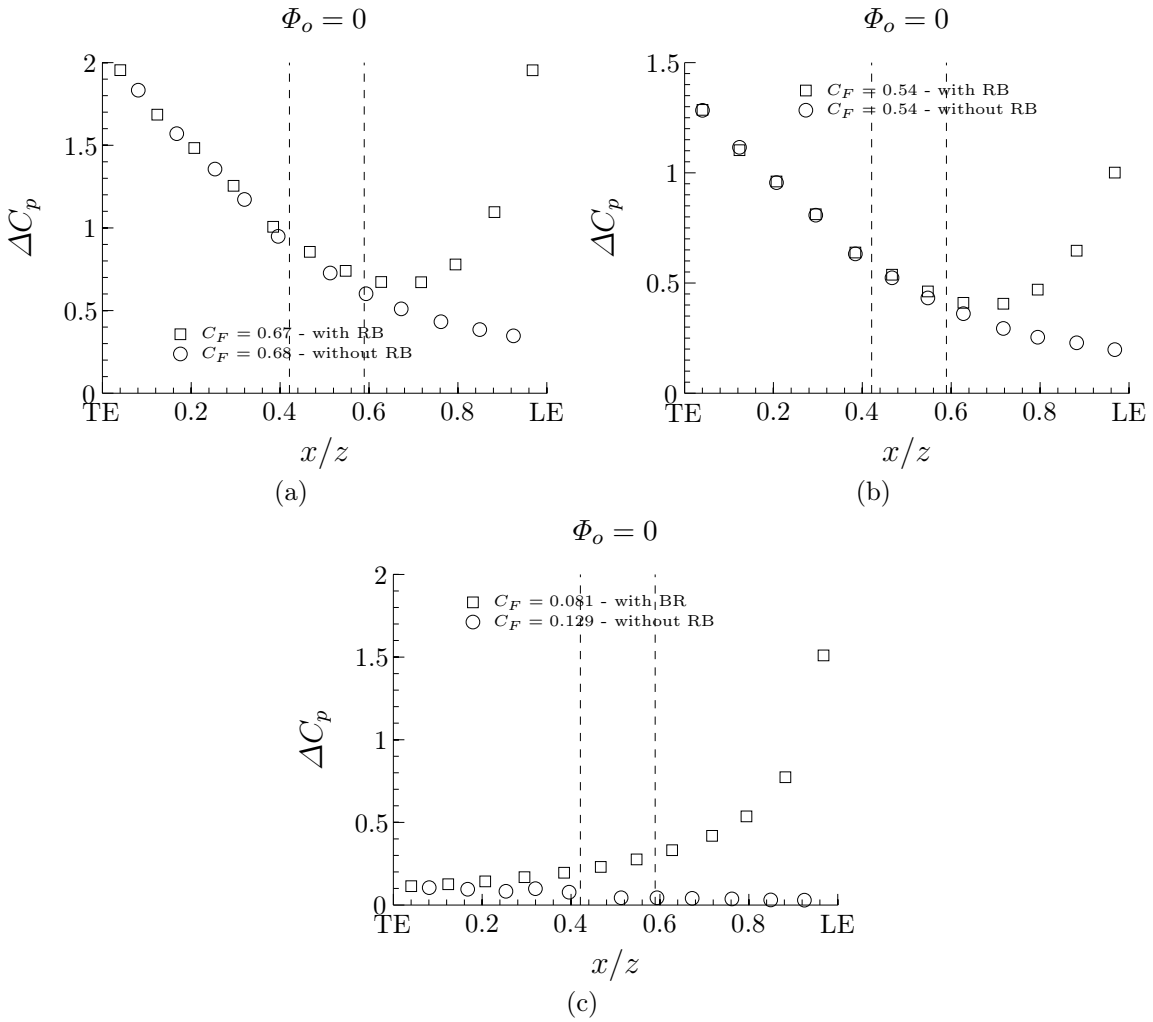

FIG. 6.5-14: ΔC_p decay between the TE of the vane and the LE of the blade at midspan for off-design conditions; (a) $C_F \approx 0.68$; (b) $C_F = 0.54$; (c) $C_F \approx 0.10$

Fig. 6.5-15 shows the time-averaged Mach number and static pressure contour plots for $C_F = 0.54$. The streamlines reveal that the relative velocity vector has almost been aligned with the projected metal angle of the rotor blade. The increase in static pressure in front of the rotor blade was caused by the stagnating flow field at the aerodynamic leading edge. The weak rotor blade potential effect limits the influence on the pressure field across the seal gap. The same behaviour applies to the $C_F = 0.68$ as observed in Fig. 6.5-16.

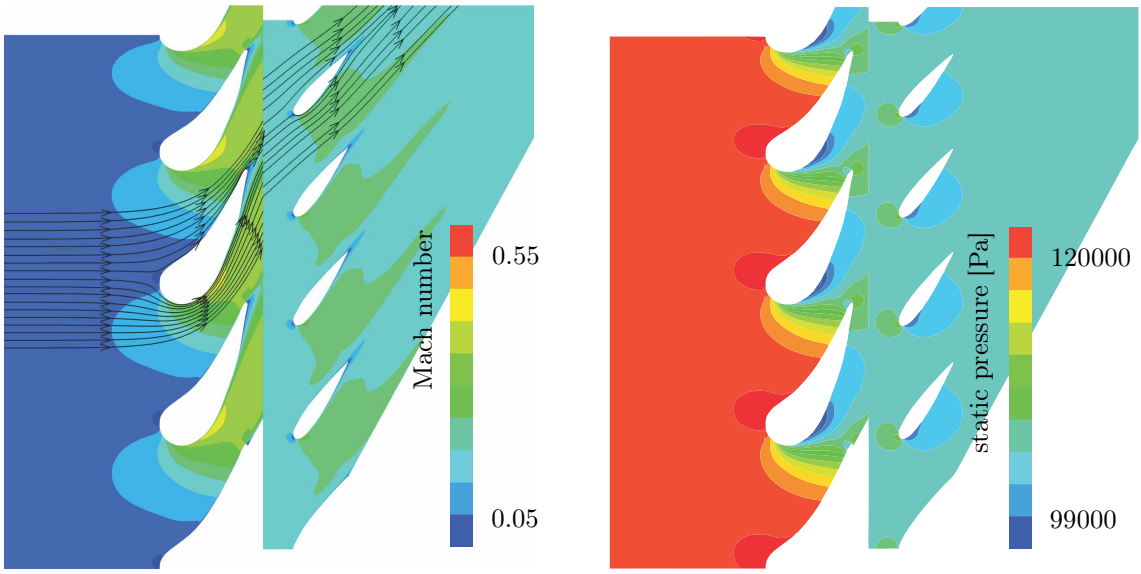

(a) (b)

FIG. 6.5-15: Flow field at $C_F = 0.54$ midspan; (a) Mach number contour plot with velocity streamlines; (b) static pressure contour plot

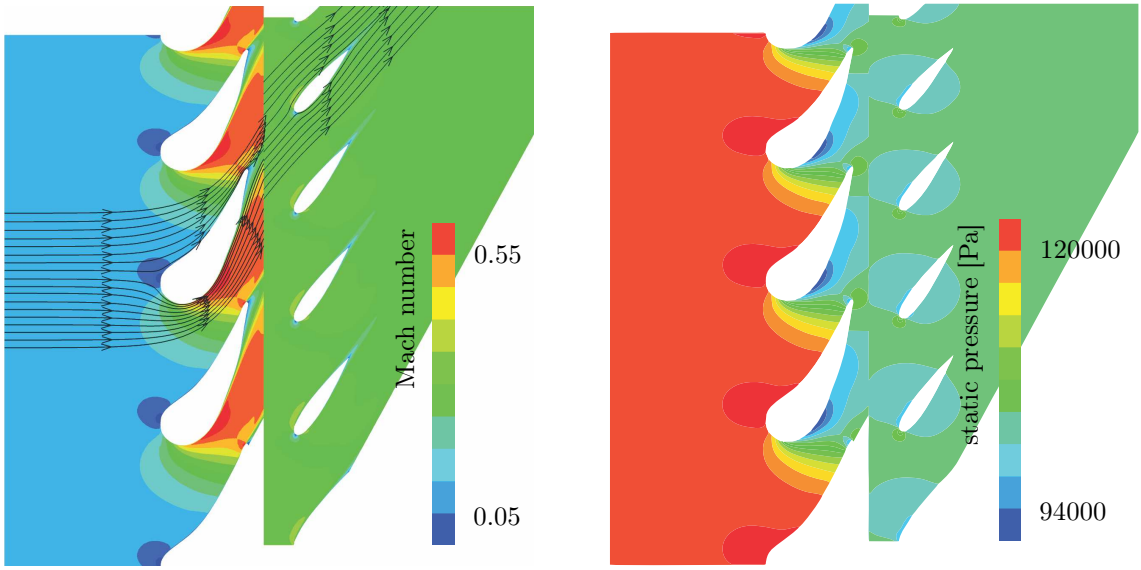

(a) (b)

FIG. 6.5-16: Flow field at $C_F = 0.76$; (a) Mach number contour plot with velocity streamlines; (b) static pressure contour plot

Fig. 6.5-17 shows the time-averaged Mach number and static pressure contour plots at $C_F \approx 0.1$. The large deviation angle, here $(\beta - \beta_o) \approx -135°$, causes an acceleration at the leading edge of the blade with a subsequent flow separation. The aerodynamic leading edge has been moved away from the geometric leading edge to the suction side of the blade. The flow field impinges with a blunt angle on this surface, which leads to an increase in static pressure. This pressure spike propagates upstream, and it is this pressure variation that has been picked up at location A and

B as dominating pressure variation. This phenomenon coincides with the increase in the measured Φ'_{min} value at the same flow coefficient.

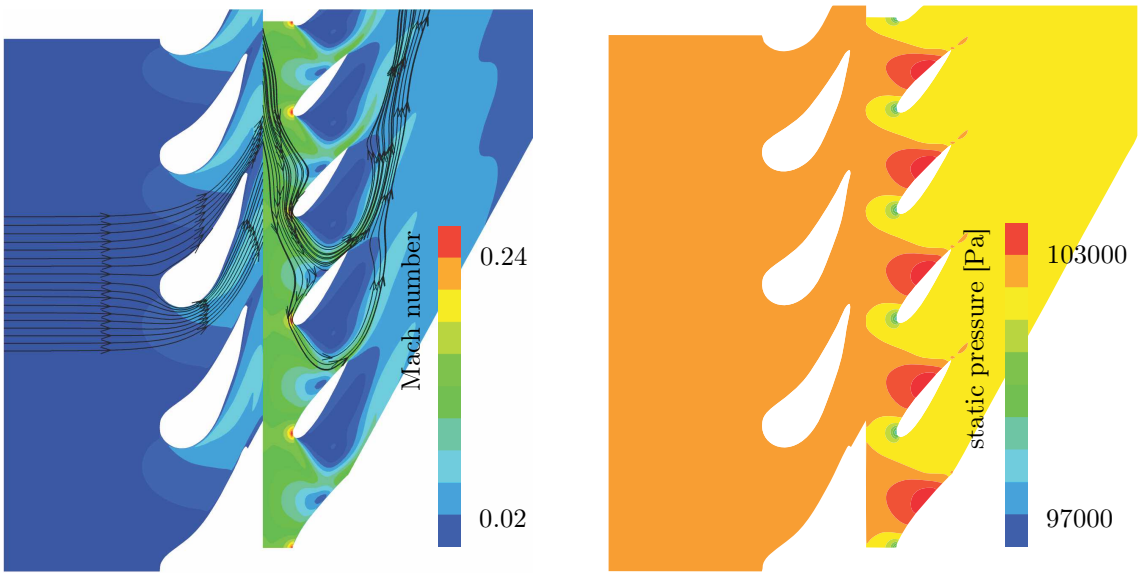

FIG. 6.5-17: Flow field at $C_F \approx 0.10$; (a) Mach number contour plot with velocity streamlines; (b) static pressure contour plot

It is unclear why the steady-state Scanivalve measurement systems fails to detect the non-linear pressure component, while the concentration measurement in the wheel-space shows an increase of Φ_{min} due to an indirect increase of the peak-to-trough pressure.

6.6 Summary

This chapter discusses the influence of off-design conditions on the external pressure coefficient ΔC_p. Static pressure measurements have shown a linear variation of $\Delta C_p^{1/2}$ with the flow coefficient C_F. The same behaviour was found numerically for $C_F \succ 0.2$. With further decreasing flow coefficient, the CFD results departed from this behaviour with an increase in $\Delta C_p^{1/2}$ as C_F decreases. This effect could be isolated and associated to the rotor blade at large deviation angle, i.e. $|\beta - \beta_o| \succ 120°$.

The gas concentration measurements were conducted for an axial- and radial-clearance seal with the tracer gas CO_2 to determine the sealing parameter Φ'_{min}. Scobie et al. (2013) used the CI equation to correlate the variation of Φ_{min} with C_F. The CI equation showed good agreement between the variation of Φ'_{min} with

C_F. For all seals an increase in Φ'_{min} was observed for a $C_F \prec 0.1$. This increase was consistent with the rise in the computed value $\Delta C_p^{1/2}$. This increase was caused by the large deviation angle at which the flow field impinges on the symmetrical rotor blade at a blunt angle.

The steady Scanivalve pressure measurement system failed to capture this non-linear pressure component induced by the rotor blade. It is recommended that the experiments are repeated with an unsteady pressure measurement to confirm the observation made by the unsteady CFD computations.

Chapter 7

Numerical and Experimental Investigation of Rim-Seal Concepts

This chapter describes the computational and experimental investigation into a novel rim-seal concept to minimise the ingress levels into rotor-stator cavities from the primary gas path in a high pressure turbine stage.

Fig. 7.0-1 shows the scope of the investigation undertaken in this and the subsequent chapter.

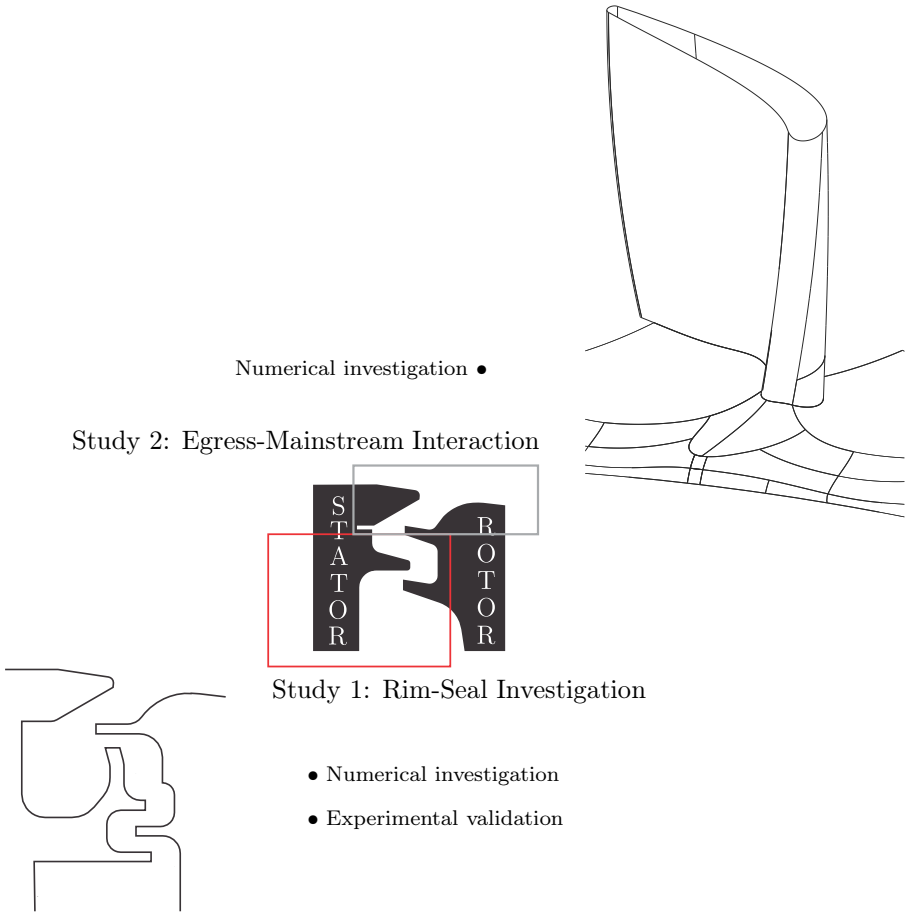

FIG. 7.0-1: Scope of investigation

The first study described in this chapter investigates various rudimentary rim-seal concepts derived by a CFD approach with subsequent validation in a rotating test facility at the University of Bath. An "optimised" rim-seal has been derived from this investigation which incorporates the various advantageous features into a single rim-seal design.

The second study focuses on the aerodynamic interaction of the discharged egress flow with the primary gas path flow. This study is conducted numerically with the objective to develop a 3D endwall design to minimise the aerodynamic interaction losses between the egress and the mainstream flow, and to reduce the losses associated to the secondary flows in the rotor blade passage. This investigation is discussed in detail in Chapter 8: "Egress-Mainstream Interaction".

Siemens has submitted three patent applications as outcome of these investigations (Teuber and Li, 2013a,b) and (Li and Teuber, 2013).

7.1 Introduction

Phadke and Owen (1988b) reported rim-seal tests for externally-induced ingress with the facility shown in Fig. 7.1-2 where they created the pressure asymmetry by using wire mesh and blocking section of honeycomb as there were no vanes and blades presented in the gas path. They investigated four seal geometries with a $Re_W \preceq 1.1 \times 10^6$ and they used Eq. 7.1-1 to correlate $C_{w,min}$ to the maximum circumferential pressure variation.

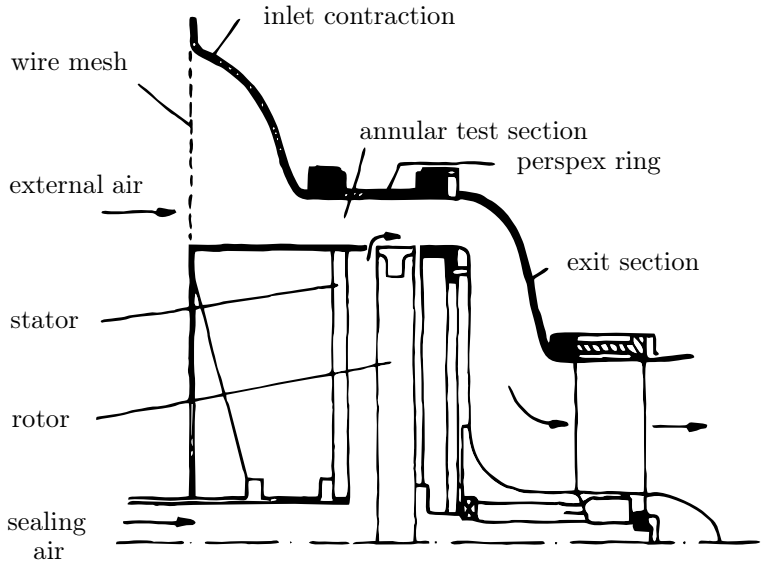

FIG. 7.1-2: Rig for *EI* ingress used by Phadke and Owen (adapted from Phadke and Owen (1988b))

$$C_{w,min} = 2\Pi K G_c P_{max}^{1/2} \tag{7.1-1}$$

where $K = \sqrt{2CC_d}$ and $P_{max} = \frac{1}{2} C_{P,max} Re_W^2$

Despite the variety of rim-seal configurations and the scatter of their experimental data, they could correlate the data using Eq. 7.1-1 with a K factor of 0.6 as shown in Fig. 7.1-3.

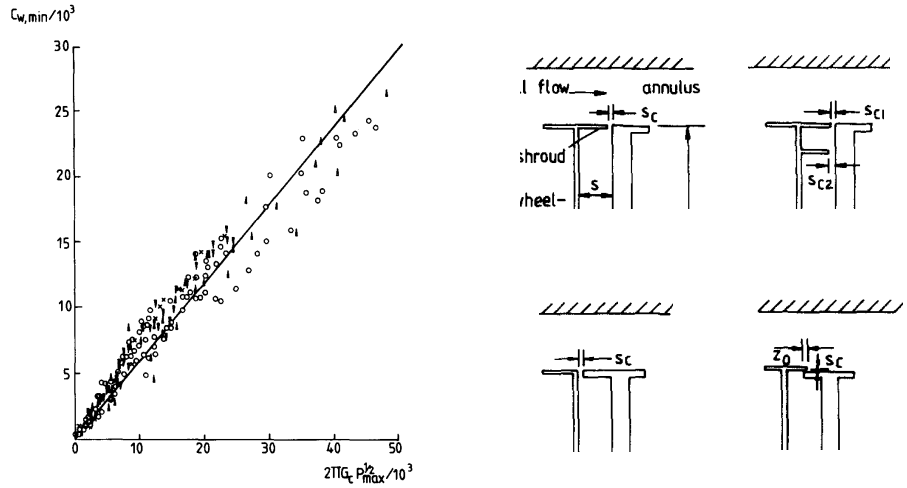

FIG. 7.1-3: Variation of $C_{w,min}$ with $2\Pi G_c P_{max}^{1/2}$ (adapted from Phadke and Owen (1988b))

Bohn and Wolff (2003) experimentally investigated (with a 1.5-stage ingress test facility) four rim-seal configurations in the Reynolds number range $8\times10^5 \preceq Re_{C1} \preceq 1.5 \times 10^6$ and $4.5 \times 10^5 \preceq Re_u \preceq 8 \times 10^5$ where $C1$ and u refer to the absolute vane exit and the rotational velocity respectively. They used CO_2 concentration measurements to determine the characteristic of these seals assessing the variation of η with $C_{w,o}$, where η is defined as cooling effectiveness as follows:

$$\eta = \frac{\Psi}{\Psi_{coolant}} \tag{7.1-2}$$

They approximated this data with a polynomial where they correlated the cooling effectiveness to $C_{w,o}$ and derived $C_{w,min}$ when the following criteria was obtained

$$\frac{\partial \eta}{\partial C_{w,o}} = 2.1 \times 10^{-6} \tag{7.1-3}$$

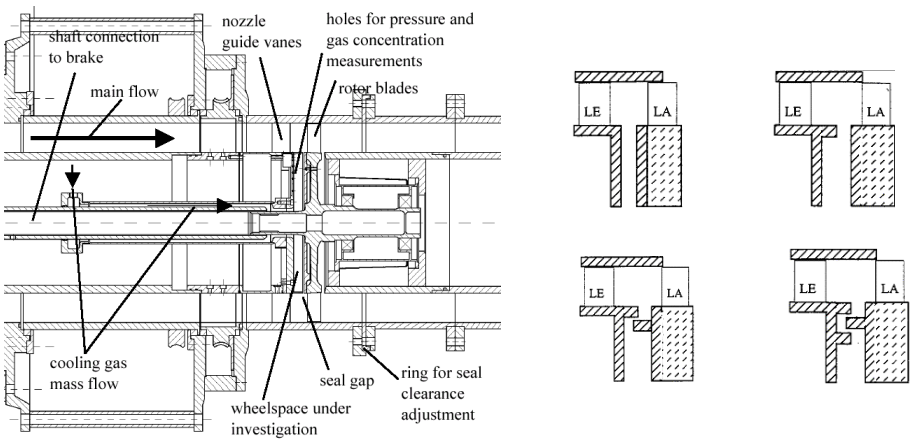

FIG. 7.1-4: 1.5-stage ingress test facility used by Bohn and Wolff (2003) to investigate four rim-seal configurations

The comparison between their $C_{w,min}$ values with the data of Phadke and Owen (1988b) confirms the linear relationship of $C_{w,min}$ with $C_{p,max}^{1/2}$ of the aforementioned researchers, as shown in Fig. 7.1-5. However, in contrast to Phadke and Owen (1988b), Bohn and Wolff (2003) obtained K values dependent upon their rim-seal configurations and they used the empirical constant to determine the relative performance of their seals, where a decreasing K value represents an increasing seal performance.

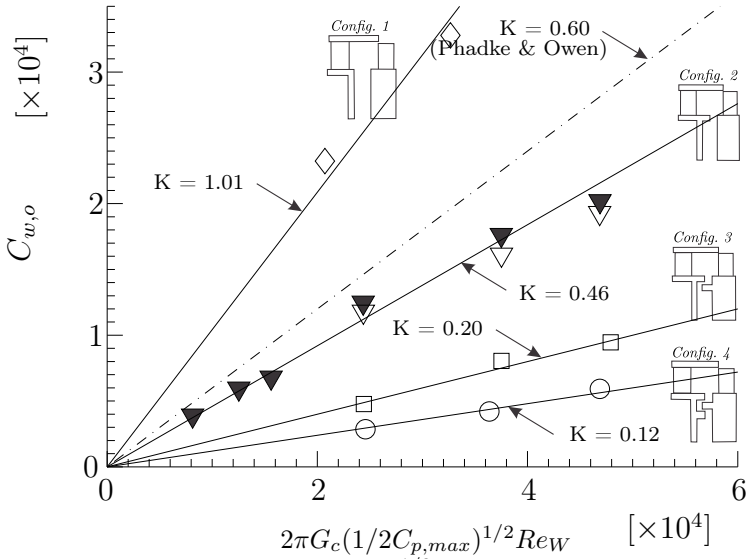

FIG. 7.1-5: Variation of $2\pi G_c(1/2C_{p,max})^{1/2}Re_W$ for 4 seal configurations and the comparison with the data from Phadke and Owen (1988b) (adapted from (Bohn and Wolff, 2003))

The caveat of this approach is that K depends on the location where $C_{p,max}$ was derived. As shown by Sangan et al. (2011a), by incorporating their experimental data in Fig. 7.1-6 for an axial- and radial clearance seal. They measured the peak-to-trough pressure at two locations in the gas path, i.e. location A behind the TE of the vane on the hub and location B on the outer casing mid-way of the rim-seal. As shown in Chapter 6 "Off-Design Conditions", the decay of ΔC_p between the TE of the vane and the LE of the blade experiences rapid gradients.

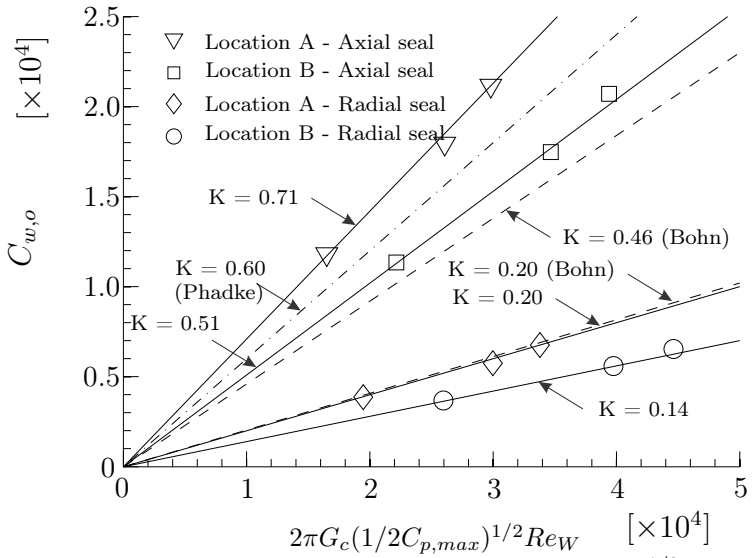

Fig. 7.1-6: Effect of ΔC_p on the variation of $2\pi G_c(1/2C_{p,max})^{1/2}Re_W$ for 2 seal configurations (adapted from Sangan et al. (2011a)

Sangan et al. (2011a) calculated their K values with Eq. 7.1-4 with their measured ΔC_p and Φ_{min} values as follows:

$$K = \sqrt{2}C_{d,e,EI}I_{min} = \sqrt{\frac{2}{\Delta C_p}}\Phi_{min,EI} \tag{7.1-4}$$

Fig. 7.1-6 shows that for both seals the K value is smaller at location A compared to location B owing to the smaller peak-to-trough pressure.

Sangan et al. (2012) extended their research and conducted for a wide variety of rim-seal configurations in the EI ingress regime where they used the sealing parameter Φ_{min} instead of the K values to assess the performance of their rim-seals. By using the effectiveness equations, Sangan et al. (2011b) de-coupled the Φ_{min} parameter from its ingress driving force, whereby for a given set of vane-blade and rim-seal configuration a unique value is derived, independently of the measured ΔC_p, M or Re_ϕ. The reader is referred to Section 2.2.5 "Experimental Work on Ingress" for a detailed description of the test facility and methods used by Sangan et al. (2012) in order to obtain Φ_{min}.

Fig. 7.1-7 summarises their test programme, both for EI and RI ingress. The black bar represents the parameter $\Phi_{min,EI}$, the value of Φ_{min} for externally-induced ingress. With increasing rim-seal complexity, by introducing various features underneath the single overlap, Φ_{min} decreases and reaches its lowest value for the double overlapping rim-seal. $\Phi_{min,RI}$, the value of Φ_{min} for rotationally-induced ingress, is also given by the red line and expresses the theoretical lowest sealing flow rate to purge the cavity. To allow for this quantitative comparison, they based the seal-

clearance s_c in the parameter Φ_o on the axial-clearance which was for all seals 2mm.

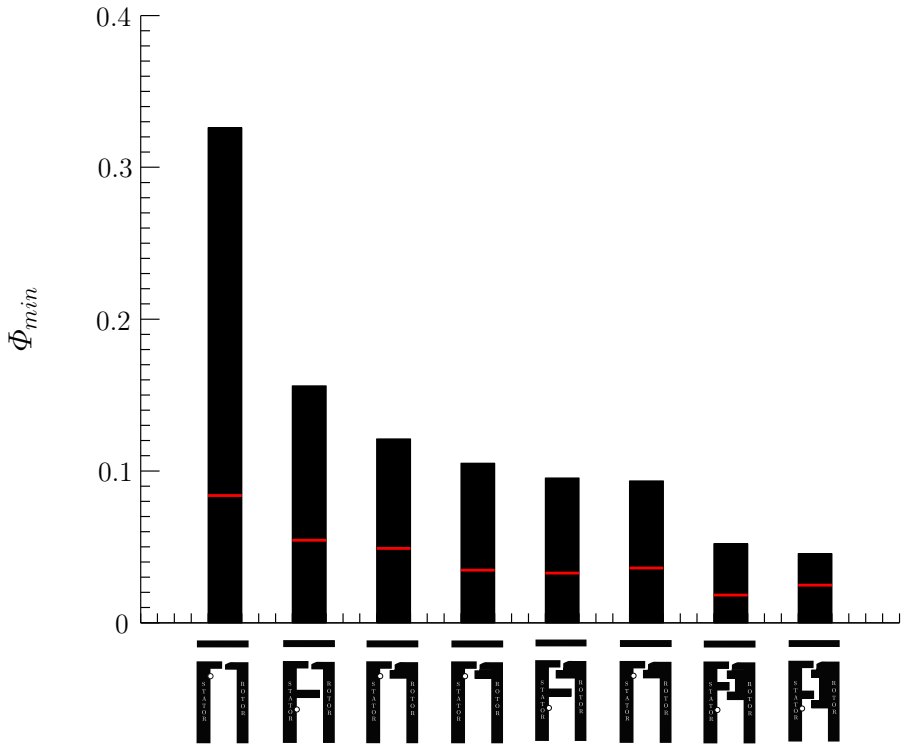

FIG. 7.1-7: Rim-seal ranking in terms of Φ_{min} with sampling point at $r/b = 0.958$ (single overlap) and $r/b = 0.85$ (double overlap) (Sangan et al. (2011a, 2012))

7.2 Investigation of Rim Seal Concepts

This section describes the investigation and development of a novel rim-seal concept based upon a CFD study. The numerical investigation was conducted at engine representative conditions with $Re_\phi \approx \times 10^7$. The promising concepts were translated into generic seals to be fitted and tested in the ingestion facility at the University of Bath as used by Sangan et al. (2011a). The rig uses an Re_ϕ which is an order of magnitude smaller than that used in gas turbines; but Owen and Rogers (1989) have shown that the turbulent flow structure in the stator and rotor wall boundary layers is mainly dictated by λ_T, the turbulent flow parameter and that the dependence on the rotor speed or Re_ϕ is negligible.

7.2.1 CFD Study

The CFD model domain consists of a stationary domain with 3 nozzle guide vanes, the wheel-space and a rotating domain with the rotor (see Fig. 7.2-8(a)). A sliding plane to connect the stationary and rotating domains was placed midway between

the rim-seal and the leading edge of the rotor blade. 7.5 million hexahedral mesh elements were used to discretise the domains in a structured way with a J-grid and H-grid topology for the NGV and RB domain respectively. Fig. 7.2-8(b) shows the mesh for the wheel-space domain with a $y^+_{WS} \approx 1$ and a grid expansion to the adjacent mesh cell of 1.3. The gas path y^+_{gp} was set to ≈ 10. The numerics are identical to those described in the Chapter "Validation" with the exception that the time-step which was set to 2.351×10^{-6}.

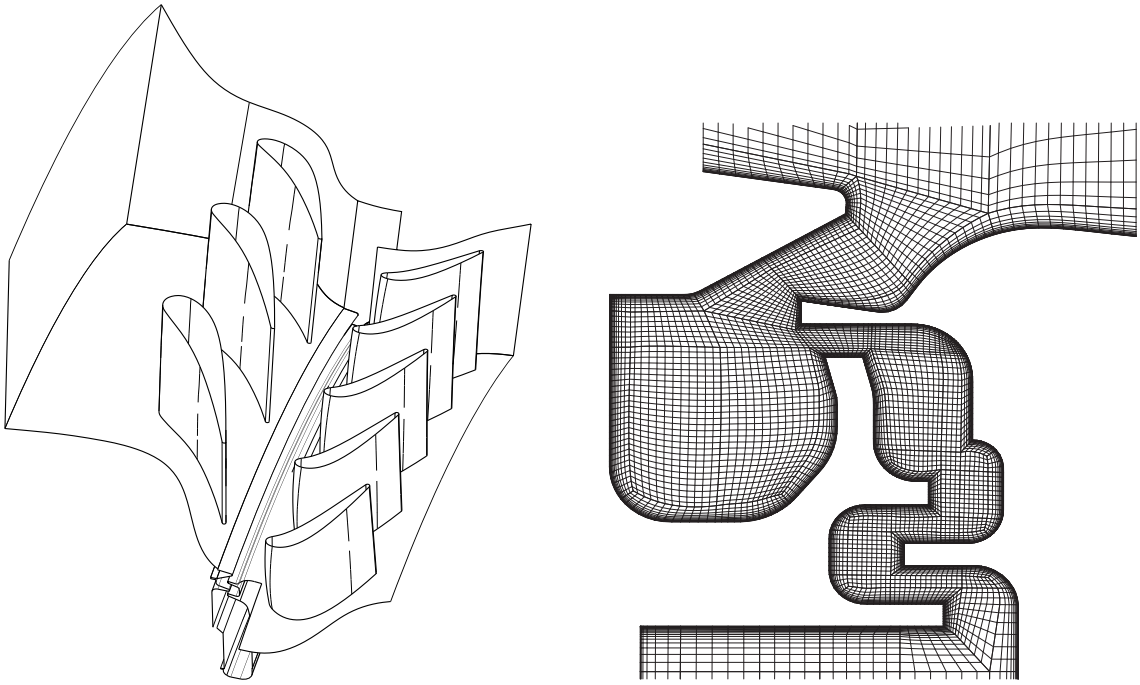

(a) (b)

FIG. 7.2-8: CFD model; (a) model domain; (b) wheel-space mesh

Fig. 7.2-9 shows a typical convergence behaviour for a transient rim-seal computation with the computed sealing effectiveness monitored at four different rim-seal positions. The starting point of the transient computation was the steady-state computation with the frozen rotor approach. The unsteady simulation took up to four revolutions before the mixed out gas composition consisting of the tracer gas and the gas path fluid was fully convected within the rim-seal and the wheel-space. The solution was considered being converged when a quasi-periodic behaviour for the sealing effectiveness, static and total temperatures and pressures was obtained at selected monitoring points. The computations were performed with 2 HP Z800 workstations ported to a cluster, resulting in computational times of up to 5 weeks with 20 parallel solvers.

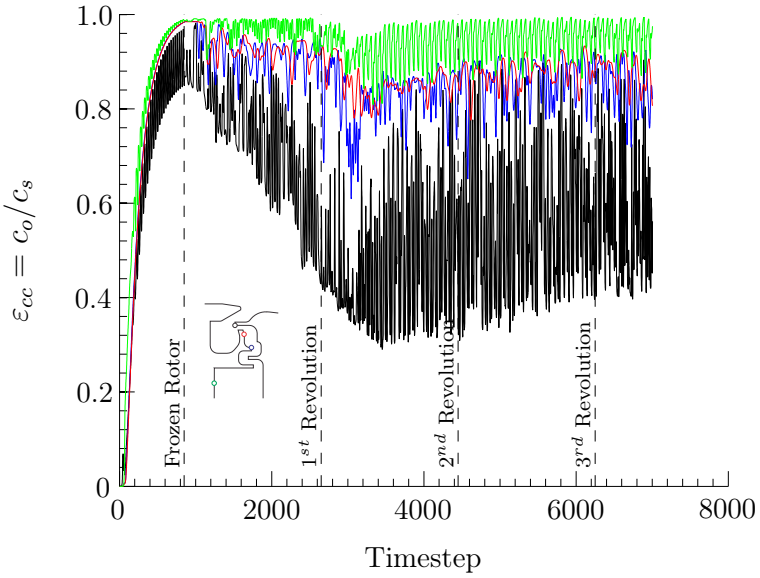

FIG. 7.2-9: Convergence behaviour for the sealing effectiveness ε_{cc} at four rim-seal positions

Fig. 7.2-10 summarises the rim-seal concepts that have been numerically investigated with the commercial CFD code CFX v13.0. The double radial overlapping rim-seal displayed in Fig. 7.2-10(a) was the starting point of the computation and acts as reference point to assess the performance of the rim-seal concepts. This first concept was a rudimentary angel wing mounted onto the stator wall as displayed in Fig. 7.2-10(b). The intention for this concept was to create a minor cavity enclosed by the angel wing to attenuate the ingestion driving circumferential pressure variation caused by the presence of the nozzle guide vanes and rotor blades. Furthermore, the angel wing ensures that the ingested hot fluid is contained within this cavity and avoids an impingement on the rotor disc. Additionally, this concept tries to take advantage of the disc pumping to provide further cooling to the rotor blade and to further reduce ingestion. The coolant supplied to the rotor stator wheel-space is entrained into the rotor boundary and is pumped upwards by the centrifugal force. Pountney et al. (2012) have proven, with their heat transfer experiments with liquid crystal sprayed on to a transparent rotor disc that the rotor disc, has a higher sealing effectiveness than the stator. This concept tries to use this effect to provide additional cooling to the rotor disc and rotor blade root. The coolant is then ejected through the radial-clearance provided by the angel wing and the radial arm which is attached to the rotor platform. The steady-state disc pumping effect provides an additional force in the opposite direction of any remaining ingress through the radial-clearance. Concepts 2 and 4 were further refined rim-seals based upon this angel wing. The detailed description of the fluid mechanics and advantages of these features will be discussed in the subsequent sections. It should be mentioned that the minimum clearance of the baseline case was maintained at all concepts.

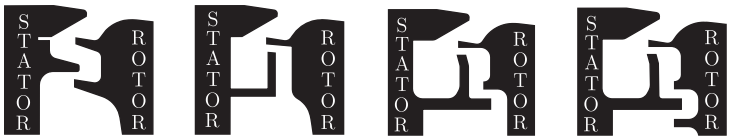

(a) (b) (c) (d)

Fig. 7.2-10: Rim-seal concepts investigated by CFD; (a) Baseline; (b) Concept 1; (c) Concept 2; (d) Concept 4

Fig. 7.2-11 shows the computed sealing effectiveness ε_{cc} with Φ_o for the concepts displayed in Fig. 7.2-10, with the sampling point placed within the wheel-space on the stator wall at $r/b = 0.96$. Three values of Φ_o were chosen and computed to assess the seal characteristic for the baseline case. The time-averaged ε_{cc} results were fitted with the method described by Zhou et al. (2011). It should be mentioned that a large portion of the sealing flow supplied to the wheel-space was subtracted at the rotor blade root as leakage flow, i.e. $\Phi_{out} \approx 0.055$. The modelling of this outflow is substantial to obtain a representative flow structure in the wheel-space. To assess the performance of the rim-seal concepts only one Φ_o was computed owing to soft- and hardware restriction. Fig. 7.2-11(b) compares the baseline case with concept 1 at $\Phi_o = 0.0725$.

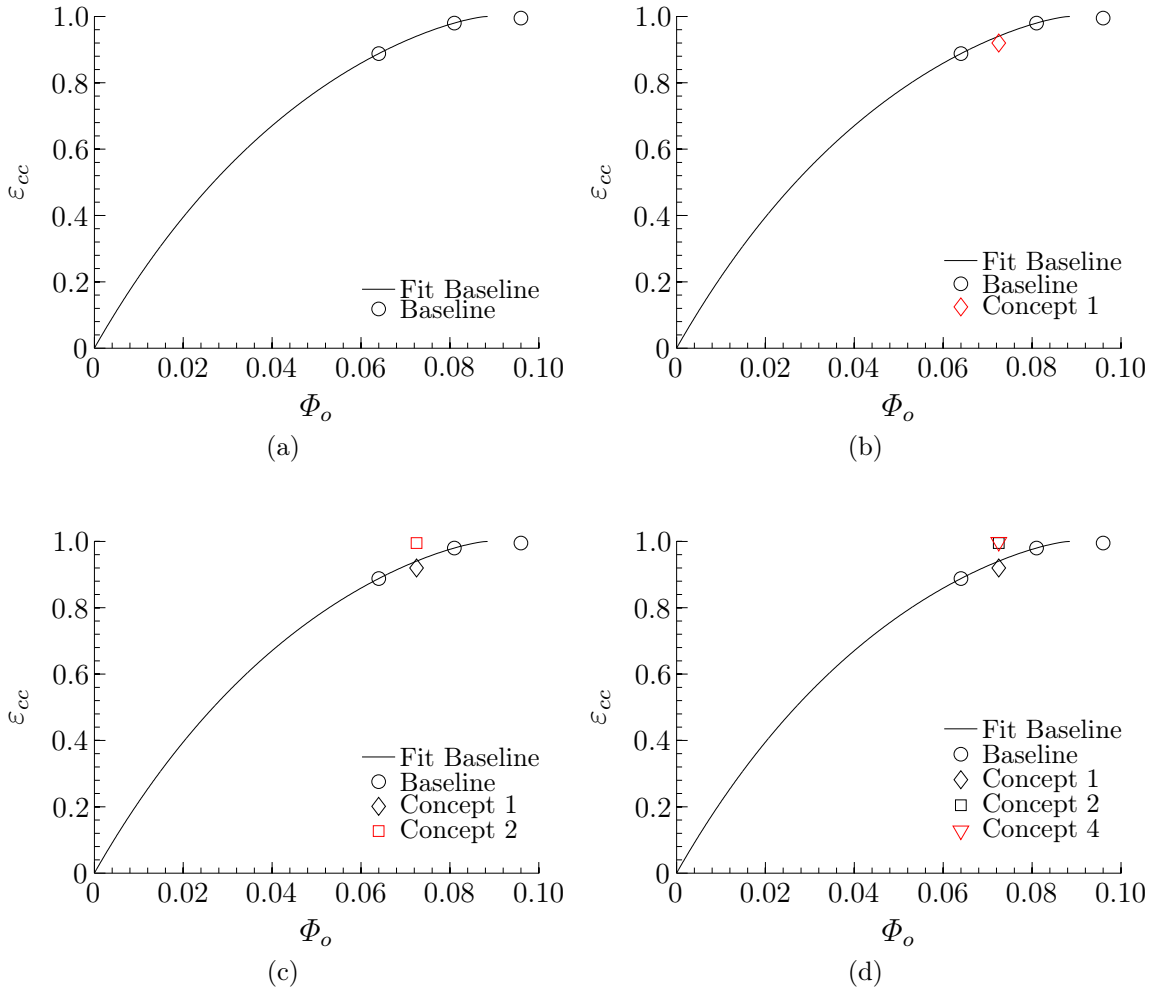

FIG. 7.2-11: Computed sealing effectiveness ε_{cc} for investigated rim-seal concepts at $\Phi_o = 0.0725$ with sampling point at $r/b = 0.96$

The computed $\Phi_o - \varepsilon_{cc}$ point of concept 1 has a slightly lower sealing effectiveness than the baseline. The small cavity size enclosed by the angel wing was not capable of attenuating the tangential pressure variation. To improve the seal performance, the cavity size was increased and an additional radial overlap was incorporated in concept $C.2$ to prevent any migration of the leakage flow into the wheel-space. This concept makes advantage of the disc pumping effect, where the sealing flow is pumped directly into the seal-clearance and opposes any remaining leakage flow. The computations could not detect any ingress at the sampling within the wheel-space, which confirms the aforementioned assumptions. Concept 4 included a second radial overlap but this comes at the expense of a minimised influence of the disc pumping effect, whereby the results are quite similar to the performance of concept 2.

7.2.2 Experimental Investigation

This section describes the experimental investigation of the rim-seal concepts tested in the ingestion facility at the University of Bath. The numerically investigated seals were translated into generic rim-seals consisting of an angel wing (which was manufactured as a 360° ring mounted on the stator wall) and an insert or a combination of inserts attached to the rotor disc/platform to investigate various radial overlapping arrangements with this angel wing as shown in Fig. 7.2-12. It should be mentioned that the minimum clearance $s_{c,min}$ was set to 1.2mm and it was maintained throughout this study.

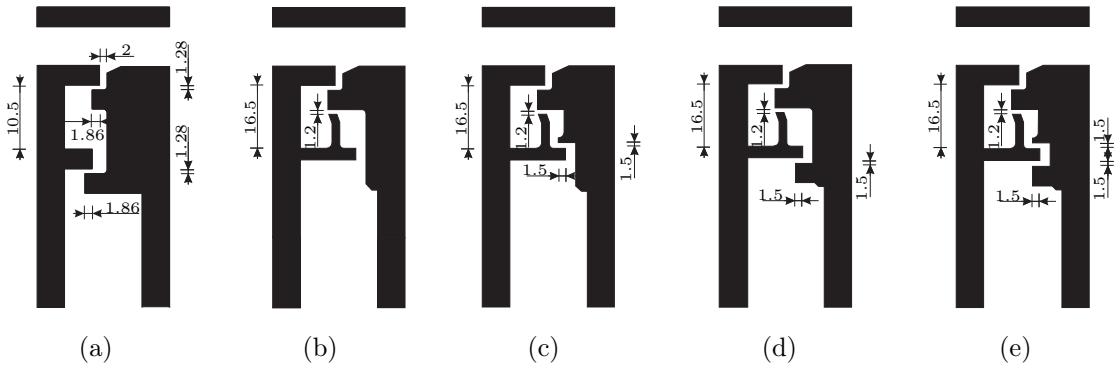

Fig. 7.2-12: Generic rim-seal concepts for testing in the ingestion facility at the University of Bath; (a) Baseline (B); (b) Concept 1 ($C.1$); (c) Concept 2 ($C.2$); (d) Concept 3 ($C.3$); (e) Concept 4 ($C.4$)

The test was conducted at incompressible external conditions for three rotational Reynolds numbers with a constant flow coefficient, e.i. $C_F = 0.538$. The conditions used throughout this investigation are tabulated in Tab. 7-1. However, for reason of safety are to avoid the risk of overloading the rotor disc by the additional weight of the rotor inserts, $C.3$ and $C.4$ were only tested by the lowest Reynolds number.

Tab. 7-1: Experimental conditions for the rim-seal study

Ω	C_F	$Re_\phi \times 10^5$	$\dot{m}$ $[kg/s]$	$Re_W \times 10^5$	$M_{NGV,exit}$
2000	0.538	5.32	0.344	3.02	0.229
3000	0.538	8.17	0.523	4.64	0.347
3500	0.538	9.68	0.615	5.49	0.406

Fig. 7.2-13 to Fig. 7.2-17 summarise the results of the concentration measurements for all concepts with the variation of the sealing effectiveness, ε_c, against the sealing parameter Φ_o with the sampling point at $r/b = 0.85$ depicted on the left-hand side and the change of ε_c with the non-dimensional radius r/b for three sealing flow rates in the right column.

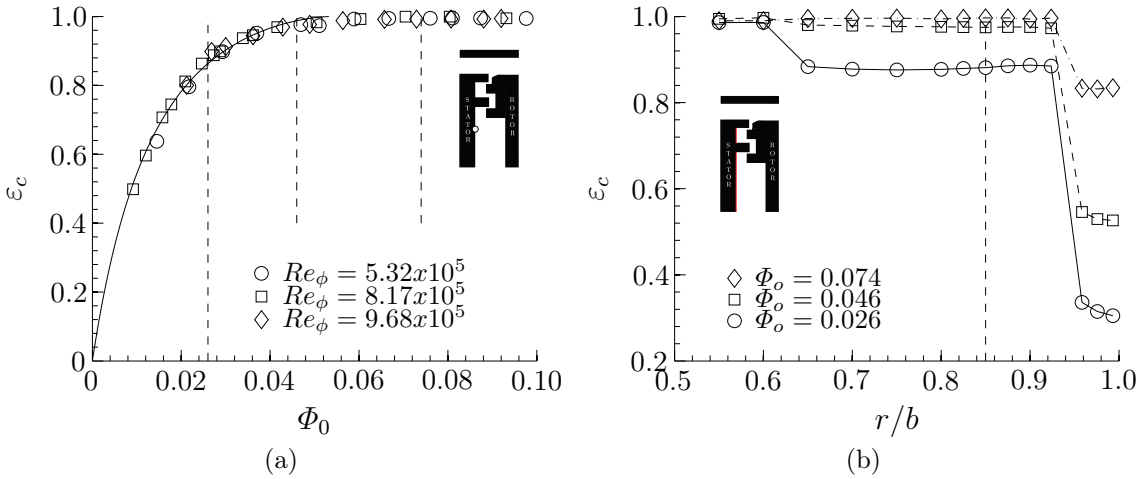

FIG. 7.2-13: Experimental data for double radial overlapping baseline case; (a) Variation of sealing effectiveness with Φ_o with sampling point at $r/b = 0.85$; (b) Variation of the sealing effectiveness with the non-dimensional radius r/b for three sealing flow rates

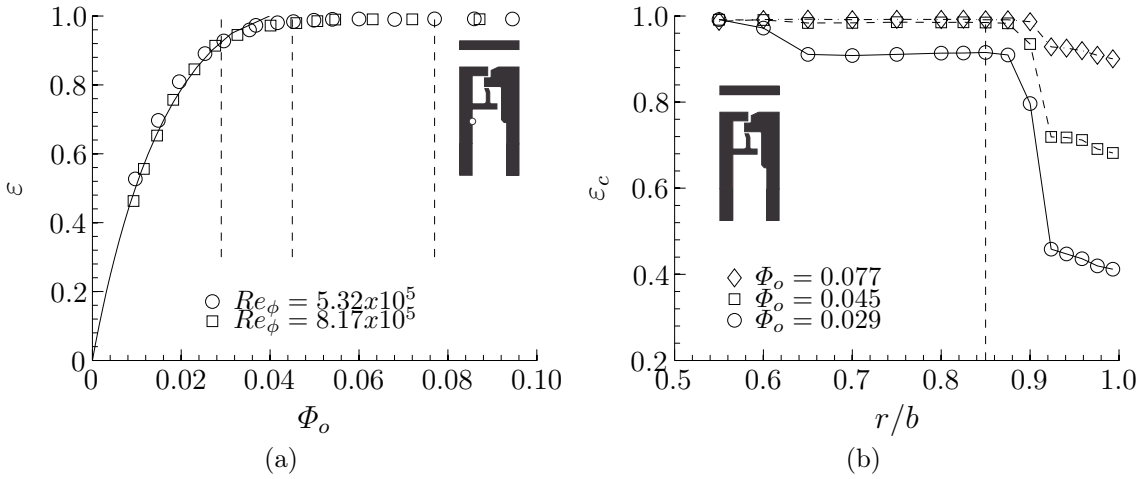

FIG. 7.2-14: Experimental data for seal concept 1; (a) Variation of sealing effectiveness with Φ_o with sampling point at $r/b = 0.85$; (b) Variation of the sealing effectiveness with the non-dimensional radius r/b for three sealing flow rates

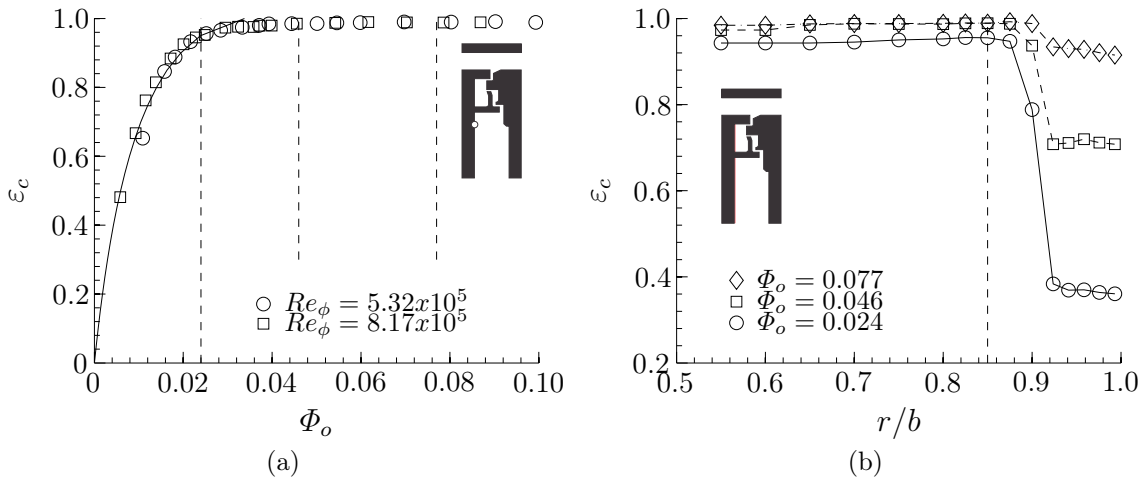

FIG. 7.2-15: Experimental data for seal concept 2; (a) Variation of sealing effectiveness with Φ_o with sampling point at $r/b = 0.85$; (b) Variation of the sealing effectiveness with the non-dimensional radius r/b for three sealing flow rates

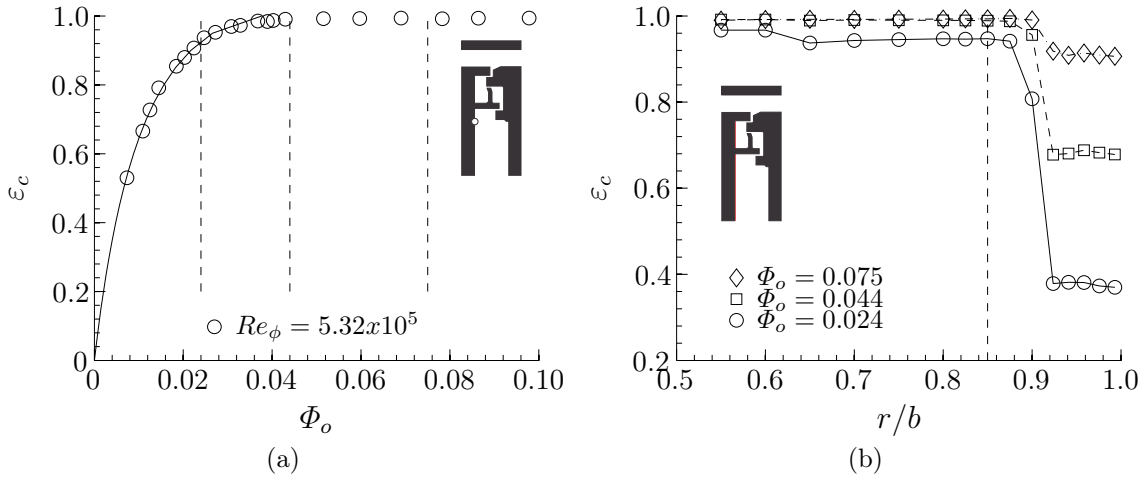

FIG. 7.2-16: Experimental data for seal concept 3; (a) Variation of sealing effectiveness with Φ_o with sampling point at $r/b = 0.85$; (b) Variation of the sealing effectiveness with the non-dimensional radius r/b for three sealing flow rates

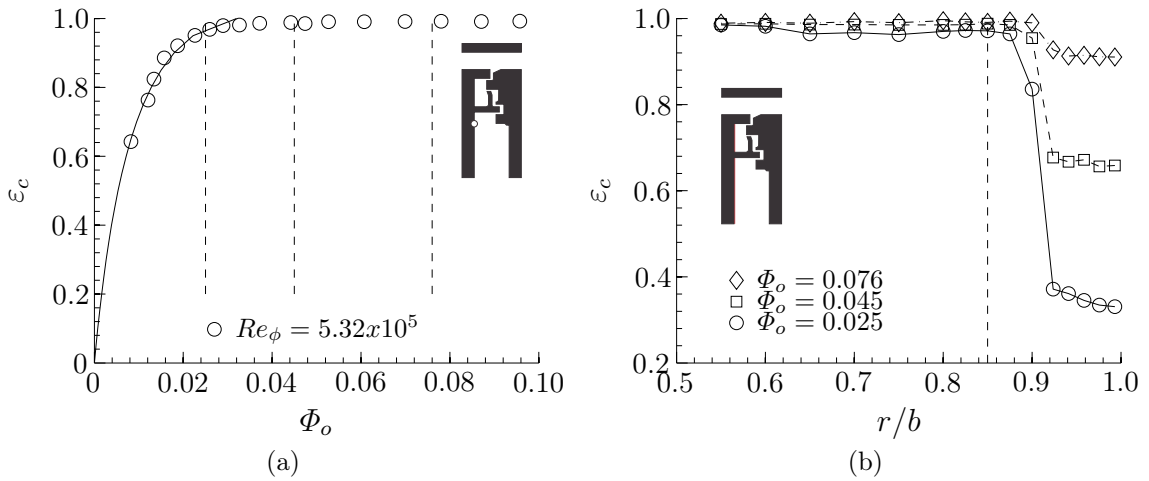

FIG. 7.2-17: Experimental data for seal concept 4; (a) Variation of sealing effectiveness with Φ_o with sampling point at $r/b = 0.85$; (b) Variation of the sealing effectiveness with the non-dimensional radius r/b for three sealing flow rates

Fig. 7.2-18 compares the sealing effectiveness curves of all concepts for the inner sampling point at $r/b = 0.85$ and the outer one at $r/b = 0.958$. This experimental data was fitted to Eq. 2.2-41 with the statistical method by Zhou et al. (2011). The parameters have been tabulated in Tab. A-1 and A-2 in Appendix A: "Experimental Uncertainty".

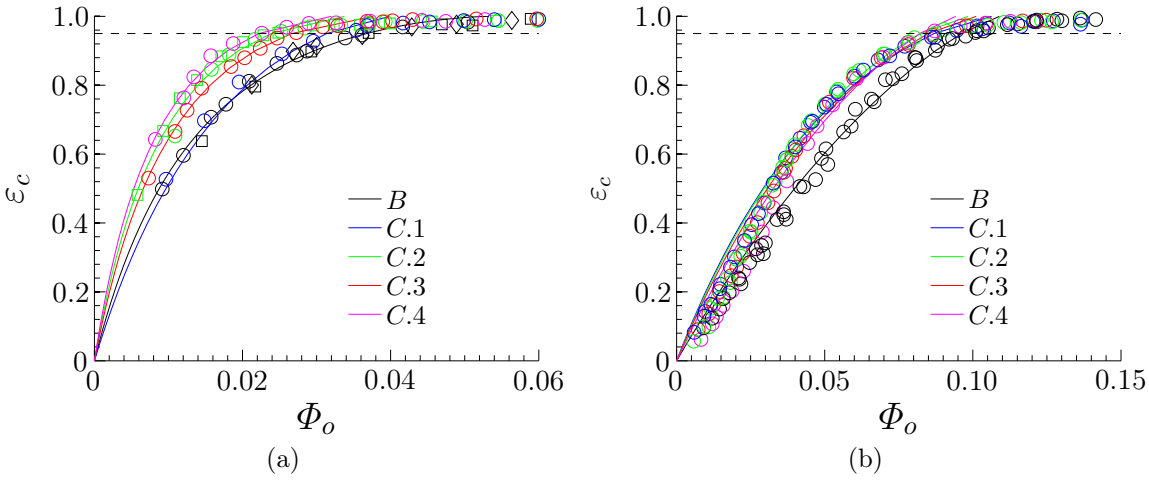

FIG. 7.2-18: Summary of all experimentally tested concepts with the sampling point at; (a) $r/b = 0.85$; (b) $r/b = 0.958$

At the inner sampling point, the sealing effectiveness curves for all concepts experience a shift to lower sealing flow rates compared to the baseline case, and this is in particular pronounced for the concepts $C3$, $C2$ and $C4$. At the outer sampling point, the concentration data for all rim-seal concepts collapses onto each other and become quasi independent of the insert combinations in the wheel-space.

Furthermore, there is also a shift of the sealing effectiveness curves to lower sealing flow rates as observed at $r/b = 0.850$.

Fig. 7.2-19 ranks the investigated rim-seals in terms of the parameter Φ'_{min} for the inner sampling point at $r/b = 0.85$, where Φ'_{min} is the value of Φ_o at $\varepsilon_c = 0.95$. This parameter was preferred to Φ_{min}, as the fits fail to capture the converging behaviour at high concentration levels before the wheel-space is fully sealed at $r/b = 0.958$, which tend to underestimate Φ_{min}.

Φ'_{min} decreases for all concepts and in particular for concept $C.2$ and $C.4$ with a reduction in Φ'_{min} by $\approx 39\%$ and $\approx 42\%$ respectively compared to the baseline case at $r/b = 0.85$. Even at the outer sampling point, there is an improvement by $\approx 15\%$ for $C.2$, $C.3$ and $C.4$ compared to the baseline case.

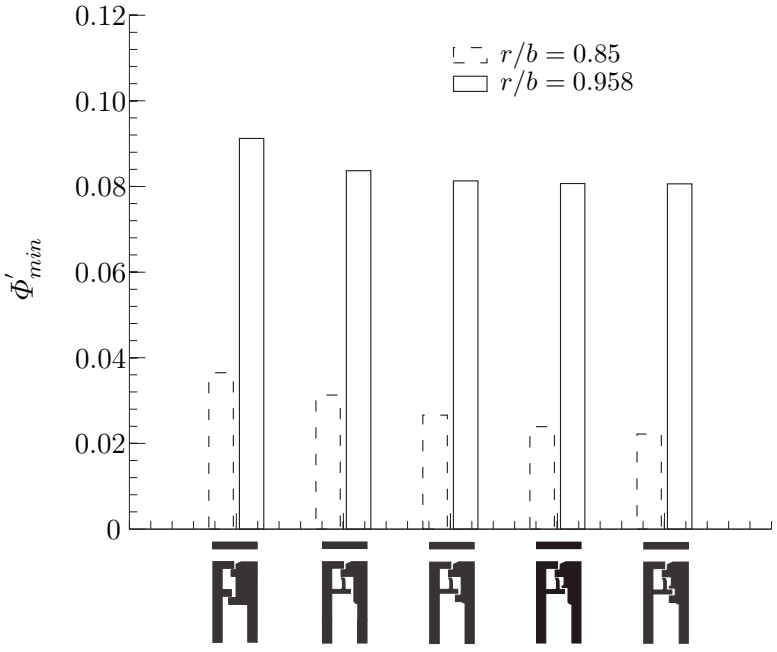

FIG. 7.2-19: Summary of all experimentally tested rim-seals with a rim-seal ranking with the sampling point at $r/b = 0.85$

The comparison of $C.2$ and $C.3$ in Fig. 7.2-19 shows that it is beneficial for the reduction of Φ'_{min} to place the inner-most rotor insert above the radial arm of the angel wing instead of putting it underneath. This arrangement allows the sealing flow to be pumped directly into the space between the rotor disc and angel wing with higher radial momentum than in $C.3$. This disc pumping force counteracts any remaining ingress flow which leads to a reduced Φ'_{min}. $C.4$ uses an additional insert underneath the angel wing to create another radial overlap but with only a marginal improvement in Φ'_{min}.

Fig. 7.2-20 and Fig. 7.2-21 compares rim-seal concepts with the variation of ε_c with wheel-space radius for three sealing flow rates on the stator wall of particular interest is Fig. 7.2-20(a) with the comparison of the baseline case with rim-seal $C.2$. The baseline shows at higher radius an increase in sealing effectiveness with decreasing radius caused by a not fully-mixed out fluid composition, while in $C.2$ the fluid has been mixed-out. This indicates that the mixing zone for $C.2$ has been moved radially outwards towards the radial overlap. At lower radius, e.g. at $r/b \prec 0.88$, the sealing effectiveness becomes invariant with radius owing to a completely mixed out fluid for both seals. In general, $C.2$ experiences lower levels of ingress, not only in the upper cavity, but also in the wheel-space relative to the baseline. The comparison of $C.1$ and $C.2$ at $r/b \succ 0.88$ in Fig. 7.2-20(b) shows almost identical profiles with the exception of the lowest flow rate where there is a mismatch between the sealing flow rates. However, the inclusion of the radial insert on the rotor wall of $C.2$ leads to a considerable increase of ε_c at $r/b \prec 0.88$.

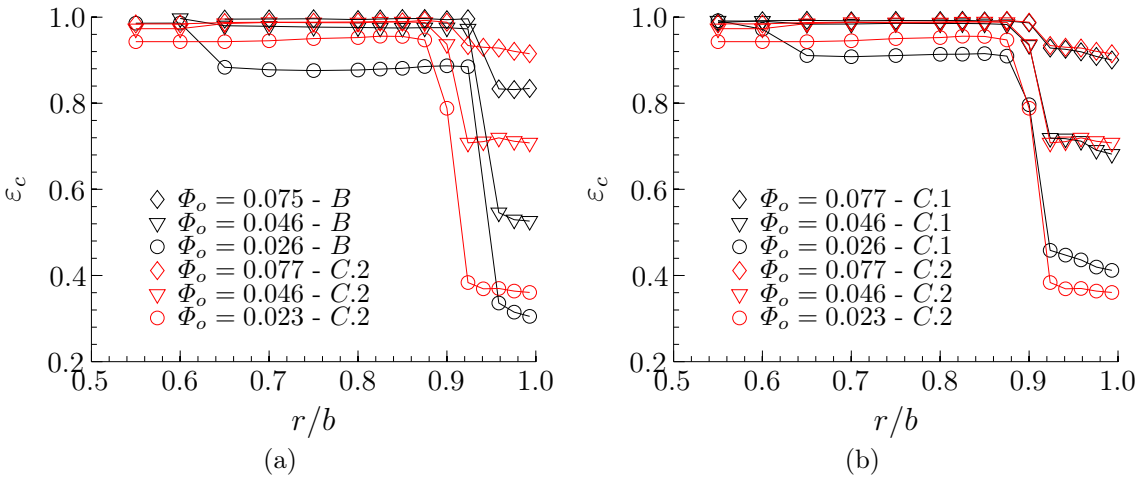

FIG. 7.2-20: Variation of ε_c with the non-dimensional radius r/b for three sealing flow rates for: (a) B and $C.2$; (b) $C.1$ and $C.2$

The comparison of $C.2$ with $C.3$ and $C.2$ with $C.4$ in Fig. 7.2-21 shows similar ε_c profiles, both in the upper cavity and the wheel-space with only marginal differences in the sealing effectiveness at $r/b \succ 0.90$.

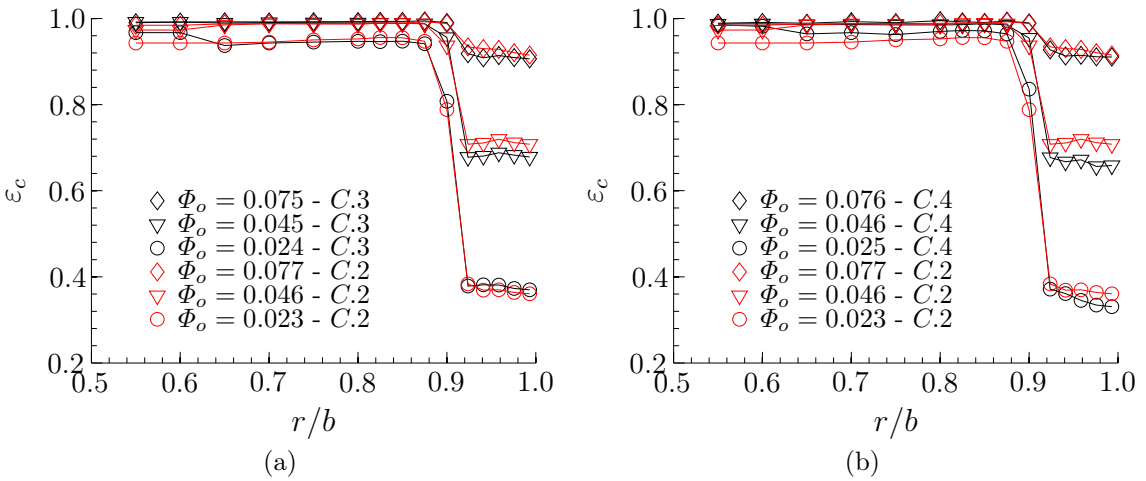

FIG. 7.2-21: Variation of ε_c with the non-dimensional radius r/b for three sealing flow rates for: (a) $C.2$ and $C.3$; (b) $C.2$ and $C.4$

This rim-seal investigation has shown an increase in sealing effectiveness by using an alternative rim-seal concept. This concept addresses main ingestion driving mechanism by attenuating the circumferential pressure variation in the cavity formed by the angel wing. This study forms the basis of the next section where a practical rim-seal design has been derived and tested which incorporates the major features and benefits of the concepts discussed within this section.

7.3 Optimised Rim-Seal

This section discusses the detailed fluid mechanics of an optimised rim-seal as shown in Fig. 7.3-22, which is based upon the numerical and experimental concept study of the previous section. This seal design has been derived to be practical for an industrial context, but still to incorporate the major benefits of each concept into a single design. This was accomplished by placing the inner-most radial rotor insert above the inner radial arm of the angel wing as seen in $C.2$, to take advantage of the disc pumping effect to further enhance the rim-seal performance. Furthermore, this seal incorporates the benefit of $C.4$ to ensure a decreasing radial seal-clearance independent of the condition of the engine without the penalty of adding additional weight on the critical rotor components.

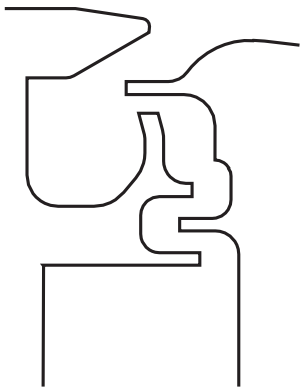

FIG. 7.3-22: Sketch of the optimised rim-seal

The ingress peak occurs when the nozzle guide vane wake is aligned with the aerodynamic leading edge and the pressure side of the rotor aerofoil. This leads to a superimposed pressure field above the rim-seal with a local peak relative to the wheel-space pressure which drives the gas path fluid into the wheel-space. Fig. 7.3-23 shows for this case the computed velocity streamlines and the tangential momentum in form of the swirl ratio β.

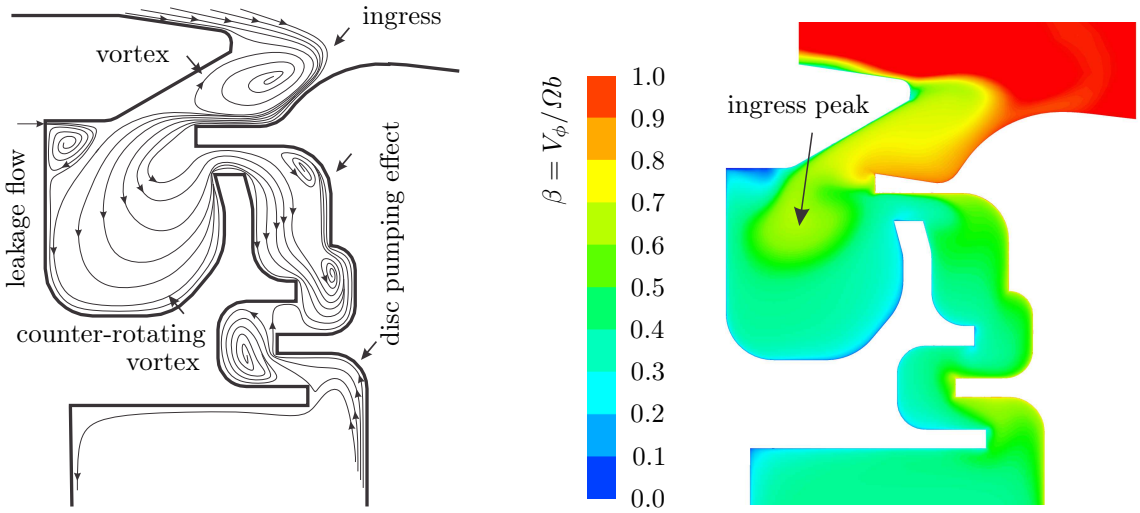

FIG. 7.3-23: Ingress peak case for optimised rim-seal; (a) computed velocity streamlines; (b) contour plot with the swirl ratio β

The gas path streamlines reverse their flow direction and move along on top of the rotor platform lip before being ingested into the cavity of the angel wing while a minor part remains in the seal gap to form a clockwise rotating vortex between the rotor platform lip and the mainstream flow. The angel wing geometry prevents any fluid entering the wheel-space directly as is the case for the baseline. The angel wing was set-up to induce a rotating vortex structure which has the beneficial effect of attenuating the circumferential pressure variation. The ingress flow carries high tangential momentum in the cavity with a swirl ratio β of ≈ 0.75 and this

mixes with the cavity fluid with a β of ≈ 0.4. The difference in swirl suppresses any deep penetration of the ingress into the cavity, and it ensures that the hot spot is maintained in the centre of the angel wing and does not contact the stator components, as shown in the computed sealing effectiveness contours in Fig. 7.3-24.

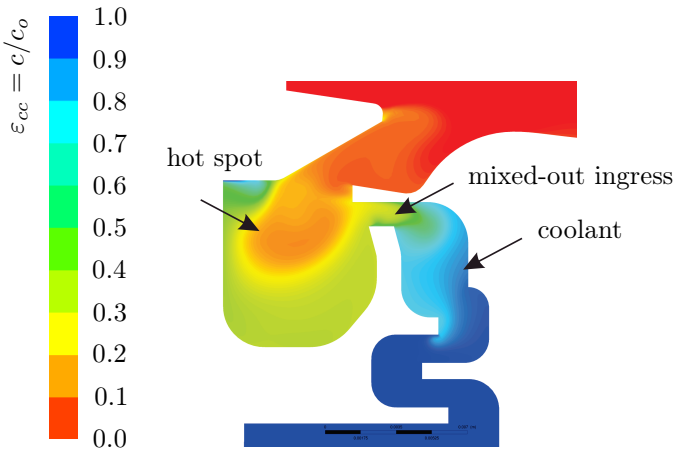

FIG. 7.3-24: Computed sealing effectiveness contour plot for the ingress peak case

Furthermore, it was found that the modelled leakage flow ejected into the angel wing cavity underneath the nozzle vane platform provides a useful cooling curtain by separating the fluid of the cavity from the components of the stator and the angel wing.

The remaining circumferential pressure asymmetry causes a leakage flow to the cavity formed by the angel wing and the rotor disc. This mixed-out ingress flow is suppressed by the radially upward pumped sealant by the disc pumping effect. This provides not only a flow in opposite direction of any residual ingress but also supplies a cooling effect to the critical rotor component due to the entrained coolant into the rotor boundary layer.

Egress occurs when the external static pressure drops below the static pressure of the wheel-space. Fig. 7.3-25 shows for this case the computed velocity streamlines and the swirl ratio. The streamlines in the angel wing cavity show the existence of the same counter-rotating vortex structure as observed for the ingress case. This structure is partially fed by the cooling flow ejected through the seal-clearance formed by the angel wing top and the rotor platform. The majority of the coolant is ejected directly into the seal gap formed between the nozzle guide vane and the rotor platform. The egress flow joins the gas path flow by damping out the difference in tangential velocity between the sealant and the gas path flow by a shear layer. This interaction between the egress and the mainstream flow is discussed in detail in the subsequent chapter 8: „Egress-Mainstream Interaction“.

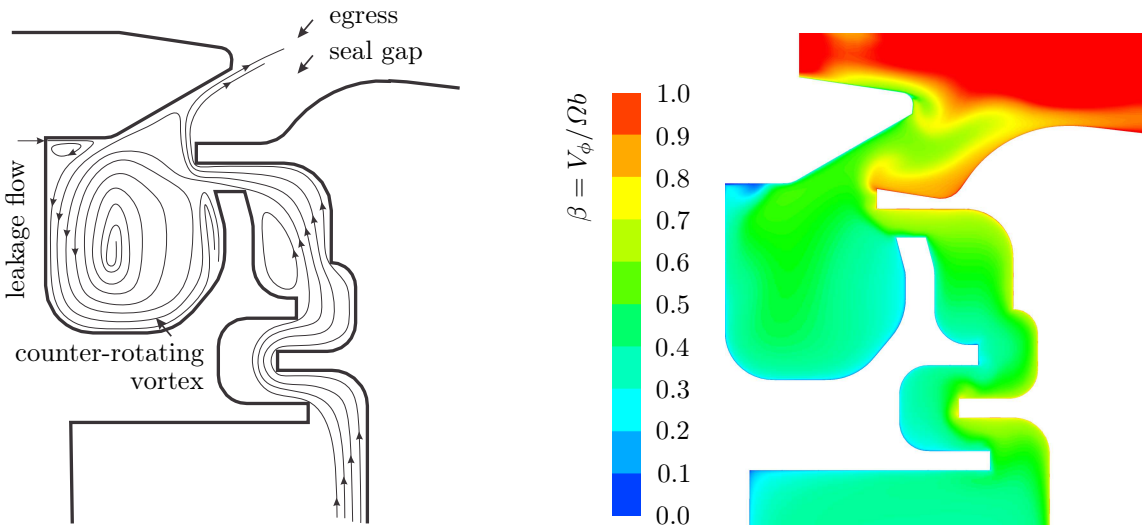

(a)

FIG. 7.3-25: Egress peak case; (a) velocity streamlines; (b) contour plot with the swirl ratio β

This rim-seal geometry was also investigated in the test facility. To gain more insight into the fluid mechanics of this seal, two holes were incorporated in the angel wing and they were connected to two CO_2 sampling probes on the stator wall. Fig. 7.3-26 shows the experimental data for this seal along with the seal sketch with the location of the sampling points. It should be noted that minimum clearance between the angel wing top and the rotor platform was maintained.

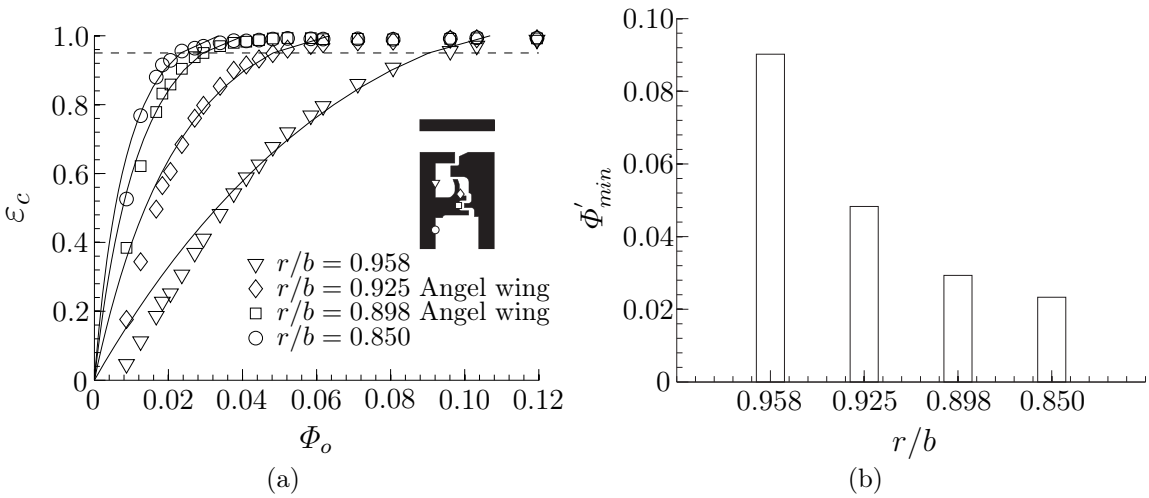

(a) (b)

FIG. 7.3-26: Experimental data for optimised seal; (a) Variation of ε_c with Φ_o at four sampling points; (b) Ranking of sampling points in terms of Φ'_{min}

The sampling point at $r/b = 0.958$ experiences the highest ingress level of all measurement points. There is a considerable reduction in terms of Φ'_{min} by $\approx 47\%$ at the next probe at $r/b = 0.925$ on the angel wing. The CFD results attribute this improvement to the disc pumping effect, the damped out circumferential pressure

variation and the fact that the fluid has been mixed-out with the cavity fluid before being ingested even further.

The lower sampling point on the angel wing shows a further improvement of the sealing effectiveness compared to the upper one. The strong viscous forces at the upper radial overlap combined with the upward pumped sealant prevent a migration of the ingress further inwardly. The concentration level at this sampling point and at $r/b = 0.85$ show almost identical behaviour. This confirms that the ingestion is contained in the upper part of the angel wing and migrate only at very low sealing flow rate into the wheel-space.

Fig. 7.3-27(a) compares the results of the concentration measurements between concept $C.4$ and optimised rim-seal. At the inner sampling point, i.e. $r/b = 0.850$, both seals show a similar profiles with a marginally worse sealing effectiveness for the optimised seal. At $r/b = 0.958$, the same trend is observed for $\varepsilon_c \prec 0.8$ but with increasing sealing effectiveness the optimised rim-seal experiences more ingress than concept 4.

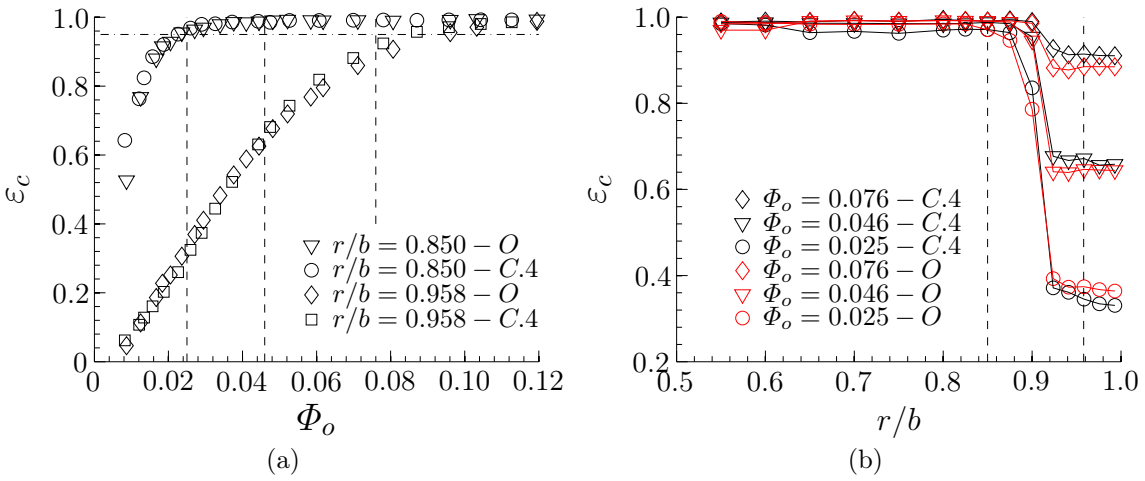

FIG. 7.3-27: Comparison of concept $C.4$ with the optimised rim-seal O; (a) Variation of ε_c with Φ_o at $r/b = 0.958$ and 0.850; (b) Variation of ε_c with the non-dimensional radius r/b for three sealing flow rates

Fig. 7.3-27(b) shows the variation of ε_c with the non-dimensional radius at three different flow rates between concept $C.4$ and the optimised seal (O). At higher radii, i.e. $r/b \succ 0.90$, $C.4$ experiences less ingress than the optimised seal with the exception of the lowest flow rate. At lower radii, i.e. $r/b \prec 0.90$, the sealing effectiveness is higher for the optimised rim-seal than for concept 4 at $\Phi_o = 0.25$. It should be noted that the sampling point at $r/b = 0.85$ for the sealing effectiveness curve in Fig. 7.3-27(a) was located in a region at which the fluid was not fully mixed-out as in contrast to $C.4$. This influences the sealing effectiveness curve whereby

the parameter Φ'_{min} gets distorted. To allow for a quantitative comparison of this parameter between both seals, the sampling point should be re-located in a region on the stator wall where the fluid is fully mixed-out. Owing to the tight testing schedule of the facility, it was not possible to repeat this test before submitting this thesis, hence the final assessment of this seal could only be done with the Φ'_{min} that is distorted to higher values.

Fig. 7.3-28 summarises all investigated rim-seals and ranks these in terms of Φ'_{min} for the inner sampling point at $r/b = 0.850$. The optimised rim-seal shows the same improvement as experienced by concept $C.2$ and $C.4$ with a reduction by $\approx 40\%$ compared to the baseline case. At the outer sampling point, however, the optimised seal experiences higher level of ingress than concept $C.2$ and $C.4$ but it still reduces Φ'_{min} by 6% to the baseline case. The increase of Φ'_{min} from concept $C.2$ and $C.4$ to the level seen by the optimised seal is unexpected as the angel wing geometry was unchanged and the concept study had shown a quasi independence of the insert combinations on Φ'_{min}.

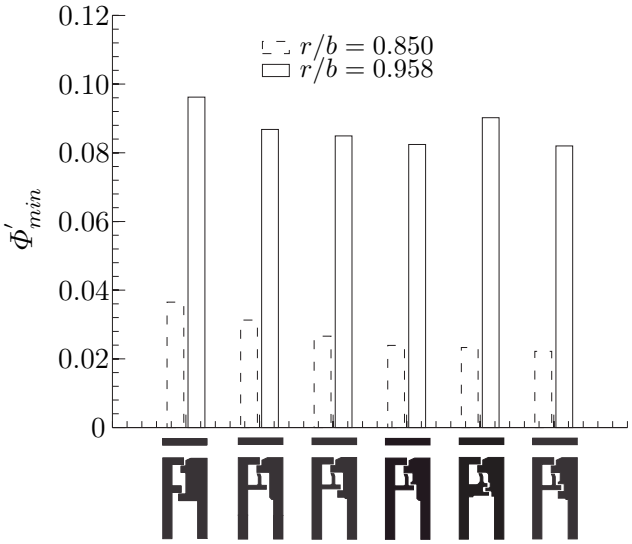

FIG. 7.3-28: Φ'_{min} of all tested rim seals at both $r/b = 0.958$ and 0.85

7.4 Summary

The proposed rim-seal design addresses the root cause of hot gas ingestion by attenuating the tangential pressure variation which reduces the ingress levels into the wheel-space by $\approx 40\%$ relative to the baseline design. There remains an unanswered question which could not be addressed during this work. What is the optimal size and shape of the cavity surrounded by the angel wing to attenuate the tangential pressure variation most effectively and what are the implications on the heat transfer of the surrounding metal components? The CFD modelling approach captured

the rim-seal mechanics correctly and it turned out that this is a promising approach to develop new rim-seal designs.

Chapter 8

Egress-Mainstream Interaction

This chapter discusses the aerodynamic interaction of the egress with the primary gas path flow. This numerical investigation focuses on the first stage of the high pressure turbine of an industrial gas turbine, with the objective to minimise the aerodynamic interactions of both the re-emerging hot gas ingestion and the sealing leakage flow from the rotor-stator system with the primary gas path flow, through a combination of a better primary gas path platform configuration and a controlled sealing leakage path configuration above the seals.

8.1 Introduction

This section covers the fundamental fluid mechanics in a rotor blade passage, the mechanisms that are associated with the secondary flow losses and it reviews the literature on the egress-mainstream interaction.

Fig. 8.1-1 shows the principle aerodynamics in a rotor passage with an idealised incoming boundary layer in the absence of any upstream ejected sealing leakage flow. This boundary layer stagnates at the aerodynamic leading edge and rolls up in front of it (owing to pressure imbalances) to create the horseshoe vortex, i.e. one vortex on the suction side and one rotating structure on the pressure side of the rotor aerofoil. The pressure gradient induced by the low static pressure of the suction side and the high pressure of the pressure side forces the flow field to migrate towards the suction side of the aerofoil as shown in Fig. 8.1-1(c). Together with the horseshoe vortex of the pressure and suction side, the crossflow forms the passage vortex at the trailing edge of the aerofoil with one or more loss cores, i.e. regions with significant total pressure drop.

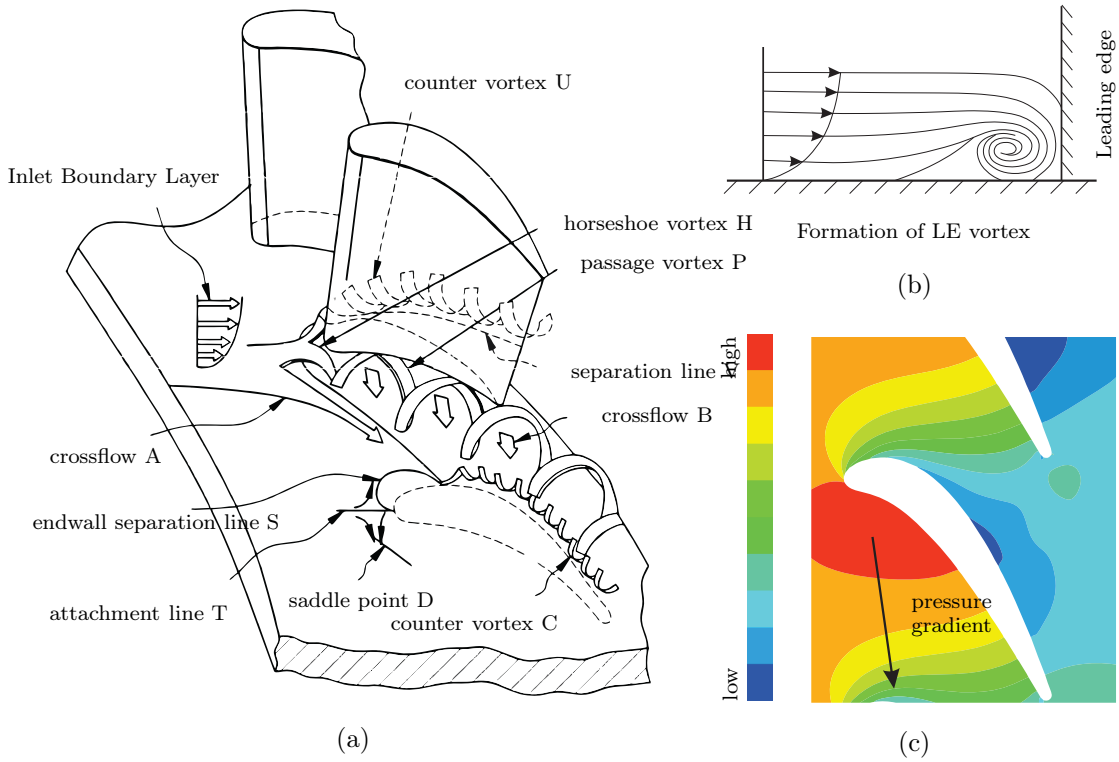

FIG. 8.1-1: Principle aerodynamics in a rotor passage; (a) secondary flow loss mechanism (adapted from Harvey et al. (2008)); (b) Boundary layer roll-up (Sieverding, 1984); (c) static pressure field

Bancalari (2000) introduced what he refers to as a leading edge vortex elimination device with the intent to overcome or eliminate the resultant radial force which acts on the streamline in front of the leading edge of the rotor aerofoil.

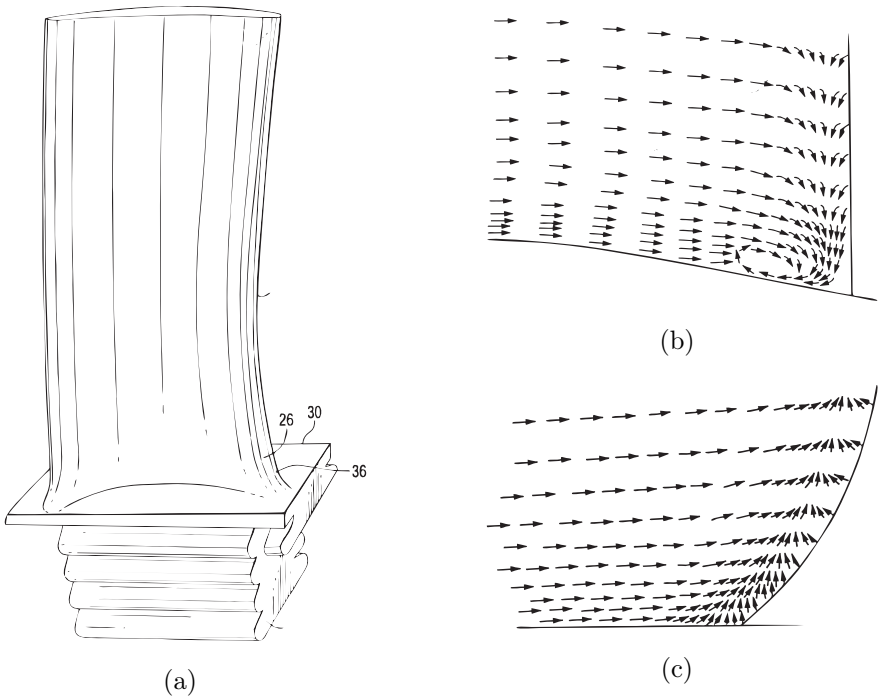

FIG. 8.1-2: Leading edge vortex elimination device (Siemens Westinghouse - (Bancalari, 2000))

Fig. 8.1-3 shows the radial pressure balance of a conventional and his own curvilinear shaped leading edge. The curved feature introduces an additional radial component and if the magnitude is sufficient this balances out the component of the stagnated flow, thus preventing the roll-up of the boundary layer and hence minimising the horseshoe vortex as the streamline passes the leading edge.

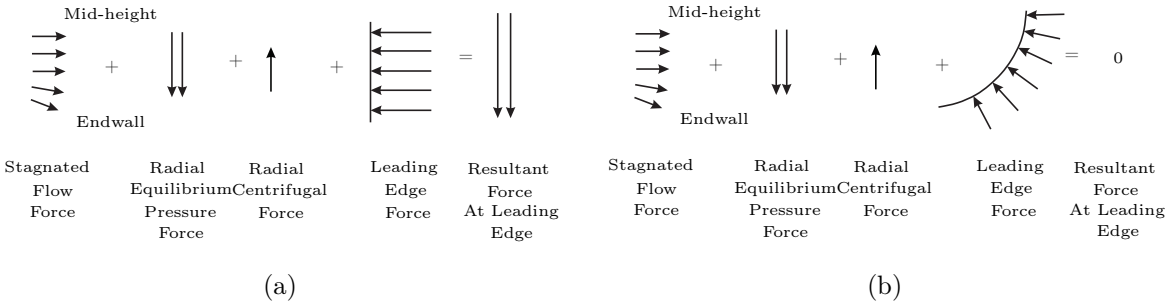

(a) (b)

Fig. 8.1-3: Radial pressure balance in front of the leading edge for the ((Bancalari, 2000)): (a) conventional platform; (b) vortex elimination device

To obtain a more favourable pressure gradient in the rotor passage to reduce the cross-passage flow, Lee (2006) introduced a contoured endwall platform with a fillet extending between the leading and the trailing edge on the pressure side of the aerofoil. Fig. 8.1-4 shows this endwall with its fillet peaking near the mid-chord. To raise the static pressure on the suction side of the aerofoil, Lee (2006) incorporated a bowl of semicircular shape which is centred behind the raised fillet on the pressure side. This concept of lowering and raising the endwall in the rotor blade passage is known as endwall contouring, with Fig. 8.1-4 showing one example of it. More variants of these contours were published by Harvey et al. (2008); Sakamoto et al. (2010) and Beeck (2013).

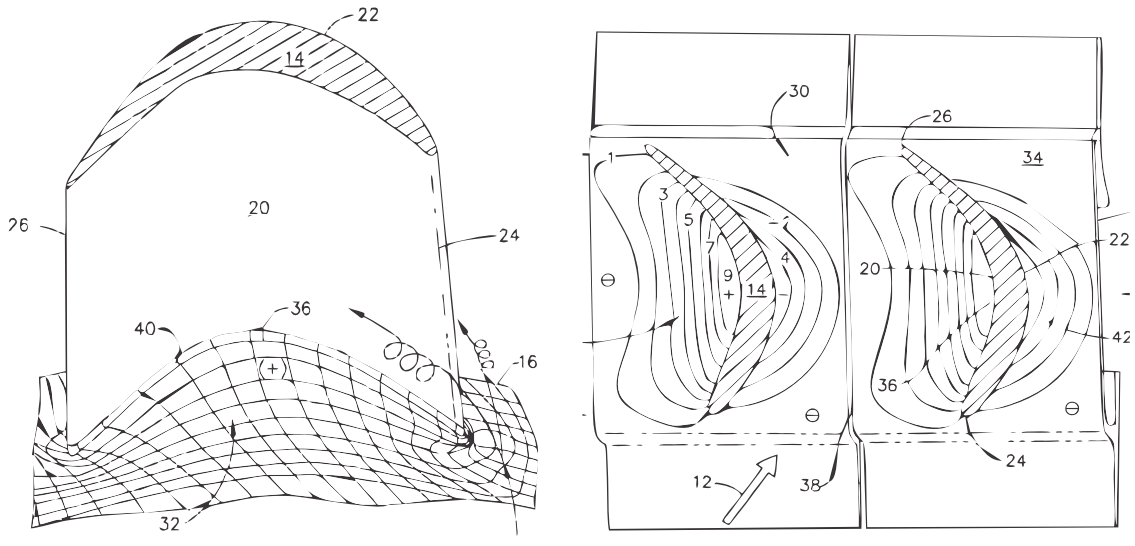

(a) (b)

Fig. 8.1-4: Rotor passage endwall contouring (Lee, 2006)

Popovic and Hodson (2012a,b) investigated various rim-seal configurations and their effect on the turbine stage efficiency and the sealing effectiveness in a large-scale linear cascade. Fig. 8.1-5 shows this rig being equipped with six low-speed aerofoil profiles (T120) and a secondary air leakage injector fitted to control independently the leakage fraction and swirl ratio.

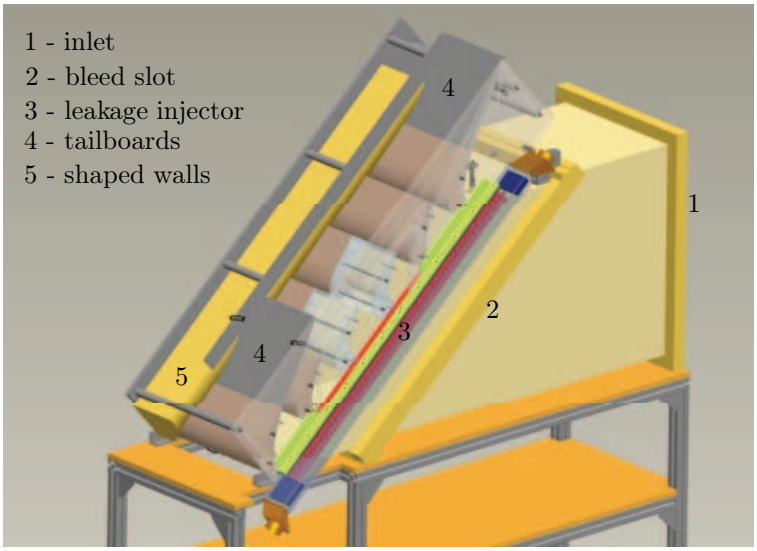

FIG. 8.1-5: Linear large-scale cascade to investigate various rim-seal configurations and the effect on the sealing effectiveness and the turbine stage efficiency (Popovic and Hodson, 2012a,b)

Fig. 8.1-6(a) summarises the rim-seals investigated, where $C2$ to $C4.1$ are as commonly used in industrial practice whereas $C5.4$ was derived during the study as an improved configuration. Fig. 8.1-6(b) shows the variation of the loss coefficient and the sealing effectiveness as variation of the leakage fraction where the sealing effectiveness was defined as

$$\eta_S = \frac{C_{Seal}}{C_L} \tag{8.1-1}$$

where C_{Seal} is the Ethylene concentration at a control plane underneath the rim-seal and C_L is the concentration in the cavity. The loss coefficient is given by:

$$Y = \frac{P_{01,EFF} - P_{02}}{P_{01,REF} - P_2} \tag{8.1-2}$$

where

$$P_{01,EFF} = \frac{\dot{m}_1 P_{01,REF} + \dot{m}_L P_{0,CAV,REL}}{\dot{m}_1 + m_L} \tag{8.1-3}$$

and $P_{01,REF}$ refers to the average freestream total pressure upstream of the

aerofoil and $P_{0,CAV,REL}$ is the average total pressure in the cavity underneath the control plane. The mass flows $\dot{m}_1$ and $\dot{m}_L$ refer to the mainstream and leakage flow rates respectively.

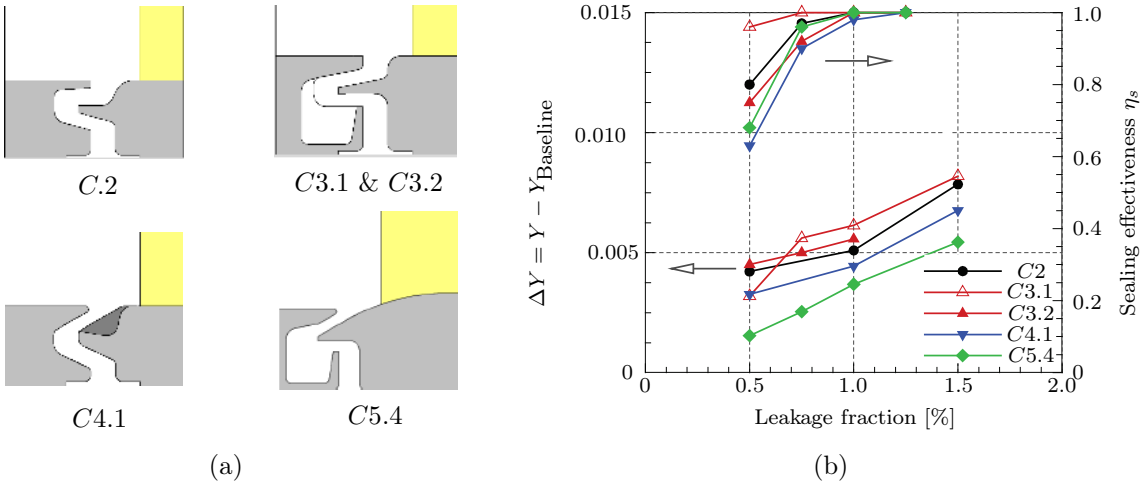

FIG. 8.1-6: Experimental investigation of various rim-seal configurations (Popovic and Hodson, 2012a,b); (a) Seal configurations ($C3.1$ with cavity and $C3.2$ without cavity); (b) variation of the loss coefficient and the sealing effectiveness with leakage fraction

The best performing rim-seal in terms of sealing effectiveness is $C3.1$ with the incorporated cavity. This result is consistent with the findings presented in Chapter 7 where a similar cavity geometry attenuates effectively the driving mechanism for EI ingress. $C5.4$ shows the lowest loss coefficient across the sealing flow rates with improvements of about 33% compared to the baseline $C2$. However, this benefit is at the expense of a dramatic loss in seal performance. The difference between $C3.1$ and $C5.4$ is only the configuration above the rotor seal lip, yet it shows the importance not only in terms of the aerodynamic loss but also in terms of the seal performance.

Zlalinov et al. (2011) used the concept of entropy generation rate per unit volume to gain insight into the quantitative spatial distribution of the entropy.

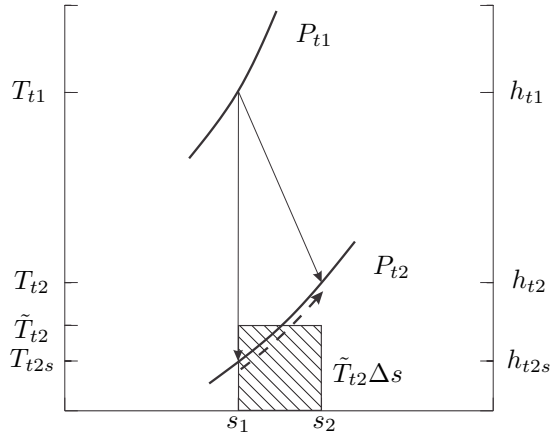

$$w_{loss} = h_{t2} - h_{t2s} \tag{8.1-4}$$

$$= \int_1^2 dh_t \tag{8.1-5}$$

$$= \int_1^2 T_t ds - \cancelto{0}{v dP_t} \tag{8.1-6}$$

$$= \tilde{T}_{t2}\Delta s \tag{8.1-7}$$

FIG. 8.1-7: Lost opportunity to do work owing to non-isentropic expansion (Zlalinov et al., 2011)

Fig. 8.1-7 shows that the entropy can be related to the lost opportunity to do work in the turbine owing to irreversible processes, i.e. viscous mixing. Zlalinov et al. (2011) give the general formation for the steady-state conservation equation for the entropy quantity with convection, diffusion and source terms as follows:

$$\underbrace{\iint_A \rho s \vec{V} d\vec{A}}_{\text{convection}} - \underbrace{\iint_A \frac{q_{in}}{T} dA}_{\text{diffusion}} = \underbrace{\iiint_V \dot{S}'''_{gen} dV}_{\text{source term}} \tag{8.1-8}$$

The convection and diffusion terms of Eq. 8.1-8 account for the entropy that is generated within the control volume.

Greitzer and Tan (2004) showed that the volumetric source term, $\dot{S}'''_{gen}$, consists of two components, i.e. the viscous and the thermal dissipations as given by Eq. 8.1-9.

$$\dot{S}'''_{gen} = \dot{S}'''_{visc} + \dot{S}'''_{therm} \tag{8.1-9}$$

Volumetric source term = viscous dissipation + thermal dissipation

where

$$\left(\dot{S}'''_{gen}\right)_{therm} = \frac{k_{eff}}{T^2}\left(\frac{\partial T}{\partial x_i}\right)^2$$
$$= \frac{k_{eff}}{T^2}\left[\left(\frac{\partial T}{\partial x}\right)^2 + \left(\frac{\partial T}{\partial y}\right)^2 + \left(\frac{\partial T}{\partial z}\right)^2\right] \quad (8.1\text{-}10)$$

$$\left(\dot{S}'''_{gen}\right)_{visc} = \frac{1}{T}\tau_{ij}\frac{\partial u_i}{\partial x_j}$$
$$= \frac{1}{T}\left[\mu_{eff}\left(\frac{\partial u_i}{\partial x_j} + \frac{\partial u_j}{\partial x_i}\right) + \lambda_{eff}\frac{\partial u_k}{\partial x_k}\delta_{ij}\right]\frac{\partial u_i}{\partial x_j}$$
$$= \frac{\mu_{eff}}{T}\left(2\left[\left(\frac{\partial u_x}{\partial x}\right)^2 + \left(\frac{\partial u_y}{\partial y}\right)^2 + \left(\frac{\partial u_z}{\partial z}\right)^2\right] + \left(\frac{\partial u_x}{\partial x_z} + \frac{\partial u_z}{\partial x_x}\right)^2\right.$$
$$\left. + \left(\frac{\partial u_x}{\partial x_y} + \frac{\partial u_y}{\partial x_x}\right)^2 + \left(\frac{\partial u_y}{\partial x_z} + \frac{\partial u_y}{\partial x_y}\right)^2 - \frac{2}{3}\left(\frac{\partial u_x}{\partial x} + \frac{\partial u_y}{\partial y} + \frac{\partial u_z}{\partial z}\right)^2\right) \quad (8.1\text{-}11)$$

where $k_{eff} = k + C_P\mu_{eff}/Pr_t$, $\mu_{eff} = \mu + \mu_{eddy}$ and $\lambda = -2/3\mu_{eff}$

$\dot{S}'''_{gen}$ is a useful tool to trace the turbine losses induced by the viscous and thermal dissipation, and Zlalinov et al. (2011) used this to relate these losses to the flow structures in the rotor passage owing to the secondary flows and the egress-mainstream interaction. Fig. 8.1-8 shows a contour plot of $\dot{S}'''_{visc}$ for several planes along a rotor blade. It can be seen that the losses induced by the rotor blade tip, becomes the dominant loss source at $C_{ax} \succ 0.5$. It should be noted that Zlalinov et al. (2011) only considered $\dot{S}'''_{visc}$ instead of $\dot{S}'''_{gen}$, as the thermal mixing is not a loss with respect to the turbine but rather with respect to the cycle.

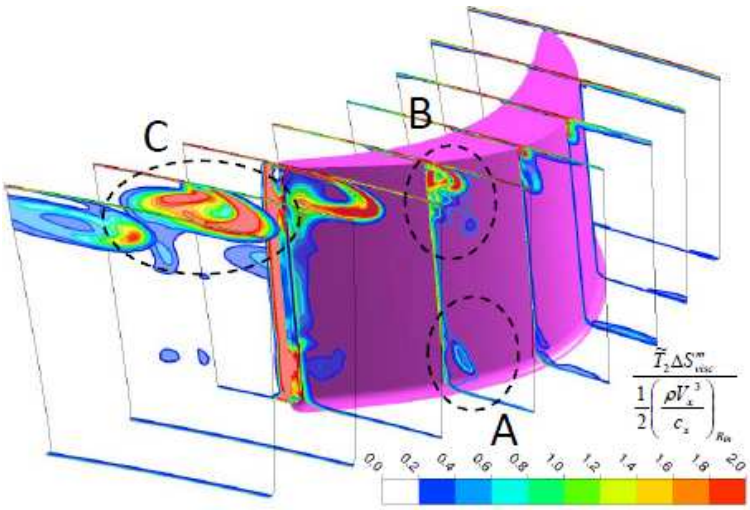

FIG. 8.1-8: Contour plot of the entropy generation per unit volume for several axial planes along the rotor blade passage (Zlalinov et al., 2011)

8.2 Computational Model

The present egress-mainstream interaction study was conducted with the CFD model which was described in Chapter 7. ICEM 13.0 was used to create the structured topology of the contoured endwalls with a hexahedral mesh with a $y^+ \approx 10$. Fig. 8.2-9 shows the mesh for a non-axisymmetric hub contour.

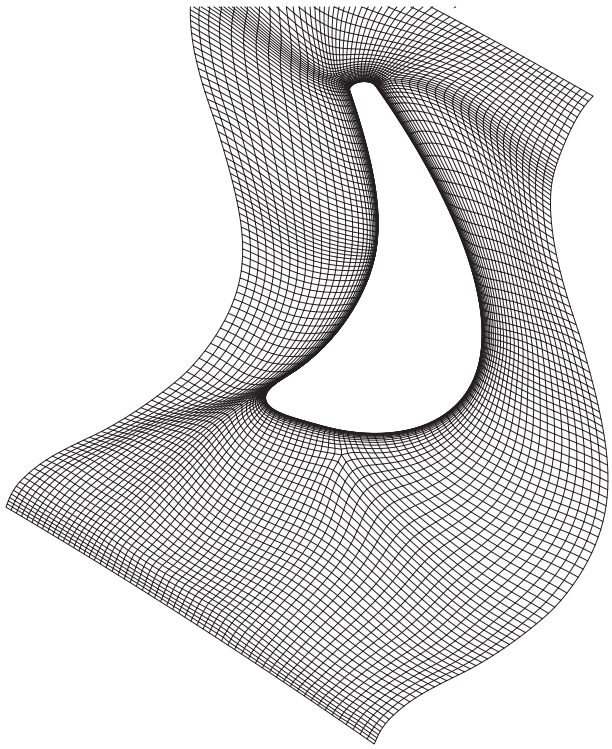

Fig. 8.2-9: Hub mesh for the 3D contour

This study was conducted with a wheel-space sealing flow leakage fraction of 1% of the mainstream flow rate. This leakage was applied as a massflow boundary at the wheel-space sealant inlet and remained constant throughout this study.

8.3 Aerodynamic Endwall Concepts

The egress-mainstream interaction was investigated with two types of endwall configurations: axisymmetric and non-axisymmetric contours. The latter has been derived as a result of the first study and is described in detail below.

8.3.1 Axisymmetric Concepts

The objective of this study was to investigate the effect of the axisymmetric endwall concepts on the leading edge loading and its influence of the upstream located wheel-

space. This was attempted first by introducing a convex axisymmetric feature as shown in Fig. 8.3-10 with its highest radial extent aligned with the leading edge of the rotor blade, with its peak values of 3.5%, 6.5% and 10% of the rotor blade span. Furthermore, a concave feature was introduced with its lowest radial extent also aligned with the leading edge of the blade with a corresponding value of 6.5% of the blade span.

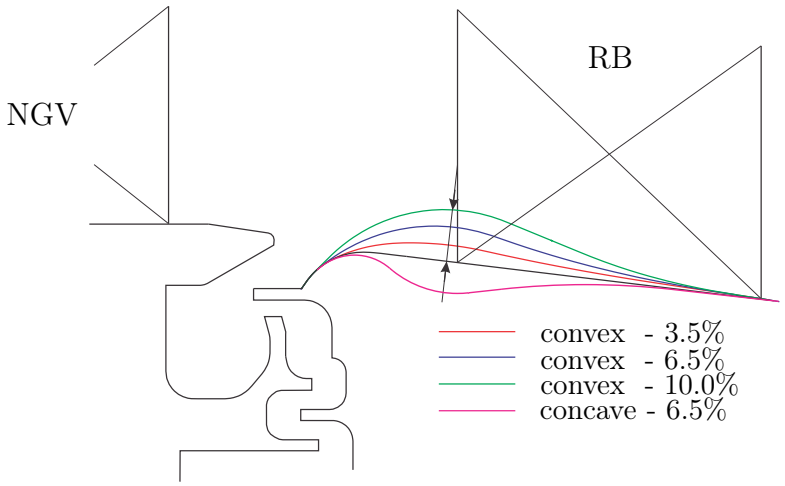

FIG. 8.3-10: Axisymmetric rotor endwall concepts

Fig. 8.3-11 shows the effect of the convex and concave concepts on the blade loading and the isentropic Mach number in the near endwall region at 5% span. All convex platforms show a drop in static pressure on the suction side near the leading edge induced by the acceleration of the fluid due to the contracted passage area. The concave platform causes the fluid to decelerate on the suction side of the aerofoil resulting in an increase of the static pressure, whereby the leading edge loading of the aerofoil is reduced. None of the concepts were found to influence substantially the static pressure distribution on the pressure side of the aerofoil.

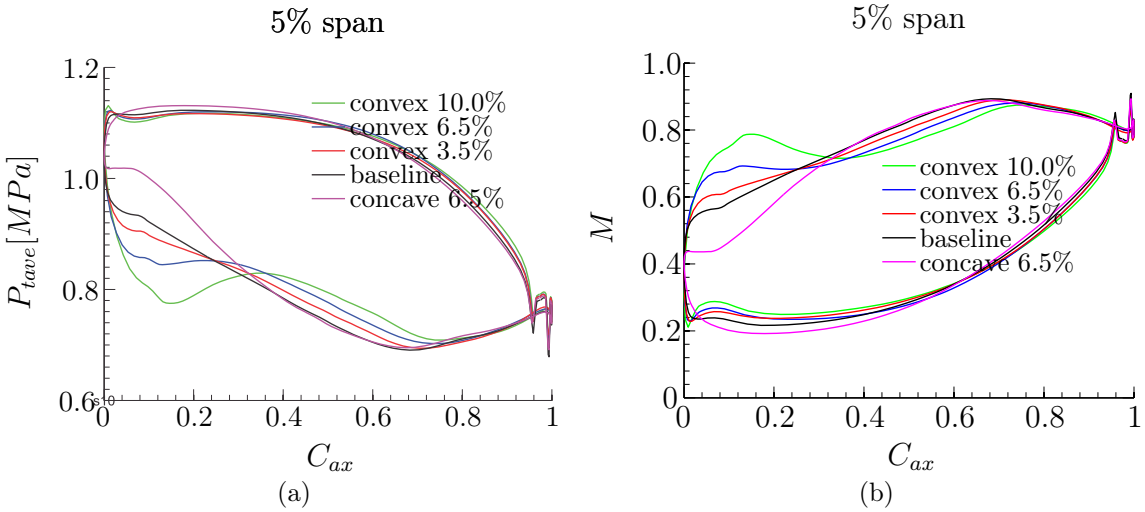

FIG. 8.3-11: Effect of the endwall concepts on the aerofoil at 5% blade span (time and pitchwise-averaged); (a) blade loading; (b) isentropic Mach number

At 15% span (Fig. 8.3-12), the same trend is observed as at 5% but the effect of the endwall diminishes with increasing span fractions and was found to collapse onto the baseline profile at around 25% blade span. It can be seen that only the concave endwall concept has achieved the objective of reduced blade loading in the leading edge regions towards the endwall platform.

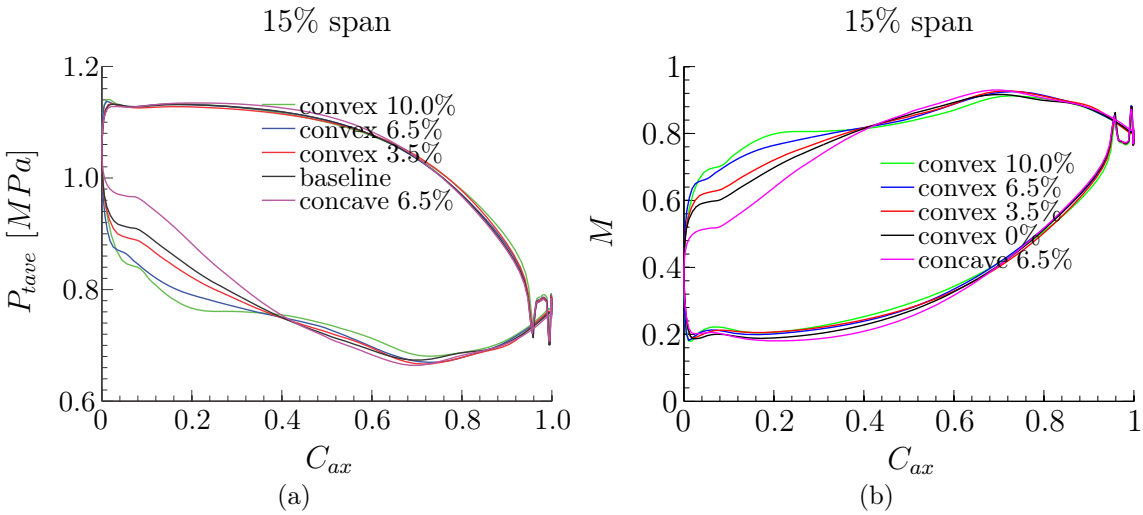

FIG. 8.3-12: Effect of the endwall concepts on the aerofoil at 15% blade span (time and pitchwise-averaged); (a) blade loading; (b) isentropic Mach number

Fig. 8.3-13 shows the circumferential time-averaged static endwall pressure in the stationary frame of reference upstream of the leading edge of the rotor blade. The circumferential pressure variation for the convex concept (here only the 6.5% case is shown but the cases with 3.5% and 10% follow the same behaviour) was off-set to higher pressure whereas the concave feature was off-set to lower pressure compared to the baseline case. The off-set to higher pressure of the convex concepts in particular is critical as more sealing flow would be required to purge the wheel-space and hence force stronger egress-mainstream interactions owing to increased egress flow. No negative impact was observed on the pressure distribution for the concave concept.

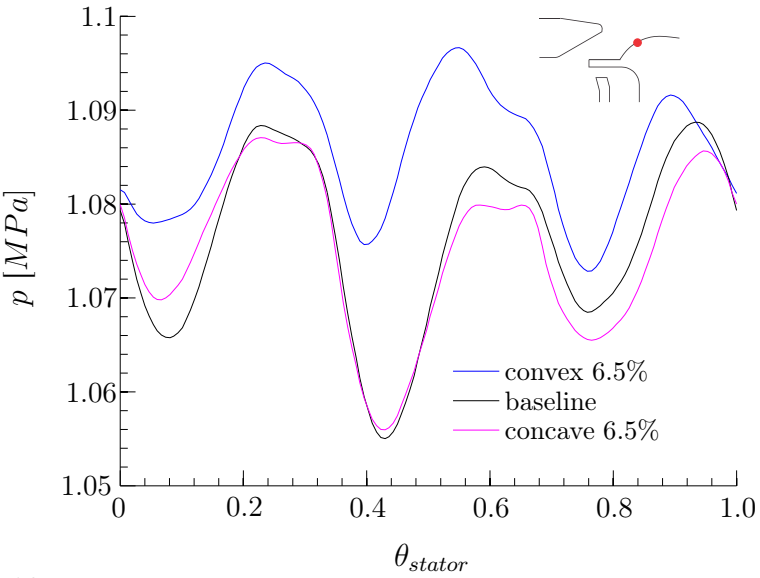

FIG. 8.3-13: Circumferential pressure variation for three endwall contours (time-averaged; across 3 stator vanes)

As shown in Fig. 8.3-14, the circumferential average static pressure in front of the convex features have been increased considerably compared to the baseline case, while the concave feature does not influence the pressure levels upstream.

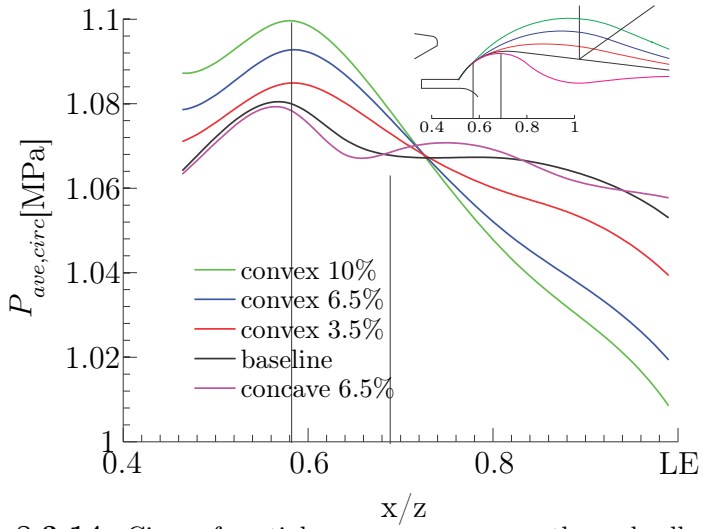

FIG. 8.3-14: Circumferential average pressure on the endwall contours

Fig. 8.3-15 shows the effect of the endwall concepts on the upstream wheel-space in terms of the sealing effectiveness. It was necessary to reduce the sealant flow for this impact study from 1% leakage fraction to 0.5% in order to obtain any ingress into the wheel-space with this rim-seal design. The convex feature forces a drop in sealing effectiveness by the off-set of the circumferential pressure variation to higher pressure compared to the baseline whereas the opposite behaviour was observed for the concave endwall, however this benefit is marginal.

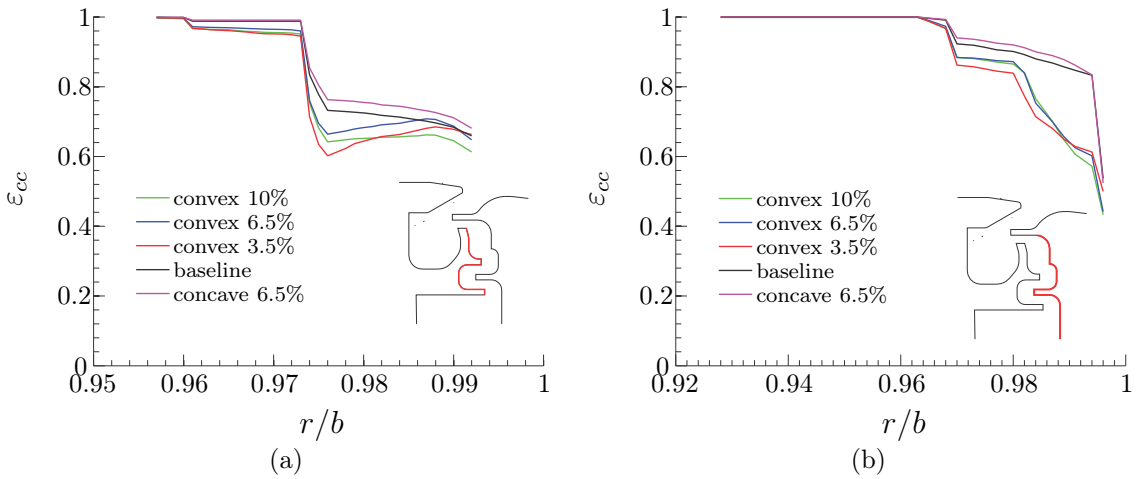

FIG. 8.3-15: Effect of the endwall concepts on the variation of sealing effectiveness ε with r/b; (a) stator wall; (b) rotor wall

For all axisymmetric endwall configurations investigated only the concave endwall seemed to effectively decrease the leading edge loading without negatively impacting the upstream wheel-space. This contour has been further developed into a 3D design (in several iterations) with various design features. The final concept is discussed in the subsequent section.

8.3.2 Non-Axisymmetric Concept

This section discusses the non-axisymmetric endwall configuration which is referred to it as 3D design. This design was directly derived from the study with the axisymmetric endwalls and the numerical investigation of the rim-seal concepts described in Chapter 7.

Fig. 8.3-16 shows the three-dimensional nature of this endwall contour with incorporated elongated leading edge feature, contoured rotor blade passage and egress channel to control the discharged leakage flow from the upstream wheel-space into the primary gas path.

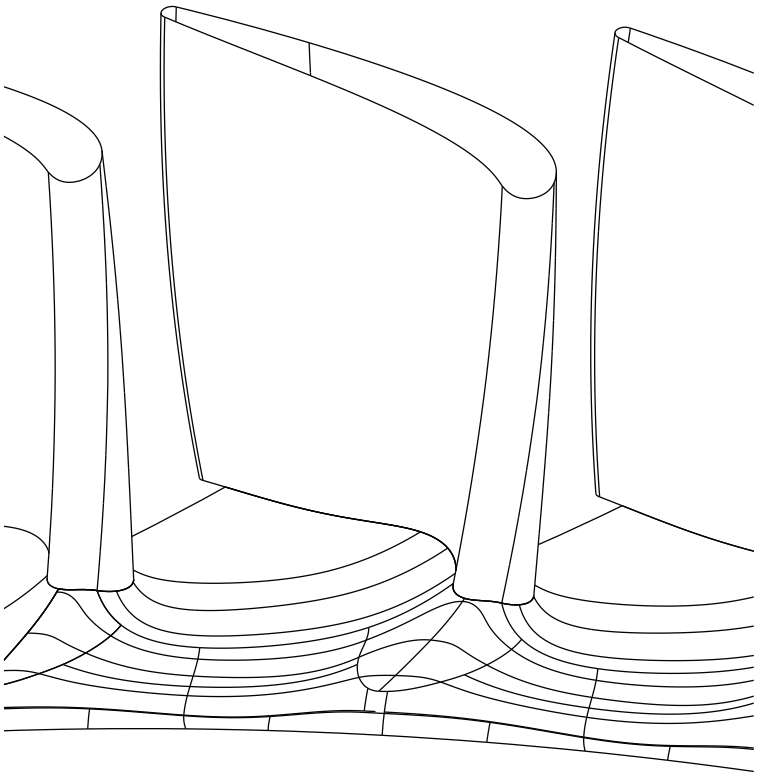

Fig. 8.3-16: 3D design with elongated leading edge feature, contoured blade passage and an egress channel

Fig. 8.3-17 shows the elongated leading edge feature being aligned with the metal blade angle with its highest radial extent at the aerodynamic leading edge with 12.5% of the rotor blade span. This feature extends upstream and merges with the rotor platform in the rim-seal region. On the downstream side, this feature extends into the blade passage on the pressure side and levels out in front of the trailing edge of the aerofoil.

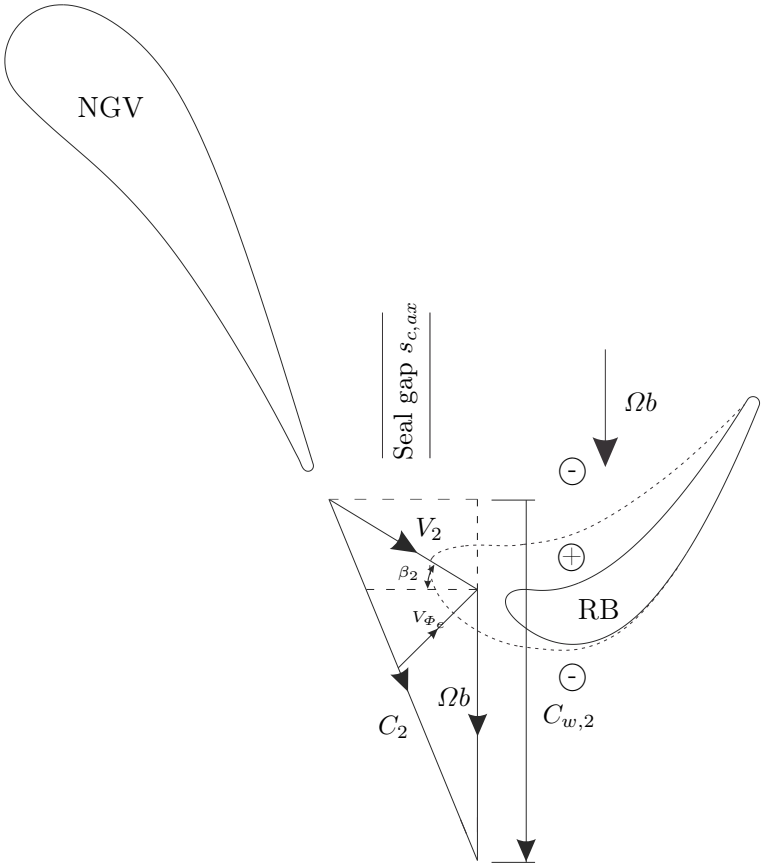

Fig. 8.3-17: Alignment of elongated leading edge feature with the metal blade angle

Fig. 8.3-18(a) shows the circumferential variation of the static pressure in form of the pressure coefficient C_p in the rotating frame mid-way between the seal region and the LE of the blade on the conventional rotor endwall. This time- and spatially averaged profile shows its trough at $\theta_{rotor} \approx 0.30$ where θ is the non-dimsionalised rotor pitch. Fig. 8.3-18(b) shows a line located between the two aerofoils with strong bias towards the suction side which marks the position of a channel path incorporated into the endwall with its lowest radial extent aligned with the leading edge with $\approx 6.5\%$ of the blade span. This channel starts within the seal region at $\theta \approx 0.32$ and it merges with the conventional endwall in front of the aerofoil throat plane to ensure an unaltered swallowing capacity through the turbine.

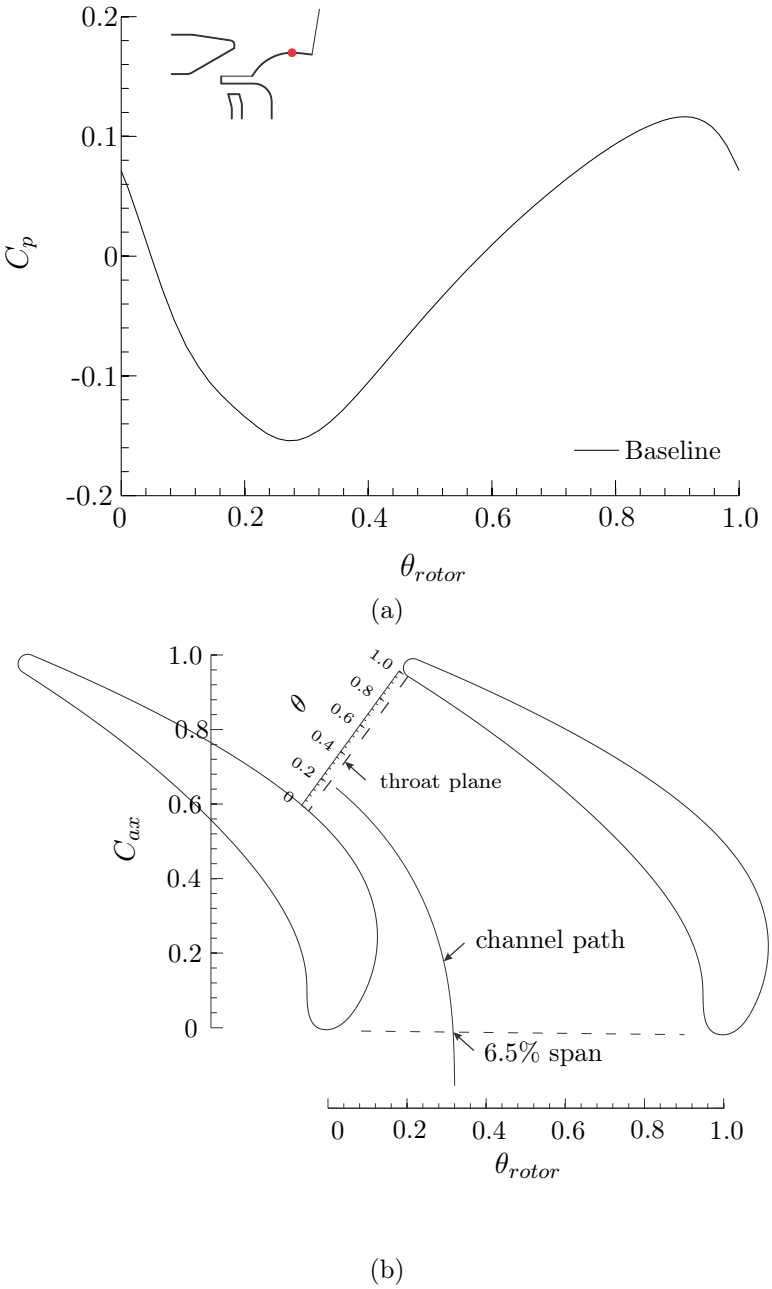

Fig. 8.3-18: 3D design with incorporated egress channel into the endwall; (a) variation of C_p with θ in rotating frame of reference; (b) egress channel

The combination of the channel on the suction side and the raised leading edge feature, extended into the blade passage on the pressure side of the aerofoil, induces a more favourable pressure gradient in the rotor passage to minimise the cross-passage flow.

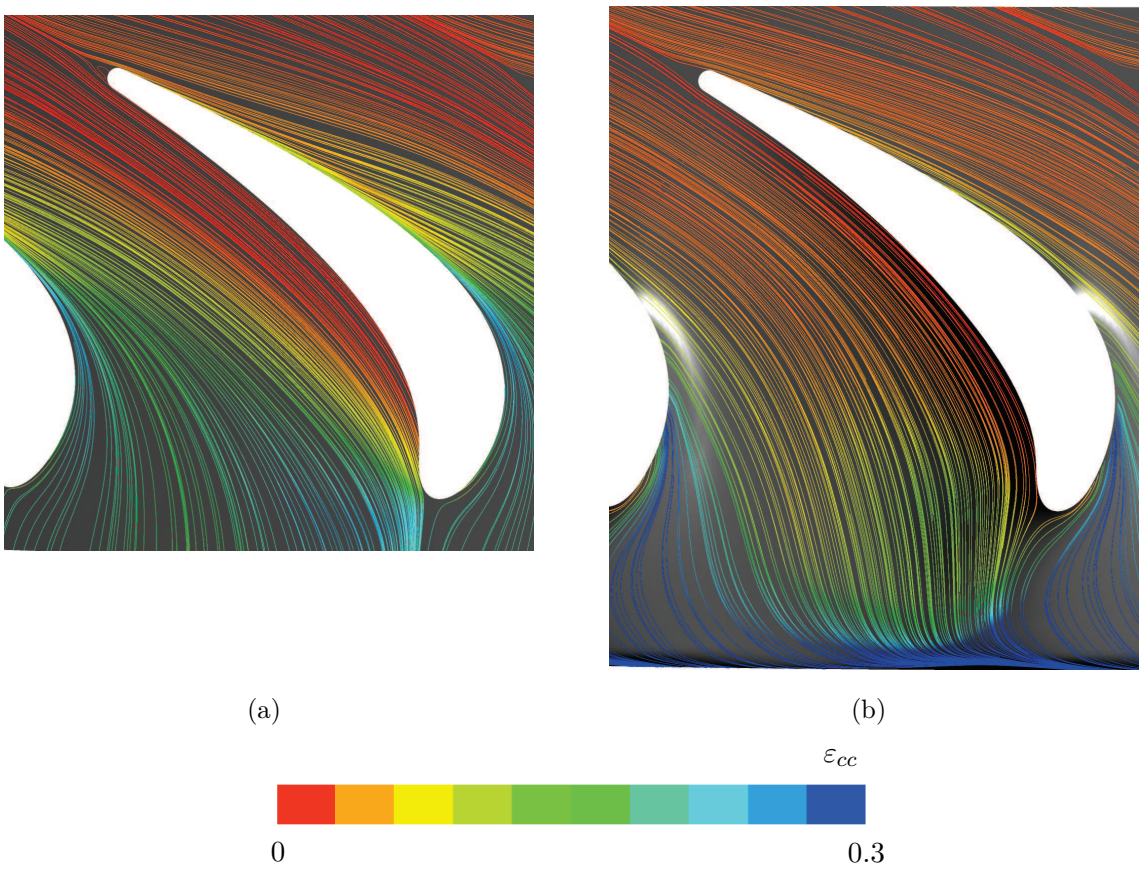

FIG. 8.3-19: Time-averaged streamlines at 4% span coloured with the sealing effectiveness; (a) Baseline; (b) 3D design

Fig. 8.3-19 shows time-averaged streamlines in the near endwall region at 4% span for the baseline case and the 3D design. The streamlines concentrate on the LE of the pressure side for the conventional platform followed by a strong migration of the flow across the rotor passage towards the suction side. The 3D design distributes the flow streamlines more evenly across the passage, without any local concentrations, following the curvature of the aerofoil with little migration towards the suction side. The coloured streamlines show the sealing effectiveness where 1.0 refers to pure unmixed wheel-space leakage flow and 0 to uncontaminated mainstream flow. The highest levels of ε are observed for the 3D design within the egress channel at $\theta \approx 0.3$ whereas the baseline design experiences lower levels, indicating more mixing of the leakage flow with the mainstream flow for the baseline case.

The effect of the leading edge feature on the formation of the horseshoe vortex is compared to the baseline design in Fig. 8.3-20. The boundary layer downstream of the seal region consists of the egress flow discharged from the upstream wheel-space and the main gas path flow. This layer was seeded with time-averaged streamlines initiated upstream of the LE of the rotor blade. The baseline case shows the low momentum boundary layer rolling up in front of the leading edge and being swept across the rotor passage towards the suction side of the aerofoil. The LE

feature introduces a radial force and hence a radial velocity component, guiding the approaching stagnating flow away from the leading edge/endwall intersection to prevent the roll-up of the low momentum boundary layer near the wall, hence eliminating or minimising the formation of the LE horseshoe vortex.

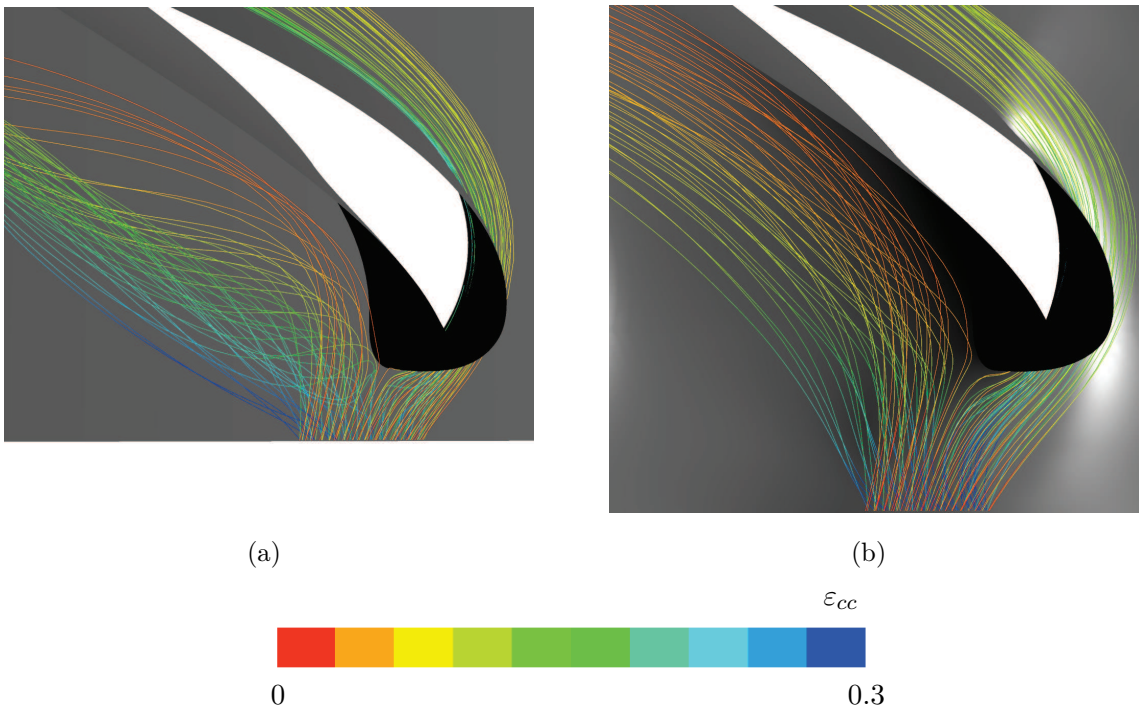

FIG. 8.3-20: Influence of the leading edge feature on the horseshoe vortex; (a) baseline case; (b) 3D design

Fig. 8.3-21 shows time-averaged surface streamlines for the hub and the rotor aerofoil for the baseline case and the 3D design. Fig. 8.3-21(a) shows a strong cross passage flow starting perpendicular to pressure side of the aerofoil near the leading edge and migrating towards the suction side of the aerofoil. The cross passage flow aligns more with the flow direction further downstream in the rotor passage but still has a strong bias towards the suction side. The 3D design shows a weaker cross passage flow owing to a more favourable pressure gradient. The saddle point, visualised by the black dot, moves closer to the aerofoil LE from ≈1.3 to ≈0.4 of the leading edge diameter which is evidence of a weaker horseshoe vortex.

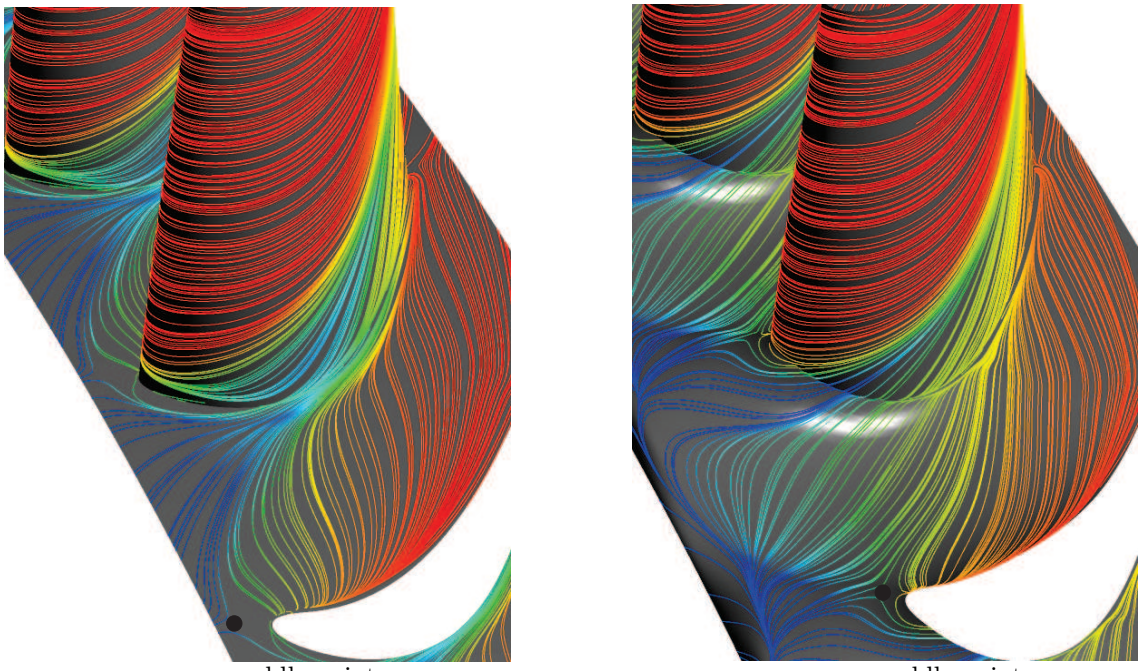

(a) (b)

FIG. 8.3-21: Surface streamlines for the; (a) baseline case; (b) 3D design

The reduction in cross-passage flow by the 3D design influences the radial velocity component in the rotor passage as shown in Fig. 8.3-22. This figure depicts the time and pitchwise-averaged radial velocity at 25% span at mid-chord and the trailing edge for the baseline case and the 3D design. Fig. 8.3-22(a) shows similar velocity profiles at mid-chord with the exception of the slightly increased peak value for the 3D design near the suction side surface. However, the 3D design produces reduced radial velocity towards the suction surface at the trailing edge plane, indicating a weaker cross-passage secondary flow.

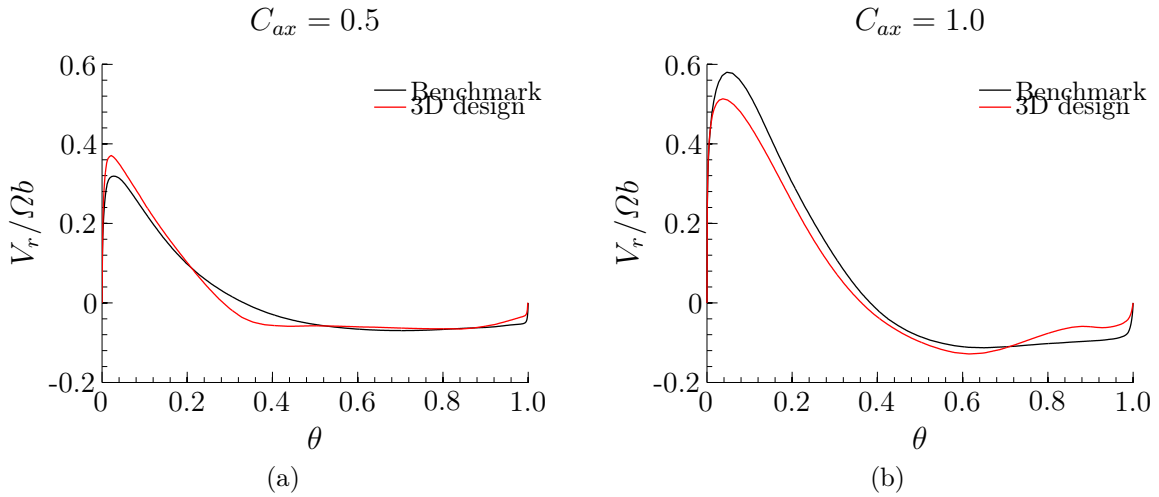

(a) (b)

FIG. 8.3-22: time- and pitchwise circumferential average of radial velocity profiles at 25% span; (a) $C_{ax} = 0.50$; (b) $C_{ax} = 1.0$

Fig. 8.3-23 shows the effect of the 3D endwall on the upstream wheel-space in terms of sealing effectiveness. The 3D design has no negative impact on the wheel-space by higher ingress levels as was seen for the axisymmetric convex platforms.

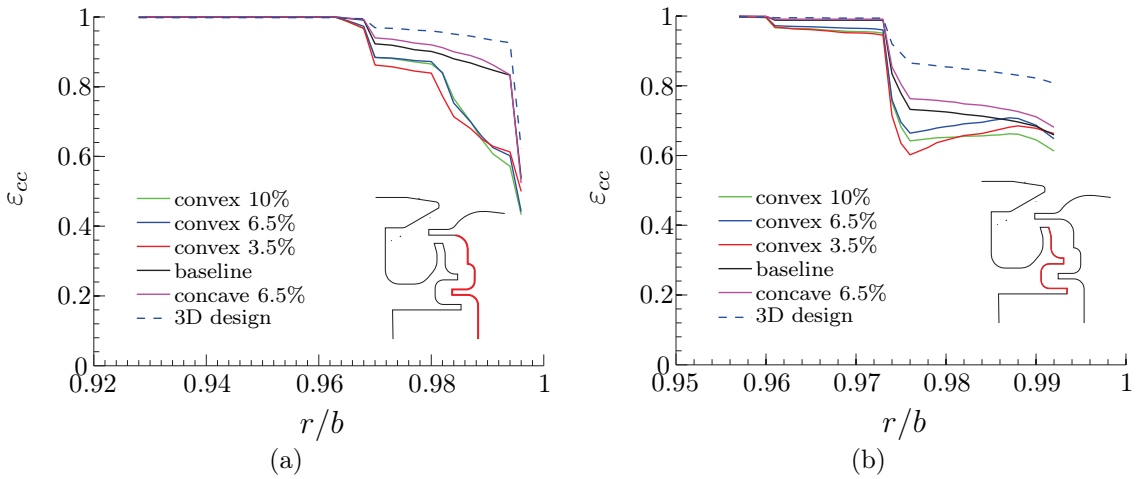

FIG. 8.3-23: Effect of the sealing effectiveness ε_{cc} as variation of the non-dimensional radius r/b for the inner wheel-space; (b) rotor wall; (a) stator wall

Fig. 8.3-24 shows the entropy generation per unit volume plotted on several axial planes across the rotor passage for the baseline and the 3D design. The scale for this plot was clipped to a lower limit of 0.2 and an upper bound of 1. The first axial plane downstream of the rim-seal shows a region of high entropy with concentration level beyond 1 for the baseline case. This accumulation of entropy was caused by a thick shear layer formed between the rotating wall, the egress flow with a swirl ratio of ≈ 0.7 and the mainstream flow with $\beta \succ 1$. This difference in tangential velocity, shown in Fig. 8.3-17, is attenuated in the shear layer shown in Fig. 8.3-24(a) which contributes to the high entropy concentration.

The combination of the elongated leading edge feature and the egress channel allows the egress flow to join the primary gas path flow in a controlled way with a reduced mixing zone and lower entropy generation intensity as shown in Fig 8.3-24(b). Fig. 8.3-25 shows the interaction of the egress flow with the main gas path flow with illustrative streamlines for the baseline case and the 3D design for the peak egress case. For the baseline case, the mainstream flow is displaced radially outward by the discharged egress flow. In the 3D design, the alignment of the endwall channel with the circumferential pressure trough ensures that the peak egress flow is ejected into this trench with a lower radially outward velocity component, minimising the interaction with the mainstream flow.

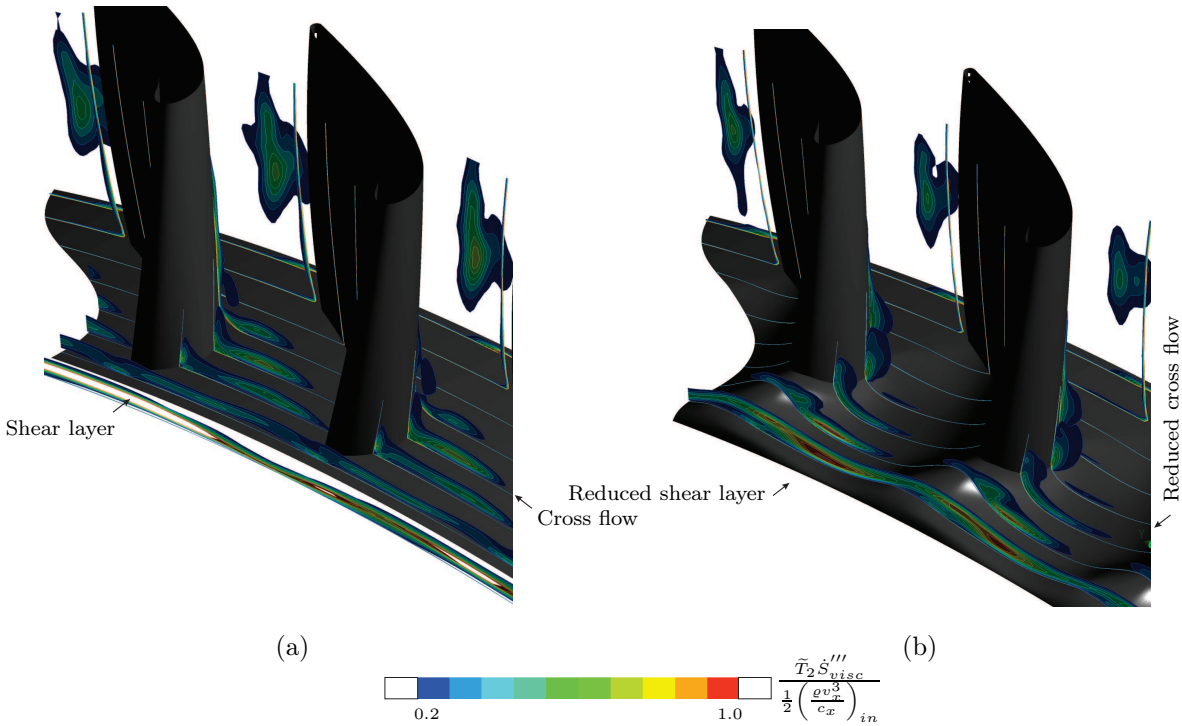

FIG. 8.3-24: Contour plot with generated entropy per unit volume; (a) baseline case; (b) 3D design

Fig. 8.3-24(a) shows an intense shear layer in the rotor passage for the baseline case owing to the unfavourable pressure gradient that drives the cross passage flow. The more favourable pressure gradient in the 3D design due to the increase of the static pressure on the suction side of the aerofoil reduces the entropy generation to only the suction side of the aerofoil.

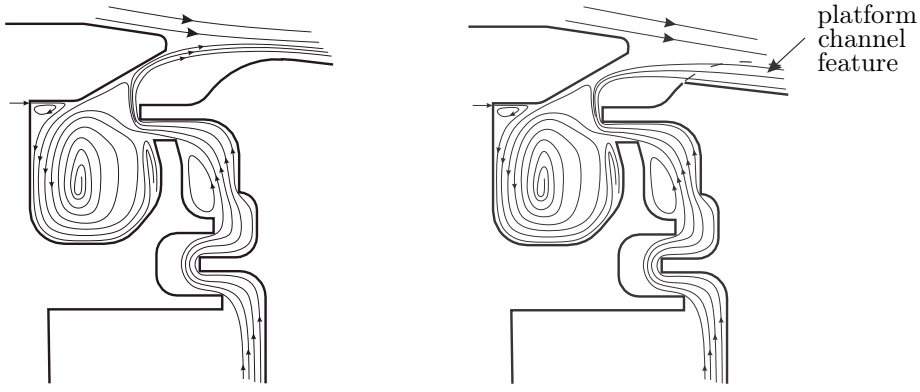

FIG. 8.3-25: Illustrative streamlines for peak egress case; (a) baseline case; (b) 3D design

Fig. 8.3-26 shows the rear view of the entropy generation on the suction side of the aerofoil with a loss core forming which grows in intensity and magnitude towards the trailing edge for the baseline case, whereas only a small loss core is observed for the 3D design due to the much reduced secondary flow. Furthermore, the baseline

case results show a strong shear layer on the suction side of the aerofoil (with a radial velocity component of $V_r \approx 0.6$) which is fuelled by the strong cross passage flow.

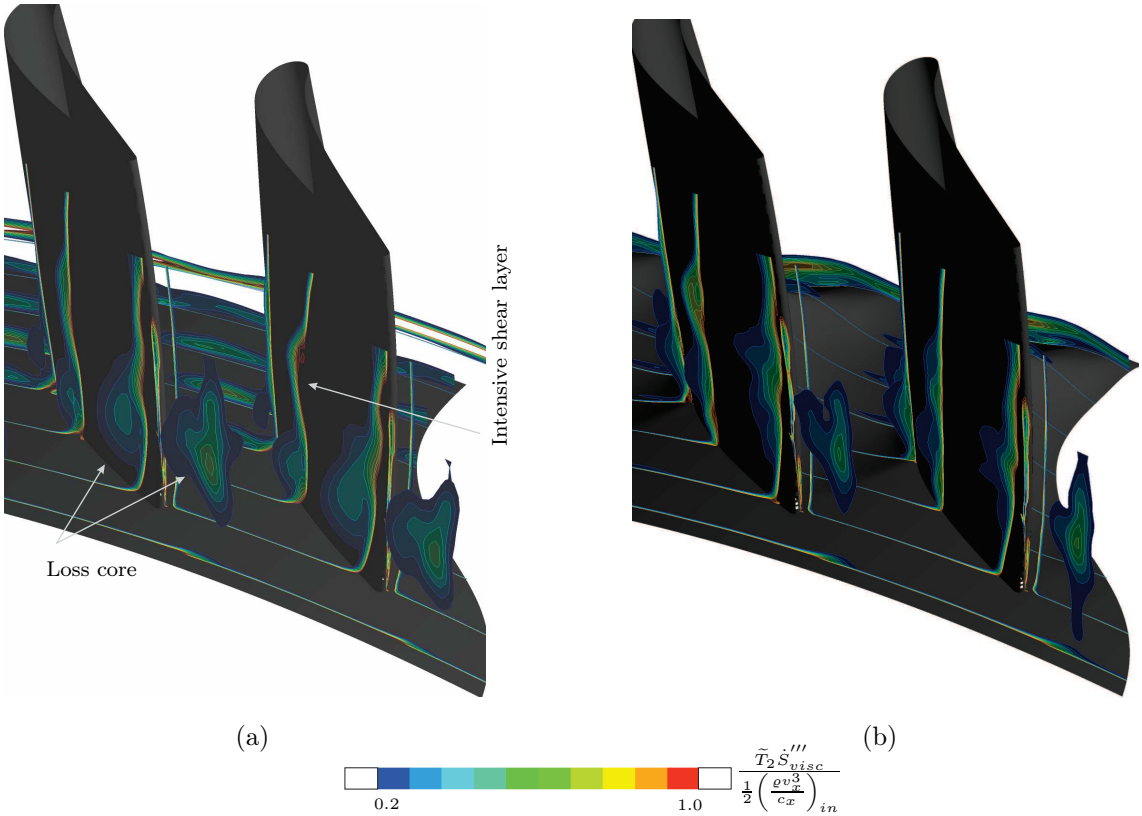

FIG. 8.3-26: Contour plot with generated entropy per unit volume; (a) baseline case; (b) 3D design

Addressing the egress-mainstream interaction in the present fashion with an interdisciplinary approach both from a secondary air system and aerodynamic point of view, contributes to an improvement of the cooled stage efficiency in excess of 1% for the 3D design compared to the baseline case.

8.4 Practical Implications

This chapter discussed the numerical investigation of egress-mainstream interaction with the intent to derive an endwall concept to minimise the interaction loss. The combination of an elongated leading edge feature and an egress channel lead to reduced aerodynamic interaction of the egress flow with the mainstream flow as well to minimised secondary flow losses.

The elongated leading edge feature extended into the rotor passage adds additional mass to the rotor endwall and increases the thermal inertia. A further

investigation needs to clarify if additional cooling technology must be applied to the endwall to maintain the temperature at acceptable levels.

To fully exploit this endwall concept, further investigation should focus on the driving parameters, i.e. channel depth and length and leading edge radial extent to name just a few. This work should be supported with an experimental rig, which could provide vital information on the validity of the numerical results. For more information on this experimental work, the reader is referred to Chapter 9.

Chapter 9

Conclusions and Future Work

This thesis covered the implementation of a newly-developed orifice model into a proprietary secondary air system 1D flow network solver. This model has become a useful tool when used together with the derived extrapolation method to scale relevant test rig input data from an incompressible regime to engine conditions. The major focus of the thesis was on the computational prediction of ingress, with the investigation of external aerodynamic off-design conditions and its effect on the wheel-space fluid dynamics, and the numerical investigation of novel rim-seal concepts to minimise ingress. The results of the latter study were validated and confirmed with experimental tests with the ingress test facility at the University of Bath. This research was complemented with a study to examine the aerodynamic interaction of the egress flow with the main gas path flow.

The conclusions from the thesis chapters are summarised below with the outlook of future work.

9.1 Secondary Air Systems

A recently developed theoretical orifice model was translated into a practical tool and successfully implemented into the Siemens SAS solver. Comparison between this model and a standard industrial procedure to capture ingress in a 1D flow network was generally good, despite a divergence at high values of sealing effectiveness.

To complement this tool, a database with various industrially relevant rim-seal geometries should be incorporated into the program to provide the engine designer support in the selection of orifice model parameters. Further research will focus on tests with a 1.5 turbine stage ingress facility with engine representative aerofoils to provide the engine designer with more accurate input for the prediction of the

ingress, egress and sealing flow rates.

9.2 CFD Model Validation

Computations of the EI ingress-driving peak-to-trough pressure in the gas path showed reasonable agreement with measurements at locations at the vane trailing edge and the outer casing. The measured radial variation of the circumferential velocity was predicted accurately with transient computations indicating that the fluid mechanics and the mixing process are well represented, despite the fact that the URANS computations could not fully re-produce the mixed-out sealing effectiveness measured in the inner part of the wheel-space.

9.3 Extrapolation Method

A procedure was derived to enable the extrapolation of the orifice model sealing parameter Φ_{min} from one Mach number to another. The extrapolation method uses the linear saw-tooth model introduced by Owen et al. (2010b) to correlate Φ_{min}, the non-dimensional sealing flow rate to prevent ingress, to the ingress driving peak-to-trough pressure difference in the gas path. This method showed good agreement with the computed values of Φ_{min} over the Mach number range investigated.

It was proposed that this method can be used to extrapolate measured sealing effectiveness obtained from a test facility to a geometrically-similar engine. $\Phi_{min,rig}$ would be provided by a test facility at incompressible conditions. Computation can be used to determine ΔC_p in the gas path at the rig and the engine relevant conditions and $\Phi_{min,eng}$ can be calculated as follows

$$\frac{\Phi_{min,eng}}{\Phi_{min,rig}} = \left(\frac{\Delta C_{p,eng}}{\Delta C_{p,rig}} \right)^{1/2} \tag{9.3-1}$$

where the subscript $_{rig}$ and $_{eng}$ refer to the conditions in the test facility and the engine respectively.

The advantage of this method is that good estimates of ΔC_p can be obtained by transient or even steady-state computation and that time-consuming simulation of ingress at the compressible conditions is not required. This gives the SAS designer a useful tool to adjust the Φ_{min} parameter to engine conditions.

A caveat is that this method was only tested for subsonic gas path conditions and that the onset of shockwaves in the transonic regime might have a significant influence.

9.4 Off-Design Conditions

The linear variation of $\Delta C_p^{1/2}$ with flow coefficient observed experimentally could be confirmed numerically with a transient CFD simulation with $C_F \succ 0.2$. With further decreasing flow coefficient, the CFD results diverged from this behaviour with an increase in $\Delta C_p^{1/2}$ as C_F decreased. This could be attributed to the effect of the rotor blade at large deviation angle, i.e. $|\beta - \beta_o| \succ 120°$.

Gas concentration measurements were conducted for an axial and radial clearance seal using CO_2 to determine the sealing parameter Φ'_{min}. Scobie et al. (2013) used the CI equation to correlate the variation of Φ_{min} to C_F. The CI equation showed good agreement with variation of Φ'_{min} with C_F. An increase in Φ'_{min} with a $C_F \prec 0.1$ for all seals was observed. This increase is consistent with the rise in the computed value $\Delta C_p^{1/2}$. This increase was caused by the blade effect, where the flow field impinges on the symmetrical rotor blade.

The steady Scanivalve pressure measurement system failed to capture this non-linear pressure component induced by the rotor blade. It is recommended to repeat this test with an unsteady pressure measurement to confirm the observation made by the unsteady computations.

Even though the off-design range investigated was beyond an operating engine off-design condition, a final conclusion can only be made generally after the experiments and computations are repeated with an engine representative blade geometry, to investigate this observed anomaly in ΔC_p at low C_F exists in engine geometries within the operating range of gas turbines.

9.5 Investigation of Rim-Seal Geometries

The proposed rim-seal design addresses the root cause of hot gas ingestion by attenuating the tangential pressure variation, which reduces the ingress levels into the wheel-space by $\approx 40\%$ relative to the baseline design.

There remains an unanswered question which could not be addressed during this work. What is the optimal size and shape of the cavity surrounded by the angel wing to attenuate the tangential pressure variation most effectively and what are the implications on the heat transfer to the surrounding metal components?

The CFD modelling approach captured the rim-seal mechanics correctly and it was shown that this is a promising approach to develop new rim-seal designs, but at the expense of high hardware and software demands due to the transient nature of the flow. The CFD model described in Chapter 6 "Off-Design Conditions", however, has the potential to overcome these limitations.

9.6 Egress-Mainstream Interaction

The egress-mainstream investigation with various endwall concepts showed that a concave axis-symmetric feature and the 3D design did not negatively impact the ingress level of the upstream-located wheel-space. However, only the 3D design with elongated LE feature with an egress channel incorporated addresses the root cause of the secondary flows by decreasing the pressure gradient within the blade passage. Channelling the egress flow out of the rim-seal region into the gas path channel reduces the viscous mixing between the flows. The LE feature prevents the roll-up of the horseshoe vortex in front of the aerodynamic leading edge by reducing the resultant pressure gradient in the near endwall region. The combination of these features effectively decrease the secondary flow losses, the losses associated with the egress-mainstream interaction, without having a negative impact on hot gas ingestion, leading to a considerable increase in turbine stage efficiency.

This work showed that major improvements in terms of engine efficiency can be made through an unified approach; i.e. the external aerodynamics and the internal air system. As a follow-on project of this dissertation, there will be a new research project between Siemens and the University of Bath to validate the benefits observed computationally with an experimental low-speed, large-scale test rig to investigate the interaction of the internal air system with the main gas path flow. The objectives of this project submitted to the Engineering and Physical Sciences Research Council (EPSRC) to attract funding, are as follows:

- To map the trajectory of the discharged egress flow from the wheel-space and its interaction with the annulus gas path flow by using Planar Laser-Induced Fluorescence (PLIF)

- To measure torque and the total pressure loss across the stage in order to quantify the aerodynamic loss
- To optimise the rim-seal geometry, clearance profile and the shape of the turbine endwall in order to minimise the aerodynamic interaction loss
- To measure the velocity and the pressure in the wheel-space and to determine the concentration sealing effectiveness
- To provide experimental data for validation the numerical models

The intention is to seed the sealing flow with 100% CO_2 which is made to fluoresce through a dye laser. The laser is split into two sources to maximize the measurement region as shown in Fig. 9.6-1. A high-resolution low-noise infrared camera moves radially through the range of z-planes. The result of the experiment is a volume of phase-averaged concentration measurements covering the inter-blade and upstream regions of the rotor blade with a resolution of approximately 0.25mm $\times$ 0.25mm $\times$ 1mm. This will allow the direct concentration comparison with the results of the CFD codes.

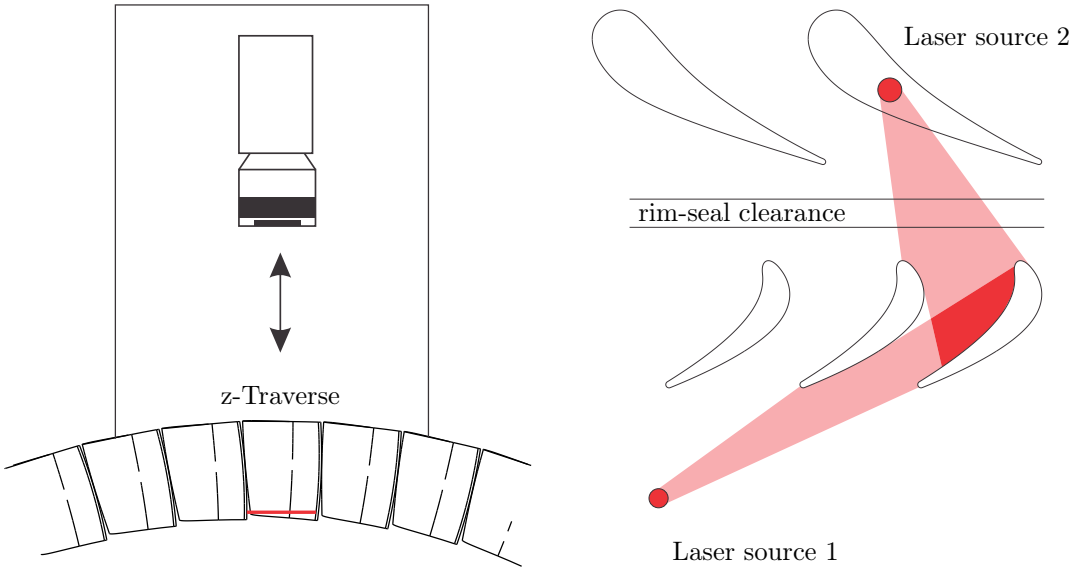

FIG. 9.6-1: Planar Laser-Induced Fluorescence system for the large scale egress-mainstream interaction test rig

Bibliography

Aktins, M. J. (1987). Secondary Losses and End-Wall Profiling in a Turbine Cascade. *IMechE*, Vol. C255/87:pp. 29–42.

Bancalari, E. (2000). Airfoil Leading Edge Vortex Elimination Device. *WO 00/61918*.

Batchelor, G. K. (1951). Note on a Class of Solutions of the Navier-Stokes Equations Representing Steady Rotationally-Symmetric Flow. *Quart. J Mech Appl. Math. 4*, pp. 29 - 41.

Beeck, A. R. (2013). Turbine Blade or Vane with Separate Endwall. *US2013/0004331 A1*.

Bohn, D. and Wolff, M. (2003). Improved Formulation to Determine Minimum Sealing Flow for Different Sealing Configurations. *Proceedings of 2003 ASME Turbo Expo: Power for Land, Sea and Air, June 16 - 19, 2003, Altanta, USA*, GT2003-38465.

Boyce, M. P. (1996). *Gas Turbine Engineering Handbook*. Gulf Professional Publishing, Third edition.

Brandvik, T. and Pullan, G. (2009). An Accelerated 3D Navier-Stokes Solvers for Flows in Turbomachines. *Proceedings of ASME Turbo Expo 2009: Power for Land, Sea and Air*, June 8 - 12, 2009, Orlando, USA. *GT2009 - 60052*.

Brandvik, T. and Pullan, G. (2010). Large-Scale Gas Turbine Simulations on GPU Clusters. *GPU Technology Conference GTC 2010*, Presentation.

Brennan, G., Harvey, N. W., Rose, M. G., Fomison, N., and Taylor, M. D. (2001). Improving the Efficiency of the Trent 500 HP Turbine Using Non-Axisymmetric End Walls: Part 1 Turbine Design. *Proceedings of ASME Turbo Expo 2001*, ASME paper *GT2001-0444*.

Brillert, D. (2001). *Calculation of Cooling and Sealing Air Flow in Gas Turbines for Optimization of the Secondary Air System*. PhD thesis, University Duisburg.

Chen, J. X., Gan, X., and Owen, J. M. (1996). Heat Transfer in an Air-Cooled Rotor-Stator System. *ASME J. Turbomach. 113(1)*, pp. 91 - 97.

Childs, P. R. N. (2011). *Rotating Flow*. Butterworth-Heinemann, Oxford.

Coren, D. D., Atkins, N. R., Turner, J. R., Eastwood, D. E., Davies, S., Childs, P. R. N., Dixon, J. A., and Scanlon, T. S. (2010). A Advanced Multi-Configuration Stator Well Cooling Test Facility. *Proceedings of ASME Turbo Expo 2010: Power for Land, Sea and Air*, ASME Paper *GT2010 - 23450*.

Dawes, W. N. (1986). A Numerical Analysis of Three-Dimensional Viscous Flow in a Transonic Compressor Rotor and Comparison with Experimental Data. ASME paper. *86-GT-16*.

Dawes, W. N. (1992). Toward Improved Throughflow Capability. ASME J. Turbo., 114(8):pp. 8 –17.

Dejc, M. E. and Zarjankin, A. E. (1960). Methods of Increasing the Efficiency of Turbine Stages. *Teploenergetika*, Vol. 2:pp. 18–24.

Denton, J. D. (1975). A Time Marching Method for Two and Three Dimensional Blade to Blade Flow. *Aero. Res.*, Coun. 3775.

Denton, J. D. (1979). Extension of the Finite Volume Time Marching Method to Three Dimensions. VKI Lecture Series 1979.

Denton, J. D. (1982). An Improved Time Marching Method for Machinery Flow Calculations. ASME paper *82-GT-239*.

Denton, J. D. (1985). Calculation of three dimensional flow through any type of turbomachine. AGARD Lecture Series 140.

Denton, J. D. (1990). The Calculation of Three Dimensional Viscous Flow through Multistage Turbomachines. ASME 90-GT-19.

Denton, J. D. and Dawes, W. N. (1999). Computational Fluid Dynamics for Turbomachinery Design. *IMechE*, Proc Instn Mech Engrs Vol 213 Part C.

Dunn, D. M., Zhou, D. W., Saha, K., Squires, K. D., Roy, R. P., Kim, Y. W., and Moon, H. K. (2010). Flow field in a single-stage model air turbine rotor-stator cavity with pre-swirled purge flow. *Proceedings of ASME Turbo Expo 2010: Power for Land, Sea and Air*, ASME Paper *GT2010 - 22869*.

Elliott, B., Sayma, A., and Imregun, M. (2005). Aeromechanical Design of Damped High Pressure Turbine Blade Subject to Low Engine Order Forcing. *Rolls-Royce plc, Derby and Imperial College London*.

Gallimore, S. J. (1997). Viscous Throughflow Modelling of Axial Compressor Blade Rows Using a Tangential Blade Force Hypothesis. ASME paper *97-GT-415*.

Gregory-Smith, D. G., Ingram, G., Jayaraman, P., Harvey, N. W., and Rose, M. G. (2001). Non-Axisymmetric Turbine End Wall Profiling. *Proceedings of the* 4^{th} *European Conference on Turbomachinery*, 653-664, ISBN 88-86281-57-9.

Greitzer, E. M. and Tan, C. S. (2004). *Internal Flow*. Cambridge University Press, New York, NY.

Hamabe, K. and Ishida, K. (1992). Rim Seal Experiments and Analysis of a Rotor-Stator System with Nonaxisymmetric Main Flow. *Proceedings of ASME Turbo Expo 1992: Power for Land, Sea and Air*, ASME Paper *92-GT-160*.

Hartland, J., Gregory-Smith, D. G., Harvey, N. W., and Rose, M. G. (1999). Non-axisymmetric turbine endwall design: Part ii experimental validation. ASME paper *99-GT-338*.

Harvey, N. W., Stokes, M. R., and Bagshaw, D. A. (2008). Turbine Blade for a Turbomachine. *EP1967694A2*.

He, L. (1996). Modelling Issues for Computation of Unsteady Turbomachinery Flows. *Unsteady Flows in Turbomachines*, VKI Lecture Series 1996-05, von Karman Institute for Fluid Dynamics.

Hirsch, C. and Denton, J. D. (1981). Throughflow Calculations in Axial Turbines. AGARD AR175.

Hodson, H. P. (1985). Measurements of Wake Generated Unsteadiness in the Rotor Passages of Axial Flow turbines. *J. Eng. Gas Turbines Power*, Vol. 107:pp. 337 – 344.

Hunt, R. J. (2011). The History of the Industrial Gas Turbine. Part 1: The First Fifty Years 1940 - 1990. *IDGTE*, 582.

Ingram, G., Gregory-Smith, D., Rose, M., Harvey, N., and Brennan, G. (2002). The Effect of End Wall Profiling on Secondary Flow and Loss Development in a Turbine Cascade. ASME paper *GT2002-30339*.

Irvine, T. F. (1998). Handbook of Heat Transfer. *McGraw-Hill, New York, ch. 2: Thermophysical Properties*, W. M. Rohsenow, J. P. Hartnett and Y. I. Cho (eds.).

Jakoby, R., Zierer, T., de Vito, L., Lindblad, K., Larsson, J., Bohn, D. E., Funcke, J., and Decker, A. (2004). Numerical Simulation of the Unsteady Flow Field in an Axial Gas Turbine Rim Seal Configuration. *Proceedings of ASME Turbo Expo 2004: Power for Land, Sea and Air*, June 14 - 17, 2004, Vienna, Austria. *GT2004 - 53829*.

Jameson, A. (1991). Time Dependent Calculations Using Multigrid with Applications to Unsteady Flows Past Airfoils and Wings. *AIAA 91 - 1596*.

Johnson, B. V., Mack, G. J., Paolillo, R. E., and Daniels, W. A. (1994). Turbine Rim Seal Gas Path Flow Ingestion Mechanisms. *AIAA Paper*, AIAA 94 - 2703.

Johnson, B. V., Wang, C. H., and Roy, P. R. (2008). A Rim Seal Orifice Model with Two Cds and Effect of Swirl in Seals. *Proceedings of ASME Turbo Expo 2008: Power for Land, Sea and Air*, ASME Paper *GT2008 - 50650*.

Julien, S., Lefrancois, J., Dumas, G., Boutet-Blais, G., Lapoint, S., and Caron, J.-F. (2010). Simulations of Flow Ingestion and Related Structures in a Turbine Disk Cavity. *Proceedings of ASME Turbo Expo 2010: Power for Land, Sea and Air*, ASME Paper *GT2010 - 22729*.

Khilnani, V. I. and Bhavnani, S. H. (2001). Sealing of Gas Turbine Disk Cavities Operating in the Presence of Mainstream External Flow. *Exp. Thermal Fluid Sci. 25(3-4):*, pages 306 – 315.

Laitone, E. V. (1951). New Compressibility Correction for Two-dimensional Subsonic Flow. *J. Aeronaut. Sci, vol. 18, no. 5*, page 350.

Lalwani, Y. (2014). *3D Steady-State Computational Study of Ingestion through Gas Turbine Rim Seals*. PhD thesis, University of Bath.

Lee, C. P. (2006). Cresentic Ramp Turbine Stage. *EP 1712737 A1*.

Li, Y. S. and Teuber, R. (2013). Siemens Patent Application 3.

Menter, F. (1994). Two-Equation Eddy-Viscosity Turbulence Models for Engineering Applications. *AIAA Journal, 32*, pp. 1598-1605.

Mirzamoghadam, A. V., Heitland, G., Morris, M. C., Smoke, J., Malak, M., and Howe, J. (2008). 3D CFD Ingestion Evaluation of a High Pressure Turbine Rim Seal Disk Cavity. *Proceedings of ASME Turbo Expo 2008: Power for Land, Sea and Air*, ASME Paper *GT2008 - 50531*.

Morris, A. W. H. and Hoare, R. G. (1975). Secondary Loss Measurements in a Cascade of Turbine Blades with Meridional Wall Profiling. ASME Paper *75-WA/GT-30*.

Owen, J. M. (2009a). Prediction of Ingestion through Turbine Rim Seals. Part 1: Rotationally-Induced Ingress. *Proceedings of ASME Turbo Expo 2009: Power for Land, Sea and Air*, June 8 - 12, 2009, Orlando, Florida, USA. *GT2009 - 59121*.

Owen, J. M. (2009b). Prediction of Ingestion through Turbine Rim Seals. Part 2: Externally-Induced and Combined Ingress. *Proceedings of ASME Turbo Expo 2009: Power for Land, Sea and Air*, June 8 - 12, 2009, Orlando, Florida, USA. *GT2009 - 59122*.

Owen, J. M., Pountney, O., and Lock, G. (2010a). Prediction of Ingress through Turbine Rim Seals. Part 2: Combined Ingress. *Proceedings of ASME Turbo Expo 2010: Power for Land, Sea and Air*, June 14 - 18, 2010, Glasgow, UK. *GT2010 - 23349*.

Owen, J. M. and Rogers, R. H. (1989). *Flow and Heat Transfer in Rotating-Disc Systems*. Research Studies Press Ltd., Taunton, UK, 1st edition.

Owen, J. M., Zhou, K., Pountney, O., Wilson, M., and Lock, G. (2010b). Prediction of Ingress through Turbine Rim Seals. Part 1: Externally-Induced Ingress. *Proceedings of ASME Turbo Expo 2010: Power for Land, Sea and Air*, June 14 - 18, 2010, Glasgow, UK. *GT2010 - 23346*.

Phadke, U. P. and Owen, J. M. (1988a). Aerodynamic Aspects of the Sealing of Gas-Turbine Rotor-Stator Systems. Part 1: The Behavior of Simple Shrouded Rotating-Disk Systems in a Quiescent Environment. *International Journal of Heat and Fluid Flow*, Vol 9, No 2: 98 – 105.

Phadke, U. P. and Owen, J. M. (1988b). Aerodynamic Aspects of the Sealing of Gas-Turbine Rotor-Stator Systems. Part 3: The Effect of Nonaxisymmetric External Flow on Seal Performance. *International Journal of Heat and Fluid Flow*, Vol 9, No 2: 113 – 117.

Popovic, I. and Hodson, H. P. (2012a). Improving Turbine Stage Efficiency and Sealing Effectiveness through Modifications of the Rim Seal Geometry. *Proceedings of ASME Turbo Expo 2012: Power for Land, Sea and Air*, June 11 - 15, 2012, Copenhagen, Denmark. *GT2012 - 68026*.

Popovic, I. and Hodson, H. P. (2012b). The Effects of a Parametric Variation of the Rim Seal Geometry on the Interaction between Hub Leakage and Mainstream Flows in HP Turbines. *Proceedings of ASME Turbo Expo 2012: Power for Land, Sea and Air*, June 11 - 15, 2012, Copenhagen, Denmark. *GT2012 - 68025*.

Pountney, O. J. (2012). *Ingestion through Gas Turbine Rim Seals: Fluid Dynamics and Heat Transfer*. PhD thesis, University of Bath.

Pountney, O. J., Sangan, C. M., Owen, J. M., and Lock, G. D. (2012). Effect of Ingestion on Heat Transfer to Turbine Disc. *Proceedings of ASME Turbo Expo 2012: Power for Land, Sea and Air*, June 11 - 15, 2012, Copenhagen, Denmark. *GT2012 - 68496*.

Praisner, T. J., Allen-Bradley, E., Grover, E. A., Knezevici, D. C., and Sjolander, S. A. (2007). Application of Non-Axisymmetric Endwall Contouring to Conventional and High-Lift Airfoils. *Proceedings of ASME Turbo Expo 2007: Power for Land, Sea and Air*, May 14 - 17, 2007, Montreal, Canada. *GT2007 - 27579*.

Rabs, M., Benra, F.-K., Dohmen, H. J., Lock, G. D., and Schneider, O. (2012). Model Simplification for Numerical Simulation of Ingestion Through Gas Turbine Rim Seals.

14^{th} *International Symposium on Transport Phenomena and Dynamics of Rotating Machinery, ISROMAC-14*, February 27 - March 2, 2012, Honolulu, HI, USA.

Rolls-Royce (1996). *The Jet Engine*. Derby: Rolls-Royce plc.

Rose, M. G. (1994). Non-Axisymmetric Endwall Profiling in the HP NGVs of an Axial Flow Gas Turbine. ASME paper *94-GT-249*.

Rose, M. G., Harvey, N. W., Seaman, P., Newman, D. A., and McManus, D. (2001). Improving the Efficiency of the Trent 500 HP Turbine Using Non-Axisymmetric End Walls: Part 2 Experimental Validation. *Proceedings of ASME Turbo Expo 2001*, ASME paper *GT2001-0505*.

Sakamoto, Y., Ito, E., Wakazono, S., and Hiyama, T. (2010). Turbine Blade Cascade Endwall. *US2010/0284818 A1*.

Sangan, C. M. (2011). *Measurements of Ingress through Gas Turbine Rim Seals*. PhD thesis, University of Bath.

Sangan, C. M., Lalwani, Y., Owen, J. M., and Lock, G. D. (2013). Experimental Measurements of Ingestion through Turbine Rim Seals. Part 5: Fluid Dynamics of Wheel-Space. *Proceedings of ASME Turbo Expo 2013: Power for Land, Sea and Air*, Asme Paper *GT2013 - 94148*.

Sangan, C. M., Pountney, O. J., Scobie, J. A., Wilson, M., Owen, J. M., and Lock, G. D. (2012). Experimental Measurements of Ingestion through Turbine Rim Seals. Part 3: Single and Double Seals. *Proceedings of ASME Turbo Expo 2012: Power for Land, Sea and Air*, June 11 - 15, 2012, Copenhagen, Denmark. *GT2012 - 68493*.

Sangan, C. M., Pountney, O. J., Zhou, K., Wilson, M., Owen, J. M., and Lock, G. D. (2011a). Experimental Measurements of Ingestion through Turbine Rim Seals. Part 1: Externally-Induced Ingress. *Proceedings of ASME Turbo Expo 2011: Power for Land, Sea and Air*, June 6 - 10, 2011, Vancouver, Canada. *GT2011 - 45310*.

Sangan, C. M., Pountney, O. J., Zhou, K., Wilson, M., Owen, J. M., and Lock, G. D. (2011b). Experimental Measurements of Ingestion through Turbine Rim Seals. Part 2: Rotationally-Induced Ingress. *Proceedings of ASME Turbo Expo 2011: Power for Land, Sea and Air*, June 6 - 10, 2011, Vancouver, Canada. *GT2011 - 45313*.

Schlienger, J., Kalfas, A. I., and Abhari, R. S. (2004). Vortex-Wake-Blade Interaction in a Shrouded Axial Turbine. *Proceedings of ASME Turbo Expo 2004: Power for Land, Sea and Air*, June 14 - 17, 2004, Vienna, Austria. *GT2004 - 53915*.

Schuepbach, P., Abhari, R. S., Rose, M. G., Germain, M., Raab, I., and Gier, J. (2008a). Improving Efficiency of a High Work Turbine Using Non-Axisymmetric Endwalls. Part II: Time-Resolved Flow Physics. ASME paper *GT2008-50470*.

Schuepbach, P., Rose, M., Abhari, R. S., Germain, M., Raab, I., and Gier, J. (2008b). Improving Efficiency of a High Work Turbine Using Non-Axisymmetric Endwalls. Part I: Endwall Design and Performance. ASME paper *GT2008-50469*.

Scobie, J. A., Sangan, C. M., Teuber, R., Pountney, O. J., Owen, J. M., Wilson, M., and Lock, G. D. (2013). Experimental Measurements of Ingestion through Turbine Rim Seals. Part 4: Off-Design Conditions. *Proceedings of ASME Turbo Expo 2013: Power for Land, Sea and Air*, June 3 - 7, 2013, San Antonio, USA. *GT2013 - 94147*.

Sieverding, C. H. (1984). Recent Progress in the Understanding of Basic Aspects of Secondary Flows in Turbine Blade Passages. ASME *84 - GT - 78*.

Smith, P. E. J., Mugglestone, J., Tham, K. M., Long, C. A., and Coren, D. D. (2012). Conjugate Heat Transfer CFD Analysis in Turbine Disc Cavities. *Proceedings of ASME Turbo Expo 2012: Power for Land, Sea and Air, June 11 - 15, 2012, Copenhagen, Denmark*, Asme Paper *GT2012 - 69597*.

Speziale, C. G., Sarkar, S., and Gatski, T. B. (1991). Modelling the Pressure-Strain Correlation of Turbulence: An Invariant Dynamical Systems Approach. *J. Fluid Mechanics, 277*, pp. 247-272.

Teuber, R. and Li, Y. S. (2013a). Siemens Patent Application 1.

Teuber, R. and Li, Y. S. (2013b). Siemens Patent Application 2.

Teuber, R., Wilson, M., Lock, G., Owen, J., Li, Y. S., and Maltson, J. (2013). Computational Extrapolation of Turbine Sealing Effectiveness from Test Rig to Engine Conditions. *Proceedings of the Institution of Mechanical Engineers, Part A: Journal of Power and Energy*, 227 (2):pp. 167 – 178.

Owen, J. M. (2010). Theoretical Modelling of Hot Gas Ingestion through Turbine Rim Seals. *Third International Symposium On Jet Propulsion and Power Engineering*, September 13 - 17, 2010, Nanjing, China.

Vasanthakumar, P. (2003). *Three Dimensional Frequency-Domain Solution Method for Unsteady Turbomachinery Flows*. PhD thesis, Durham University.

Wang, C. Z., Mathiyalagan, S. P., Johnson, B. V., Glahn, J. A., and Cloud, D. F. (2013). Rim Seal Ingestion in a Turbine Stage from 360 Degree Time-Dependent Numerical Simulations. *J. Turbomach.*, 136(3), 031007.

Wilcox, D. C. (1986). Multiscale Model for Turbuent Flows. *In AIAA 24th Aerospace Sciences Meeting.*

Wu, C. H. A. (1951). A General through Flow Theroy of Fluid Flow with Subsonic or Supersonic Velocities in Turbomachines of Arbitrary Hub and Casing Shapes. NACA paper. TN2302.

Zhou, K., Wood, S. N., and Owen, J. M. (2011). Statistical and Theoretical Models of Ingestion through Turbine Rim Seals. *Proceedings of ASME Turbo Expo 2011: Power for Land, Sea and Air*, ASME Paper *GT2011 - 45139*.

Zlalinov, M. B., Tan, C. S., Montgomery, M., Islam, T., and Seco-Soley, M. (2011). Turbine Hub and Shroud Sealing Flow Loss Mechanisms. *Proceedings of ASME Turbo Expo 2011: Power for Land, Sea and Air*, June 6 - 10, 2011, Vancouver, Canada. *GT2011 - 46718*.

Appendix A

Experimental Uncertainty

The uncertainty of the concentration measurements were reported by Sangan et al. (2012). For convenience, the equations have been re-produced and were used to computed the average standard deviation.

The concentration effectiveness ε_c is given by eq. A.0-1

$$\varepsilon_c = \frac{c_s - c_a}{c_o - c_a} \tag{A.0-1}$$

where the subscripts s, o and a refer to fluid at the sampling point, to the superimposed air, the fluid in the main gas path. The uncertainties to these quantities are defined by δ_ε, δ_s, δ_o and δ_a.

$$\begin{aligned}
\varepsilon_c \pm \delta_\varepsilon &= \frac{c_s \pm \delta_s - (c_a \pm \delta_a)}{c_o \pm \delta_o - (c_a \pm \delta_a)} \\
&= \frac{(c_s - c_a)[1 + (\pm\delta_s \pm \delta_a)/(c_s - c_a)]]}{(c_o - c_a)[1 + (\pm\delta_o \pm \delta_a)/(c_o - c_a)]} \\
&= \varepsilon_c \frac{[1 + (\pm\delta_s \pm \delta_a)/(c_s - c_a)]}{[1 + (\pm\delta_o \pm \delta_a)/(c_o - c_a)]}
\end{aligned} \tag{A.0-2}$$

If $(\pm\delta_o \pm \delta_a)/(c_o - c_a) \prec\prec 1$ then

$$\varepsilon_c + |\delta_\varepsilon| \leq \left(1 + \frac{|\delta_s| + |\delta_a|}{c_s - c_a} + \frac{|\delta_o| + |\delta_a|}{c_o - c_a}\right) \tag{A.0-3}$$

Hence,

$$\frac{|\delta_{\varepsilon_c}|}{\varepsilon_c} \leq \left(\frac{|\delta_s| + |\delta_a|}{c_s - c_a} + \frac{|\delta_o| + |\delta_a|}{c_o - c_a}\right) \tag{A.0-4}$$

$$\frac{|\delta_{\varepsilon_c}|}{\varepsilon_c} \leq 2\delta \frac{1+\varepsilon_c^{-1}}{c_o - c_a} \tag{A.0-5}$$

$$|\delta_{\varepsilon_c}| \leq 2\delta \frac{1+\varepsilon_c}{c_o - c_a} \tag{A.0-6}$$

The average standard deviation, σ, is found with eq. A.0-6 in the following range $0 \prec \varepsilon_c \prec 1$ as follows

$$\sigma = \frac{2\delta}{c_o - c_a} \sqrt{\int_0^1 (1+\varepsilon_c)^2 d\varepsilon_c} = 3.06 \frac{\delta}{c_o - c_a} \tag{A.0-7}$$

In the ingestion experiments presented in this thesis were used a CO_2 concentration in the sealing flow. The scale of the gas analyser was set to a maximum scale of 1% which gives with eq. A.0-6 and A.0-7 a $\sigma = 0.046$.

Tab. A-1: Summary of seal parameter for all concepts based for $r/b = 0.850$

Seal	Φ_{min}	Φ'_{min}	Γ_c	σ
B	0.0520	0.365	0.470	0.0103
$C.1$	0.0398	0.313	1.022	0.0169
$C.2$	0.0339	0.239	0.487	0.0171
$C.3$	0.0377	0.266	0.489	0.0112
$C.4$	0.0319	0.222	0.450	0.0117
O	0.0253	0.209	1.663	0.0210

Tab. A-2: Summary of seal parameter for all concepts for $r/b = 0.958$

Seal	Φ_{min}	Φ'_{min}	Γ_c	σ
B	0.1089	0.0962	4.479	0.0146
$C.1$	0.1063	0.0868	1.451	0.0159
$C.2$	0.0984	0.0824	1.915	0.0124
$C.3$	0.1011	0.0849	2.002	0.0120
$C.4$	0.0942	0.0820	3.419	0.0137
O	0.1071	0.0902	2.063	0.0158

Tab. A-3: Summary of seal parameter for optimised seal

r/b	Φ_{min}	Φ'_{min}	Γ_c	σ
0.958	0.1069	0.0902	2.117	0.0137
0.925	0.0636	0.0483	0.771	0.0120
0.898	0.0404	0.0293	0.570	0.0113
0.850	0.0336	0.0233	0.447	0.0132

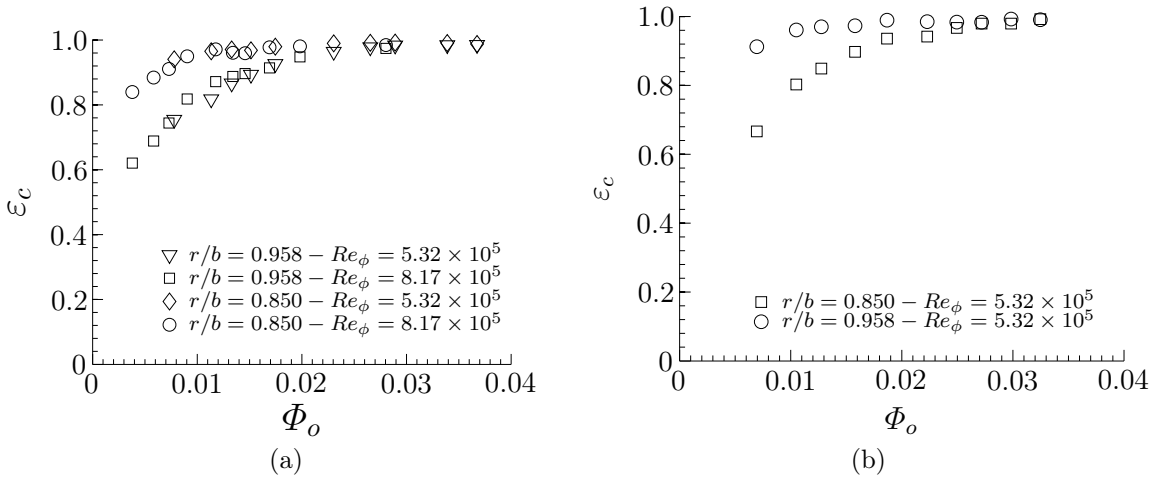

FIG. A.0-1: Variation of sealing effectiveness with Φ_o for $C.2$ and $C.4$ for RI ingress